ISTITUTO NAZIONALE DI FISICA NUCLEARE
Laboratori Nazionali di Frascati

FRASCATI PHYSICS SERIES

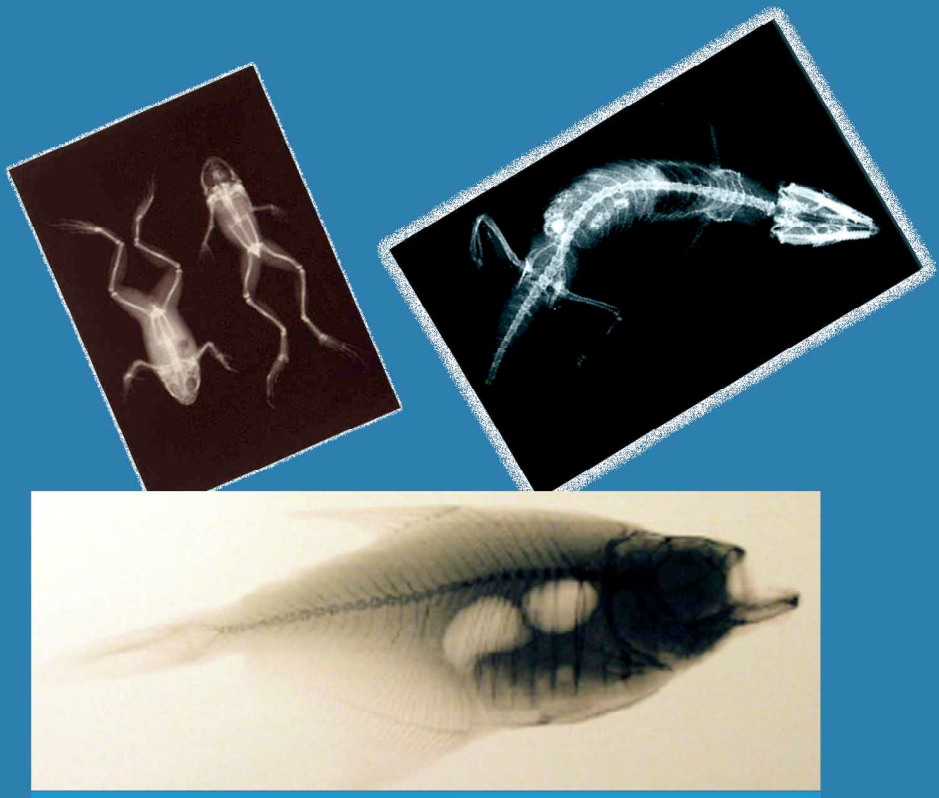

Editors
A. Bianconi, A. Marcelli, N.L. Saini

19th INTERNATIONAL CONFERENCE ON X-RAY AND INNER-SHELL PROCESSES

FRASCATI PHYSICS SERIES

Series Editor
Stefano Bianco

Technical Editor
Luigina Invidia

Cover: *Top left – X-ray image of a frog in belly and upside-down position by Wilhelm Conrad Röntgen (spring 1896) – Top right - X-ray image of a lizard using a parallel synchrotron radiation beam of ADONE and a conventional radiographic film (Frascati, 1993 – courtesy E. Burattini) - Bottom - X-ray image of a fish body using a micro focus conventional tube (2002, courtesy A.V. Soldatov and M.A. Kumakhov)*

Volume XXXII

Istituto Nazionale di Fisica Nucleare – Laboratori Nazionali di Frascati
Divisione Ricerca – SIS – Ufficio Pubblicazioni
P.O. Box 13, I–00044 Frascati Roma Italy
email: sis.publications@lnf.infn.it

This book is dedicated to Igor' M. Ternov and Mikhail N. Yakimenko.
Their invaluable contribution to the advancement and the diffusion of the synchrotron radiation can not be disregarded.

FRASCATI PHYSICS SERIES

19th INTERNATIONAL CONFERENCE ON X-RAY AND INNER-SHELL PROCESSES

ISBN 88-86409-39-07

FRASCATI PHYSICS SERIES

Volume XXXII

19th INTERNATIONAL CONFERENCE ON X-RAY AND INNER-SHELL PROCESSES

Editors
A. Bianconi, A. Marcelli, N.L. Saini

Università di Roma "La Sapienza" June 24-28, 2002

International Scientific Committee

S.O. Aksela	*Finland*
Y. Azuma	*Japan*
U.E. Becker	*Germany*
P. Beiersdorfer	*USA*
N. Berrah	*USA*
A. Bianconi	*Italy*
J.E. Burgdoerfer	*USA*
C. Cohen	*France*
D.S. Gemmell	*USA*
A.N. Grum-Grzhimailo	*Russia*
D.W. Lindle	*USA*
A. Marcelli	*Italy*
G. Materlik	*Germany*
N.O.T. Martenson	*Sweden*
P.H. Mokler	*Germany*
T. Mukoyama	*Japan*
M. Pajek	*Poland*
S.A. Sheinerman	*Russia*
M. Simon	*France*
S.H. Southworth	*USA*
T. Suric	*Croatia*
K. Ueda	*Japan*
J. Ullrich	*Germany*
E. Weigold	*Australia*
Y. Yamazaki	*Japan*

Advisory Committee

M. Altarelli	*Italy*
M. Ya Amusia	*Israel, Russia*
J. Baruchel	*France*
E. Burattini	*Italy*
C.T. Chen	*Taiwan*
B. Crasemann	*USA*
P. Durham	*UK*
J. Fadley	*USA*
A. Fontaine	*France*
F. Gianturco	*Italy*
S. Hasnain	*UK*
A. Kotani	*Japan*
I. Lindau	*USA*
J. Mustre de Leon	*Mexico*
H. Oyanagi	*Japan*
M.P. Piancastelli	*Italy*
P. Pianetta	*USA*
D. Raoux	*France*
A. Renieri	*Italy*
A. Soldatov	*Russia*
B.F. Sonntag	*Germany*
H. Tolentino	*Brazil*
Z. Wu	*China*
F. Wuilleumier	*France*

Conference Chair

A. Bianconi	*Roma*
A. Marcelli	*Frascati - Co-chairman*

Local Organizing Committee

A. Bianconi	*Chairman*
A. Marcelli	*Co-chairman*
M. Colapietro	
G.E. Gigante	
N.L. Saini	

Conference Secretary

Anna De Grossi	*Roma La Sapienza*
Lia Sabatini	*Frascati*

ISC Committee X02 Roma

S.O. Aksela	*Finland*
Y. Azuma	*Japan*
U.E. Becker	*Germany*
P. Beiersdorfer	*USA*
N. Berrah	*USA*
A. Bianconi, *Chairman*	*Italy*
J. Burgdörfer	*USA*
C. Cohen	*France*
D.S. Gemmell	*USA*
A.N. Grum-Grzhimailo	*Russia*
D.W. Lindle	*USA*
A. Marcelli, *co-Chairman*	*Italy*
G. Materlik	*Germany*
N.O.T. Martensson	*Sweden*
P.H. Mokler	*Germany*
T. Mukoyama	*Japan*
M. Pajek	*Poland*
S.A. Sheinerman	*Russia*
M. Simon	*France*
S.H. Southworth	*USA*
T. Suric	*Croatia*
K. Ueda	*Japan*
J. Ullrich	*Germany*
E. Weigold	*Australia*
Y. Yamazaki	*Japan*

Constitution of the X-Ray and Inner-Shell Processes Meetings

The continuity of the organization of the X-meetings shall be maintained by the International Scientific Committee.

I

The International Scientific Committee is composed of about 20 members, principally chosen on a scientific basis. Nationalities should be considered in the choice of the members of the Committee. The regular term of members of the Committee is six years. No more than 50% of the members of the Committee can stay for more than six years. The chairpersons of the past, present, and next conferences must be members of the Committee. The members of the Committee are nominated and elected by the previous Committee.

II

The International Scientific Committee will choose the site and chairperson of the next Conference, receive notice of any proposals, and make a preliminary decision regarding the following meeting. Proposals may be submitted at any time up to the next conference. The Committee will define the topics of the conferences and their general orientation. It will make recommendations to the chairperson regarding the list of invited speakers. The Committee will meet at least once during each Conference. Between conferences the Committee will continue to work under the chairperson.

III

At the beginning of each Conference, the chairperson of that Conference shall assume the chair of the International Scientific Committee.

IV

The chairperson of a Conference is in charge of the organization of the meeting, and of securing the necessary funds. He or she decides on the invited speakers upon recommendation of the members of the International Scientific Committee and of the Program Committee.

V

The Program Committee members shall be chosen by the chairperson of the International Committee, on a scientific basis, in such a way that all major topics of the Conference are represented. Under the responsibility of the Chairperson of the International Scientific Committee, the Program Committee examines the contributed papers which have been submitted to a Conference. The Program Committee makes recommendations to the chairperson concerning the list of invited talks and speakers.

VI

To amend the Constitution, the approval of 2/3 of the members of the International Scientific Committee is required. All other Committee action shall be by majority vote of members present at a constitutionally convened meeting which has a quorum. A quorum for such a meeting shall be one half of the members of the Committee plus one. In emergencies, a vote may be taken by mail.


19 th international conference on
X-RAY AND INNER-SHELL PROCESSES
Roma, June 24-28, 2002
Roma X 2002


USCITA DI SICUREZZA

PREFACE

This book, published under the existing long Frascati Physics Series, is the first of its kind, devoted to the solid state problems in physics. In addition to some of the contributions presented at the 19th International Conference on *X-Ray and Inner-Shell Processes (X02)* held in Rome in 2002, which did not appear in the AIP Conference volume (Vol. No. 652, 2003), the present book contains also a few selected contributions relevant to the field.

The X02 *X-Ray and Inner-Shell Processes* Conference was part of the series of conferences devoted to the X-ray science. This X-ray and Inner-Shell conference series was resulted from earlier two series of conferences on X rays, started in 1965 and 1972, which merged together in 1978 in Sendai, Japan. After that, following conferences under the X-ray and Inner-Shell series were held in Europe and America coming back again in Europe, and in Italy for the first time in 2002. The X02, held in Roma was chaired by A. Bianconi and A. Marcelli, and jointly organized by the University of Rome "*La Sapienza*" and the Frascati National Laboratories (LNF) of the INFN, bringing together about 300 scientists from 30 countries.

In addition to a large organizational contribution, the LNF has also made a full support for the publication of this book, including several significant scientific contributions presented at the X02. Although role of the LNF in the frontiers of the X-ray science has been known from early years of the development of Synchrotron radiation sources, e.g., in the early sixties, the pioneering research using the synchrotron light emitted by the electro-synchrotron was performed at Frascati, the present book witnesses the major role of the INFN, and in particular of the LNF, in the X-ray science, and specifically in the advancement of the Italian X-ray Synchrotron radiation research program. Indeed, recently a new synchrotron radiation laboratory at DA□NE is operational at the LNF in Frascati.

It is beyond mentioning that the last decades have seen a large increase in the number of users in the field of X-ray science, not only due to availability of new high-brilliance X-ray sources, but also due to large developments of new spectroscopic techniques. This growth has significantly improved the quality of the research in many interdisciplinary areas of science where x-ray techniques have been applied with a large success. Therefore, this book should serve as a basic reference material for the advancement of the X-ray science.

A sincere acknowledgement is due to the technical editor L. Invidia and to G. Cibin for the professional and enthusiastic contribution given to the preparation of this book.

Antonio Bianconi
Naurang L. Saini
Augusto Marcelli

HISTORICAL REMARKS ON X-RAY SYNCHROTRON RADIATION RESEARCH AT FRASCATI

The publication of the first book of the Frascati Physics Series completely devoted to the condensed matter physics represents certainly the best opportunity to write a brief note about the contribution given by the *Frascati National Laboratories* (LNF) of the *National Institute of Nuclear Physics* (INFN) to the development of the X-ray science during last four decades. The *Frascati National Laboratories* were founded in 1955, a few years before the beginning of the first synchrotron light activities. In fact, already in 1961 a small group of Italian researchers, deeply involved with pioneering works using the first storage ring built in the world, called ADA, to optimize the injection apparatus efficiency monitored the synchrotron radiation emitted in the visible region by less than 100 electrons, using an RCA-6342 photomultiplier.

Almost at the same time, on the basis of an Italian-French cooperation, pioneering absorption spectroscopy measurements began at Frascati, exploiting the parasitic mode of the radiation emitted by the 1.1 GeV electro-synchrotron operating here since 1959. Aim of some of the early experiments was the determination of the absorption coefficients of the Bi, Pb and Ta thin films (1,2) in the soft x-ray region, a domain in which it is difficult to perform experiments. The success of these pioneering synchrotron radiation activities was so exciting that with great enthusiasm new instruments were assembled and at the beginning of 1970 an Italian group was able to operate two new beamlines optimised to work in the near and in the far UV region respectively (3,4,5).

The experimental activity at the electro-synchrotron continued until the end of 1975 when a new wide research program started exploiting the radiation emitted by the ADONE storage ring, the new accelerator built at Frascati and earlier used only for high energy physics experiments. The first X-ray beamline at ADONE, covering the energy range from 3 keV to 12 keV, collected the photons emitted by a bending magnet and was mainly utilized for the X-ray absorption spectroscopy inside a dedicated laboratory called PULS (*Progetto Utilizzazione Luce di Sincrotrone*).

The PULS Laboratory has been managed, up to the beginning of 1993, by a team of scientists who, on the basis of an agreement with the *Italian Research Council* (CNR) and several international cooperations, utilizing five different beamlines carried out a large number of experiments in the x-ray, VUV and optical domains training to many different synchrotron radiation experimental techniques (6,7) tens of young scientists and students which later exported their competences to many other synchrotron radiation facilities.

After an International Summer School on "*Synchrotron Radiation Research*" held in Alghero in September 1976, in collaboration with SSRL (*Stanford Synchrotron Radiation Laboratory*) under the direction of Herman Winick, started the construction of a conventional transverse six-full-poles equivalent wiggler. The Frascati wiggler, the first

built in Europe, with a maximum field of 1.85 T, i.e., near the iron magnetic saturation, became operative in the early 80's (8). The first experimental station, optimized for X-ray absorption spectroscopy in the x-ray region operated a bit later inside a new dedicated synchrotron radiation laboratory named PWA (*Program Wiggler Adone*). Since then, from 1985, three beam lines had been intensively utilized carrying out pioneering experiments on LIGA process for microfabrication technology and, the first biomedical investigations using X-ray synchrotron sources.

In these decades many conferences, meetings, workshops dedicated to synchrotron radiation researches have been supported and hosted by the *Frascati National Laboratories* of the INFN and, certainly LNF represented for many years, for the entire Italian community but not only, a reference site where to discuss new ideas in this field. In addition several pioneering International agreement were signed by INFN with foreigner countries such as Argentina, China, Poland, Russia and Spain and involved synchrotron radiation researches performed at the *Frascati National Laboratories*.

During the last years of operation, before the shut down of ADONE, at the PWA Laboratory started also a medical research program on Synchrotron Radiation Radiology. For the first time, in Frascati, a monochromatic X-ray source other than a Coolidge tube has been used to X-ray image diagnostic. Many mammographic images were collected using a "scanning beam" technique, employable in human in vivo applications, and demonstrated beyond any doubt that the synchrotron radiation mammography has the capability to display a large number of structures, inside a neoplastic lesion present in specimens surgically excised by in vivo surgery, with a resolution and a contrast not achievable with any conventional apparatus.

In May 1993 when experimental activities at the ADONE storage ring ended, synchrotron radiation research continued. A small team started the construction of a beamline (GILDA) at the ESRF while other scientists started to consider the new scientific opportunities offered by the collider under consideration. In 1994 the construction of DA□NE, the new low energy double storage ring for electrons and positrons with a circulating current ranging up to about two Ampere, started. Nowadays, three beamlines are operational in the new laboratory and collect the radiation emitted by the DA□NE. These apparatus were designed and optimised to work in the soft X-ray region, in the near UV region and in the infrared region. This latter beamline, called *SINBAD*, because of the high circulating current is one of the most intense IR synchrotron radiation source in the world .

After more than 40 years from the early pioneering experiments performed at Frascati with the electro-synchrotron, when just a few people in the world were interested to this research, all around the world an impressive number of storage rings, specifically designed and built to operate as fully dedicated synchrotron radiation sources host a very large multidisciplinary scientific community working in almost all scientific disciplines: physics, chemistry, biology, medicine, mineralogy, environmental science, archeometry, etc..

Nowadays, although still in a parasitic mode, synchrotron radiation activities are again possible at Frascati within the framework of the DA□NE-Light Laboratory, where three beamlines, for some aspects unique in the world are open to users. This is an additional demonstration that the *Frascati National Laboratories* are qualified and unique not only from the historical point of view or for the many brilliant experiments performed in the field of nuclear or subnuclear physics, but also for their capability to promote new and still unexplored synchrotron radiation researches on view of the construction of the 4^{th} generation of x-ray sources.

Emilio Burattini

[1] Jaglé P., Missoni G. and Dhez P., *Phys. Rev. Lett.*, **18** (1967) 887
[2] Jaglé P., Combet-Farnaux F., Dhez P., Cremonese M. and Onori G., *Phys. Lett. A*, **26** (1968) 364
[3] Balzarotti A., Bianconi A., and Burattini E., *Phys. Rev. B*, **9** (1974) 5003
[4] Balzarotti A., Bianconi A., Burattini E., and Strinati G., *Solid State Commun.*, **15** (1974) 1431
[5] Balzarotti A., Bianconi A., Burattini E., Grandolfo M., Habel R. and Piacentini M., *Phys. Status Solidi B*, **63** (1974) 77
[6] Nannarone S., Patella F., Perfetti P., Quaresima C., Savoia A., Bertoni C.M., Calandra C. and Manghi F., *Solid State Commun.*, **34** (1980) 409
[7] Balzarotti A., Comin F., Incoccia L., Piacentini M., Mobilio S. and Savoia A., *Solid State Commun.,* **35** (1980) 145
[8] Barbini R., Bassetti M., Biagini M.E., Boni R., Cattoni A., Chimenti V., De Simone S., Dulach B., Faini S., Guiducci S., Luccio A.U., Preger M.A., Sanelli C., Serio M., Tazzari S., Tazzioli F., Vescovi M., Vignola G., Vitali A., Burattini E., Cavallo N., Foresti M., Mencuccini C., Pancini E., Patteri P., Rinzivillo R., Troya U., Dalba G., Ferrari F., Fornasini P., Jackson A. and Worgan J., *Riv. Nuovo Cimento*, **4** (1981) 8

CONTENTS

ATOMIC AND MOLECULAR X-RAY PROCESSES

Frascati Physics Series Vol. XXXII (2003), pp. 3-8
19th INTERNATIONAL CONFERENCE ON X-RAY AND INNER-SHELL
PROCESSES – Roma, June 24 - 28, 2002

ON THE EFFECT OF INTRA-DOUBLET CORRELATIONS UPON THE NONDIPOLE PARAMETERS IN Xe

M. Ya. Amusia
The Hebrew University, Jerusalem 91904, Israel
Ioffe Institute, St.Petersburg 194021, Russia
A. S. Baltenkov
Arifov Institute , Tashkent 70127, Uzbeck Republic
L. V. Chernysheva
Ioffe Institute, St.Petersburg 194021, Russia
Z. Felfli, A. Z. Msezane
Clark Atlanta University, Atlanta, GA 30314, USA
S. T. Manson
Georgia State University, Atlanta, GA 30303, USA

ABSTRACT

It is demonstrated that the inclusion of interaction between $3d_{3/2}$ and $3d_{5/2}$ electrons in Xe leads to a qualitative alteration of the nondipole parameters, that characterize the angular distribution of the photoelectrons from the 3d subshell. Namely, a rather specific maximum appears in the non-dipole parameters for the $3d_{5/2}$ level, while the $3d_{3/2}$ is affected much weaker. The results are obtained whithin the framework of the Generalized Random Phase Approximation with Exchange (GRPAE), that takes into account, along with RPAE effects, the rearrangement of all atomic electrons due to the creation of a 3d vacancy.

1 Introduction

It was demonstrated recently that the interaction between electrons belonging to different components of a spin-orbit doublet $3d_{3/2}$ and $3d_{5/2}$ in Xe, Cs and

Ba affects dramatically the partial photoionization cross section. Namely, it was shown [1] that due to this interaction the partial $3d_{5/2}$ cross section acquires an additional prominent maximum. This gave an interpretation of recent experimental observation of this effect in Xe [2] and simultaneously predicted similar, or, better to say even stronger results for $3d$ in Cs and Ba.

Here we present the results of our studies based on the approach developed in [1], of the angular anisotropy nondipole parameters for $3d$ photoelectrons in Xe. We observed an impressive manifestation of intra-doublet interactions, in fact completely new maximum in its nondipole parameters.

It is convenient to apply to the problem under consideration the nonrelativistic approach [1]. The main point of this approach is that we consider the $3d_{5/2}$ and $3d_{3/2}$ electrons as semi-filled atomic levels. This permits us to apply straightforwardly the method of accounting inter-electron correlations for semi-filled subshells. The exchange is neglected between these two sorts of electrons, namely that six which forms $3d_{5/2}$ (called "up"), and that four forming $3d_{3/2}$(called "down") electrons. However, in the real half-filled 3d subshell one would have five electrons. But these corrections, 5/6 and 5/4, respectively can be introduced easily into the calculational scheme.

Then we will investigate the influence of "up" and "down" electrons upon each other and demonstrate that the effect of the "down" electron upon the "up" ones manifests itself strongly in the nondipole parameters of the photoelectron angular distributions, $\gamma(\omega)$ and $\eta(\omega)$, defined in [3] and [4]. In all these cases the action of $3d_{3/2}$ electrons upon $3d_{5/2}$ leads to the creation of an additional maximum in the nondipole parameters, while the effect of $3d_{5/2}$ upon $3d_{3/2}$ is considerably smaller.

2 Main Formulas

The angular distribution of photoelectrons from nl subshell created by unpolarized light, which includes nondipole parameters [5] was presented long ago in the following form

$$\begin{aligned}\frac{d\sigma_{nl}(\omega)}{d\Omega} &= \frac{\sigma_{nl}(\omega)}{4\pi}[1-\frac{\beta_{nl}(\omega)}{2}P_2(\cos\theta)+ \\ &+ \frac{\omega}{c}[\gamma_{nl}(\omega)P_1(\cos\theta)+\eta_{nl}(\omega)P_3(\cos\theta)] \qquad (1)\end{aligned}$$

where $\sigma_{nl}(\omega)$ is the partial photoionization cross section, $\beta_{nl}(\omega)$ is the angular anisotropy parameter, $\gamma_{nl}(\omega)$ and $\eta_{nl}(\omega)$ are nondipole parameters, $P_i(\cos\theta)$ are the Legendre polynomials and c is the speed of light.

Here we are interested in the case $l = 2$, and the following formulae for $\gamma_{n2}(\omega)$ and $\eta_{n2}(\omega)$ have to be employed [3, 4]

$$\begin{aligned}\gamma_{n2}(\omega) &= \frac{3}{5[2d_1^2+3d_3^2]}\{\frac{6}{7}d_3[6q_4\cos(\delta_4-\delta_3)-q_2\cos(\delta_2-\delta_3)]- \\ &- \frac{6}{5}d_1[q_0\cos(\delta_0-\delta_1)-q_2\cos(\delta_2-\delta_1)]\} \qquad (2)\end{aligned}$$

$$\begin{aligned}\eta_{n2}(\omega) &= \frac{3}{5[2d_1^2+3d_3^2]}\{\frac{12}{7}q_4[2d_1\cos(\delta_4-\delta_1)-d_3\cos(\delta_4-\delta_1)]- \\ &- 2q_0d_3\cos(\delta_0-\delta_3)+\frac{4}{7}q_2[4d_3\cos(\delta_2-\delta_3)-d_1\cos(\delta_2-\delta_1)]\} \qquad (3)\end{aligned}$$

Here $d_{2,1}$, $q_{4,2,0}$ are the dipole and quadrupole matrix elements in the one-electron Hartree-Fock approximation and $\delta_{3,1}(\epsilon)$, $\delta_{42,0}(\epsilon)$ are the photoelectron's elastic scattering phase shifts, $\epsilon = \omega - I_{n2}$, I_{n2} being the $n2$ subshell ionization potential. The matrix elements $d_{3,1}$ and $q_{4,2,0}$ are defined as

$$\begin{aligned}d_{3,1} &\equiv d_{n2,\epsilon 3,1} = \int_0^\infty \phi_{n2}(r)r\phi_{\epsilon 3,1}(r)dr, \\ q_{2\pm 2,0} &\equiv q_{n2,\epsilon 2\pm 2,0} = \frac{1}{2}\int_0^\infty \phi_{n2}(r)r^2\phi_{\epsilon 2\pm 2,0}(r)dr. \qquad (4)\end{aligned}$$

Here $\phi_{n2}(r)$ and $\phi_{\epsilon 2'}(r)$ are the Hartree-Fock one-electron initial and final state radial wave functions.

The interaction between atomic electrons results in new amplitudes, both dipole $D_{3,1}$and quadrupole $Q_{4,2,0}$. To obtain the corresponding expressions for γ_{n2} and η_{n2} and one has to perform the following substitutions [3]

$$|d_{3,1}|^2 \rightarrow |\,\Re D_{3,1}\,|^2 + |\,\Im D_{3,1}\,|^2,$$

$$|q_{4,2,0}|^2 \rightarrow |\,\Re Q_{4,2,0}\,|^2 + |\,\Im Q_{4,2,0}\,|^2,$$

$$\begin{aligned}&d_{3,1}q_{4,2,0}\cos(\delta_{4,2,0}-\delta_{3,1}) \rightarrow \{[\Re D_{3,1}\Re Q_{4,2,0}+ \\ &+\Im D_{3,1}\Im Q_{4,2,0})]\cos(\delta_{4,2,0}-\delta_{3,1})- \\ &-[\Re D_{3,1}\Im Q_{4,2,0}-\Im D_{3,1}\Re Q_{4,2,0})]\sin(\delta_{4,2,0}-\delta_{3,1})\} \qquad (5)\end{aligned}$$

The method that we use here, just as in [1], is the so-called spin-polarized random-phase approximation with exchange (SPRPAE). SPRPAE equations are rather complex, so we present them in the symbolic form, where $\uparrow$ and $\downarrow$ denote the "up" and "down" photoelectron vacancy spin projection. However,for the intermediate $3d$ subshell SPRPAE is not sufficient; the effects of rearrangement must be taken into account. This is done by going from SPRPAE to its generalized SPGRPAE version. The latter takes into account that while a slow photoelectron leaves the atom, the field of the vacancy is modified due to the alteration of the states of all other atomic electrons, which is a result of the creation of an inner-subshell vacancy. Generalized RPAE is discussed at length in [6]. Its extension for a system with two types of electrons "up" and "down" is straightforward. The symbolic version of the equation is the following

$$\begin{pmatrix} D_\uparrow(\omega) & D_\downarrow(\omega) \end{pmatrix} = \begin{pmatrix} d_\uparrow & d_\downarrow \end{pmatrix} + \begin{pmatrix} D_\uparrow(\omega) & D_\downarrow(\omega) \end{pmatrix} \begin{pmatrix} \chi_{\uparrow\uparrow} & 0 \\ 0 & \chi_{\downarrow\downarrow} \end{pmatrix} \begin{pmatrix} U_{\uparrow\uparrow} & V_{\uparrow\downarrow} \\ V_{\downarrow\uparrow} & U_{\downarrow\downarrow} \end{pmatrix} \tag{6}$$

Here $U_{\uparrow\uparrow(\downarrow\downarrow)}$ are combinations of the direct and exchange Coulomb interelectron interaction matrix elements, while $V_{\uparrow\uparrow(\downarrow\downarrow)}$ are the pure Coulomb matrix elements. The equation for the quadrupole matrix element $Q_{\uparrow(\downarrow)}$ can be obtained from (6) by substituting $q_{\uparrow(\downarrow)}$ instead of $d_{\uparrow(\downarrow)}$ and $Q_{\uparrow(\downarrow)}$ instead of $D_{\uparrow(\downarrow)}$. The one-electron matrix elements $d_{n2,\epsilon 3,1,\uparrow(\downarrow)}$ and $q_{n2,\epsilon 4,2,0,\uparrow(\downarrow)}$ are defined in the so-called "length" form by

$$\begin{aligned} d_{n2,\epsilon 3,1,\uparrow(\downarrow)} &= \int_0^\infty \phi_{n2,\uparrow(\downarrow)}(r) r \phi_{\epsilon 3,1,\uparrow(\downarrow)}\, dr \\ q_{n2,\epsilon 4,2,0,\uparrow(\downarrow)} &= \frac{1}{2}\int_0^\infty \phi_{n2,\uparrow(\downarrow)}(r) r^2 \phi_{\epsilon 4,2,0,\uparrow(\downarrow)}\, dr \end{aligned} \tag{7}$$

The corresponding equation for $D_{\uparrow(\downarrow)}(\omega)$ and $Q_{\uparrow(\downarrow)}(\omega)$ were solved numerically, in accord with the procedure described in [6] .

Nondipole parameters for "up" and "down" electrons are obtained from (2) and (3) by substituting $d_{3,1\,\uparrow(\downarrow)}$ and $q_{4,2,0\,\uparrow(\downarrow)}$ calculated in HF by $D_{3,1\,\uparrow(\downarrow)}$ and $Q_{4.2,0\,\uparrow(\downarrow)}$ defined according to (5), for "up"($\uparrow$) and "down"($\downarrow$) electrons, respectively.

To adjust "up" and "down" approach to the situation with 5/2 and 3/2 electrons, the second term in (6) was multiplied by 6/5 for "up" ($\uparrow$) and 4/5 for "down" ($\downarrow$) electrons. Thus we obtain $D_{l\pm 1;5/2(3/2)}(\omega)$ and $Q_{l\pm 2,0;5/2(3/2)}(\omega)$

values. Then corresponding expressions for $\gamma_{3d\ 5/2(3/2)}(\omega)$ and $\eta_{3d\ 5/2(3/2)}(\omega)$ with account of intra-doublet interaction were obtained from (2), (3) using (5) with these modified values of $D_{l\pm1;5/2(3/2)}(\omega)$ and $Q_{l\pm2,0;5/2(3/2)}(\omega)$.

3 Results

In experimental papers on nondipole parameters (e.g. [7]) the factors ω/c in front of the nondipole terms in (1) are included in γ and η and instead of them the following combinations of them are presented

$$\begin{aligned} \gamma^c &\equiv \frac{\omega}{c}\eta, \\ \delta^c &\equiv \frac{\omega}{c}(\gamma + \frac{1}{5}\eta). \end{aligned} \tag{8}$$

These values are given in the following figures. The nondipole parameters are usually measured [7] at the magical angle, θ_{mag}, at which $P_2(\cos\theta_{mag}) = 0$. At this angle only the combination $(\gamma^c + 3\delta^c)$ can be obtained from experiment, so along with separate data on γ^c and δ^c the values for $(\gamma^c + 3\delta^c)$ are also presented.

Fig. 1 depicts γ^c for $3d_{5/2}$ and $3d_{3/2}$ levels, with (denoted as SRPAE) and without (denoted as HF) electron correlations taken into account. Fig. 2 gives results for $(\gamma^c + 3\eta^c)$. We see, that although the curves are quite peculiar even without taking into account the interaction, the inclusion of "up" and "down" $(3d_{5/2} \leftrightarrow 3d_{3/2})$ electron interaction adds a qualitatively new feature to the nondipole parameters for the $3d_{5/2}$ electrons, namely a specific maximum in the $3d_{3/2}$ threshold region. Note, that, extra maximum in Fig. 1 marked by an arrow is a result of the influence of $3d_{3/2}$ electrons upon $3d_{5/2}$ electrons in the dipole channel, just as in the partial cross section [1].

4 Discussion and Conclusion

The presented results are of interest as an object for experimental studies since the prediction of an additional maximum in the nondipole parameter that appear due to the intra-doublet interaction is far from being trivial. There is no doubt that the modification of the non-dipole parameters of the $3d$ electrons in other atoms, e.g. like I, Cs, Ba and in their A^+ and A^- ions is similar to that of Xe. The same effect will take place whenever the multi-electron subshell is splitted into two levels by any static external field, e.g. due to molecular binding.

5 Acknowledgment

M. Ya. A. and L. V. C. are grateful for the financial support of this research by the International Science and Technology Center under the Project No 1358. A. Z. M. and Z. F. are supported by DoE, Division of Chemical Sciences, Office of Basic Energy Sciences.

References

1. M.Ya. Amusia *et al*, Phys. Rev. Lett. **88**, 093002 (2002).
2. A. Kivimäki *et al*, Phys. Rev. A **63**, 012716 (2000).
3. M. Ya. Amusia *et al,* Phys. Rev. A **63**, 052512 (2001).
4. M. Ya. Amusia *et al*, Phys. Rev. A **64**, 032711 (2001).
5. M. Peshkin, Adv. Chem. Phys. **18**, 1 (1970).
6. M. Ya. Amusia and L. V. Chernysheva, *Computation of Atomic Processes, A Handbook for the Atom Programs* (Institute of Physics Publishing, Bristol-Philadelphia, 1997).
7. M.Yung *et al*, Phys. Rev. A. **54**, 2127 (1996)

Frascati Physics Series Vol. XXXII (2003), pp. 9-14
19th INTERNATIONAL CONFERENCE ON X-RAY AND INNER-SHELL PROCESSES – Roma, June 24 - 28, 2002

QUASIATOMIC Cs L-EDGE X-RAY ABSORPTION IN A Cs/Na ALLOY

Iztok Arčon
Nova Gorica Polytechnic, Vipavska 13, 5000 Nova Gorica, Slovenia
Alojz Kodre
Faculty of Mathematics and Physics, University of Ljubljana, Slovenia
Jana Padežnik Gomilšek
Faculty of Mechanical Engineering, Smetanova 17, Maribor, Slovenia
Andrej Mihelič
Jožef Stefan Institute, Jamova 39, 1000 Ljubljana, Slovenia
Marjan Hribar
Jožef Stefan Institute, Jamova 39, 1000 Ljubljana, Slovenia

ABSTRACT

X-ray absorption coefficient in the vicinity of L edges of Cs has been measured on an alloy of Cs and Na. The absorption spectrum of the solid sample is virtually free of strucutural signal, similarly to spectra of monatomic gases. It exhibits the same pattern of sharp multielectron photoexcitation features as in the L edge absorption spectrum of the adjacent element xenon.

1 Introduction

The study of x-ray atomic absorption, measured either directly on a monatomic gas sample [1 – 5] of an element or derived from an x-ray absorption spectrum of a compound sample after removal of the structural signal [6 – 10] (EXAFS = extended x-ray absorption fine structure), provides data on correlation in the atomic system. The tiny sharp features on the smooth energy dependence of the

photoabsorption cross section are fingerprints of multielectron photoexcitations (MPE). These reaction channels arise from the change of the mean atomic field in the photoeffect but also from the correlated motion of atomic electrons. A detailed analysis can elucidate particularities in the coupling scheme and configuration interaction of the atom [1, 2, 4, 5].

The atomic absorption spectrum is a very good approximation to the atomic absorption background (AAB) in the XAFS structural analysis. Since the structural signal and MPE occupy the same spectral region above a major absorption edge, the small MPE features, if unrecognized, interfere with the interpretation of the structural signal leading to errors in the structure parameters determined in the XAFS analysis [8, 9].

In recent studies a parallel analysis of K-edge MPE in neighbor elements (Ar – K; Kr – Rb) was successfully introduced [4, 5]. The method exploits the fact that the cores of the two neighbor elements (noble gas and alkali metal) are largely the same, apart from the unit difference in the nuclear charge, and an additional loosely bound electron in the outer shell of the alkali metal atom. From the comparison of MPE excitations it was possible to deduce that common features in the spectra follow from a specific interaction of core configurations, while the differences in the MPE features of the two elements stem from the additional coupling of the valence s electron.

In this study we compare L-edge MPE in neighbor elements Xe and Cs. Complete L-subshell MPE spectra have already been measured on Xe gas [2]. On the other hand, pure Cs atomic L-edge spectrum has not been measured yet. Only the most prominent resonant MPE features have been extracted from the Cs L-edge EXAFS spectra measured on amorphous materials [11, 12, 13]. A measurement of the full atomic Cs L-edge absorption spectrum, comparable in detail to that of Xe, promises another fruitful comparison MPE study.

The L-edge absorption spectrometry on monoatomic Cs metal vapor requires a very demanding and costly heat-pipe cell [4]. Instead we measured the absorption on a thin layer of Cs/Na alloy in the vicinity of its melting point (70 °C), where the weak EXAFS signal can be removed numerically. Surprisingly, the experiment showed that the strong disorder in the alloy produces practically pure Cs atomic absorption spectrum almost without an EXAFS component.

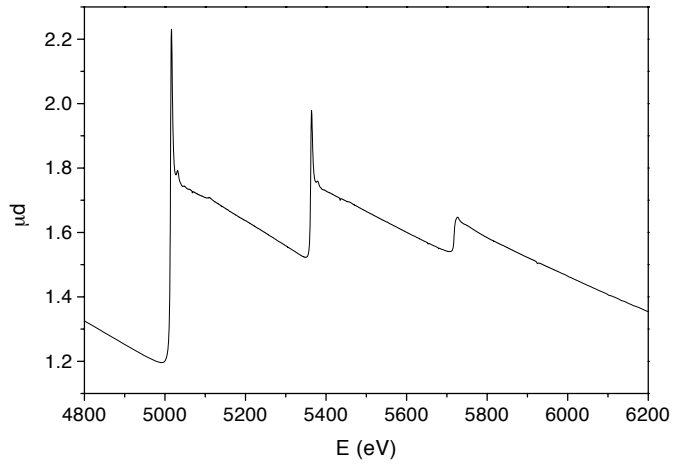

Figure 1: *The L-edge absorption spectrum of Cs measured on a thin layer of the Na/Cs alloy.*

2 Experiment

Cs/Na alloy with a concentration ratio of 1 : 9 was prepared. A small amount of the alloy was placed, together with a drop of paraffine oil to prevent oxidation, into a small lucite container between two kapton foils and squeezed into a thin layer. The container and the oil kept the metal perfectly stable for several hours of the experiment: no sign of oxidation was observed after demounting. The stability of the sample was confirmed also by the perfect reproducibility of the scans that were recorded in sequence at each of the L subshell edges.

The absorption experiment was performed at the E4 station of the DORIS ring at HASYLAB synchrotron facility, DESY (Hamburg, Germany). The beamline provides a focused beam from Au-coated mirror and a Si(111) double-crystal monochromator with 0.8 eV resolution at Cs L_3-edge. Harmonics are effectively eliminated by a plane Au coated mirror and by detuning the monochromator crystal using a stabilization feedback control. Exact energy calibration was established with a simultaneous measurement on a Ti metal foil ($E_K = 4966\,\mathrm{eV}$) between the second and the third ionisation cell.

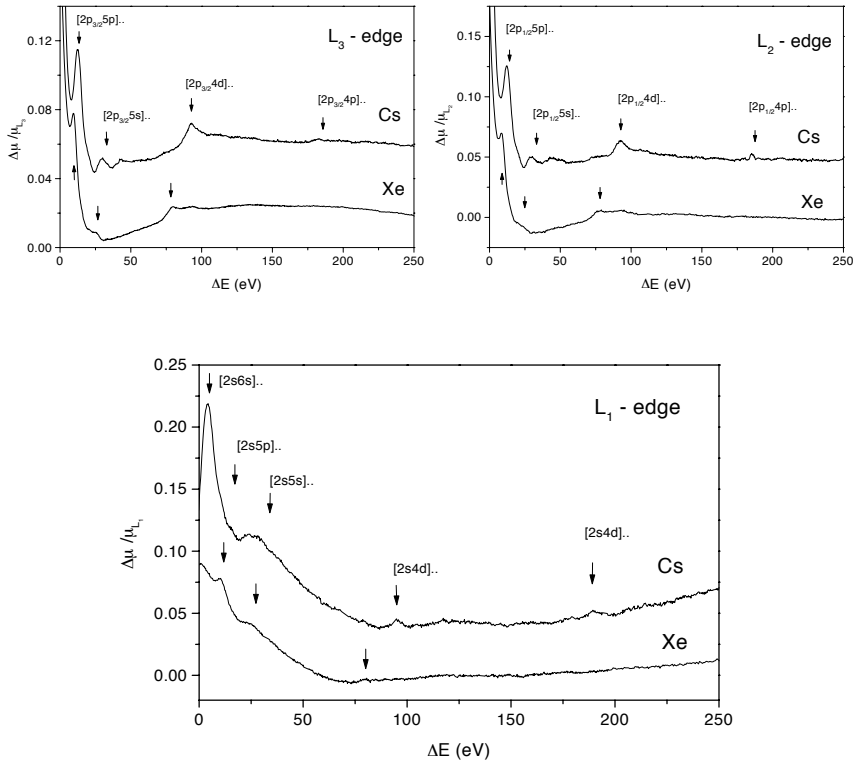

Figure 2: *The comparison of the absorption in the L subshell regions of Cs and Xe after removal of the average trend to enhance the detail. Theoretical estimates of the energy of double excited states are shown by arrows. For each subshell, the origin of the energy scale is shifted to the respective ionization threshold.*

3 Results

A compound picture of the L edges (Fig. 1) is obtained as a superposition of three scans per subshell region. Each of the edges is preceded by a resonance due to the excitation of the 2p or 2s electron to the unoccupied bound states just below the continuum.

The spectra above each of the edges are remarkably flat, almost without

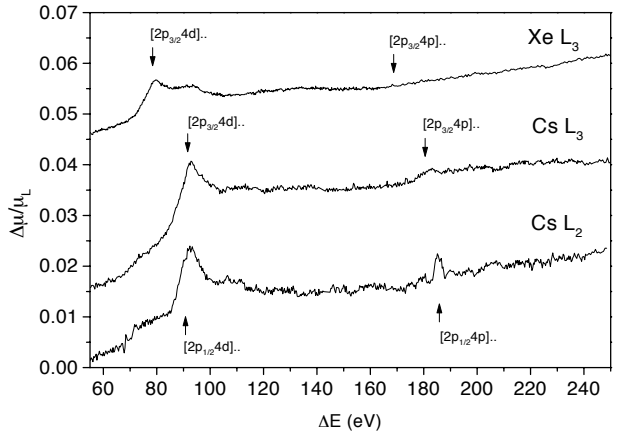

Figure 3: *The comparison of the [2p4d] and [2p4p] MPE features above Cs L_2 and L_3 and Xe L_3 edges spectra.*

oscillatory EXAFS signal characteristic of solid samples. A slight convexity of the spectrum above the L_3 and L_2 edge, observed already in the L absorption spectra of some heavy elements, has been explained as a consequence of subshell polarization [14].

The strongest of the sharp MPE features are just barely visible in the spectrum. To expose the details, the average trend of each subshell region is removed from the relative cross section (Fig. 2). Several groups of MPE can be clearly discerned above each absorption edge. The groups can be identified by their energy as multiple excitations involving electrons in consecutively deeper subshells from 6s to 4p, in complete analogy with the MPE groups in the neighboring Xe [2], shown below. Hartree–Fock estimates [15] of the threshold energies of the corresponding double excitations are indicated by arrows.

Even at this level of magnification the oscillatory structural signal is visible only close to the edge. The amplitude of EXAFS oscillations is smaller than the MPE features and vanishes in the noise level about 80 eV above each edge.

The marked difference between MPE in Cs L_1 and $L_{2,3}$ spectra point to the same orbital-momentum-sensitive mechanism of multielectron coexcitation

as already established in Xe [2]. Closer inspection of the Cs L_2 and L_3 absorption spectra shows similarities in [2p4d] and [2p4p] MPE features, and reveals differences in their amplitude and shape compared to those in Xe $L_{3,2}$ spectra (Fig. 3). Differences may be ascribed to resonant and shake-up transitions into specific final states of a bound Cs atom.

Acknowledgments

Support by the Ministry of Science and Technology of the Republic of Slovenia, and by Internationales Buero BMBF (Germany) is acknowledged. K. V. Klementiev of HASYLAB provided expert advice on beamline operation.

References

1. S. J. Schaphorst *et al*, Phys. Rev A **47**, 1953 (1993).
2. I. Arčon *et al*, Phys. Rev. A **51**, 147 (1995).
3. R. Prešeren *et al*, Nucl. Inst. Meth. Phys. Res. B **111**, 161 (1996).
4. J. Padežnik Gomilšek *et al*, Phys. Rev. A **64**, 22508 (2001).
5. A. Kodre et al, J. Phys. B (submitted).
6. G. Li, F. Bridges, and G. S. Brown, Phys. Rev. Lett. **68**, 1609 (1992).
7. A. Filipponi and A. Di Cicco, Phys. Rev. A **52**, 1072 (1995).
8. P. D'Angelo *et al*, Phys. Rev. A **47**, 2055 (1993).
9. A. Kodre, I. Arčon, R. Frahm, J. Phys. IV France 7 **C2**, 195 (1997).
10. R. Prešeren *et al*, J. Synch. Rad. **8**, 279 (2001).
11. A. Kodre *et al*, J. de Physique C-9 **4**, 397 (1994).
12. A. Kodre *et al*, Physica B **208&209**, 379 (1995).
13. J. A. Solera, J. Garcia, M. G. Proietti, Phys. Rev. B **51**, 2678 (1995).
14. W. Jitschin *et al*, Phys. Rev. A **35**, 5038 (1987).
15. C. Froese Fischer, Comput. Phys. Commun. **43**, 355 (1987).

Frascati Physics Series Vol. XXXII (2003), pp. 15-22
19th INTERNATIONAL CONFERENCE ON X-RAY AND INNER-SHELL
PROCESSES – Roma, June 24 - 28, 2002

PHOTOIONIZATION OF THE Li@C_{60} ENDOHEDRAL ATOM

A. S. Baltenkov
Institute of Electronics, Tashkent 700187, Uzbekistan
V. K. Dolmatov
University of North Alabama, Florence, AL 35632, U.S.A.
S. T. Manson
Georgia State University, Atlanta, GA 30303, U.S.A.

ABSTRACT

Photoelectron angular distributions due to near-threshold 1s photoionization of the Li atom from the oriented-in-space Li@C_{60} endohedral fullerene are investigated within the framework of our recently developed photoionization theory of multi-centre formations. The off-the-centre confined Li atom is considered, and off-the-centre effects are shown to be of extreme importance.

1 Introduction

In recent years, the need to understand energy structures and spectral properties of endohedral fullerenes A@C_{60}, consisting of an atom A confined inside the C_{60} empty spherical cage of the fullerene (also referred to as an endohedrally confined atom or simply an endohedral atom), has triggered a splash

of research activities world-wide. As for photoionization of endohedral atoms alone, most of the research performed to date has been devoted to total photoionization cross sections, $\sigma_{\rm tot}(\omega)$, as functions of photon frequency ω, revealing strong, important modifications in $\sigma_{\rm tot}(\omega)$ brought about by the C_{60} confining cage as compared to photoionization cross sections of free atoms (see, e.g., [1, 2, 3, 4, 5, 6, 7, 8, 9] and references therein).

As for photoelectron angular distributions from endohedrally confined atoms, to date there remain significant gaps in our knowledge on these distributions. In [8], e.g., devoted to the investigation of the 1s photoionization of the endohedral Li atom from the Li@C_{60} formation, the 1s-differential photoionization cross section of Li was taken as the same as for randomly oriented free atoms:

$$\frac{d\sigma}{d\Omega} = \frac{\sigma_{\rm tot}(\omega)}{4\pi}[1 + \beta(\omega)P_2(\cos\vartheta)], \qquad (1)$$

where $\beta(\omega)$ is the dipole angular-asymmetry parameter, $P_2(\cos\vartheta)$ is the Legendre polynomial of the second order, ϑ is the angle between the photon polarization vector $\mathbf{e}$ and the photoelectron momentum $\mathbf{k}$. However, it is clear that eq.1 is valid only if a spherical average over target orientations is taken. Normally, however, the confined atom A is located off the centre of the cage [11, 12], and it remains unexplored how strong such asymmetry of the A@C_{60} formation can affect the photoelectron angular distribution from the fixed-in-space "off-the-centre" confined atom compared to the photoelectron angular distribution from the fixed-in-space "at-the-centre" confined atom in the A@C_{60} formation.

It is the aim of this paper to establish fundamental trends in photoelectron angular distributions from the "asymmetrically" confined atoms in the A@C_{60} formation. Given that our aim is to uncover general trends in photoelectron angular distributions rather than to make detailed calculations for a particular system, we choose Li@C_{60}, and we let the Li atom remain neutral upon the confinement. To investigate, we use our recently developed multi-centre theory applicable to near-threshold inner-shell photoionization of molecular

formations [13]. Consequently, we limit our discussion to $1s$ near-threshold photoionization of endohedral Li.

2 Basic Concepts of the Theory

Obviously, energies and wave functions of bound states of innermost subshells in confined atoms remain essentially atomic-like. Consequently, the 1s orbital in the confined Li atom can be calculated within approximation of a free atom; this does not pose a significant approximation. The main problem is then concerned with a description of the motion of the outgoing photoelectron in a multi-centre field of the C_{60} cage. To a good approximation [13], the latter can be found within the approximation of non-overlapping spherical potentials of atom-scatterers (the 60 C atoms) surrounding the ionized atom (the Li atom). In atomic units, used throughout this paper, the differential photoionization cross section of the $1s$ subshell of the endohedrally confined Li atom is given by [13]

$$\frac{d\sigma}{d\Omega} = \frac{3}{4\pi}\sigma_{1s}(\omega)S(\mathbf{k}). \tag{2}$$

Here, $\sigma_{1s}(\omega)$ is the total photoionization cross section of the free Li atom, ω is the photon energy, and $\mathbf{k} = k\mathbf{n}$ is the photoelectron momentum. According to eq.2, the differential photoionization cross section is a product of two dynamical factors. The first depends on the bound and continuum wave functions for the free atom, whereas the second, referred to as a structural function $S(\mathbf{k})$, defined as

$$S(\mathbf{k}) = \left|(\mathbf{e}\cdot\mathbf{n}) + ie^{-i\Delta_1}\frac{k}{2\pi}\sum_{j=1}^{N} C_j^+(-\mathbf{k})\chi_{k1}^+(R_j)(\mathbf{e}\cdot\mathbf{q}_j)\right|^2 \tag{3}$$

depends only on the multi-centre structure of the Li@C_{60} formation and the details of the continuum wave function. Here, $\mathbf{e}$ is the photon polarization vector, the vectors $\mathbf{R}_j$ define the positions of the nuclei of the C atoms in the coordinate system whose origin is at the nucleus of the ionized endohedral

atom, $\mathbf{q}_j = \mathbf{R}_j/R_j$ are the associated unit vectors, $\chi^+_{k1}(r) = i\varphi_{k1}(r) - \chi_{k1}(r)$ is a linear combination of the regular $\varphi_{k1}(r)$ and irregular $\chi_{k1}(r)$ solutions of the radial Schrödinger equation for the photoelectron (with orbital angular momentum l=1) moving in the field of the 1s ionized Li atom, $\Delta_1(k)$ is the phase shift of the photoelectron wave function in the field of the residual ion, and the $C^+_j(-\mathbf{k})$ are solutions of a system of inhomogeneous linear equations

$$C^+_j(-\mathbf{k}) - 2\pi f^j_0 \sum_{i\neq j}^{N} C^+_i(-\mathbf{k}) G^+_k(\mathbf{R}_i, \mathbf{R}_j) = 2\pi f^j_0 \psi^+_{-\mathbf{k}}(\mathbf{R}_j). \qquad (4)$$

Here, $j = 1, ..., N$, $f^j_0 = (e^{2i\delta^j_0} - 1)/2ik$ is the s-wave amplitude for photoelectron scattering by the j-th C atom-scatterer, $\delta^j_0(k)$ is the s-wave phase shift, $G^+_k(\mathbf{R}_i, \mathbf{R}_j)$ are Green's functions of the Schrödinger equation for a photoelectron moving in the field of the $Li^+(1s^{-1}$ ionized confined atom). The wave function $\psi^+_{\mathbf{k}}(\mathbf{r})$ is given by [8]

$$\psi^+_{\mathbf{k}}(\mathbf{r}) = 4\pi \sum_{l,m} i^l e^{i\Delta_l} Y_{lm}(\mathbf{r}) Y^*_{lm}(\mathbf{k}) \varphi_{kl}(r), \qquad (5)$$

where $Y_{lm}(\mathbf{R_j})$ and $Y_{lm}(\mathbf{k})$ are spherical harmonics.

What is unique in the present theory is that the structural function $S(\mathbf{k})$ contains all of the differences in differential photoionization cross sections of inner ns-electrons between the confined atom and the free atom. Investigation of the structural function is thus of obvious importance. In the present work, following [15], we use the Hartree-Fock approximation to calculate $\delta_0(k)$ as well as both the regular and irregular photoelectron wave functions in the field of the ionized $Li^+(1s^{-1})$ to find $S(\mathbf{k})$. Furthemore, we use experimental values of the diameter D of the fullerene cage, $D = 7.113$ Å, and the mean length d of bonds between the nearest C atoms in the cage, $d = 1.440$ Å [16], and we neglect the difference between the bond lengths for pentagon and hexagon in the C_{60} cage. When considering the off-the-centre confined Li atom, we position Li at about 1 Å [17] from the centre of one of the C-hexagons in the geometrical structure

of the C_{60} fullerene cage. Finally, we use tabulated values [15] values for the polar θ_j and azimuthal φ_j angles that define directions of the 60 vectors $\mathbf{R}_j$, needed to calculate $S(\mathbf{k})$.

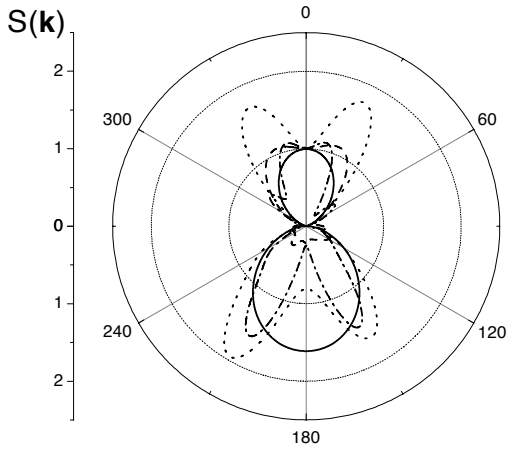

Figure 1: *The structural function $S(\mathbf{k})$ for the 1s photoelectron angular distribution for the off-the-center endohedral Li atom in the Li@C_{60} formation, as function of the polar angle ϑ_k, at fixed $\varphi_k = 0$ for k = 0.1 au (solid line), 0.5 au (dashed line), 0.8 au (dotted line) and 1.0 au (dashed-dotted line), calculated using the present theory. All curves are normalized to unity at $\vartheta_k = 0$.*

3 Calculated Results for the Off-The-Centre Confined Li

Calculated results for the Li 1s photoelectron angular distribution upon photoionization of the off-the-centre confined Li atom in the Li@C_{60} formation are shown in Fig. 1 for k = 0.1, 0.5, 0.8, and 1.0 au. A rich variety of functional forms of the photoelectron angular distribution is seen. Importantly, the shape of each curve in this figure is dramatically different from that suggested by eq.1 for free atoms or a spherical average. This is primarily because of a further deviation from spherical symmetry of Li@C_{60}, due to the displacement of the

Li atom from the center of the C_{60} cage. In addition, the shape of the photoelectron angular distribution turns out to depend strongly on the magnitude of k. This is because the presence of a neighboring atom near the ionized atom leads to the diffraction of the outgoing photoelectron wave by the neighboring atom [13]. Intensities of related diffraction maxima turn out to depend on the angle between the photoelectron momentum $\mathbf{k}$ and the molecular axis that connects the ionized atom with the neighboring atom, a phenomenon that has been seen experimentally [18]. In Li@C_{60}, not one but sixty C atoms surround the Li atom, so that the overall diffraction pattern seen in Fig. 1 is a superposition of sixty diffraction patterns.

4 Conclusion

It follows from this paper that the photoelectron angular distribution for the off-the-centre endohedral atom is substantially different from the photoelectron angular distribution for both the isolated atom and the at-the-center endohedral atom. It was demonstrated that the photoelectron angular distribution from the off-the-center endohedral atom is extremely sensitive to small variations in the photoelectron energy, due to the crucial role of the phenomenon of diffraction of the photoelectron wave from sixty "asymmetrically" positioned atoms of the fullerene cage C_{60}. Hence, the significant importance of "off-the-center" effects in inner-shell photoelectron angular distributions from endohedrally confined atoms is established, in contrast to the conventional wisdom [8] that such effects might be minor for inner-shell photoionization.

5 Acknowledgements

This work was supported by the US Civilian Research and Development Foundation for the Independent States of the Former Soviet Union (CRDF), Grant No. ZP1-2449-TA-02 and NSF.

References

1. J.-P. Connerade, V. K. Dolmatov, and S. T. Manson. J. Phys. B **33**, 2279 (2000).
2. M. Ya. Amusia, A. S. Baltenkov, and U. Becker. Phys. Rev. A **62**, 012701 (2000).
3. M. J. Puska and R. M. Nieminen, Phys. Rev. A **47**, 1181 (1993).
4. G. Wendin and B. Wastberg, Phys. Rev. B **48**, 14764 (1993).
5. A. S. Baltenkov, Phys. Lett. A **254**, 203 (1999); J. Phys. B **32**, 2745 (1999).
6. J.-P. Connerade, V. K. Dolmatov, P. A. Lakshmi, and S. T. Manson. J. Phys. B **32**, L239 (1999).
7. J.-P. Connerade, V. K. Dolmatov, and S. T. Manson. J. Phys. B **32**, L395 (1999).
8. P. Decleva, G. De Ati, G. Fronzoni, and M. Stener. J. Phys. B **32**, 4523 (1999).
9. M. Venuti, M. Stener, G. De Ati, and P. Decleva. J. Chem. Phys. **111**, 4589 (1999).
10. J. Cooper and R. N. Zare. J. Chem. Phys. 48, **942** (1968).
11. P. P. Schmidt et al. J. Phys. Chem. **95**, 10537 (1991).
12. J. Cioslowski and E. D. Fleischmann. J. Chem. Phys. **94**, 3730 (1991).
13. A. S. Baltenkov, V. K. Dolmatov, and S. T. Manson. Phys. Rev. A **64**, 062707 (2001).
14. L. D. Landau and E. M. Lifshitz, *Quantum Mechanics. Non-Relativistic Theory* (Pergamon Press, Oxford, 1965).

15. A. S. Baltenkov, V. K. Dolmatov, and S. T. Manson. Phys. Rev. A (2002) (in press)

16. K. Hedberg, L. Hedberg, D. S. Bethune, C. A. Brown, H. C. Dorn, R. D. Johnson, and M. de Vries. Science. **254**, 410 (1991).

17. K. Ohno, Y. Maruyama, K Esfarjani, and Y. Kawazoe, Phys. Rev. Lett. **76**, 3590 (1996).

18. O. Gessner, F. Heiser, N. A. Cherepkov, B. Zimmermann, and U. Becker, J. Electron Spectrosc. Relat. Phenom. **101-103**, 113 (1999).

Frascati Physics Series Vol. XXXII (2003), pp. 23-28
19th INTERNATIONAL CONFERENCE ON X-RAY AND INNER-SHELL PROCESSES – Roma, June 24 - 28, 2002

EVOLUTION OF Au $L\beta_2$ SATELLITES of X-RAY EMISSION SPECTRA AROUND THRESHOLDS

Oohashi Hirofumi, Shigeoka Nobuyuki, Tochio Tatsunori, and Ito Yoshiaki
Laboratory of Atomic and Molecular Physics, Institute for Chemical Research, Kyoto University, Gokasho, Uji 611-0011 Japan
Aurel Mihai Vlaicu, Nisawa Atsushi, Yoshikawa Hideki, and Fukushima Sei
National Institute for Material Science, SPring-8, Mikazuki, Hyogo 679-5198 Japan

ABSTRACT

Au $L\beta_2$ satellites were investigated around L_1 absorption edge with a high-resolution Johann-type spectrometer at the BL15XU undulator beam line, SPring-8. The intensity of the $L\beta_2$ satellites was drastically changed at the threshold. Therefore, it is confirmed that the two visible satellites, $L\beta_2'$ and $L\beta_2''$ are mainly attributed to the L_1-$L_3M_{4,5}$ Coster-Kronig transitions accompanied with the double-hole states of L_3M_4 or L_3M_5.

1 Introduction

For heavy elements there are many electrons that have the ability to be concerned with the transition, and in the 6th period *L-LM* Coster-Kronig (C-K) transition reappear. Therefore, it is very interesting to investigate theoretically and experimentally satellites due to such a transition. With the advent

of the third generation synchrotron radiation, we can do the experiments on the threshold behavior of the satellites including the electron correlation.

It is well known that Au $L\beta_2$ diagram line has two satellites, $L\beta_2'$ and $L\beta_2''$ on its higher energy side. Their energy shifts from the diagram line are enough large to confirm their existences in the data. The $L\beta_2'$ and $L\beta_2''$ satellites have previously been assigned to the L_3M_5-N_5M_5 and L_3M_4-N_5M_4 transitions, respectively. However, the mechanism of the creation of M_4 or M_5 spectator hole is not clarified. M_i spectator hole can be created by either or both L_3M_i shake-off process or/and L_1-L_3M_i C-K transition. According to the report of Chen *et al.* [1], C-K transition is allowed for $i = 4, 5$ in the case of $_{79}$Au. In the present work, the $L\beta_2$ visible satellites are investigated by the evolution of the photo-excited $L\beta_2$ emission spectra in order to elucidate the mechanism of the origin in the satellites.

2 Experimental

The measurements were carried out at BL15XU, Spring-8, Ako, with a curved crystal x-ray spectrometer [2, 3]. A Si double crystal monochromator with a bandpass of $\sim 3\,$eV and a flux of $\sim 5 \times 10^{11}\,$photons/sec was used. The sample was a high-purity Au foil. The fluorescence spectrometer employed the Johann geometry with a 1.5 m diameter Rowland circle on Si(444) crystal providing $< 1\,$eV resolution. BL15XU is a planer type undulator. Therefore it is easy to reduce the harmonic components with the slit. The coherent radiation out of the monochromator is onto the sample in the sample chamber of the spectrometer. The light then goes into the crystal housing in which three kinds of crystals are mounted. The optical focusing condition can be met by moving the sample, crystal and detector to satisfy the Rowland geometry. The measurement was carried out changing the excitation energy around L_1 edge in order to investigate the energy-dependency on the visible satellites' intensity. Spectrometer angle and Scintillation Counter (SC) or CCD detectors were fixed at which we can get $L\beta_2'$ and $L\beta_2''$ satellites and scanned in order to obtain the spectral profile in SC, and then excitation energy were tuned around L_1 edge. The observed absorption spectra in L edges were used to determine the values of the excitation energy.

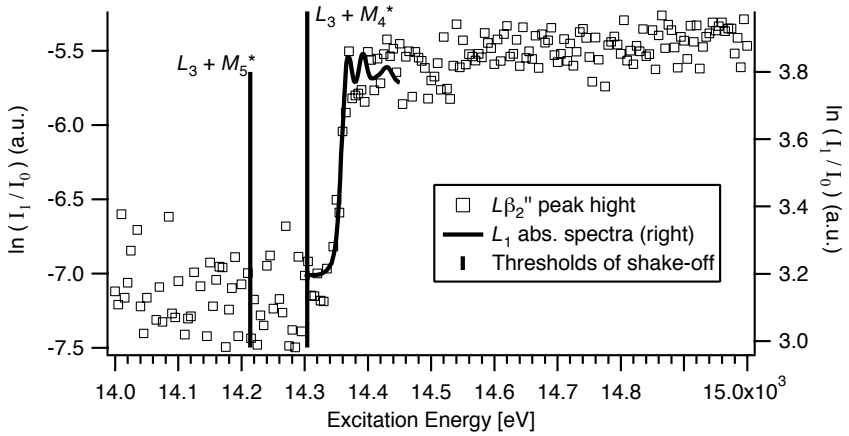

Figure 1: *The dependence of $L\beta_2''$ peak hight on excitation energy.*

3 Results and Discussion

It is generally considerable that the double-hole state L_3M_4 which is the initial state of $L\beta_2''$, is ascribed to two processes: one is L_3-M_4 shake-off process. This is the direct ionization process, so that its transition probability depends on the excitation energy. The onset of this process can be estimated to be L_3 + M_4^* [1] binding energies. Another is L_1-L_3M_4 C-K transition process. This is indirect ionization process and therefore independent of the excitation energy. The data measured by SC are shown in Fig. 1. The result suggests that the L_3M_4 double-hole state is mainly due to C-K transition.

The evolution of the $L\beta_{2,3,15}$ emission spectra around the L_1 edge are shown in Fig. 2. These were hitherto studied only for high-energy excitation in conventional x-ray tubes [4, 5, 6]. The most outstanding feature of the data is the abrupt increase of the satellite intensity over a considerable energy range around the threshold. The spectra obtained by CCD camera were analyzed by fitting the $L\beta_{2,3,15}$ diagrams and $L\beta_2$ satellites by single Lorentzian profile. We obtained relative intensities of satellites to the diagram line. $L\beta_3$ diagram line

[1] $*$ means $Z+1$ element ($_{79}$Au $\rightarrow$ $_{80}$Hg)

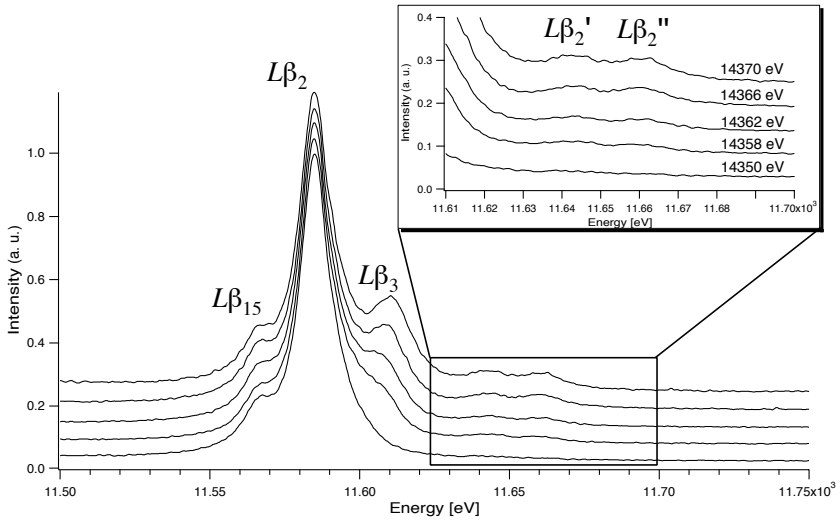

Figure 2: *Change of Au $L\beta_2$, $L\beta_3$, $L\beta_{15}$, $L\beta_2$ satellites spectra near the Au L_1 edge.*

and $L\beta_2$ satellites appear just around the L_1 edge with the excitation energy. $L\beta_3$ disappear with the excitation energy around the threshold because of the transition to L_1 subshell. The dependence of the intensity of each satellite on the excitation energy is shown in Fig. 3. The relative intensities of both satellites to the diagram line $L\beta_2$ increase along with L_1 absorption spectra. The behavior is similar to the abrupt edgelike behavior observed in single-electron-correlated spectra. Moreover, a fine structure was clearly confirmed around the L_1 edge.

4 Conclusions

We presented here a study of the near-threshold of the satellites ascribed to C-K transition in Au. The observed $L\beta$ spectra are analyzed by a single Lorentzian fitting.

The contribution of C-K transition to Au $L\beta$ satellites were clearly confirmed through the present work, that is, Au $L\beta_2$ visible satellites are mainly

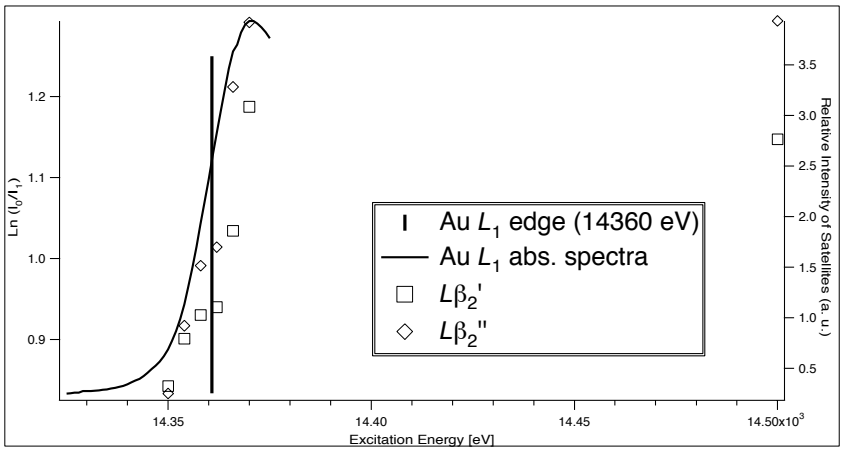

Figure 3: *The dependency of relative intensities of both $L\beta_2$ satellites for $L\beta_2$ on excitation energy.*

caused by L_1-L_3M_i ($i = 4, 5$) C-K transition. Further investigations are planned to elucidate the details of the dependence of the intensity in the satellites on the excitation energy in heavy elements.

References

1. M.H. Chen *et al*, Atom. Data Nucl. Data Tables **19,** 97 (1977)

2. Y. Ito, A. M. Vlaicu, T. Tochio, K. Mutaguchi, H. Oohashi, N. Shigeoka, T. Shoji, J. Harada, S. Emura, and T. Uruga, in Proceedings of International Workshop on Physical Properties of Matter by x-ray absorption and emission spectroscopy, 24-26 July 2000, Osaka Electro-Communication University, Osaka, Japan, p32.

3. Y. Ito, A. M. Vlaicu and T. Tochio, **CP576,** Application of Accelerators in Research and Industry edited by J. L. Duggan and I. L. Morgan (AIP) (2001)

4. J. H. William, Phys. Rev. **45,** 71 (1934)

5. F. K. Richtmyer, S. W. Barnes, and E. Ramberg, Phys. Rev. **46,** 843 (1934)

6. P. Amorim, L. Salgueiro, F. Parente, and J. G. Ferreira, J. Phys. B **21,** 3851 (1988)

Frascati Physics Series Vol. XXXII (2003), pp. 29-37
19th INTERNATIONAL CONFERENCE ON X-RAY AND INNER-SHELL PROCESSES – Roma, June 24 - 28, 2002

IONIZATION OF ELECTRON-HOLE PAIRS IN CRYSTALS BY THE SLOW ELECTRONS

O.F. Panchenko
A.A. Galkin Donetsk Institute of Physics and Technology, Ukrainian National Academy of Sciences, 72 Rozy Luxemburg Street,83114 Donetsk, Ukraine
L.K. Panchenko
A.A. Galkin Donetsk Institute of Physics and Technology, Ukrainian National Academy of Sciences, 72 Rozy Luxemburg Street,83114 Donetsk, Ukraine

ABSTRACT

A study is made of the cascade process, which describes the energy loss and multiplication of highly non-equilibrium secondary electrons and holes in crystalline silicon irradiated by low energy electrons. The pair creations scattering rates are evaluated in framework of statistical model which takes into account the electron band structure of silicon. Kinetic equations for the excited electron and hole energy distributions are solved numerically in the isotropic scattering approximation for some primary energies E_p-$E_F \leq \omega_{pl}$. The derived energy distribution function permits a smooth interpolation $f(E) \sim |E - E_F|^{-s}$. The calculations result in a weak energy dependence of the mean pair creation energy.

1 Introduction

The development of the experimental technique has produced recently a large variety of low energy electron spectroscopy methods such as the inverse photoemission [1,2], bremsstrahlung isochromate spectroscopy [1,3], the angle-resolved secondary emission [4–7] and so on [8,9]. All these phenomena are caused by presence of a low but finite concentration of highly excited carriers in the volume of a crystal. The slow electrons with energy $E_p \leq 1$ keV, when going through a substance, create the cloud of the electron-hole (e-h) pairs which are in some way distributes by the energies. The same situation occurs in the result of ion bombardment, X-ray and γ-irradiation of crystals. The energy distribution of the secondaries is an important factor for determination of the shape of measured spectra and for calculations of the sensitivity and optimal parameters of semiconducting ionizing-radiation detectors and solide-state photomultipliers.The problem of evaluation of the energy distribution function may be divided into two independent ones. The first is determination of scattering rates of the electrons and holes due to the pair and plasmon production, the electron-phonon interaction and so on. There is some progress in solving the problem. The most important success is achieved in description of the electron interaction in the framework of the jellium model for the free-electron-like metals [4,10]. The similar model has worked out for a semiconductor with an isotropic gap [11]. The model has only two parameters to characterize a real crystals. There are the Fermi energy E_F and forbidden gap E_G. The other approximation [12] to evaluate the pair production rate has dealt with true final state statistical weights calculated via the real energy bands of the crystal. It is clear that the above models describe only the isotropic scattering. Another way is the simulation of electron-electron (e-e) scattering by the Monte Carlo method [5].The second problem consists in calculation of the energy distribution function with the help of so evaluated scattering rates and that is the aim of our paper. As opposed to the other known works on this problem [4,10,11] including those concerning silicon [11], our paper deals with the pair scattering rates in the framework of the statistical model based on pseudopotential band structure calculation. It has to investigate the effect of the electron density of state *ρ(E)* singularities on the energy distribution function *f(E)*. Besides we consider coupled electron and hole distributions as we have done previously for the case of simple metal [13]. We carry out our calculations by an example of

the silicon crystal. For simplicity we remain only the pair production scattering that is well justified for primaries energy E_p not exceeding the plasmon one, $kT \ll E_p - E_F \leq \omega_{pl}$, for the case of silicon $\omega_{pl} \approx 17$ eV.

2 Statistical model of the pair production scattering

Kane [12] was the first to adapt this model to calculation of electron and hole energy losses in silicon. Following [12] let us consider the scattering rate of the electron in the initial state $\boldsymbol{p}_1$ interacting with an electron $\boldsymbol{p}_4$ from the Fermi sea:

$$\omega(p_1, p_2; p_3, p4) = \frac{2\pi}{h} |M \begin{matrix} p_1 & p_2 \\ p_3 & p_4 \end{matrix}|^2 \delta(E_{p_1} - E_{p_2} - E_{p_3} + E_{p_4}) \qquad (1)$$

where

$M \begin{matrix} p_1 & p_2 \\ p_3 & p_4 \end{matrix} = \langle p_1 p_2 | \hat{H} | p_3 p_4 \rangle$

is the matrix element ($\hat{H}$ is the e-e interaction).

Summing up probability (1) by two free indices we get

(a) the electron scattering rate with transition from E_1 to E_2 energy level:

$$S_{ee}(E_1, E_2) = C\rho(E_2) \int\limits_{max(E_c, E_1 - E_2)}^{E_1 + E_2 + E_V} \rho(E_3)\rho(E_2 - E_1 + E_3) dE_3, E_2 \geq E_c; \quad (2)$$

(b) the same for hole:

$$S_{hh}(E_1, E_2) = C\rho(E_2) \int\limits_{E_1 - E_2 + E_c}^{E_V} \rho(E_3)\rho(E_2 - E_1 + E_3) dE_3, E_2 \geq E_v; \quad (3)$$

(c) the rate of generation of a hole on the E_2 level by the scattering of an electron on the E_1 level:

$$S_{eh}(E_1, E_2) = C\rho(E_2) \int\limits_{E_c}^{E_1 + E_2 - E_c} \rho(E_3)\rho(E_1 + E_2 - E_3) dE_3, E_2 \geq E_v; \quad (4)$$

(d) vice versa for electron:

$$S_{he}(E_1, E_2) = C\rho(E_2) \int\limits_{E_1+E_2-E_V}^{E_V} \rho(E_3)\rho(E_1 + E_2 - E_3)dE_3, E_2 \geq E_c; \quad (5)$$

In equations (2)-(5) E_v is the valence band top, E_c is the conduction band bottom, the bottom of the valence band corresponds to the zero energy; C denotes the mean square of matrix element from equation (1). The above values (2), (3) give the total scattering rates or inverse lifetimes of electrons and holes:

$$\Gamma_e E_1 = \frac{1}{2} C \int\limits_{E_c}^{E-E_G} S_{ee}(E_1, E_2)dE_2, E_1 \geq E_c; \quad (6)$$

$$\Gamma_h E_1 = \frac{1}{2} C \int\limits_{E+E_G}^{E_V} S_{hh}(E_1, E_2)dE_2, E_1 \leq E_V; \quad (7)$$

The factor $\frac{1}{2}$ in equations (6) and (7) takes into account the identity of the final states which differ only by commutation of indices E_2 and E_3. Finally this factor in the kinetic equation describes the cascade multiplication of electrons and holes [13]. The density of states $\rho(E)$ was obtained on the basis of the real band structure of silicon calculated in the framework of the empirical pseudopotential method. We obtain the valence bandwidth $E_v = 12.5$ eV, the conduction band bottom $E_c = 13.6$ eV and the forbidden gap $E_G = E_c$ - E_v = 1.1 eV.

Figure 1 presents the hole and electron total scattering rate or inverse mean lifetime $\Gamma(E) = 1/\tau(E)$ for which the coefficient C was chosen by the best fit of our curve to that from Ref. [12]. All unknown scattering processes are taken into account efficiently by adding energy independent term $\Gamma_0 = 0.1$ eV as it was done by Kane [12]. Figure 1 shows sharp thresholds for $\Gamma_h(E)$ and $\Gamma_e(E)$ arising from the pair creation process, the threshold energy $E_{th} \sim 3E_G$. The above-mentioned constant term Γ_0 in $\Gamma(E)$ plays an important role only in the energy range $|E - E_{C,V}| \leq E_{th}$. For excitations having energies much higher than E_{th} the electron-phonon and impurity scattering may be neglected. In Figure 1 we have also plotted probabilities of energy losses:

$$P_{\alpha\beta}(E_1, E_2) = S_{\alpha\beta}(E_1, E_2)/\Gamma_\alpha(E_1), (\alpha, \beta = e, h) \tag{8}$$

for $E_1 = 5.5$ eV and $E_1 = 20.5$ eV. These probabilities are independent of C. They increase rapidly for losses $|E_1 - E_2| > 2E_G$ and have some singularities which reflect the shape of the electron density of states $\rho(E)$.

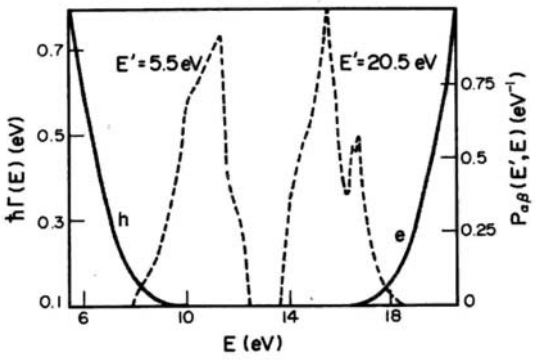

Figure 1: *Total scattering rate or inverse means lifetime $\Gamma(E)$ for holes (h) and electrons (e) – the solid line. Probabilities of energy losses $P_{hh}(E',E)$ for E' = 5.5 eV and $P_{ee}(E',E)$ for E' = 20.5 eV – the dashed line, on the right scale.*

created by the flow of primary electrons at energy E_p. Confining ourselves to isotropic scattering we get the following system of kinetic (Boltzmann-type) integral transport equations (analogous to Refs. [14–16]):

$$N_e(E)\Gamma_e(E) = \int_{E+E_G}^{E_p} S_{ee}(E', E)N_e(E')dE' +$$
$$+ \int_{max(0,E_V+E_C-E_p)}^{2E_V-E} S_{he}(E', E)N_h(E')dE' +$$
$$+ I_p\delta(E - E_p), E \geq E_c; \tag{9}$$

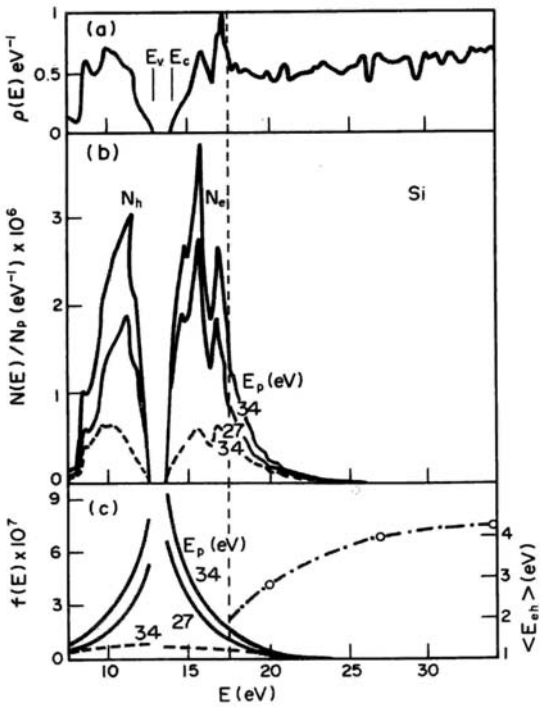

Figure 2: *(a) The electron density of states for silicon, E_v is the top of valence band and E_c is the bottom of the conduction band. (b) The solid curves are the energy distribution of excited holes $N_h(E)$ and electrons $N_e(E)$ concentrations for the various energies E_p of primary electrons pointed out at the curves. The dashed curve is the first iteration result. (c) The solid curves are the occupation numbers at various E_p; the dashed curve is the first iteration. The dashed and dotted line on the left scale is the E_p dependence of the mean energy of e-h pair.*

$$N_h(E)\Gamma_h(E) = \int\limits_{max(0,E_V+E_C-E_p)}^{E-E_G} S_{hh}(E',E)N_h(E')dE' +$$
$$+ \int\limits_{2E_C-E}^{E_p} S_{eh}(E',E)N_e(E')dE', E \le E_V; \qquad (10)$$

Equation (9) takes into account the fact of coupling between $N_e(E)$ and $N_h(E)$ in some energy range. The last term in equation (9) is a source function and I_p is the primaries creation rate.
Using the numerical quadrature method to solve equations (9), (10) we derive recurrent relations for $N_e(E)$ and $N_h(E)$. Scaling E from E_p to E_c in equation (9) and correspondingly from 0 to E_v in equation (10) one may get every subsequent value of the distributions via preceding ones.

Figure 2(b) shows the results of the numerical solution of equations (9), (10) $N(E)/N_p$ for various E_p, here $N_p = I_p/\Gamma_e(E_p)$ is a concentration of primaries. The vertical dashed line in Figure 2(b) denotes the vacuum level, the dashed curves are the first iteration results at $E_p = 34$ eV:

$$N_{1e}(E)/N_p = S_{ee}(E_p,E)/\Gamma_e(E), E \ge E_c;$$
$$N_{1h}(E)/N_p = S_{eh}(E_p,E)/\Gamma_h(E), E \ge E_v; \qquad (11)$$

For comparison the electron density of states $\rho(E)$ has been plotted in Figure 2(a). In Figure 2(c) we display graphs of the quantity $f(E) = N(E)/N_p\rho(E)$ which is the electron state occupation number normalized to the unit concentration of primaries. The dashed curve is the first iteration result $f_1(E) = N_1(E)/N_p\rho(E)$. The dashed and dotted curve is the dependence of the mean e-h pair creation energy on energy E_p:

$$< E_{eh} >= \frac{\int\limits_{E_C}^{E_p} EN_e(E)dE}{\int\limits_{E_C}^{E_p} N_e(E)dE} - \frac{\int\limits_{0}^{E_V} EN_h(E)dE}{\int\limits_{0}^{E_V} N_h(E)dE} \qquad (12)$$

3 Discussion

In this paper we have demonstrated an application of the statistical model to the problem of energy relaxation of secondaries in silicon. We have obtained the threshold energy in this model $E_{th} \approx 3E_G$ that much exceeds the value obtained in Ref. [17] from the energy conservation law $E_{th} = E_G$ or from the energy and momentum conservation laws $E_{th} = 3E_G/2$. These discrepancies are due to using the real band structure of silicon in contrast to Ref. [17].
The energy distribution of concentration of secondaries *N(E)* calculated in our work has some singularities generated by oscillations in *ρ(E)*. Such a behaviour of *N(E)* is caused by the scattering rates in the form of equations (2)-(5). However, for further application, we have got some very surprising and important results that the energy distribution function *f(E)* does not contain any singularities and permits a smooth interpolation, for example, $f(E) \sim |E - E_f|^{-S}$.
The mean pair creation energy $<E_{eh}>$ is an important characteristic of a semiconducting detector of ionizing radiation. Usually one believes that $<E_{eh}>$ is independent of the energy of primaries E_p. So measuring the number of created *e-h* pairs $n = E_p/<E_{eh}>$ one may evaluate the energy E_p. Our calculations indicate possible deviations of the counters from proportionality for low energies E_p in stationary conditions.
So the statistical model allows us to describe the pair ionizing relaxation of excited carriers. The derived energy distribution function may be used for the photo- and secondary emission spectra calculations (see, for example, Refs. [6,7,18,19]) and for the related problems.

4 Acknowledgements

This work was supported by the Government Fund for Basic Research of Ukraine.

References

1. Unoccupied electronic states: Fundamentals for XANES, EELS, IPS and BIS (ed. J.C. Fuggle and J.E. Inglesfield), in: Topics in Applied Physics, **69** (Springer, Berlin-Heidelberg, 1992).

2. A.B. Hayden *et al.*, J. Phys.: Condensed Matter **7**, 9475 (1995).

3. A. Goldmann *et al.*, Solid State Commun. **79**, 511 (1991).

4. M. Rösler, Particle induced electron emission I, in: Springer Tracts in Modern Physics, **122**, 1 (Springer, Berlin, 1991).

5. J. Devooght *et al.*, Theoretical descriptions of secondary electron emission induced by electron or ion beam impinging on solids (Springer, Berlin, 1998).

6. O.F. Panchenko, Surf. Sci. **482-485**, 723 (2001).

7. O.F. Panchenko *et al.*, Surf. Sci. **507-510**, 192 (2002).

8. A. Liebsch, Electronic excitation at metal surfaces (Plenum Press, New York, 1997).

9. W.S.M. Werner, Surf. Interf. Anal. **31**, 141 (2001).

10. C.J. Tung *et al.*, Phys. Rev. B **16**, 4302 (1977).

11. L.C. Emerson *et al.*, Phys. Rev. B **7**, 1798 (1973).

12. E.O. Kane, Phys. Rev. **159**, 624 (1967).

13. O.F. Panchenko *et al.*, J. Electron Spectrosc. Relat. Phenom. **83**, 21 (1997).

14. P.A. Wolff, Phys. Rev. **95**, 56 (1954).

15. D.R. Penn *et al.*, Phys. Rev. Lett. **55**, 518 (1985).

16. I.S. Tilinin *et al.*, Prog. Surf. Sci. **52**, 193 (1997).

17. R.C. Alig *et al.*, Phys. Rev. B **22**, 5565 (1980).

18. O.F. Panchenko *et al.*, Solid State Commun. **89**, 849 (1994).

19. O.F. Panchenko *et al.*, Solid State Commun. **101**, 483 (1997).

Frascati Physics Series Vol. XXXII (2003), pp. 39-45
19th INTERNATIONAL CONFERENCE ON X-RAY AND INNER-SHELL
PROCESSES – Roma, June 24 - 28, 2002

K X-RAY SATELLITE AND HYPER SATELLITE SPECTRUM OF SCANDIUM EXCITED BY PHOTONS

B.Seetharami Reddy, S.S.Raju, T.Seshi Reddy, M.L.N.Raju
Andhra University, Visakhapatnam, India
B.Mallikarjuna Rao, M.V.R.Murti, L.S.Mombasawala
IIT, Bombay, India

ABSTRACT

K X-ray emission spectrum generated by photon excitation has been studied with a crystal spectrometer. The energies and relative intensities of K_α X - ray satellite, hyper satellite, K_β X - ray satellite, KLL and KMM peaks have been measured and compared with the reported values obtained by proton, helium and oxygen ion bombardment and also with theoretical estimates whereever available. A dependence of mode of excitation on both the energy shifts and relative intensities is observed. K_αX-ray satellite energy shift is compared with the semi - empirical value of Torok and its modified version, where a better agreement is found.

1 Introduction

When an atom ionized simultaneously in different shells de-excites, x-ray satellites are produced. If some holes are present in the L-Shell along with a hole

in the K-shell, the transitions to the K-Shell from the higher shells give rise to K x-ray satellites, with the holes in the L-shell acting as spectators. These satellites are usually denoted as KL^n, where n stands for the number of holes in the L-shell. In the absence of any such L-holes, the diagram line KL^0 is emitted. The transitions originating from the L and M –shells give rise to K_α and K_β satellites respectively. The spectator L-holes reduce the screening effect of the L-shell resulting in higher binding energy of the L-shell and hence the K_α satellite lines have energies higher than that of the K_α diagram line. So is the case with K_β satellites. K x-ray satellites have been studied using ion, electron and photon excitation. With the photon excitation technique, satellites up to only second order can be studied. In addition to these high energy satellites, lines appear on the low energy side of the diagram lines which are usually called low energy satellites. These low energy satellites are interpreted by Aberg [1] as RAE (Radiative Auger Emission) structures. In the KMMRAE an M electron fills are 1 s hole and another M electron is excited into a bound or continuum state. Similarly in the KLLRAE an L electron fills 1s hole and another L electron is simultaneously excited into a bound or continuum state.

Of special interest are the hyper satellites, the weak lines that appear on the high energy side of the diagram lines. If the atom is doubly ionized in the K-shell and if these holes are filled by transitions from outer shells, KX-ray hyper satellites are emitted. Such transitions originating from L,M,N.... Shells are called K_α, K_β, K_γ .... hyper satellites respectively. If there is ionization only in the K-shell and all other shells are filled, the resulting hyper satellites are called pure hyper satellites. Pure K_α hyper satellites are denoted as ${K_\alpha}^h L^0$, indicating that there is no ionization in the L-shell. But if there is simultaneous ionization in the L-shell also, de-excitation of the atom gives rise to satellites of hyper satellites denoted as ${K_\alpha}^h\ L^n$, where n stands for the number of holes in the L-shell. The atoms that are completely empty in a particular shell, say K-shell are christened as 'hollow atoms' by Briand [2] and of late bestowed special interest. They have also been proposed as a way of achieving population inversion and lasing for hard x-ray lasers [3]. The information about such hollow atoms can be obtained by studying pure hyper satellites only. In ionization by ions, owing to simultaneous heavy multiple ionization in L-shell in addition to K-shell, either ${K_\alpha}^h\ L^0$ is suppressed or dominated by ${K_\alpha}^h\ L^n$ lines. Hence, for the study of pure ${K_\alpha}^h L^0$ hyper satellites uncontaminated by ${K_\alpha}^h\ L^n$ lines,

photon ionization is the best process of excitation. Study of hyper satellites is also useful in understanding Breit interaction [4].

In the present work energies and relative intensities of K_α satellites and hyper satellites and K_β satellites of scandium are measured and compared with the previous values obtained by ion excitation and theoretical values wherever available. Previous work [5] on scandium by photon excitation was confined to $K_\alpha L^1$ satellites and hence the present study, which is comprehensive covering both K_α and K_β satellites, hyper satellite lines and KLL and KMMRAE structures, was thought worth undertaking.

2 Experimental Details

The principle involved and the general experimental details and procedure have already been reported (Parathasaradhi et al [6]). In the present study a Philips 1410 model wavelength dispersive spectrometer was employed. This system, in brief, consists of an x-ray tube, a plane crystal and a continuous flow type p-10 gas (90% argon – 10% methane) proportional counter with a thin (1μm) polypropylene window. The x-ray tube was operated at 40 KV voltage and 30mA current. LiF (200) plane crystal (2d = 4.07 Å) was used. Pure powder of Sc_2O_3 pressed into pellets 5mm thick and 5cm diameter were used for fluorescent x-ray emission. The spectra were scanned in 2θ steps of 0.02^0. The energy calibration was done taking $K_\alpha L^0$ lines of Ca, K and Ti as the reference lines and assuming their energies reported by Bearden [7].

3 Results and Discussion

The spectrum of scandium is shown in fig.1. the analysis of spectra was carried out using the standard peak deconvolution technique starting from the high energy end. The energies of KLL, $K_\alpha L^{0,}$ $K_\alpha L^1$, $K_\alpha{}^h L^0$, KMM, $K_\beta L^0$ and $K_\beta L^1$ are presented in table 1 along with the previous values obtained by ion excitation[8] and theoretical (HFS) values [8] wherever available. It is the usual practice in the study of satellite spectra to compare the experimental energy shifts of the satellites from therein respective diagrams lines with theoretical estimates.

The present experimental value of the energy shift AE($K_\alpha L^1$) is not much dependent of the mode of excitation, as it is lower only about 1.5ev than the

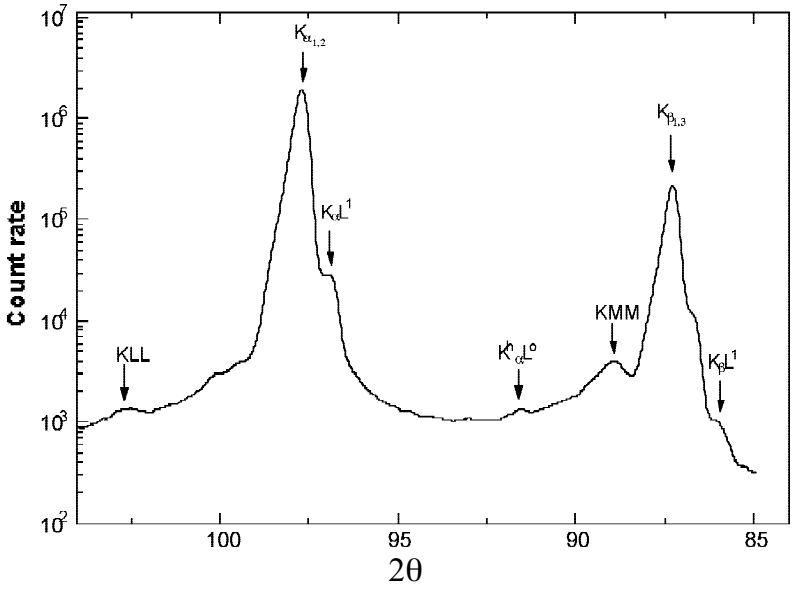

Figure 1: *K X-ray satellite spectrum of scandium*

value by helium and oxygen ion [8] excitation (Table 1). The semi-empirical formula of Torok etal [9] underestimates this shift. Their formula based on energy systematics is, AE($K_\alpha L^1$) = 1.530 (Z-6.828), where 6.828, is the slater's screening constant. Our group has also undertaken a similar study of energy systematics. Retaining the screening constant we proposed a slightly modified version of the above semi empirical formula [10], AE($K_\alpha L^1$) = 1.703 (Z-6.828) The energy shift predicted by this is in better agreement with the experimental value than that of Torok. The values of this energy shift estimated by SCF [11] (Self Consistent Field theory) is in good agreement (with in 1eV) with the present experimental value.

No previous experimental values of KLLRAE structure energy and relative intensity of scandium by any mode of excitation are available in literature. Perhaps the present experimental value is the first to be reported for scandium. In the spectrum of scandium generated by oxygen ions, the hyper satel-

Table 1: *K x-ray Satellite and hyper satellite energies (eV) of scandium*

Line	Present work- Photon Excitation	Ion excitation Protons[8]	He ions[8]	O ions[8]	Theory HFS[8]
KLL	3947.5±0.4	–	–	–	–
$K_\alpha L^0$	4089.0±0.2	4089	4089	4090	4089
$K_\alpha L^1$	4112.9±0.4	4113	4114	4115	4111
$K_\alpha^h L^0$	4296.2±0.4	–	–	–	–
KMM	4395.9±0.4	–	4404	–	4404
$K_\beta L^0$	4460.6±0.2	4461	4460	4460	4461
$K_\beta L^1$	4509.5±0.4	–	4512	4518	4515

lites $K_\alpha{}^h L^3$, $K_\alpha{}^h L^4$ and $K_\alpha{}^h L^5$ only were emitted and the pure hypersatellite $K_\alpha{}^h L^0$, corresponding to the hollow atom was not to be seen. This once again demonstrates the usefulness of the photon excitation technique in the study of pure hyper satellite. The present experimental energy shift of $K_\alpha{}^h L^0$ from the diagram line $K_\alpha L^0$ is lower by about 4 eV when compared with the MCDF (Multi Configurational Dirac – Fock) theoretical estimate. This theoretical formalism takes into consideration Breit interaction also. The present experimental energy shift of the KMMRAE structure from the $K_\beta 1,3$ diagram line is higher by about 8 eV than the value obtained by helium ion excitation [8] (Table 2).

Table 2: *K x-ray satellite and hypersatellite energy shifts (eV) of scandium*

Line	Present work	Ion excitation Protons[8]	He ions[8]	O ions[8]	Semiempirical Torok[9]	Modified[9]	Theory HFS[8]	SCF[11]	MCDF[4]
ΔE(KLL)	141.5±0.6	–	–	–	–	–	–	–	–
$\Delta E(K_\alpha L^1)$	23.9±0.6 24.9[5]	24	25	25	21.7	24.1	–	24.5	–
$\Delta E(K_\alpha^h L^0)$	207.2±0.6	–	–	–	–	–	–	–	203.3
ΔE(KMM)	64.7±0.6	–	56	–	–	–	57	–	–
$\Delta E(K_\beta L^1)$	48.9±0.6	–	52	58	–	–	54	–	–

Table 3: *Relative intensities of K x-ray satellite and hypersatellites of scandium*

Line	Present work- Photon Excitation	Ion excitation Protons[8]	He ions[8]	O ions[8]
$KLL/K_{\alpha}^{1,2}$	0.0028±0.0003	–	–	–
$K_{\alpha}L^{1}/K_{\alpha}^{1,2}$	0.0183±0.002	0.092	0.336	3.09
$K_{\alpha}^{h}L^{0}/K_{\alpha}^{1,2}$	0.0024±0.0003	–	–	–
$KMM/K_{\beta}^{1,3}$	0.026±0.003	–	0.037	–
$K_{\beta}L^{1}/K_{\alpha}^{1,2}$	0.0025±0.0003	–	0.27	2.06

This is surprising since generally the energy shifts by photons excitation are lower than those by ion excitation. The target used in the present experiment is scandium oxide. Hence chemical effect may be partly responsible for the larger shift, but that can not fully account for the shift of 8 eV. Perhaps this peak is contaminated by some other unresolved peak. The present experimental energy shift of the $K_{\beta}L^{1}$ is lower than that due to ion excitation and also the theoretical estimate (Table 2). The relative intensity of KLL structure is being reported perhaps for the first time (Table 3). The present measured value of relative intensity of $K_{\alpha}L^{1}$ with respect to the diagram line $K_{\alpha}1,2$ is very much lower than values obtained by proton, helium and oxygen ion excitation.

Heavier the ion higher is this relative intensity. The present experimental values of the relative intensities of the KMMRAE peak and $K_{\beta}L^{1}$ satellite line with respect to the diagram line $K_{\beta}1,3$ are also very much lower than those measured by ion excitation (Table 3).

4 Conclusions

The energy shifts and relative intensities of the satellite lines $K_{\alpha}L^{1}$ and K_{β} L^{1}, hyper satellite line ${K_{\alpha}}^{h}L^{0}$ and the KLL and KMM RAE peaks measured by photon excitation using a plane crystal spectrometer are reported. The pure hyper satellite ${K_{\alpha}}^{h}L^{0}$ absent in the spectra generated by ion excitation mode can be seen in the spectrum in the present study thus once again demonstrating the useful ness of photon excitation mode in the study of 'hollow' atoms. While a dependence of mode of excitation is observed both in energy shifts as well as relative intensities of the satellites, it is more pronounced in the case of relative intensities. The measured energy shift of $K_{\alpha}L^{1}$ is in good agreement with the

estimate of our modified version of Torok's semi-empirical formula and also with the theoretical value. While the energy shift of hyper satellite $K_\alpha{}^h L^0$ is higher than the theoretical value, that of $K_\beta L^1$ is lower than the theoretical value.

5 Acknowledgements

The authors gratefully acknowledge the financial assistance provided by Department of Science and Technology, Govt. of India, under a collaborative research project entitled "Study of K x-ray satellites, hyper-satellites and allied aspects by photon interaction" sanctioned to Dept. Nuclear Physics, Andhra University, and CSRE, IIT, Bombay

References

1. Aber, T. Phys. Rev A **4**, 735 (1971).
2. Briand, J. et al., Phys. Rev. Lett. **65**, 159 (1990).
3. Moriabashi, K. et al., Phys.Rev A **59**, 2732 (1999).
4. Chen, M.H. and Crasemann.B., Phys. Rev. A **25**, 391(1982).
5. Parratt, L.G., Phys.Rev **50**, 1 (1936).
6. Parthasaradhi, K. et al., Nucl. Instr. Meth. A **255**, 54 (1987).
7. Bearden, J.A., Rev. Mod. Phys. **39**, 78 (1967).
8. Hodge, B. et al., J. Phys. B : Atom. Molec. Phys., **6** 2468 (1973).
9. Torok, I. et al., Nucl. Inst. Meth. B **150**, 8 (1999).
10. Suresh, P. Ph.D. Thesis, Andhra University, Visakhapatnam, India.
11. Bhattacharya, J. et al., Phys. Rev. A **37**, 3162 (1988).

Frascati Physics Series Vol. XXXII (2003), pp. 47-52
19th INTERNATIONAL CONFERENCE ON X-RAY AND INNER-SHELL PROCESSES – Roma, June 24 - 28, 2002

INVESTIGATION OF THE SHAKE PROCESS IN Fe $K\alpha$ SATELLITES

Nobuyuki Shigeoka, Hirofumi Oohashi,
Tatsunori Tochio, Yoshiaki Ito
Laboratory of Atomic and Molecular Physics,
Institute for Chemical Research, Kyoto University,
Gokasho, Uji, Kyoto 611-0011 Japan

Aurel M. Vlaicu, Atsushi Nisawa, Hideki Yoshikawa,
Sei Fukushima, and Mamoru Watanabe
Advanced Materials Laboratory, in SPring-8,
Mikazuki, Hyogo 679-5198 Japan

ABSTRACT

Fe $K\alpha_{3,4}$ satellite spectra were investigated with Johann-type spectrometer at the BL15XU undulator beam line, SPring-8. Intensity of the $K\alpha_{3,4}$ satellite relative to the $K\alpha_1$ emission line asymptotically increased up to 9,000 eV for the excitation energy, and almost saturated around 9,500 eV. Threshold energy of satellites was 7,950 eV. This value is corresponding to the ionization energy of Fe 1s+2p*, where * means the value of Z+1 approximation. The growth of satellite intensity with the excitation energy indicates that the 2p spectator holes, which are considered as the origin of the $K\alpha_{3,4}$ satellite emissions, are mainly created by shake-off in Fe, as suggested by Fritsch et al. [5] on a previous work for Cu. The general conclusion is obtained that the 2p spectator holes are the origin of the $K\alpha_{3,4}$ satellites. The contribution from 2s spectator transitions are also observed. Moreover, the propose by Deutsch et al. [14] that 3d spectator holes are found to broaden the widths of the corresponding x-ray emission lines by up to a few hundreds of an eV, is confirmed by the experiment of the threshold evolution in Fe $K\alpha$ spectrum.

1 Introduction

Most of studies on the contributions from the effects of shake processes in solids and vapors etc to x-ray absorption have mainly been carried out by Italian group, Slovenian group, and Japanese group, respectively, in order to elucidate the electron correlation in atoms. The sharp multielectron photoexcitation features due to resonant and shake-up, and the extended shake-off saturation profiles are of special interest in x-ray absorption spectroscopy.

The x-ray absorption of 3d transition metals was examined in the energy region of $K+L$ double photoabsorption. However, no significant features attributable to multiple photoexcitation are found in the spectra, so that $K+L$ edges for 3d elements were not confirmed [1, 2]. The result could be explained by theoretical predictions due to lower shake-up probabilities for $K+L$ transitions [2]: the transition edges observed in x-ray absorption spectra are due to the shake-up process only, i.e. the probabilities of resonance and shake-up for $K+L$ transition for 3d elements are lower than the accuracy of the detection and it is difficult to obtain the pure long-range shake-off profile in XAFS oscillation.

With the advent of the third generation synchrotron radiation, we can do experiments on the threshold behavior of the satellites including the excitation dynamics in atoms. Especially, x-ray emission spectroscopy is a suitable tool to study the satellites on the electron correlation. First detailed photoexcitation measurements were performed by Deslattes et al. [3], where both emission and absorption spectroscopy are combined to examine multielectron vacancies on atomic Ar, by Deutsch and co-workers [4, 5] finding a pure shake-off behavior of the Cu $K\alpha$ x-ray satellite complex, by Sternemann et al. [6] measuring the valence fluorescence satellites KM - $N_{2,3}M$ transition of a solid in Ge target, and more recently, by Raboud et al. [7] measuring the KL x-ray emission of Ar induced by impact with monoenergetic photons to investigate the $K+L$ double excitation from threshold to saturation.

The contributions from 2s and 2p spectator transitions and 3d spectator transitions (hidden satellites) have not been investigated in Fe. We report the effect on the spectator transitions in Fe.

2 Experiment

The measurements were carried out at BL15XU, SPring-8, Ako, with a curved crystal x-ray spectrometer [8, 9]. A Si double crystal monochromator with a bandpass of ~ 3 eV and a flux of $> 10^{12}$ photons/sec was used. The sample was a polycrystalline high-purity Fe foil. The fluorescence spectrometer employed the Johann geometry with a 1.5 m diameter Rowland circle on Si (400) crystal providing < 1 eV resolution. BL15XU has helical and planer type undulator, and planer type undulater was selected for our focused energy region. The coherent radiation out of the monochromator is onto the sample in the sample chamber of the spectrometer. The light then goes into the crystal housing in which three kinds of crystals are mounted. The optical focusing condition can be met by moving the sample, crystal and detector to satisfy the Rowland geometry. The measurement was carried out changing the excitation energy from 7,850 eV to 10,000 eV [10] in order to investigate the energy-dependency on $K\alpha_{3,4}$ satellites' intensity. At first spectrometer angle was fixed at which we can get $K\alpha_{3,4}$ satellites and then excitation energy were tuned in the region between 7,850 eV and 10,000 eV. Next at selected excitation energies spectrometer angle was scanned in order to obtain the spectral profile.

3 Results and discussions

An onset of $K\alpha_{3,4}$ satellite emission for threshold energy was estimated with the results of first scan shown in Fig. 1. With the results of second scan $K\alpha_1$ contribution was removed by subtracting a Lorentzian tail fitted to the spectrum outside the energy range of the satellites. The intensity of the satellite with excitation energy is shown in Fig. 2, with a comparison of the theoretical and experimental data. The experimental intensity data were obtained only for high-energy excitation in conventional x-ray tubes. The feature of the data is the smooth increase of the satellite intensity over a wide energy range above threshold. Since an abrupt intensity jump is predicted for shake-up at threshold while shake-off should increase smoothly from zero [1, 2, 11, 12], the shape of the curve in Fig. 2 marks the behavior as a pure shake-off process similar to that in Cu [4, 5]. HFS calculations yield shake probability of 0.12 %, 0.61 %, 0.46 %, 3.50 %, and 9.66 % for the respective 2s, 2p, 3s, 3p, and 3d shake electrons accompanying K ionization in Fe [13]. The saturation intensity,

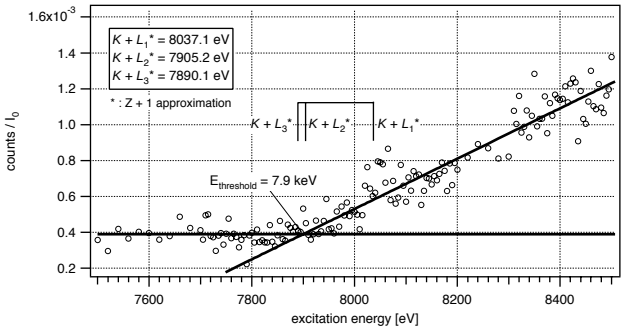

Figure 1: *Intensity at $K\alpha_{3,4}$ satellite position with excitation energy*

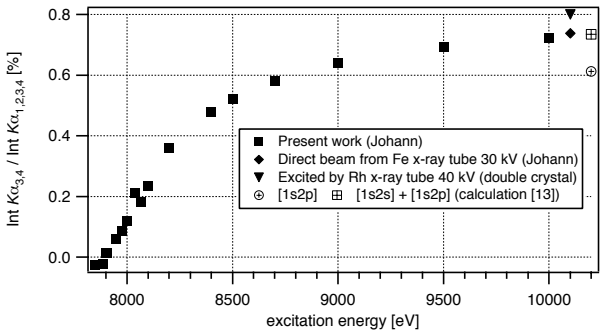

Figure 2: *Intensity of the $K\alpha_{3,4}$ satellite with excitation energy*

0.72 % of the $K\alpha_1$ line, is in excellent agreement with the high-energy, x-ray-tube-measured intensity of 0.74 %, and the sudden-approximation theoretical intensities of 0.61 % [13]. It is interesting that a sum of [1s2s] and [1s2p] transition probabilities is good consistent with the observed one.

According to Deutsch et al. [14], the presence of a spectator hole during the emission process introduces additional splitting in the initial and final energy levels and consequently increases considerably the number of the distinct transition lines. It was possible to separate out the contribution of these transitions from those of the diagram ones by fitting the measured line shape by an ab initio calculated transition array. They reported that 3d spectator holes broaden the widths of the corresponding x-ray emission lines by up to a few tenths of an eV. The width of the FWHM in Fe $K\alpha_1$ with excitation energy is

shown in Fig. 3. The feature of the data is the abrupt increase of the width till a few hundreds of an eV above the [1s3d] threshold. This tendency is in contrast with that in [1s2p] transitions. The matured width is about 0.4 eV broader than that at [1s3d] threshold. This value is significantly corresponding to that reported by Deutsch et al. [14]. It may be considerable that the width is broadened by the presence of an additional 3d spectator hole in the atom by as much as a few tenths of an eV. Further measurements are planned to elucidate the details of the $[KM]$ double photoexcitation in the energy region.

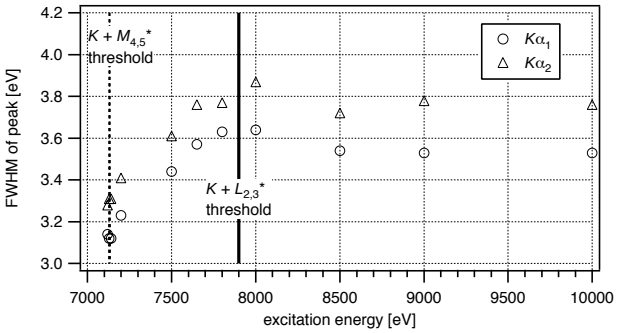

Figure 3: *FWHM of the $K\alpha_1$ and $K\alpha_2$ with excitation energy*

Anagnostopoulos [15] showed that the lifetime of the K hole is affected by the presence of the L hole and it depends on the particular L subshell. Although it is difficult to elucidate the significance and causes of these differences, the investigation on the influence of additional holes on level widths in atoms is very important in atomic physics.

References

1. A. Kodre, M. Hribar, I. Arcon, D. Glavic-Cindro, M. Stuhec, R. Frahm, and W. Drube, Phys. Rev. A **45**, 4682 (1992).

2. Y. Ito, H. Nakamatsu, T. Mukoyama, K. Omote, S. Yoshikado, M. Takahashi, and S. Emura, Jpn. J. Appl. Phys. **32**, Suppl. 32-2, 58 (1993).

3. R. D. Deslattes, R. E. LaVilla, P. L. Cowan, and A. Henins, Phys. Rev. A **27**, 923 (1983).

4. M. Deutsch, O. Gang, K. Hämäläinen, and C. C. Kao, Phys. Rev. Lett. **76**, 2424 (1996).

5. M. Fritsch, C. C. Kao, K. Hämäläinen, O. Gang, E. Forster, and M. Deutsch, Phys. Rev. A **57**, 1686 (1998).

6. C. Sternemann, A. Kaprolat, M. H. Krisch, and W. Schulke, Phys. Rev. A **61**, 020501(R) (2000)

7. P.-A. Raboud, M. Berset, J.-Cl. Dousse, Y.-P. Maillard, O. Mauron, J. Hoszowska, M. Polasik, J. Rzadkiewicz, Phys. Rev. A **65**, 062503 (2002)

8. Y. Ito, A. M. Vlaicu, T. Tochio, K. Mutaguchi, H. OoHashi, N. Shigeoka, T. Shoji, J. Harada, S. Emura, and T. Uruga, in *Proceedings of International Workshop on Physical Properties of Matter by x-ray absorption and emission spectroscopy*, 24-26 July 2000, Osaka Electro-Communication University, Osaka, Japan, p32.

9. Y. Ito, A. M. Vlaicu and T. Tochio, CP576, *Application of Accelerators in Research and Industry*, edited by J. L. Duggan and I. L. Morgan (AIP) (2001)

10. A private communication with Jana Gomilsek.

11. S. J. Schaphorst, A. Kodre, J. Ruscheinski, B. Crasemann, T. Xberg, J. Tulkki, M. H. Chen, Y. Azuma, and G. S. Brown, Phys. Rev. A **47**, 1953 (1993).

12. Y. Ito, H. Nakamatsu, T. Mukoyama, K. Omote, S. Yoshikado, M. Takahashi, and S. Emura, Phys. Rev. A **46**, 6083 (1992)

13. T. Mukoyama and K. Taniguchi, Phys. Rev. A **36**, 693 (1987).

14. M. Deutsch, O. Gang, G. Holzer, J. Hartwig, J. Wolf, M. Fritsch, and E. Forster, Phys. Rev. A **52**, 3661 (1995).

15. D. F. Anagnostopoulos, J. Phys. B **28**, 47 (1995).

Frascati Physics Series Vol. XXXII (2003), pp. 53-58
19th INTERNATIONAL CONFERENCE ON X-RAY AND INNER-SHELL PROCESSES – Roma, June 24 - 28, 2002

THE MECHANISM OF $_{74}$W $L\beta 2$ X-RAY EMISSION SATELLITE EXCITED BY SYNCHROTRON-RADIATION

A. M. Vlaicu
National Institute for Materials Science, BL15XU Spring-8, Mikazuki, Hyogo 679-5198, Japan
Y. Ito, N. Shigeoka, H. Oohashi
Institute for Chemical Research, Kyoto University, Gokasho, Uji, Kyoto 611-0011, Japan
S. Fukushima, H. Yoshikawa, A. Nisawa
National Institute for Materials Science, BL15XU Spring-8, Mikazuki, Hyogo 679-5198, Japan

ABSTRACT

The origin of the visible $L\beta 2'$ $(L_3M_5N_5)$ of $_{74}$W was investigated by a high resolution Johann type spectrometer using synchrotron radiation (SR) at beam-line BL15XU in SPring-8. The satellite to diagram relative intensity $(L_3M_5N_5/L_3N_5)$ shows a clear threshold at the L_1 edge with a net intensity increase of about 3% within less than 20 eV over the L_1 absorption edge, and becoming constant afterward. The experimental results confirm the L_1-L_3M_5 Coster-Kronig (C-K) for $_{74}$W - previously considered forbidden from theoretical calculations - as the origin of the M_5 spectator hole participating in the $(L_3M_5N_5)$ satellite transition of $_{74}$W.

1 Introduction

The $L\beta 2$ (L_3N_5) x-ray emission spectra of tungsten $_{74}$W excited by synchrotron radiation (SR) at beam-line BL15XU in SPring-8 were measured by a high reso-

lution Johann type spectrometer. The satellite transition at the higher energy side of $L\beta 2$ appeared for exciting photon energies above the L_1 absorption edge. This satellite has been previously assigned to the $L_3M_5N_5$ transition, however the mechanism for the creation of M_5 spectator hole during the initial ionization is not certain: the M_5 spectator hole can be created by either by a L_3M_5 shake-off transition, or by a L_1-L_3M_5 Coster-Kronig (C-K) transition. Theoretical calculations [1)] for the L_1-L_3M_5 C-K energy (-2.7 eV) show that this process is forbidden for $_{74}$W. Several experimental studies by electron bombardment [2, 3)] investigated the C-K origin of this satellite transition of tungsten. However, in the case of electron bombardment, only a part of the incident electron energy is transferred to the atom, and the results were not conclusive. In the case of photon excitation, the whole energy of the incoming photon is transferred to the atom. In the present work we measured the satellite to diagram relative intensity ($L_3M_5N_5/L_3N_5$) for incident photon energies around the L_1 edge. The measured energy dependence shows a net increase of 3% within less than 20 eV over the L_1 absorption edge, and becoming constant afterward. The experimental results confirm the C-K origin of this satellite. The contribution of the spectator holes to the multiplet transition [4)] is taken into consideration during the analysis of data.

2 Experiment

A Johann type spectrometer with the Rowland circle diameter of 2R=1500 mm was used for detecting the fluorescence x-ray excited by synchrotron radiation (SR) from a 18 μm tungsten foil. In a first experiment, a NaI scintillation counter (SC) was used, equipped with a slit enough large (d_s=0.6 mm) in order to cover a substantial energy range. Considering the spatial resolution of the spectrometer (dE/E= 4 $*10^{-4}$) , the energy range covered by the 0.6 mm slit is about 4 eV at 10 keV. In this setup, the angle of the detector on the Johann spectrometer was set at the position corresponding to $_{74}$W $L\beta 2$' ($L_3M_5N_5$), and the energy of the incident SR radiation was scanned in the energy range around the $_{74}$W L_1 edge (12099.8 eV). After repeating the same measurement for $_{74}$W $L\beta 2$ (L_3N_5) and dividing the two data, the qualitative dependence of the satellite to diagram relative intensity in respect with the exciting SR energy was obtained (see Fig. 1).

The relative intensity of the satellite $L\beta 2$' to the *$L\beta 2$* diagram line *(Is(E))*

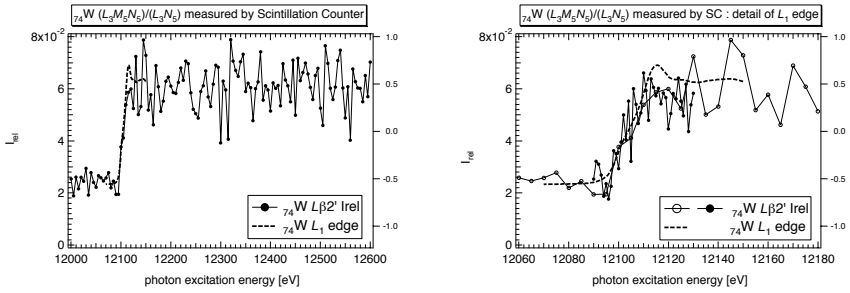

Figure 1: *The $L\beta 2$' relative intensity $(L_3M_5N_5)/(L_3N_5)$ versus incident SR energy around the $_{74}W$ L_1 edge measured by Johann spectrometer with the scintillation counter and 0.6 mm slit set at the corresponding Bragg angle for the satellite line and the diagram line; b) detail of the $_{74}W$ L_1 absorption edge.*

in Fig. 1 has a sharp increase at the $_{74}$W L_1 (12099.8 eV) edge from 2% to 5.5% within 15 eV. The residual intensity relative intensity of 2% at exciting energies below the L_1 edge comes actually from the tail of $L\beta 2$ diagram line itself, so that the actual jump of the relative is from zero to about 3.5%. The sharp onset of relative intensity at the L_1 edge, and the almost constant dependency for higher energies, qualitatively confirms the Coster-Kronig origin of the $L\beta 2$' $(L_3M_5N_5)$ satellite. In order to determine the actual dependence of the *Is(E)* a second experiment was performed using a photon counting CCD camera detector with a spatial resolution of 20 μm. The energy range covered by one pixel of the CCD camera is about 0.13 eV, but the actual energy resolution of the spectrometer is somewhat larger due to the Darwin width of the crystal rocking curve, evaluated at about 0.6 eV for the Si(440) reflection at 10 keV. In the energy range of 12076 eV - 12300 eV of the incident SR beam several emission spectra were measured with the center of the CCD camera set on the Johann type spectrometer at the Bragg angle corresponding to $_{74}$W $L\beta 2$ (L_3N_5). The CCD camera active region covers an energy range of about 150 eV by the Si(440) reflection at 10 keV. In this case the sample was set out of focus, at grazing incidence into the SR beam in order to obtain a wide spot-size on the sample. The wide spot size corresponds to a virtual source in the focus position. The virtual source intensity distribution was measured by a linked θ-2θ scan of the Johann spectrometer and recording of the peak of the $_{74}$W

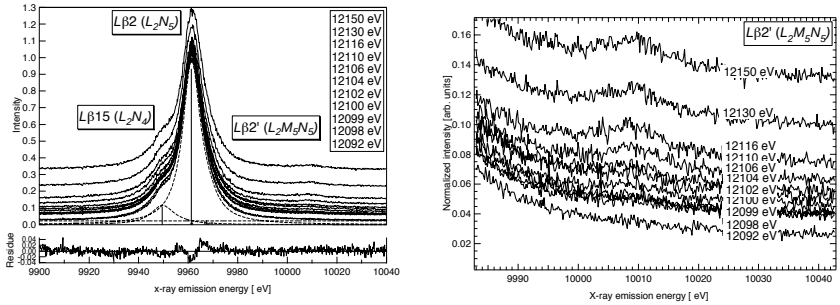

a) *b)*

Figure 2: *a)* $_{74}W$ *Lβ2, Lβ15, and Lβ2' ($L_3M_5N_5$) x-ray emission spectra excited by SR radiation tuned at energies around the* $_{74}W$ L_1 *absorption edge (12099.8 eV); b) detail of the Lβ2' ($L_3M_5N_5$) satellite.*

$L\beta2$ (L_3N_5), which was chosen as reference peak. The obtained source profile corrected spectra are shown in Fig. 2.

3 Results and Conclusions

The spectra measured by CCD camera were analyzed by fitting the *Lβ2, Lβ2'*, and *Lβ15* emission line by single Lorentzian profile, and by Lorentzian multiplet structure corresponding to the diagram line and the associated spectator hole satellite structure. For the multiplet fitting, the relative position , and intensity of the diagram and satellites was derived from theoretical calculations performed in the sudden approximation limit, and the obtained values were used as fixed fitting parameters, while the FWHM, the total shift of the multiplet and the overall amplitude were let free during the fitting. By this method, the FWHM of the emission lines and the relative intensity of the multiplets can be determined by taking into account the contribution of the spectator hole satellites. The FWHM was fixed during the Lorentzian fitting for $L\beta2$, $L\beta15$, and $L\beta2$' at 10.34 eV, 10.88 eV, and 11.87 eV respectively. For the multiplet fitting the FWHM was fixed during the fitting for $L\beta2$, $L\beta15$, and $L\beta2$'at 8.93 eV, 12.60 eV, and 13.33 eV respectively. These values were chosen as the average FWHM values obtained with free fitting parameters, at high photon excitation energy.

The relative intensity to the diagram line *Lβ2* of the *Lβ2'* ($L_3M_5N_5$)

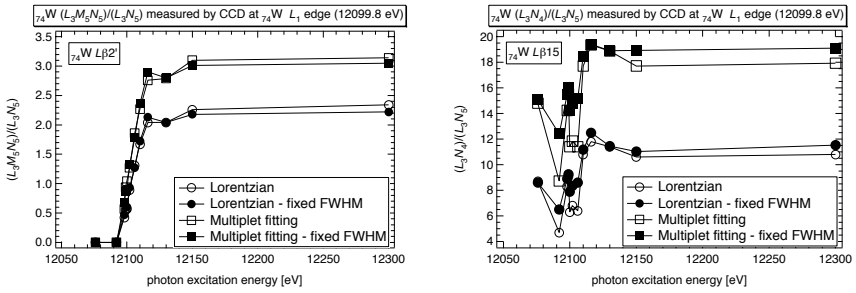

Figure 3: *Relative intensity to $_{74}W$ $L\beta 2$ at SR exciting energy around the W L_1 edge (12099.8 eV) determined from individual spectra by Lorentzian fitting, and multiplet fitting, and with free / fixed FWHM fitting parameters for a) $_{74}W$ $L\beta 2$ satellite, and b) $_{74}W$ $L\beta 15$.*

satellite shows a clear threshold at the photon excitation energy corresponding to the $_{74}$W L_1 absorption edge, and becomes almost constant afterwards (see Fig. 3a)). This result confirms that the origin of the M_5 spectator hole participating in the $(L_3M_5N_5)$ satellite transition is due to the $L_1L_3M_5$ Coster-Kronig transition.

When considering the multiplet structure in the fitting model, the $L\beta 2$ multiplet is composed of the digram line itself and the Coster-Kronig spectator holes situated in the N_{1-7}, O_{1-4}, and P_1 sub-shells. This spectator holes cause satellite transition which are very close situated near the diagram line, on the higher energy side of it. For this reason they are called also hodden satellites. The total contribution of these satellites to the intensity of the multiplet is about 12.27%. When fitting with a single Lorentzian for the whole multiplet, the contribution of the satellites is added to that of the diagram, and the total intensity of the diagram line is over-estimated. This effect can be observed when comparing the relative intensity of the $L\beta 2$' $(L_3M_5N_5)$ satellite: for the multiplet fitting the actual relative intensity of the satellite is about 150% bigger than the estimation obtained by single Lorentzian fitting.

The effect of the satellite structure when estimating the relative intensity can be also observed for the case of partly overlapping multiplets, as is the case with $L\beta 15$, and $L\beta 2$. The average of the N_{1-5} satellite structure of the $L\beta 15$ is situated with 8.7 eV on the higher energy side of the diagram line, toward the

$L\beta 2$ multiplet. When fitting with single Lorentzian for the whole multiplet, the $L\beta 15$ satellite structure is artificially added to the $L\beta 2$ multiplet during the fitting procedure. In this case, the error in estimation can go as high as 180% (see Fig. 3 b)).

The second visible effect is the change of the $L\beta 15/L\beta 2$ relative intensity at the L_1 absorption edge. This effect is due to the fact that the satellite to diagram relative intensities has different terms depending on the value of the photon excitation energy. For photon excitation energies between the L_2 and the L_1 absorption edge, the satellite relative intensity contains only the term due to the L_2L_3X Coster-Kronig transition, where X is the spectator hole level situated in the N_{1-5}, O_{1-3} sub-shell, while for photon excitation energies higher than the L_1 absorption edge, the relative satellite intensity contains an additional term corresponding to the L_2L_3X Coster-Kronig transition. This change of the satellite structure of the $L\beta 2$, $L\beta 15$ multiplets when the photon excitation energy traverses the L_1 absorption edge is assumed to be the origin of the change in the $L\beta 15/\ L\beta 2$ relative intensity.

References

1. M. H. Chen, B. Crasemann, K. N. Huang, M. Aoyagi, and H. Mark, *At. Data Nucl. Data Tables*, **19**, 97, (1977)

2. L. Salgueiro, M. L. Carvalho, and F. Parente, *J. Phys.* (Paris), Colloq. **48**, C9-609 (1987)

3. A. M. Vlaicu, T. Tochio, T. Ishizuka, D. Ohsawa, Y. Ito, T. Mukoyama, A. Nisawa, T. Shoji, *Phys. Rev. A* **58**, 3544 (1998)

4. M. Deutsch, G. Holzer, J. Hartwig, J. Wolf, M. Fritsch, and E. Forster, *Phys. Rev. A* **51**, 283 (1995)

SOLID STATE X-RAY SPECTROSCOPIES

Al and Mg K-edge absorption study on the superconducting $Al_{1-x}Mg_xB_2$ system
S. Agrestini, A. Marcelli, G. Cibin, Z. Wu and A. Bianconi

X-ray photoinduced charge ordering in oxygen doped $La_2CuO_{4.1}$ system
G. Campi

EXAFS study of $Co_x(SiO_2)_{1-x}$ granular alloy
J.C. Cezar, H.C.N. Tolentino, J. Denardin and M. Knobel

Magnesium X-ray Absorption Near-Edge Structure (XANES) spectroscopy on synthetic model compounds and minerals
G. Cibin, A. Marcelli, A. Mottana, G. Giuli, G. Della Ventura, C. Romano, E. Paris, A. Cardelli and F. Tombolini

Small-Angle X-ray Scattering study on the conformation of polystyrene in compressed CO_2-toluene mixture
B. Dong, L. Rong, Y. Liu, D. Li, B. Han, Z. Liu and G. Yang

Studies of valence band structure of lithium compounds by XAS and XPS
Y. Iwata, K. Maeda, M. Fujita, J. Tsuji, D. Sawa, N. Ozawa, T. Yao, K. Kojima, S. Ikeda and K. Taniguchi

Sulfur K-edge XANES study in iron sulfide
A.N. Kravtsova, I.E. Stekhin, A.V. Soldatov, X. Liu and M.E. Fleet

Photoemission study of Ba^{2+} and Nd^{3+} substitution for Ca^{2+} in the BSCCO(2212) superconducting system
K. Kumari, R.K. Singhal, K.B. Garg, M. Heinonen, J. Leiro, A. Gupta and S.K. Agarwal

The PIXE (Proton-Induced X-ray Emission) analytical technique to detect insoluble atmospheric microparticles archived in the EPICA-Dome C ice-core (Antarctica): paleoclimatic implications
F. Marino, V. Maggi , G. Ghermandi, D. Ceccato and R. Cecchi

Comparative study of the electronic structure of natural and synthetic rubies using X-ray absorption and EDAX analysis
P. Parikh, D.M. Bhardwaj, R. P. Gupta, N.L. Saini, S. Fernandes, R.K. Singhal, D.C. Jain and K.B. Garg

The local geometrical structure of Zn_7-Metallothionein-2 probed by XANES spectroscopy
G. Smolentsev, A. Soldatov and M. Stillman

Effect of the surfactants on the local atomic structures of cerium oxide nanoparticles
Z. Wu, J. Zhang, Z. Chen, Z. Wu and L. Guo

Frascati Physics Series Vol. XXXII (2003), pp. 61-71
19th INTERNATIONAL CONFERENCE ON X-RAY AND INNER-SHELL
PROCESSES – Roma, June 24 - 28, 2002

Al AND Mg K-EDGE ABSORPTION STUDY ON THE SUPERCONDUCTING $Al_{1-x}Mg_xB_2$ SYSTEM

S. Agrestini
Unità INFM and Dipartimento di Fisica,
Università di Roma "La Sapienza", P. le Aldo Moro 2, 00185 Roma, Italy
A. Marcelli
Istituto Nazionale di Fisica Nucleare, Laboratori Nazionali di Frascati,
Via E. Fermi 40, I-00044 Frascati RM, Italy
G. Cibin
Istituto Nazionale Ricerca Scientifica e Tecnologica sulla Montagna,
P.za dei Caprettari,70 - 00186 Roma, Italy
and I.N.F.N. - L.N.F.,Via E. Fermi 40, I-00044 Frascati RM, Italy
Z. Wu
Beijing Synchrotron Radiation Facility, Institute of High Energy Physics,
Chinese Academy of Sciences, P.O. Box 918, Beijing 100039,
Peoples Republic of China
and I.N.F.N. - L.N.F.,Via E. Fermi 40, I-00044 Frascati RM, Italy
A. Bianconi
Unità INFM and Dipartimento di Fisica,
Università di Roma "La Sapienza", P. le Aldo Moro 2, 00185 Roma, Italy

ABSTRACT

We performed used high-resolution Al and Mg K edge X-ray absorption near-edge structure (XANES) experiments to explore the local structure and unoccupied electronic states in the $Al_{1-x}Mg_xB_2$ high T_c superconducting system as function of (Mg, Al) content. A strong reduction of absorption intensity is observed in the main peaks of both Al and Mg K-edge XANES spectra as Al decreases. The experimental features are interpreted by means of multiple scattering calculations for the Al and Mg K-edge XANES spectra and correlated with electronic and structural properties of Mg diborides.

1 Introduction

About two years ago a great excitement in the solid state physics community was raised by the surprising discovery of superconductivity in the binary boride, MgB_2, with a T_c of about 39 K, which is the highest known transition temperature for a non-copper-oxide bulk material [1]. Although several other compounds are know with similar critical temperatures, this discovery stimulated intense investigations from both experimental and theoretical fronts [2] because of the apparent simplicity of the MgB_2 stoichiometry, crystal structure and electronic properties. For this simplicity the understanding of superconductivity in this binary compound is expected to be easier than in the high-T_c cuprate materials, studied extensively for more than ten years now. However, mechanism of the superconductivity in this compound is still an open question. In fact its critical temperature of about 39 K is higher than the theoretical value predicted by the BCS theory [3], making a case to consider MgB_2 a non-conventional superconductor.

MgB_2 is an intermetallic compound with a layered structure where boron planes having honeycomb lattice such as graphite, are intercalated with metallic planes having hexagonal close-packed lattice. Band structure calculations [4, 5] show that Mg is almost ionized with a charge state 2+ while the transferred charge goes to the metallic boron sheets where strong covalent bonds form. The bands near the Fermi energy are primarily derived from B $2p_{xy}$ (σ) and $2p_z$ (σ) states.

The nearly filled p_z bands address superconductivity behavior to σ-band holes [5]. As a consequence trivalent aluminum has been used to replace divalent Mg in order to test the effect of electron concentration on the superconducting transition temperature T_c [6, 7, 8]. It was found that the T_c decreased with increasing Al concentration and the superconductivity is suppressed at the Al concentration x=0.6 in the proximity of the critical electron doping, at which the number of holes in the σ bands vanishes. Consequently, the observed loss superconductivity in the $Mg_{1-x}Al_xB_2$ system could be explained as a result of the filling of the σ bands [7]. The thermoelectric power study indicated that $Mg_{1-x}Al_xB_2$ is a hole-type metallic conductor with electron doping [9]. A recent B NMR result was also consistent with this hole theory [10].

To have further insight to the superconducting and normal state behavior of the MgB_2 system as a function of charge density and lattice parameters, it

is important to explore their electronic versus local structure. Actually, X-ray absorption near edge structure (XANES) is a probe of intermediate/short-range structural order and electronic structure in complex materials, and hence a suitable tool to investigate the electronic and local structural properties in the $Mg_{1-x}Al_xB_2$ system.

The X-ray absorption coefficient μ(E) is given by the product of the matrix element and the joint density of states for the electronic transitions from the initial to final states. The dipole matrix element from the initial state, the core level of well defined symmetry, selects the local and partial density of final states for the allowed electronic transitions. The XANES spectroscopy probes the final states in an energy range of about 50 eV above the chemical potential. While at the Fermi level the photoelectron mean free path is very large, it decreases rapidly with increasing the energy of the final state due to strong scattering by the many body electronic excitations resulting in the mean free path to become of the order of 5 Å. Therefore the XANES spectra can be solved in the real space describing the final state as an outgoing spherical wave which interferes with the waves backscattered from the neighbouring atoms within a cluster of atoms in the intermediate range of the order of a few Angstrom [11, 12, 13, 14, 15].

Here we have investigated the $Al_{1-x}Mg_xB_2$ superconducting system by Al and Mg K edge X-ray absorption near-edge structure (XANES) spectroscopy. We find a reduction of absorption intensity of the main peaks for both Al and Mg K-edge XANES with decreasing Al concentration. The experimental features will be discussed and explained comparing experimental data and multiple scattering theory.

2 Experimental

High quality $Mg_{1-x}Al_xB_2$ samples were synthesized by direct reaction of the elemental magnesium, aluminium (rod, 99.9 mass% nominal purity) and boron (99.5% pure <60 mesh powder). The elements in a stoichiometric ratio were enclosed in tantalum crucibles sealed by arc welding under argon atmosphere. The tantalum crucibles were then sealed in heavy iron cylinder and heated for one hour at 800℃ and two hours a 950℃ in a furnace. An important improvement in the synthesis process was that of avoiding use of quartz tube (unlike in Ref. 8 was used quartz), for preparation of the diborides, since the

Mg gas at high temperature reacts with quartz and induces a MgO impurity phase in the final compound.

The samples were characterized for their superconducting properties by the temperature dependence of the complex conductivity using the single-coil inductance method [7]. The structural properties of the samples were determined by powder X-ray diffraction using synchrotron radiation at the XRD beamline at the Elettra storage ring facility [7].

X-ray absorption spectroscopy measurements were carried out at the Stanford Synchrotron Radiation Laboratory (SSRL), using the light emitted by the SPEAR electron storage ring, that operated at 3.0 GeV with current decreasing from ∼90 to ∼60 mA during a time span of 12-16 h. The Al and Mg K edges were recorded at beamline SBO3-3 under high vacuum (10^{-7} torr), using the double-crystal JUMBO monochromator equipped with two plates of YB_{66}(400) crystals. The spectral acquisition range was from 1540 to 1670 eV for Al K edge and from 1280 to 1380 eV for Mg K edge, counting at 0.3∼0.5 eV intervals for 2∼4 s at a time. The measurements were made in the "total electron yield" (TEY) mode. Experimental resolution at the Mg and Al edges was estimated <0.46 eV. Specimens were made to adhere on the flat silvered sample-holder. Metallic Al foil and MgO powder were used as a reference for energy calibration. Great care was taken of the absorption-edge energy drift during data acquisition. It was corrected by recording at regular time intervals the standards and by calibrating its main-edge energy value against the ring current. In order to increase the signal-to-noise ratio several absorption scans were collected for each samples.

3 Results and Discussion

Fig. 1a shows normalized experimental Al K-edge absorption spectra measured on the $Mg_{1-x}Al_xB_2$ system as a function of Al content. The higher noise observed in the XANES spectrum of the $Mg_{0.92}Al_{0.08}B_2$ compound is due to the very small Al content in the sample. There is an evident rise of the intensity of the main absorption peak in the region between 1566 eV to 1574 eV with increasing Al content. This trend can be better observed in the difference between the absorption spectra measured on samples with different Al concentration and the absorption spectrum measured on the $Mg_{0.92}Al_{0.08}B_2$ sample (Fig. 1b). To understand the origin of different features in the Al K-edge

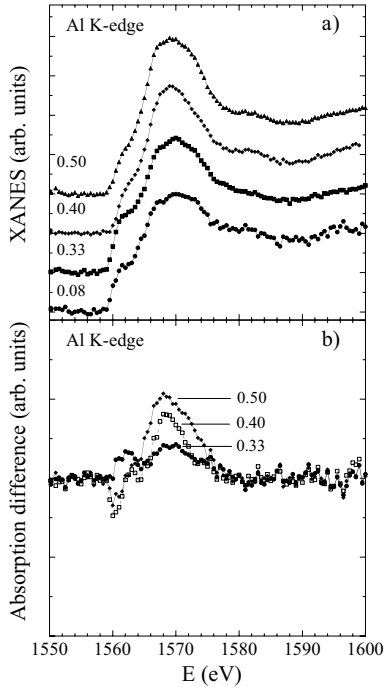

Figure 1: *(a) Normalized experimental Al K-edge absorption spectra measured at T=300 K on the $Mg_{1-x}Al_xB_2$ system for different Al content. b) Absorption difference of the XANES spectra respect to that measured on the $Mg_{0.92}Al_{0.08}B_2$ sample.*

XANES spectra multiple-scattering (MS) calculations [12, 13, 14, 15, 16, 17], based on one-electron full MS theory, have been carried out using the CONTINUUM code [18]. In Fig. 2a the calculated XANES spectrum is compared to the experimental one measured on the $Mg_{0.50}Al_{0.50}B_2$ sample. A reasonable agreement between the multiple scattering calculations and the experimental data is observed with respect to the energy position and intensity of different features.

The Al K-edge absorption spectrum shows six different features labelled with A, A', B, C D and E in Fig. 2a. The B and C peaks are due to multiple scattering resonances of an electron emitted by Al ion and scattered in a cluster of 179 atoms within a sphere of 7 Å radius. Theoretical polarized XANES spectra are plotted in Fig. 2b to distinguish the contributions of the scattering in the z direction from that in the xy plane. This figure shows that the A' and E peaks are mostly due to the photoelectron scattering with Al and Mg ions in the Mg/Al plane near the Al substituted ion. On the other hand the D peak is due only to contribution of the scattering in the z direction.

Therefore it appears that the increase of intensity of the B and C absorption peaks (Fig. 1) is related to a crossover from the $Mg_{0.92}Al_{0.08}B_2$ sample having Mg layer with Al impurities to the $Mg_{0.5}Al_{0.5}B_2$ sample having Al layer alternated with Mg layer.

From the comparison between the calculated absorption spectrum and the experimental spectra it results that the one measured on $Mg_{0.5}Al_{0.5}B_2$ sample is more close to the theoretical prediction than the XANES spectrum of $Mg_{0.92}Al_{0.08}B_2$ sample. The broadening of the B and C absorption peaks in the $Mg_{0.92}Al_{0.08}B_2$ sample could be explained by two different physical phenomena: 1) inelastic scattering of the photoelectron with the valence electrons; 2) strong lattice disorder in the Mg plane (large Debye-Waller factor). The Mg K-edge spectra measured on $Mg_{0.92}Al_{0.08}B_2$ and $Mg_{0.5}Al_{0.5}B_2$ samples at room temperature are displayed in Fig. 3. The difference between the two XANES spectra is also shown in this same figure. A clear broadening of the main characteristics of the XANES spectrum measured on the $Mg_{0.92}Al_{0.08}B_2$ sample can be seen. Furthermore the main peak corresponding to the $1s \rightarrow 3p$ transition exhibits a strong absorption intensity reduction very similar to that observed in the Al K-edge XANES spectra.

Real-space multiple scattering of the photoelectron ejected from the Mg

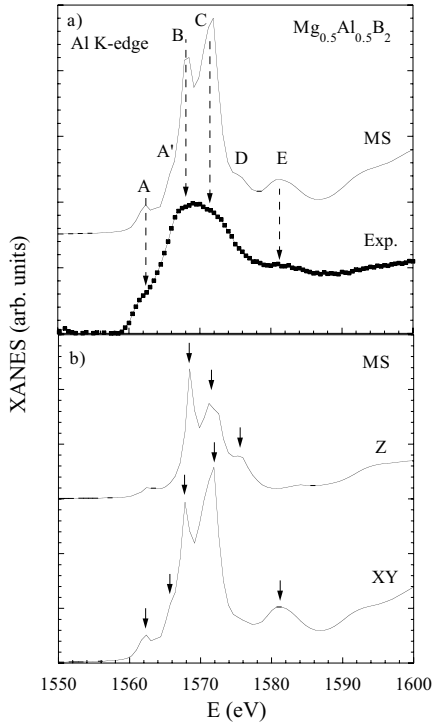

Figure 2: *panel a): Calculated Al K-edge XANES spectrum* (MS) *compared with the experimental spectrum* (Exp.) *measured on* $Mg_{0.5}Al_{0.5}B_2$ *sample. Panel b): theoretical XANES spectra polarized along the z axis and along the xy plane.*

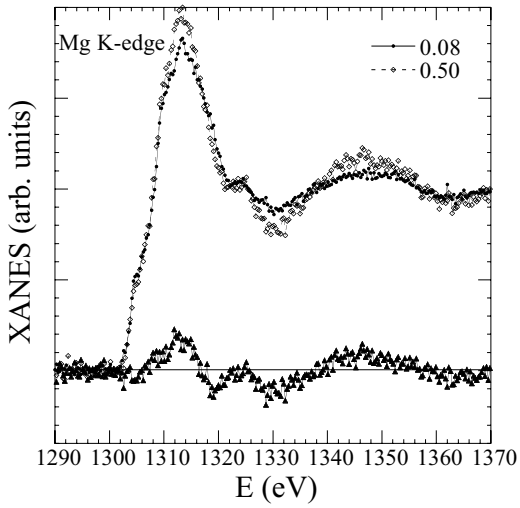

Figure 3: *Normalized experimental Mg K-edge absorption spectra measured on $Mg_{1-x}Al_xB_2$ system for two different Al content. The absorption difference of the XANES spectra is also plotted.*

1s state has been also calculated by considering a cluster of 179 atoms surrounding the central Mg atom. The calculated Mg K-edge absorption spectra for the MgB_2 and $Mg_{0.5}Al_{0.5}B_2$ compounds are plotted in Fig. 4 together with their difference. A good agreement between the experimental and theoretical spectra can be observed. The absorption intensity drop in the main peak is more evident if one compares the theoretical and experimental difference of the XANES spectra. In summary Al and Mg K-edge absorption spectra have been measured on the $Mg_{1-x}Al_xB_2$ system with different Al content. Multiple scattering calculations have been performed and a reasonable agreement between the experimental spectra and the theoretical ones is observed. A strong reduction of absorption intensity is observed as a function of Al content in the main peaks of both Al and Mg K-edge XANES spectra. The observed behavior e.g., the drop of the absorption could be associated to inelastic scattering of the photoelectron with the valence electrons in this layered system; however, strong lattice disorder in the Mg plane (large Debye-Waller factor) plays an important role and certainly affect the electronic properties of Mg diborides.

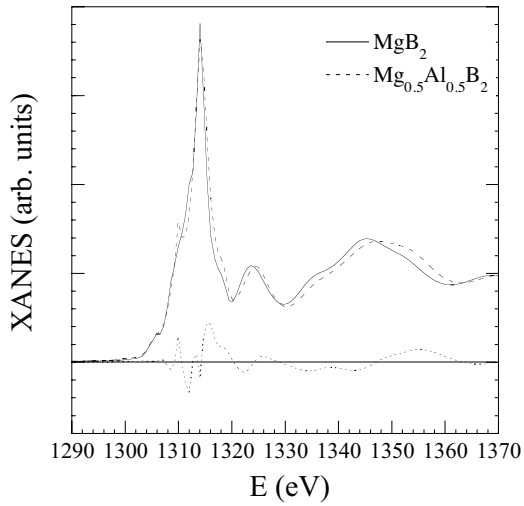

Figure 4: *Calculated Mg K-edge absorption spectra for the MgB_2 and $Mg_{0.5}Al_{0.5}B_2$ compounds. The theoretical absorption difference of the XANES spectra is indicated by a dotted line.*

4 Acknowledgments

The authors thank the SSRL staff for their cooperation during the experiments. This research has been supported by MURST (under the project 'cofinanziamento leghe e composti intermetallici: stabilità termodinamica, proprietà fisiche e reattività'), by the Istituto Nazionale per la Fisica della Materia (INFM), and by CNR (under the project '5% Superconduttività'). One of us (ZYW) acknowledges the financial support of the *100-Talent Research Program* of the Chinese Academy of Sciences and of the *Outstanding Youth Fund* (10125523) of the National Natural Science Foundation of China.

References

1. J. Nagamatsu, N. Nakagawa, T. Muranaka, Y. Zenitani, and J. Akimitsu, *Nature* **410**, 63 (2001).

2. C. Buzea and T. Yamashita, *Supercond. Sci. Technol.* **14**, R115 (2001).

3. W. L. McMillan, *Phys Rev* **167**, 331 (1968).

4. J. M. An and W. E. Pickett, *Phys. Rev. Lett.* **86**, 4366 (2001).

5. J. Kortus, I. I. Mazin, K. D. Belashchenko, V. P. Antropov, and L. L. Boyer, *Phys. Rev. Lett.* **86**, 4656 (2001).

6. S. Agrestini, D. Di Castro, M. Sansone, N. L. Saini, A. Saccone, S. De Negri, M. Giovannini, M. Colapietro, and A. Bianconi, *J. Phys.: Condens. Matter* **13**, 11689 (2001).

7. A. Bianconi, S. Agrestini, D. Di Castro, G. Campi, G. Zangari and N. L. Saini, A. Saccone, S. De Negri, M. Giovannini, G. Profeta, A. Continenza, G. Satta, S. Massidda, A. Cassetta, A. Pifferi, and M. Colapietro, *Phys. Rev.* B **65**, 174515 (2002).

8. J. S. Sluski, N. Rogado, K. A. Regan, M. A. Hayward, P. Khalifah, T. He, K. Inumaru, S. Loureiro, M. Haas, H. W. Zandbergen, and R. J. Cava, *Nature* **410**, 343 (2001).

9. B. Lorenz, R. L. Meng, Y. Y. Xue and C. W. Chu, *Phys. Rev.* B **64**, 52513 (2001).

10. M. Pissas, G. Papavassiliou, M. Karayanni, M. Fardis, I. Maurin, I. Margiolaki, K. Prassides and C. Christides, *Phys. Rev.* B **65**, 184514 (2002).

11. See e.g. a review by A. Bianconi, in *X Ray Absorption: Principles, Applications, Techniques of EXAFS, SEXAFS and XANES*, 573, edited by D. Koningsberger and R. Prins (J. Wiley and Sons, New York, 1988).

12. P.J. Durham, in *X-ray Absorption: Principles, Applications, Techniques of EXAFS, SEXAFS, XANES*, 53, edited by D. Koningsberger and R. Prins (J. Wiley and Sons, New York, 1988)

13. A. Bianconi, J. Garcia, and M. Benfatto, in: *Topics in Current Chemistry*, edited by E. Mandelkow, vol. **145**, 29 (Springer-Verlag, Berlin, 1988).

14. A. Bianconi, J. Garcia, A. Marcelli, M. Benfatto, C. R. Natoli, and I. Davoli, *J. Phys.* (Paris), Colloque C9 **46**, 101 (1985).

15. M. Benfatto, C. R. Natoli, A. Bianconi, J. Garcia, A. Marcelli, M. Fanfoni and I. Davoli, *Phys. Rev.* B **34**, 5774 (1986).

16. Z. Y. Wu, M. Benfatto, and C. R. Natoli, *Phys. Rev.* B **45**, 531 (1992).

17. Z. Y. Wu, M. Benfatto, and C. R. Natoli, *Solid State Commun.* **87**, 475 (1993).

18. C. R. Natoli, M. Benfatto, C. Brouder, M.Z. Ruiz Lopez, D.L. Foulis, *Phys. Rev. B* **42**, 1944 (1990).

Frascati Physics Series Vol. XXXII (2003), pp. 73-85
19th INTERNATIONAL CONFERENCE ON X-RAY AND INNER-SHELL
PROCESSES – Roma, June 24 - 28, 2002

X-RAY PHOTOINDUCED CHARGE ORDERING IN OXYGEN DOPED $La_2CuO_{4.1}$ SYSTEM

G. Campi
Unità INFM and Dipartimento di Fisica, Università di Roma "La Sapienza", P. le Aldo Moro 2, 00185 Roma, Italy

ABSTRACT

High resolution x-ray diffraction is used to investigate the charge and the oxygen ordering in $La_2CuO_{4.1}$single crystal. The temperature dependence study, allowed us to identify the coexistence of two different 3D oxygen ordered phases and order to disorder like phase transitions at 350 K and 370 K for a lower and higher oxygen concentration respectively. We found clear evidence for photo-induced short range charge ordering, by clustering formation after rapid quenching from 380 K to 100 K and by pumping electron- hole excitation using high flux synchrotron radiation illumination at 100 K. Furthermore, under this continuous x-ray illumination, the second harmonic reflections behaviour shows the transformation of a 1D sinusoidal incommensurate charge density wave (ICDW), into striped domains in the CuO_2 plane.

1 Introduction

A large number of experimental efforts, supported by advancement of the materials science and development of new experimental techniques have helped to get considerable insight into the peculiar electronic properties of transition metal oxides showing novel phenomena such as high T_c superconductivity in the cuprates, and colossal magneto resistance (CMR) in the rare earth manganites [1, 2, 3]. The studies suggest that the ground states of these oxides is intrinsically inhomogeneous due to inter-playing orbital, spin and charge excitations, with strong tendencies towards a microscopic phase separation with formation of static and dynamic stripes [4, 5].

Although the inhomogeneous state of these metal oxides seems to be related with inter-playing of various degrees of freedoms, the role of lattice fluctuations is now getting well recognized. While recent experiments on cuprates suggest that charge ordered domains have an intimate relationship with the strain field due to the lattice mismatch of bcc CuO_2 layer with neighbor rock-salt fcc layers [6, 7], similar observations have come up for the case of manganites [3, 8]. In fact, it has been observed that the stripe phases in the cuprates appear for an elastic strain larger than a critical value [6].

We have shown that the stripe phases in the cuprates appear for an elastic strain due to the lattice mismatch between the bcc CuO_2 plane and the intercalated fcc layers [2], larger than a critical value [6]. The oxygen doped La_2CuO_{4+x} superconducting system, where the oxygen atoms (which were determined to occupy the interstitial sites between adjacent LaO layers) remain mobile down to near 200 K has a high value of micro-strain and is a simple system to study the ordering of dopants, and the charge ordering in the CuO_2 plane [9, 10, 11, 12]. Recently we have found the formation of different structural ordered phases in $La_2CuO_{4.1}$ with x$\sim$0.1 [12, 13] and in this paper we report influence of x-ray illumination at different temperatures on these inhomogeneous phase. Control of material phases by external stimuli, especially by light, has been a subject of much interest in recent years in view of potential applications for memory and storage devices in the future. While the phenomenon has been widely studied by laser photon pumping in this class of materials, the present work exploits possibility of x-ray photon by pumping electron-hole excitation using high flux synchrotron radiation. We find a clear signature of x-ray photo-induced ordered phase as a function of temperature

and x-ray photon dose.

2 Experimental

Diffraction measurements on the $La_2CuO_{4.1}$ single crystal, grown by flux method and doped by electrochemical process [14], were performed on the crystallography beam-line at the Elettra storage ring at Trieste. The X-ray beam emitted by the wiggler source on the Elettra 2 GeV electron storage ring, was monochromatized by a Si(111) double crystal monochromator, and focused on the sample. The temperature of the crystal was monitored with an accuracy of ±1K. We have collected the data in the κ geometry, with a photon energy of 12.4 KeV (wavelength λ=1), using a CCD detector assembly. The sample oscillation around the b axis was in a range $0 \leq \Phi \leq 30^o$, where Φ is the angle between the direction of the photon beam and the a axis. We have investigated a portion of the reciprocal space up to 0.6 $Å^{-1}$ momentum transfer, i.e., recording the diffraction spots up to the maximum indexes 3, 3, 19 in the a^*, b^*, c^* direction respectively. Thanks to the high brilliance source, it has been possible to record a large number of weak superstructure spots around the main peaks of the average structure. Twinning of the crystal has been taken into account to index the superstructure peaks. The lattice parameters of the single crystal were determined to be a=5.351 Å, b=5.418 Å, c=13.171 Å, at room temperature.

3 Results and Discussion

At room temperature we found four types of superstructure peaks [12]. The superstructures are classified through the staging [9], i.e., the modulation wave-vectors along the c axis. The first two superstructures are characterized diffraction peaks with the wave-vectors (stage 2):

$$q_1 = 0.089(\pm 0.003)a^* + 0.248(\pm 0.002)b^* + 0.495(\pm 0.005)c^* \qquad (1)$$

and

$$q_2 = 0.049(\pm 0.003)a^* + 0.268(\pm 0.002)b^* + 0.495(\pm 0.005)c^* \qquad (2)$$

The modulation with wavevector q_1 is the only one commensurate with the lattice and it's due to the formation of a superlattice that shows a period-

icity of about 11 unit cells and 4 unit cells along the a and b axis respectively, and doubling the unit cell along the c-axis [12, 13]. The superstructure peaks q_1 and q_2 coexist with other diffuse spot [12] with the wavevector (stage 3.5)

$$q_3 = 0.008(\pm 0.002)a^* + 0.208(\pm 0.003)b^* + 0.290(\pm 0.005)c^* \qquad (3)$$

and an overlapping narrower period-3.5 superstructure peak with a wavevector;

$$q_4 = 0.037(\pm 0.001)a^* + 0.198(\pm 0.002)b^* + 0.290(\pm 0.005)c^* \qquad (4)$$

The modulation with wavevector q_3 has the a^* component near to zero and it's diffuse along this direction with a coherence length of 17 unit cells, as shown in Fig.1; therefore it's due to the formation of 2D and short range ordered domains namely O3. On the other hand the q_1, q_2, and q_4 are resolution limited superstructures due to the formation of 3D and long range ordered domains. The peaks at stage 2 correspond to the ordered phases, namely O1 and O2. The study of the two coexisting phases O1 and O2, associated with the superstructure peaks q_1 and q_2, as a function of temperature, has revealed two different critical temperatures for their formation, as shown in Fig.2, where the integrated intensity of the peaks is plotted as a function of temperature between 300 K and 380 K. The commensurate phase O1, occurs at T ~350 K, while the incommensurate one O2, resists until T ~375 K. This means that at T_{O1} ~355 K, a crossover from the coexistence of the two phases O1 and O2 to a unique incommensurate phase occurs. On the other hand, the q_3 and q_4 are slightly affected by the temperature and show a nearly constant behaviour (Fig.2), indicating that the different stage characterizes a different physical nature. Since the oxygen ordering, is expected to be above 180 K where the mobility of doped oxygen ions is high, the O1 and O2 phases have been associated to the oxygen ordering in the two different ordered domains and T_{O2} ~375 K is the critical temperature above which the oxygen ions are completely disordered in the system; moreover the relative intensity of q_1 (~40%) and q_2 (~60%) means that at room temperature the oxygen ordered domains O1 and O2 are characterized by a lower and higher concentration respectively. Starting from the disordered phase reached by heating the sample up to 380 K, we have

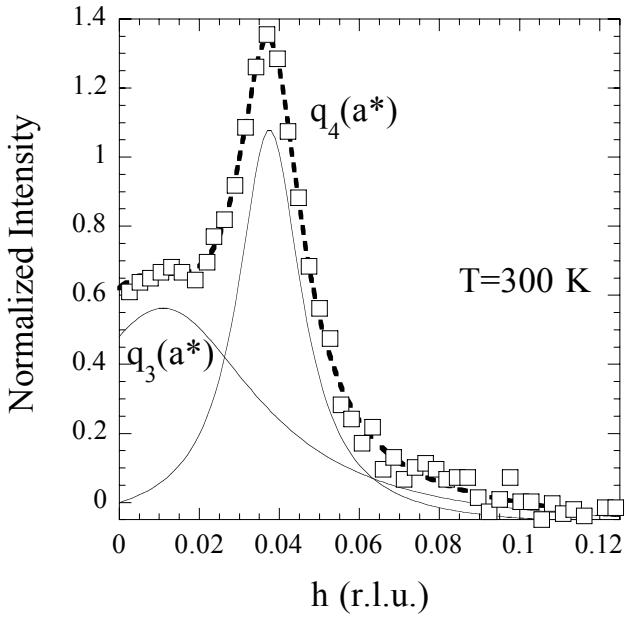

Figure 1: *Profiles of the superstructures q_3 and q_4 in the Q= (0,h,6+0.29) direction at T=300K.*

performed a rapid quenching down to 100 K and afterwards, we have pumped electron-hole excitation using high flux synchrotron radiation illumination at this temperature in order to investigate the diffuse peak's physical origin without oxygen motion. With this new experimental approach, based on the use of the high intensity x-ray flux to create a relevant number of photo-doped charges in a surface layer of thickness determined by the x-ray penetration depth, it has been possible to probe the charge ordering in the same slab, using a fast 2D detection and observing an increase of the intensity of the weak superstructure spots [6, 15].

We have observed an increase of the charge modulations, q_3 and q_4 revealing a short-range polaron ordering of the photo-doped charges. The relative weight of the two ordered phases changes under x-ray illumination, as evident

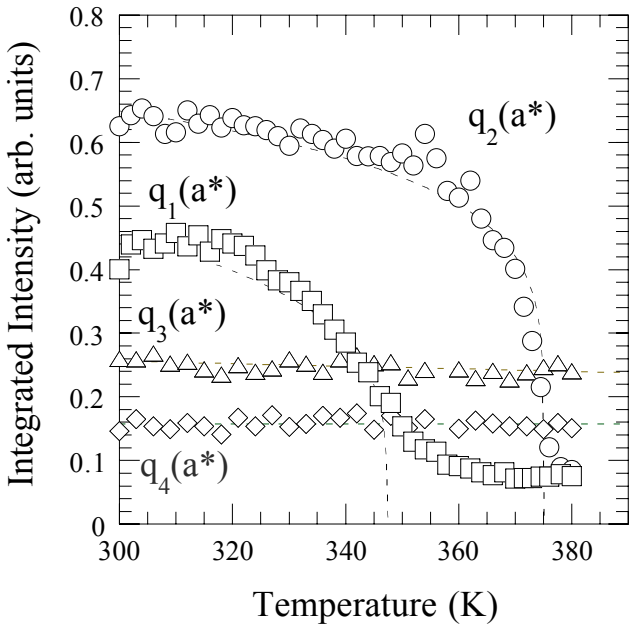

Figure 2: *Integrated intensities of the q_1, q_2, q_3 and q_4 superstructures as a function of temperature. The superstructures with period-3.5, q_3 and q_4, are independent of temperature in the plotted range, while the period-2 superstructures, q_1 and q_2 reveal order parameter like behaviour.*

from Fig.3, where we have shown the profiles of the two superstructures for different x-ray dose values. Fig.4a shows evolution of the relative weight of the superstructures q_3 and q_4 as a function of x-ray doses. Here the relative weight corresponds to the integrated intensity (I/I_0), where I is the intensity of the peak under illumination while I_0 without illumination. We have observed that weight of the peak q_3 and q_4 was increased by $\sim$2.5 and $\sim$2.0 times respectively of its initial value, while the 2 staging superstructures q_1 and q_2 remained not detectable, indicating that at T=100 K the oxygen ions are frozen in the disordered phase. After the low temperature increase, due to the continuous x-ray illumination, the number of ordered domains O3 and O4, proportional to the

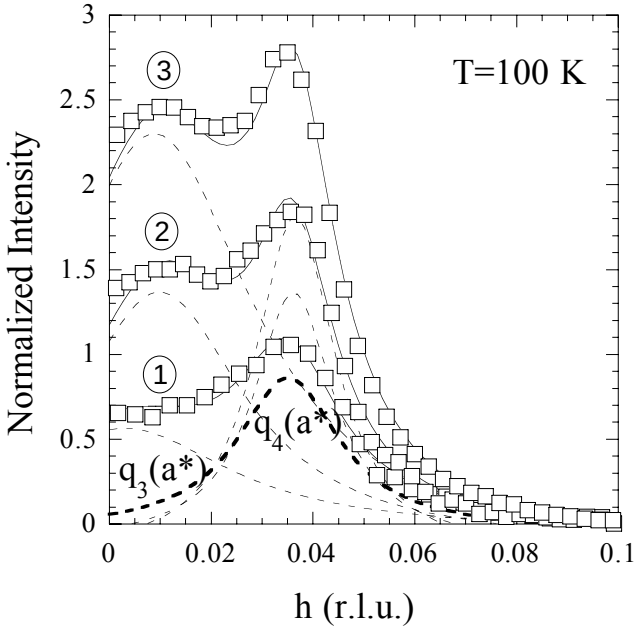

Figure 3: *Profiles of the q_3 and q_4 superstructures in the a* direction at (0,h,6.29) for increasing dose values.*

integrated intensity of the peaks q_3 and q_4 respectively, returns to the initial value by heating the sample, as shown in Fig 4b. The temperature derivative $\Delta I/\Delta T$ of the q_3 and q_4 integrated intensity shows two temperature regimes centered at 220 K and 175 K for which the photo-induced charges give raise to ordered local lattice distortions in the O3 and O4 phases, respectively (Fig.5).

Thanks to the high brilliance synchrotron radiation it has been possible to record the second harmonics reflections in the diffraction patterns. Their x-ray incident flux dependence, during the pumping at 100 K is similar to the first harmonics' one, except the short range and 2D ordered domains associated to the q_3 modulation. The singular increase of q_3 is shown in Fig.6, where the profiles of the q_3 and q_4 diffraction peaks in the Q= (0,k,6+0.29) direction are

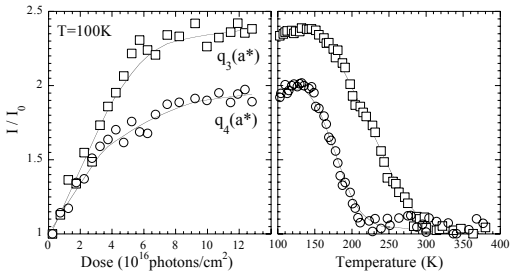

Figure 4: *(a) Effect of the x-ray illumination on the integrated intensity of the charge ordering modulations q_3 and q_4 at T=100 K (right); where I_0 is the initial value of the integrated intensities, without the illumination effect. (b) Temperature annealed behavior of the same superstructure peaks, obtained by heating the sample after the rapid quenching.*

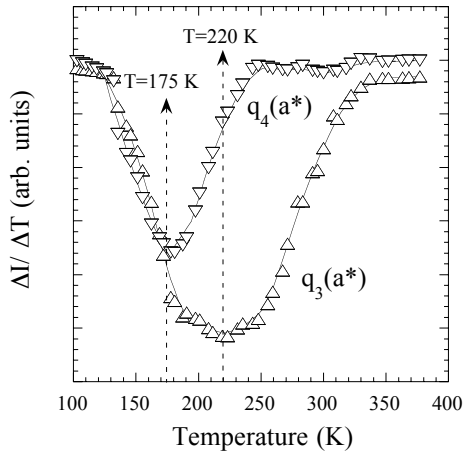

Figure 5: *Temperature derivative of the integrated intensity of the q_3 and q_4 superstucture peaks.*

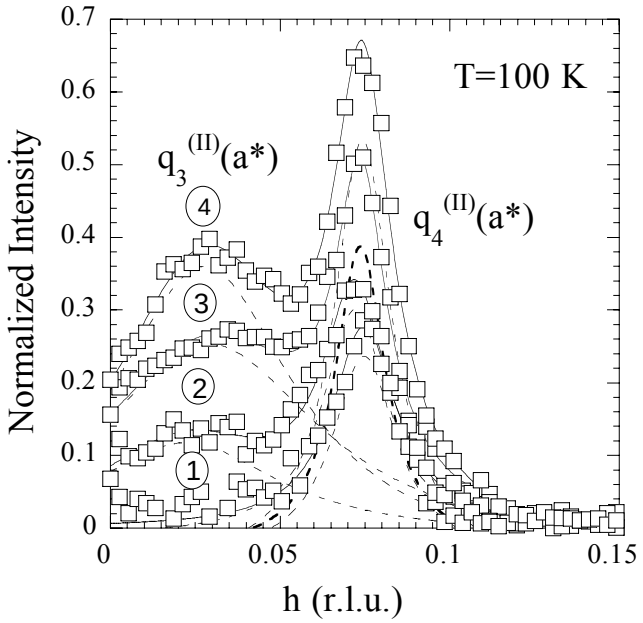

Figure 6: *Profiles of the second harmonics of q_3 and q_4 in the Q= (0,h,6+0.29) direction for three different dose values (denoted by 1, 2 and 3) at T=100K.*

reported at four different dose values.

We can clearly see that the second harmonics of the q_3 superstructure peak, in fact, takes place just by pumping the sample at 100 K and rises by $\sim$45 times of initial background value (Fig.7a). The effect of the rising of the II harmonics is to transform the sinusoidal ICDW, giving to the q_3 modulation a striped shape in the ab plane. Also in this case, the integrated intensity of the peaks q_3, after the continuous x-ray illumination at 100 K, returns to the initial value by heating the sample, as shown in Fig 7b.

Finally, we move to investigate the evolution of the (I^{II}/I^{I})ratio, where I^{II} and I^{I} are the integrated intensity of the second and the first harmonic of the q_3 superstructure reflection. In this way, we have been able to study the behaviour of the anharmonicity degree of the charge modulation q_3, as a

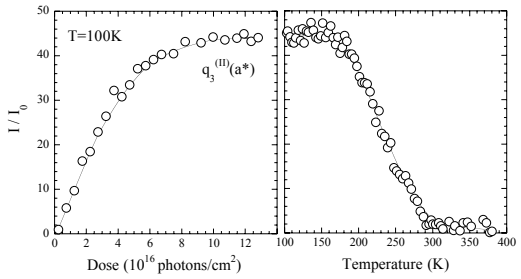

Figure 7: *(a) Effect of the x-ray illumination on the integrated intensity of the second harmonics of q_3 and q_4 at T=100 K; I_0 is the initial value of the integrated intensities, without the illumination effect. (b) Normalized integrated intensity I/I_0 of the two superstructures as a function of the temperature. The superstructure intensity decreases in a large temperature regime, returning to the initial value.*

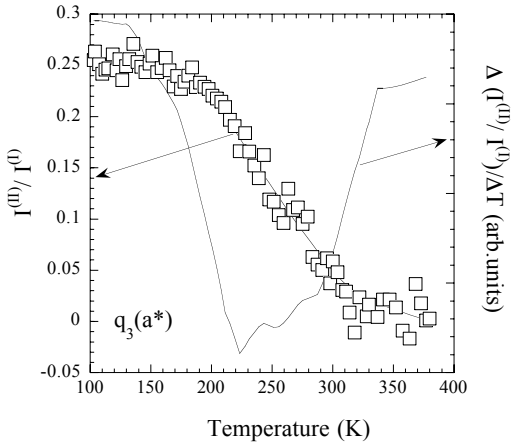

Figure 8: *(a) Evolution of the I^{II}/I^{I} ratio, where I^{II} and I^{I} are the integrated intensity of the second and the first harmonic of the q3 superstructure reflection respectively; the derivative $\Delta(I^{II}/I^{I})/\Delta T$ is also plotted.*

function of the temperature. We observed that the II harmonics of q_3 peaks, produced by x-ray illumination at T=100 K and transforming the O3 sinusoidal incommensurate charge density wave (ICDW), into striped domains, go to disappear with a large, glassy-like transition between 200 K and 300 K, as shown in figure 8 by plotting the derivative of the I^{II}/I^{I} ratio.

In summary we have investigated the photo-induced charge ordering, as a function of the temperature, in oxygen doped $La_2CuO_{4.1}$ by high resolution x-ray diffraction. At T$\sim$355 K a commensurate resolution limited oxygen ordering occurs; this phase coexists with an incommensurate oxygen ordering that disappears when the system reaches the temperature of T $\sim$375 K. Pumping electron-hole excitations at T = 100 K by high flux synchrotron radiation illumination, with the oxygen ions frozen in a disordered phase, we had evidence that the photo-induced charges get ordered in incommensurate short range and 2D striped domains. A temperature dependent study of x-ray illumination allowed to determine the T_{O3} $\sim$220K, a temperature below which the x-ray induced charges are able to get ordered in the 2D and short range ordered phase O3. On the other hand, in the phase O4 the photo-induced charges are self trapped into a 3D crystal of long range ordered domains, when the temperature is up T_{O4} $\sim$175 K. In conclusion, the experimental approach reported in this paper provides possibilities to manipulate the charge ordered phases by temperature and x-ray illumination in complex systems as the high T_c cuprates.

4 Acknowledgments

We would like to thank D.C.Johnston for providing the single crystal sample. This research has been supported by the MURST (under the project 'cofinanziamento Leghe e composti intermetallici: stabilità' termodinamica, proprietà' fisiche e reattività'), by the INFM (under the project PA-LLDS-SCS), and by the CNR (under the project '5% Superconduttività').

References

1. M. Imada, A. Fujimori, Y. Tokura, Rev. Mod. Phys., **70**, 1039-1263 (1998) and references therein.

2. Y.Tokura and N.Nagaosa, Science **288**, 462 (2000).

3. C.N.R. Rao, A. Arulraj, A.K. Cheetham and B. Raveau, J. Phys.: Cond. matter **12**, R83 (2000); A. J. Millis, Nature **392**, 147 (1998)

4. See e.g. several contributions in 'Stripes and Related Phenomena' edited by A. Bianconi and N.L. Saini (Kluwer Academic/Plenum Publishers, New York, 2000).

5. *Proceedings of of the 3rd International Conference on Stripes and High Tc Superconductivity* eds. N.L. Saini, & A. Bianconi, [speciale issue of Int. J. Mod. Phys. B. **14**, No.25-27 (2000)].

6. A. Bianconi, G. Bianconi, S. Caprara, D. Di Castro, H. Oyanagi and N.L. Saini, J. Phys.: Condens. Matter **12**, 10655 (2000).

7. N. L. Saini, A. Bianconi, and H. Oyanagi, J. Phys. Soc. Jpn. **70**, 2092 (2001).

8. T. Egami and D. Louca, Phys. Rev. B **65**, 094422 (2002).

9. B. O. Wells, Y. S. Lee, M. A. Kastner, R. J. Christianson, R. J. Birgeneau, K. Yamada, Y. Endoh, and G. Shirane, Science **277**, 1067 (1997).

10. J. C. Grenier, N. Lagueyte, A. Wattiaux, J. P. Doumerc, P. Dordor, J. Etourneau, M. Pouchard, J. B. Goodenough and J. S. Zhou, Physica C **202**, 209 (1992).

11. C. Chaillout, J. Chenavas, S. W. Cheong, Z. Fisk, M. Marezio, B. Morosin and J. E. Schirber, Physica C **170**, 87 (1990).

12. A. Bianconi, D. Di Castro, G. Bianconi, A. Pifferi, N.L. Saini, F.C. Chou, D.C. Johnston and M. Colapietro Physica C 341-348, 1719-1722 (2000); D. Di Castro, M. Colapietro and G. Bianconi, Int. J. Mod. Phys. B **14**, 3438 (2000).

13. F. V. Kusmartsev, D. Di Castro, G. Bianconi, A. Bianconi, Physics Letters A **275** (No. 1-2), 118-123 (2000).

14. F. C. Chou, D. C. Johnston, S. W. Cheong and P. C. Canfield, Physica C **216**, 66 (1993).

15. G. Bianconi, D. Di Castro, N.L. Saini, A. Bianconi, M. Colapietro, A. Pifferi, (2000) in "X-ray and Inner Shell Processes" eds by R.W. Dunford et al. (AIP proceedings, Woodbury, NY) pag. 358-371.

Frascati Physics Series Vol. XXXII (2003), pp. 87-94
19th INTERNATIONAL CONFERENCE ON X-RAY AND INNER-SHELL
PROCESSES – Roma, June 24 - 28, 2002

EXAFS STUDY OF $Co_x(SiO_2)_{1-x}$ GRANULAR ALLOY

Júlio C. Cezar, Hélio C. N. Tolentino
Laboratório Nacional de Luz Síncrotron, Campinas, Brazil
Juliano Denardin, Marcelo Knobel
Laboratório de Magnetismo e Baixas Temperaturas,
IFGW, UNICAMP, Campinas, Brazil

ABSTRACT

Here we present the structural characterization of granular alloy composed by cobalt particles embedded in a silica matrix by means of EXAFS spectroscopy. The results showed an increasing number of metallic first neighbors with increasing Co content in the sample. For the lowest Co concentration (36 at. %) we observed an important contribution of oxygen neighbors in the coordination shell. From the coordination number obtained from EXAFS we propose a simple model to estimate the cobalt cluster diameter which resulted in particle diameters ranging from 0.9 up to 1.3 nm.

1 Introduction

Granular alloys attracted the interest of solid state physics community, due to their magnetic properties. Among these properties, we should call attention to

the giant magneto-resistance (GMR), that is, the variation of electric resistivity with the application of a magnetic field [1]. We report here, the study of the granular alloy composed by cobalt particles embedded in a silica (SiO_2) matrix. In this case, as the matrix is an electrical insulator, the electronic transport through the sample is achieved by tunnel effect. Systems based on this principle have been studied as potential materials for non-volatile Random Access Memories [2]. Here we present the results of structural characterization of these granular alloys by means of EXAFS spectroscopy.

2 Materials and Methods

The samples are sputtered films on kapton tapes. All films have thickness of approximately 1 micrometer. We have worked on four compositions: 36, 41, 44 and 50 at. % of cobalt. Previous work showed that each concentration has different magnetic properties [3]. Figure 1 shows a cross-sectional HRTEM bright field image (A) and dark field image (B) of an as prepared granular film with x = 0.36. The images were obtained at the Electron Microscopy Laboratory, of Synchrotron Light National Laboratory (LNLS), using a Jeol JEM-3010 microscopy. The bright image displays microstructure characteristic of typical granular metal films, containing small metallic particles, nearly spherical in shape. The dark field HRTEM images were taken by selecting a quarter of the strong diffraction rings, hence only the grains satisfying the selected diffraction conditions appear bright. The particle size histogram, was determined from several dark field TEM images, over a total number of 800 particles. The histogram was fitted using a log-normal distribution of particle diameters, from which we obtained a median particle diameter equals 3.2 nm and the distribution width of 0.43 [4]. The previous characterization of these samples demonstrates the importance of the interaction between the particles to understand their magnetic behavior. On the other side, this behavior also depends on the structural characteristics of the sample. Information about

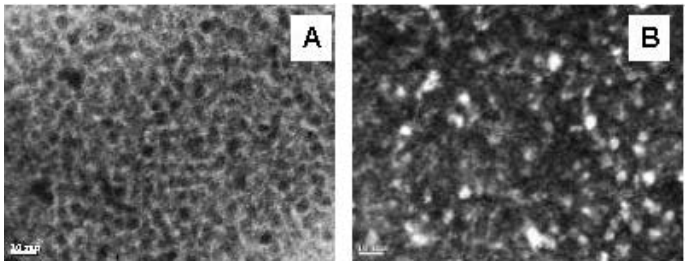

Figure 1: *Cross-sectional HRTEM bright field image (a) and dark field image (b) of the as prepared granular film with metal volume fraction $x = 0.36$.*

particle size, particle size distribution, interface roughness between particle and matrix, among others, are of key importance to model and optimize the magnetic properties. The EXAFS measurements have been performed at D04B (XAS1) beam line of LNLS, at K edge of cobalt (7709 eV), in transmission mode, using air filled ionization chambers as intensity detectors. The final spectrum for each sample is the average of at least 10 spectra.

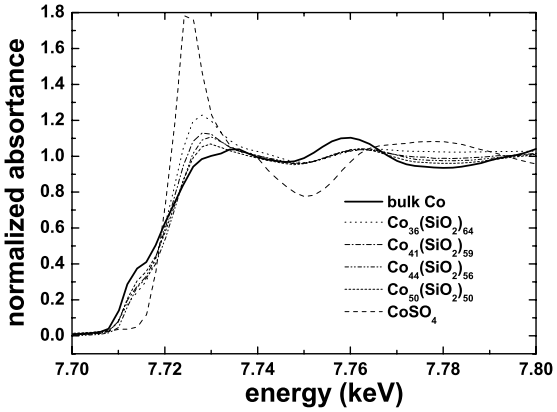

Figure 2: *XANES evolution of $Co(SiO_2)$ samples. As Co concentration increases, the spectra tends to the bulk Co.*

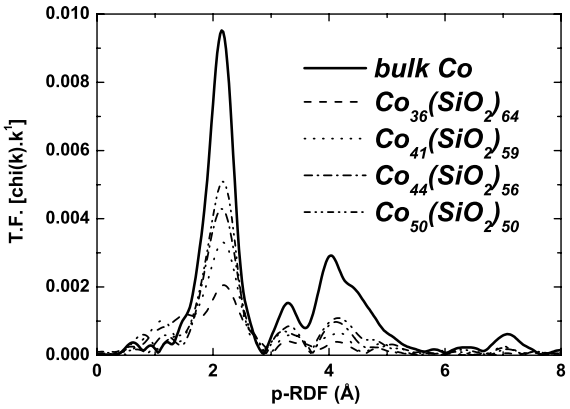

Figure 3: *Fourier transform of the EXAFS data on $Co(SiO_2)$ samples.*

The data analysis has been done within the WinXAS program, using the following steps:

- Fitting of Victoreen function in the pre-edge region;
- E_0 determination from the root of the second derivative of the spectra;
- Extraction of μ_0 with a polynomial (5^{th} degree) weighted by k^1;
- Fourier transform weighted by k^1, with a Hanning apodization window;
- Fitting in back-Fourier filtered space, with distances fixed at bulk values (2.497 Å for Co-Co and 2.064 Å for Co-O), using experimental phases and amplitudes extracted from bulk cobalt and $Co(SiO_4)$.

3 Results

In figure 2, the XANES part of the spectra shows that there is a mixture of Co-O bonds. One can observe a variation of the first main peak from signal more similar to that of $Co(SiO_4)$ for 36 at. % of Co, to a spectra similar to

Table 1: *Results from fitting the EXAFS data on $Co(SiO_2)$ samples.*

	Co neighbor #	$\sigma^2(\times 10^{-3}\mathring{A}^2)$	D_{EXAFS}(nm)
$Co_{36}(SiO_2)_{64}$	5.5 ± 0.6	5.7 ± 1.5	0.9 ± 0.1
$Co_{41}(SiO_2)_{59}$	6.3 ± 1.0	3.2 ± 1.9	1.1 ± 0.2
$Co_{44}(SiO_2)_{56}$	7.1 ± 1.0	3.2 ± 2.0	1.3 ± 0.2
$Co_{50}(SiO_2)_{50}$	6.3 ± 0.7	0.5 ± 0.5	1.1 ± 0.1

bulk Co, for the 50 at. % Co concentration. The Fourier transform of the samples and of the bulk Co are shown in figure 3, where one can observe the contribution from the oxygen and cobalt neighbors. Preliminary fittings of the EXAFS data have been done in Fourier filtered space. Due to the superposition of the oxygen and metal peak we performed the fitting with contributions of Co and O neighbors. The fitting results can be observed in figure 4, whereas the numerical results are listed in table 1. As we fixed the coordination distance, the results are the metallic coordination number and Debye-Waller factor (σ^2), which is related with the disorder of the system. We observe an increasing coordination number, with increasing Co concentration up to 44 at. %. The $Co_{50}(SiO_2)_{50}$ sample have a smaller coordination number, but also a Debye-Waller an order of magnitudine smaller.

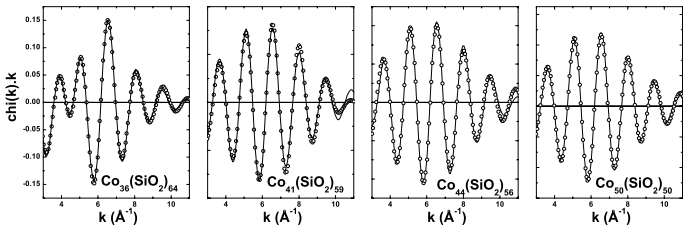

Figure 4: *Fitting results for cobalt-cobalt distance in Fourier filtered space.*

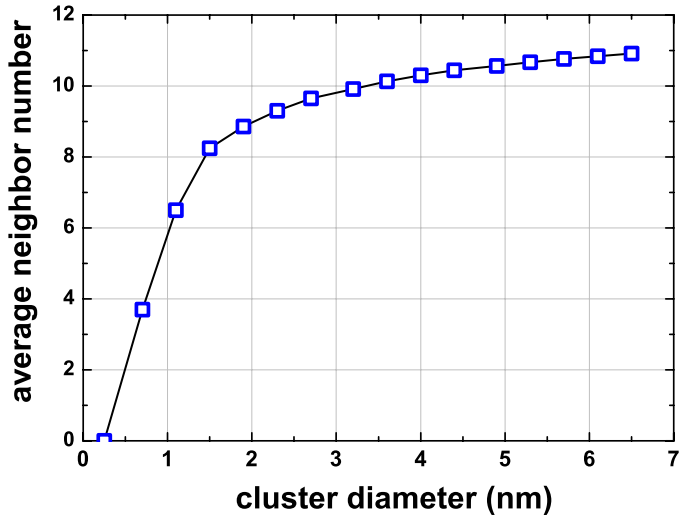

Figure 5: *Average neighbor number expected for different cobalt cluster diameter. The line is just a guide for the eyes.*

4 Particle size determination

One can estimate the cobalt particle size from the fact that cobalt atoms at the particle surface will have a reduced number of neighbors, while cobalt atoms inside the particle will have 12 neighbors, as expected for bulk cobalt. Assuming a FCC packing and the interatomic distance of bulk Co, one can build a table of cobalt clusters with increasing number of closed shells [5]. For each particle size is possible to determine the number of atoms on surface and inside the particle. In order to calculate the average nearest neighbor that should be observed by EXAFS for every particle size, we assumed that the number of metallic neighbors for surface and inner atoms are equal to 6 and 12 respectively. These results are shown in figure 5. In fact, the assumption of six metallic neighbors for surface atoms is not adequate for small clusters, where the Co atoms on the surface may have even less than six metallic neighbor. For closed particles with 1, 13 and 55 (isolated atom, one and two closed shells, respectively) we used

another number of metallic neighbor for the surface atoms, just counting how many neighbors are metalic or not. Comparing the average neighbor number (N) obtained from the EXAFS measurements with the values displayed in figure 5, then one can estimate the average diameter of the cobalt particles. These results are shown in the last column of table 1. One can observe that for the sample with 35 at. % of Co, we obtained an average diameter of 0.9 nm, whereas the analysis of TEM images on the same sample lead to a value of 3.2 nm. We interpreted this difference as consequence of the fact that TEM can note probe the very tiny particles (usually below 2 nm for this kind of system). So the histogram of particle diameter obtained in such way is shifted towards an average higher then the real one. On the other hand, the EXAFS data analysis used here can underestimate the neighbor number value. We should call attention for the fact that the number of neighbor obtained from EXAFS is highly correlated with the disorder of the system (expressed by the Debye-Waller factor in the EXAFS formalism). Once that the disorder in these systems is quite high, a more sophisticated data analysis is necessary. Also our assumption is quite simple, and models that take in account the reduction of neighbor for second and third neighbors can be used [6].

5 Conclusions

We obtained from EXAFS measurements, significant information about the structure of Co clusters embedded in a silica matrix, for different Co concentrations. The XANES and Fourier transform of the EXAFS signal showed that for the smaller concentration (36 at. %) of Co, the influence of the oxygen neighbor is quite important. Indeed, in the EXAFS data analysis is impossible to analyze separately the contribution of Co and O, and the fit must be performed taking both elements simultaneously. Based on a simple model we estimated the particle diameter from the average neighbor number obtained from the EXAFS data analysis. The results ranged from 0.9 up to 1.3 nm for

increasing Co concentration. These values are somewhat smaller than the value observed by HRTEM. This can be related with two causes: first, one should note that HRTEM is not able to observe the smaller particles with (for this system, particles with diameter less than 2 nm), which tends the average particle diameter for higher values. Second, taking properly in account the role of the disorder in this systems will lead to an increase the neighbor number observed and consequently increase the particle diameter obtained from EXAFS.

6 Acknowledgements

Research performed at LNLS - National Synchrotron Light Laboratory, Brazil. Financial support from FAPESP (98/16329-0) is also acknowledged.

References

1. See e.g.: Allia, P.,*et al.*, Phys. Rev. B **52**, 15398, 1995; Xiao, J.Q., *et al.*, Phys. Rev. Lett. **68**, 3749; Parkin, S.S.P., *et al.*, Europhys. Lett. **22**, 455.

2. See e.g.: Prinz, G. A., Science, **282**, 1660, 1998.

3. Denardin, J. C., *et al.*, J. Mag. Mag. Mater., **226-230**, 680-682, 2001.

4. Denardin, J. C., *et al.*, Phys Rev B, **65**, 064422, 2002.

5. Patterson, A.L.,*et al.*, in International Table for Crystallography, ed. Kasper, J.S.,*et al.*, Kluwer Academic Publishers, 1989.

6. Arcon, I., *et al.*, J. Synchr. Rad., **8**, 575-577, 2001.

Frascati Physics Series Vol. XXXII (2003), pp. 95-150
19th INTERNATIONAL CONFERENCE ON X-RAY AND INNER-SHELL PROCESSES – Roma, June 24 - 28, 2002

MAGNESIUM X-RAY ABSORPTION NEAR-EDGE STRUCTURE (XANES) SPECTROSCOPY ON SYNTHETIC MODEL COMPOUNDS AND MINERALS

G. Cibin
I.N.R.M. P.za dei Caprettari 70, I-00186 Roma, Italy
A. Marcelli
L.N.F. - I.N.F.N. Via Enrico Fermi 40, I-00044 Frascati RM, Italy
A. Mottana
Dipartimento di Scienze Geologiche, Universita' degli Studi Roma Tre
L.go S. Leonardo Murialdo 1, I-00146 Roma RM, Italy
G. Giuli
Dipartimento di Scienze della Terra, Universita' degli Studi di Camerino
Via Gentile III da Varano, I-62032 Camerino MC, Italy
I.N.F.M., Sezione Gestione Distaccata Adriatico Centrale
G. Della Ventura, C. Romano
Dipartimento di Scienze Geologiche, Universita' degli Studi Roma Tre
E. Paris
Dipartimento di Scienze della Terra, Universita' degli Studi di Camerino
A. Cardelli and F. Tombolini
L.N.F.- I.N.F.N. Via Enrico Fermi 40, I-00044 Frascati RM, Italy

ABSTRACT

Magnesium K-edge X-ray absorption near-edge structure spectra have been recorded on a series of synthetic compounds (25) that are representative models for a variety of crystal structures and compositions, and on minerals (33) from various geological environments. In most samples Mg is coordinated by oxygen, but in a few of them a halogen (Br, Cl, F) is the first-coordination ionic ligand, and in one case Si and N are bound to it by covalent bond. The first Mg K-edge XANES intense feature, which in the reference metal sheet where Mg is in twelve-fold coordination is at 1303.6 eV, is located at ca. 1310 eV in all compounds, but it shifts to lower energy with decreasing coordination when Mg^{2+} is located in a cage with 8, 6, 5 or 4 anions. However, the individual values for Mg in such coordination are spread and depend upon the ligand type. Although limited, the average measured shift (2.2 eV) largely exceeds instrumental accuracy (better than 0.5 eV) and provides a useful indication of

the coordination of Mg for glasses and semi-amorphous materials, as well as for materials available only as nanoparticles, or more generally for all materials with unknown coordination number. Magnesium yields a large variety of XANES features both at the edge and in the multiple scattering regions when coordinated by O *viz.* OH. These features do not correlate with either point or space group symmetry. More precisely, they depend upon the actual shape of the coordination polyhedron, as expressed by geometrical parameters such as bond-length, central angle and polyhedral distortion. Polyhedral distortion may even determine the formation of a weak pre-edge feature at ca. 2 eV lower energy than the first intense absorption line; the intensity of this additional feature is further affected by positional disorder of atoms substituting for Mg in the relevant structural site. Furthermore, the linkage between the independent Mg sites in the structure, which simultaneously absorb under the impinging synchrotron radiation that generates the photoelectrons, plays a very significant role in shaping the XANES spectrum. Therefore, in general, XANES spectroscopy at this energy probes both short- (i.e., local) and medium-range orders around the absorbing Mg atom, its scanning width being a sphere ca. 0.6-0.8 nm in radius; in other words, the photoelectrons are able to interact along multiple scattering pathways with atoms as far away as in the fourth or fifth coordination shell around the Mg absorber, and even farther in certain ordered structural systems where the atoms are collinear.

1 Introduction

Magnesium is the eighth most abundant element in the Earth crust and increases downward to become the third one in the Earth lower mantle. The number of mineral species in which Mg is an essential constituent is very large indeed, but it is comparatively minor when related to the number of minerals where Mg may substitute in substantial amounts for other cations. The number of artificially-prepared Mg compounds is extremely large, in the order of several thousands, as Mg is very important for numberless applications not only in Mineralogy and Chemistry, but in Metallurgy, Agriculture, Environmental science and, most recently, even Biotechnology. In Material Science and Petrology the role of Mg is even greater than in Mineralogy: quite often Mg was the starting material that proxied for Fe and Mn in systems where these atoms could not be used due to their easy oxidation in the atmosphere and/or at high temperature. Consequently, Mg-bearing systems are now much better known than any other systems; indeed, they are the reference systems for any divalent-metal-cation-bearing system (Bowen 1928).
Yet, the crystal-chemistry of Mg is far from being completely understood. Indeed, the Mg atomic and electronic properties are such as to make investigation

difficult; e.g., it is known for a long time that electron microprobe (EMP) cannot provide quantitative analyses unless affected by a large error because of the poor primary fluorescence emission of the Mg atom under the electron beam (Cliff & Lorimer 1975; Pouchou 1996), with the additional problem of the rapid attenuation of the emitted X-rays, as their low energy makes them easily captured by the matrix (Tertian 1986).

For similar reasons and for quite a long time, X-ray absorption spectroscopy (XAS) for Mg did not develop satisfactorily, despite having had its first trial at the very dawn of this technique (Fricke 1920). Only recently, the availability of suitable monochromator crystals and other special apparatus has allowed recording Mg spectra worth analyzing in detail, as they have the appropriately high signal to noise ratios as well as resolutions (Wong et al. 1990, 1994, 1999; Murata et al. 1992; Ildefonse et al. 1995; Kinoshita et al. 1997; Takata & Kosugi 1999; Takata et al. 2001). Consequently, during the last decade a large enough number of experimental and theoretical XAS studies has been carried out on various chemical and physical systems which increases the knowledge not only of the Mg electronic behavior, but of the local ordering around the Mg atom also, thus contributing to understanding the chemical and crystal-chemical role of this element (e.g., Henderson et al. 1992; Yoshida et al. 1995a,b; Mottana et al. 1996a,b, 1999, 2000, 2002; Wu et al. 1996b, 1999; Bradley et al. 1997; Cabaret et al. 1998; Li et al. 1999; Aritani et al. 2000, 2001; Brigatti et al. 2000; Kosaka et al. 2000; Giuli et al. 2002; Peng & Li 2002; Tombolini et al. 2002, 2003).

In this paper, we intend to review in an organized way the scattered information available on the Mg K-edge spectra of minerals, synthetic mineral analogues and inorganic compounds, and add more data aiming at cover the existing gaps so as to reach the ultimate goal of showing that the whole evidence can be systematized to draw useful information on the Mg coordination number (CN), a major parameter for crystal-chemistry, and on the size and distortion of the coordination polyhedron around the Mg atom. This is indeed the case even for samples that are unfavorable for X-ray diffraction (XRD) studies such as the nanoparticles, either because of their very fine grain size (e.g., clay minerals), or for being poorly crystalline (e.g., semi-amorphous precipitates) and even non-crystalline at all (e.g., glasses). We will also show that, under favorable conditions, even the type of next-nearest neighbors to Mg, against which the photoelectrons emitted by it in the excitation process are bound to interact, may turn out to be recognizable, in spite of the absence of previous chemical information, from a careful analysis of Mg K-edge spectra.

There are several spectroscopic methods that are highly sensitive to local atomic environment, but most of them fail in the case of Mg, mainly because it is a far too light atom. NMR provides excellent data, but it will be disregarded throughout this research as being physically incompatible; thus, the only other method that can give support to our spectra interpretation is elec-

tron energy loss spectroscopy (EELS). This technique is based essentially on the same physical process and theoretical background as XAS and is best suited for investigating edges up to an energy loss of ca. 1000 eV i.e., in the soft and ultrasoft X-ray region that is notoriously difficult to investigate by XAS (Brydson et al. 1992; Garvie & Buseck 1999). By contrast, for the 1.0-2.5 KeV energy region, which encompasses the K edges of the light elements Mg, Al and Si, XAS is slightly superior to EELS, even in resolution. Yet the two methods do compare favorably and sometimes give complementary results. In the case of Mg, best agreement is obtained when using in the near-edge region of the spectra for both X-ray absorption (XANES) and electron energy loss (ELNES). As a matter of fact, XANES and ELNES Mg spectra for model compounds have proved to be able to provide information not only about the electronic transitions from core to unoccupied states in the conduction band, but also on the environment around the excited Mg (absorber) such as coordination, bonding, and site symmetry (Lindner et al. 1986; Egerton et al. 1987; Brydson et al. 1991; Garvie et al. 1994; Wu et al. 1996a; Garvie & Buseck 1999; Mizoguchi et al. 2000). Unfortunately, the number of ELNES spectra suitable for such a comparison is small (cf. Appendix 1).

Conventional XAS was in distress with light elements such as Na, Mg, Al, Si, etc., at least in the past. However, these times are now fading away because of two substantial technical improvements:

1. Increasing brilliance of the synchrotron facilities. In the last decades, several new storage rings – namely, third generation synchrotron radiation (SR) facilities - become operational all around the world. These dedicated sources are equipped with wigglers and undulators and in this way deliver a very intense and brilliant beam even in the soft X-ray energy region. An increase of brilliance (i.e., flux normalized to solid angle and to source size) of several orders of magnitude has been achieved, with exponential increase over the years; from the 10^{13} photons/s/0.1%bw/mrad^2/mm^2 of first generation SR sources that used bending magnets to the present 10^{20} photons/s/0.1%bw/mrad^2/mm^2 reached by undulator beam lines. These results were achieved through the optimization of the whole ring design for low emittance undulator radiation (Laclare 2001).
2. Increased performance and stability of monochromator crystals in the soft X-ray energy region. Substituting the cumbersome Grasshopper grating monochromator (Brown et al. 1978) with crystal monochromators equipped with β-alumina or quartz or beryl, which developed in the years '80s to cope with the requirements of modern high-resolution XAS spectroscopy, had already produced a first substantial improvement in the resolution of the acquired spectra (Wong et al. 1982). However, the real breakthrough came when the novel crystal YB_{66} went into use, because it increased dramatically the performance even of the apparatus that had been designed for the previously mentioned crystal monochromators (Wong et al. 1990). Indeed, this new crystal proved to have not only a good mechanical strength and low thermal

expansion, but also a much better high-vacuum and thermal stability as well as a better radiation-damage resistance than the old ones, and it is second only to quartz for reflectivity (Wong et al. 1994, 1999). Very recently, another crystal has been introduced, KTP i.e., $KTiOPO_4$, which appears to be even more effective for both reflectivity and scanned energy range (Takata & Kosugi 1999; Takata et al. 2001; cf. Rogalev et al. 1998), so that great future developments of Mg and Al XAFS can easily be forecasted. Grating monochromators remain very difficult to use for solid material systems because of their ultra high vacuum requirements; consequently, despite their potentially higher resolution, they are mainly used for spectra acquisition below the 800 eV energy i.e., for the investigation of very light atoms.

2 Experimental materials and methods

2.1 Sample preparation.

All mineral samples were first carefully purified, the grains appropriate for EMPA and single-crystal X-ray diffraction refinement (SC-XRD) selected, and an aliquot finely ground to record powder X-ray diffraction data (P-XRD) and XAS spectra. Special care was taken to obtain powders not only pure under the resolving power of P-XRD, but also homogeneous in grain size: all our measured samples pass the No. 230 mesh sieve (< 0.0625 mm) and are retained by the No. 325 one (> 0.044 mm). The same preparation was followed for synthetic mineral analogues and for chemical compounds, most of which, nevertheless, were available only as precipitates much finer than the ground powders; thus, they too warrant against errors due to textural effects (Pettifer 1990; Mottana et al. 2002).
A complete list of the studied samples is given in Tables 1 and 2 (for synthetic and natural materials, respectively) in order of decreasing Mg coordination number. Those tables report not only our own spectra, but also other spectra recorded by other groups at the same facilities and under experimental conditions that are either the same as ours or closely comparable, so that meaningful comparisons might be made. Although most conclusions that follow are based on our own spectra, we deem it convenient to take into due consideration and discuss spectra that were taken by others on related or complementary materials, as long as experimental conditions were closely similar (e.g., Wong et al. 1999 for SSRL, Li et al. 1999 for UVSOR). In this way we will have a set of reliable data as large as possible.
Appendix 1 lists all experimental spectra concerning Mg that we could retrieve from literature. They will be used only for qualitative comparisons because we have no experience on certain facilities (e.g., Henderson et al. 1992; Ildefonse et al. 1995). In addition, Appendix 1 lists a number of samples recorded at

anyone of the two facilities where we also could operate, but of which we have no electronic data (e.g., Yoshida et al. 1994, 1995a,b; Li et al. 1997; etc.). We will not make use of them in drawing our conclusions, but we must point out that some of those spectra should be kept in mind for other, possible future reference.

2.2 XAS experimental spectra recording.

Most experimental XANES spectra were recorded at SSRL, the Stanford Synchrotron Radiation Laboratory. At that facility SPEAR2, the now dismantled electron storage ring, was operating at 3 GeV with ring currents decreasing from 90 to 60 mA over a 20 h lifetime. We operated at the soft X-ray beam line SB03-3, which derived synchrotron radiation from the ring via a bending magnet. This line used the double crystal JUMBO monochromator (Cerino et al. 1980; Hussain et al. 1982), modified by the insertion of two parallel (400) plates cut from the same YB_{66} crystal ($2d_{004} = 1.172$ nm: Wong et al. 1990). The powdered samples were homogeneously mounted on Ag-coated brass slides after dispersion in acetone or ethanol. No additional care was taken to avoid the systematic errors due to preferred orientation, but for exposing the flat sample at a skew angle (usually ca. 35-40°) to the impinging SR beam. The spectra were recorded in the total yield (TEY) mode that,for light atoms, is a detection method proportional to the absorption coefficient (Gudat & Kunz 1977). The experimental resolution at the Mg K-edge energy was in the order of ca. 0.5 eV (Schäfers et al. 1992) to better than 0.4 eV (Rowen et al. 1993). Step-scan spectra were recorded over a range of 150-200 eV across the absorption edge with a 0.3 eV step and 5 s counting time. The energy was calibrated in two ways: i) against a glitch occurring in all spectra at 1385.6 eV, which was due to an anomalous scattering for the 006 reflection at the Y $L_{2,3}$ edges that was inherent the YB_{66} crystal and invariable as long as the monochromator crystal was unchanged (cf. Kinoshita et al. 1997, 1998; Tanaka et al. 1998; Wong et al. 1999); ii) by recording at regular time intervals the sharp Mg K-edge first feature of one out of the following three synthetic samples: periclase, åkermanite and pyrope.
A number of experimental spectra were recorded at UVSOR, the SR source of Institute for Molecular Science (IMS) at Okazaki, Japan. This 750-MeV electron storage ring usually operates at a current decreasing from 200 to 100 mA within a lifetime of ca. 4 h (Watanabe 1991). The soft X-ray beam line BL7A derives synchrotron radiation by a super-conducting wiggler under an acceptance angle of 1 mrad in the horizontal plane and 0.15 mrad in the vertical plane, yielding photons in the energy range 800-4000 eV. The beam line was equipped with a double-crystal monochromator of natural beryl cut along the (10.0) plane ($d_{10.0} = 0.79825$ nm), which ensures a better than 1.0 eV resolution, estimated to be in the order of 0.7 eV (Murata et al. 1992). A thin

film of powder was stuck onto a bi-adhesive graphite tape, the opposite surface of which is attached on the first photocatode of an electron multiplier located directly in the experimental chamber, which is held under vacuum at less than 10^{-7} torr. The Mg K edge was scanned at angle steps 0.1 $^{\circ}\theta$ in the total electron yield (TEY) mode. The energy calibration was done with reference either to the edge inflection of a metal Al standard sheet at 1559.6 eV, or to one of the several glitches that show up in the transmission spectrum of the beryl crystal, in particular to the sharp minimum occurring at about 1550 eV.

2.3 XAS experimental spectra processing.

When needed, the recorded experimental spectra were first energy-corrected as a function of ring current, then fitted with a Victoreen polynomial function to account for the base line and normalized to 1 at high energy (between 50 and 150 eV above the absorption edge inflection according to a visual evaluation of the spectrum). The observed features were carefully located using algorithms able to detect changes in the peak signal of the order of 10^{-3}-10^{-4}. They first fit the whole spectrum with an arctangent to account for the edge jump, and then each feature with either a Gaussian or a Lorentzian function. Derivatives were also used to locate the high-energy region features that were always assumed to have a Gaussian shape.

3 Results

The studied (synthetic) model compounds are listed in Table 1 and the (natural) minerals in Table 2. Their normalized experimental Mg K-edge spectra are shown in Figs. 1 and 2.

3.1 Model compounds

A wide set of compounds synthesized strictly on composition and with their crystal structure well refined so as to provide reliable site characterization were selected to model the behavior of Mg in the different possible structural environments forecasted by Pauling's first rule.

3.2 Twelve-fold coordination (Fig. 1a)

Magnesium metal crystallizes in the **hcp** structure type (space group $P6_3/mmc$) with CN = 12 i.e., with the Mg first-shell neighbors of the Mg absorber central atom arranged as the corners of an anticuboctahedron, each one at a 0.162 nm distance (the atomic radius). The K-edge XANES spectrum of Mg metal

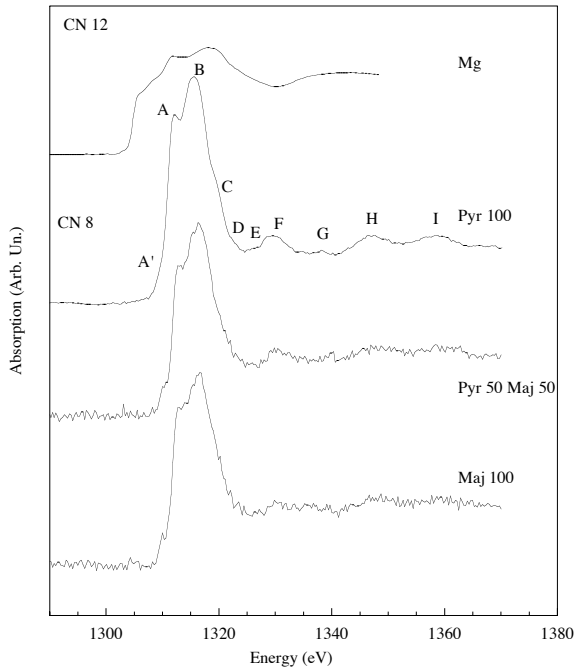

Figure 1a: *Mg K-edge XANES spectra of synthetic model compounds with Mg in 12- and 8-fold coordination.*

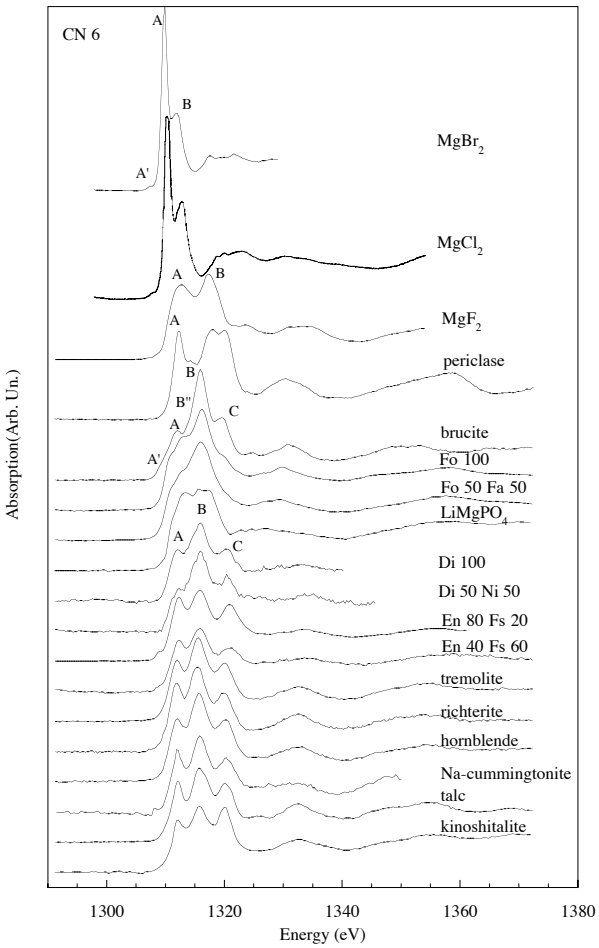

Figure 1b: *Mg K-edge XANES spectra of synthetic model compounds with Mg in 6-fold coordination.*

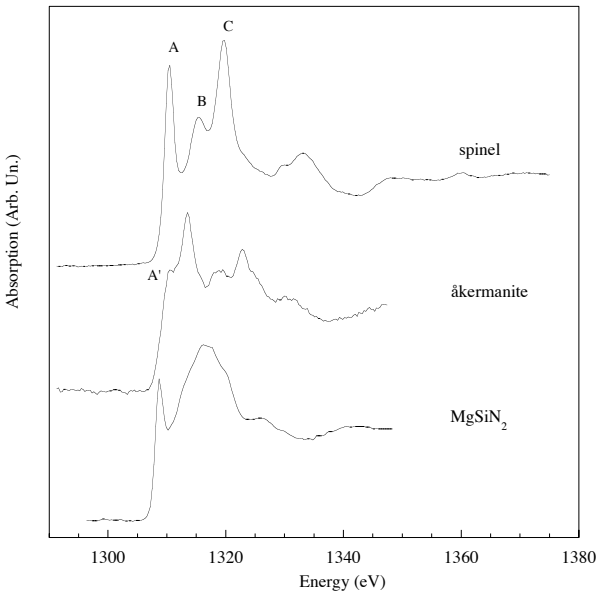

Figure 1c: *Mg K-edge XANES spectra of synthetic model compounds with Mg in 4-fold coordination.*

consists of a rather weak but sharply rising first intense feature with its top at 1303.6 eV(Fuggle & Inglesfield 1992) followed by a number of broad shoulders and features up to reach an even more intense, but fairly broad top at 1313.0 eV. The edge inflection is constrained to be 1303.0 eV (Fuggle & Mårtensson 1980). Although this spectrum was recorded repeatedly and consistently at SSRL on a Mg foil and using the YB_{66} crystal monochromator (Wong et al. 1997 Fig. 1; Wong et al. 1999 Fig. 15c), it appears to have little in common with the K-shell excitation spectra for polycrystalline Mg metallic films recorded by EELS (Bradley et al. 1985 Fig. 5). Nevertheless, knowing the XANES spectrum of Mg metal taken with the same instrumental setup and conditions as all other experimental spectra that follow is important to interpret the modifications present in these, where Mg is excited to become a divalent cation and is coordinated by ligands having different bonding properties (Wong et al. 1997, 1999).

3.3 Eight-fold coordination (Fig. 1a)

Magnesium is far too small a divalent cation (0.089 nm effective radius for NC = 8: Shannon 1976) to rest comfortably in a coordination polyhedron such as the hexahedron (cube) unless constrained under high pressure. Consequently, there are only few compounds where Mg is eight-fold coordinated, but these few ones are significant because they document what the Mg behavior under a high-pressure environment is; moreover, they have natural counterparts originating from the Earth depths, and garnets are the most important ones.
Pure Mg-Al garnet end member (Pyr_{100}, pyrope) is the model compound for such a coordination, the more so as its O cage that surrounds Mg is the least distorted cubic site among all pyralspite garnets ([Δ(X-O) = 0.01427]: cf. Ungaretti et al. 1995) having four long and four short evenly distributed Mg-O bonds (Armbruster et al. 1992; Pavese et al. 1995). The full multiple-scattering region (FMS: Natoli & Benfatto 1986) of end member synthetic pyrope shows a strong first absorption line (A) at 1309.1 eV, which is immediately followed by an even stronger one (B: 1315.6 eV) having on its high-energy limb a poor but detectable shoulder (C: 1319.8 eV). In the intermediate multiple-scattering region (IMS: Natoli & Benfatto 1986) a number of broad features (D, E, F, G, H, I) follow and progressively fade into the EXAFS oscillations characteristic of the single scattering (SS: Natoli & Benfatto 1986) region. In the pyrope system the entire edge, or XANES region, extends over ca. 70 eV (1307-1375 eV) i.e., significantly farther away than in other simple, model compounds, where it is conventionally taken to be 50 eV (Bianconi 1988). Note that a faint but definite change of slope (A') shows up on the low energy side of the first absorption line A. This feature occurs in all the garnet spectra that follow as well as in all pyrope spectra published so far (cf. Appendix 1); occasionally it is resolved to the point of showing up as a shoulder.

With increasing pressure, garnets undergo a structural transition to tetragonal symmetry that some calcian garnets display even at ambient conditions, but magnesian garnets would show it only at very high pressure (up ca. 13.5 GPa: Gasparik 2002) so as to occur very deep in the Earth's mantle (Stachel 2001). Indeed, majorite, the extreme case where such a structural transition is accomplished, is known as a mineral only because of extraordinary findings as inclusions in diamonds (Moore & Gurney 1985) and in chondritic meteorites (Smith & Mason 1970).
The synthetic solid solution series between pyrope and majorite displays Mg *K*-edge XANES spectra having no apparent shifts in energy for their individual features, but with significant changes in their intensities. This appears to be a function of their structural transition from cubic to tetragonal (Parise et al. 1996; Heinemann et al. 1997). In particular, the 1:1 pyrope-majorite intermediate member ($Pyr_{50}Maj_{50}$), still having cubic symmetry, displays an Mg-XANES spectrum that is almost indistinguishable from the pyrope end-member, but for the IMS region, which shows a much lesser resolution, and for a better resolved pre-edge feature A'. The observed decrease in the signal-to-noise ratio is probably related to increasing positional disorder, since the total Mg content of the sample actually increases.

The majorite end member (Maj_{100}) shows a very high structural complexity. Most Mg is located in two distinct cubic sites, independent because of the symmetry reduction from cubic to tetragonal, but a minor fraction of it is disordered over two, again distinct, octahedral sites and competes there with Si (Angel et al. 1989). This complex Mg distribution, which is representative for coexistence of eight- and six-fold coordinations, reflects onto the XANES spectrum with a much better resolved A' feature and a less resolved A and B doublet. Here again, the entire IMS region becomes even weaker and broader than it was in $Pyr_{50}Maj_{50}$, thus further supporting our interpretation that it originates from structural disorder, as the total Mg content increases again.
The very high-pressure polymorph of $MgSiO_3$ ("perovskite"), believed to be present near the base of the lower mantle (Hutchison et al. 2001), is another candidate to contain Mg in eight-fold coordination. Indeed this happens for Fe^{2+} in the intermediate $Mg_{1-x}Fe^{2+}{}_xSiO_3$ composition (Farges et al. 1994; Lauterbach et al. 2000). However, nobody could record such a Mg-XANES spectrum yet.

3.4 Six-fold coordination (Fig. 1b)

In excellent agreement with Pauling's first rule, with ligands such as O, OH and F, the Mg^{2+} cation (effective radius 0.0720 nm: Shannon 1976) prefers the six-fold coordination. The octahedron is mostly very regular, but sometimes it

may be considerably distorted if the covalent fraction of the Mg-to-ligand bond becomes significant i.e., when the ligand undergo strong attraction by other cations outside the octahedron. A further problem arising when dealing with octahedrally coordinated Mg-compounds is in the number of independent octahedral sites present in the structure, which may be as high as seven. This is no minor problem; theoretical analyses carried out *ab initio* showed that experimentally recorded XANES spectra are the weighed sums of all the independent partial spectra generated by the absorber when located in each different environment within the investigated structure (Wu et al. 1996b, 1999; Cabaret et al. 1998; Giuli et al. 2002).

Keeping these preliminary facts in mind, we will display and discuss the experimental spectra of model octahedrally-coordinated Mg compounds according first to their relationships with the type of ligand i.e., with Mg bound to a monovalent halogen anion first, then with oxygen, which is the only significant divalent anion. As a matter of fact, we also looked for spectra of compounds the Mg of which is bound to sulfur, but we found no useful information. Then, we will describe the investigated compounds on the basis of their increasing number of independent octahedral sites. Finally, we will take into account the increasing deformation shown by these sites, which results from competing forces acting on their corner anions (thus reflecting onto the degree of ionicity of the Mg-to-ligand bond) and is geometrically assessed by the octahedral angle variance of the site (OAV: cf. Smyth & Bish 1988).

The three model compounds that follow are representative for Mg at the center of a coordination polyhedron having six halogens at its corners.

Magnesium bromide ($MgBr_2$) has the CdI_2 structure, which is characterized by layers of anions in the **hcp** arrangement with their all equivalent octahedral voids filled by Mg cations in alternate layers (Partin & O'Keeffe 1991). This compound was occasionally used as an alternative to MgO as reference model for the octahedral coordination (Murata et al. 1992 Fig. 6) because of its very sharp first line A at 1309.8 eV. In addition, the spectrum shows a second significant feature B at 1312.0 eV that is followed by several after-features at higher energy; furthermore, on the low-energy rising limb of line A it shows a very small feature A', which is weak but well resolved.

Such an anomalous A' feature is present also in magnesium chloride ($MgCl_2$, chloromagnesite), the structure of which derives from the $CdCl_2$ structure where the anions are in the **ccp** arrangement and the Mg cations again fill the octahedral voids in alternate layers (Partin & O'Keeffe 1991). The Mg-XANES spectrum is very similar, and actually complements the previous one for its IMS region extends to 1360 eV. Both previous compounds have their Mg in an octahedral site that is geometrically rather loose, because the cation to anion ratio significantly exceeds Pauling's first rule best value, whereas anions such as F^{1-} (0.136 nm), OH^{1-} (0.137 nm) or O^{2-} (0.140 nm) fit it nearly exactly.

Magnesium fluoride (MgF_2, sellaite), although having nearly the same cation to anion radius ratio as MgO, crystallizes in the rutile structure, which is made up of chains of edge-connected octahedra, all equivalent and with a very limited degree of deformation (OVA = 28: Bauer 1976). The Mg-XANES spectrum is rather simple: it shows two major features in the FMS region, both rather broad and with the line A at 1311.4 eV less intense than line B at 1317.2 eV, followed by several minor features in the IMS region that extends to ca. 50 eV above threshold. Such a spectrum is essentially unchanged at 35 K (Naoe' et al. 1989).
These three spectra have only been recorded by Japanese scientists aiming at finding a suitable material to be used as reference for the energy position of $^{[6]}Mg^{2+}$ first absorption line. Elsewhere, and in Japan too in recent times (e.g., Takata & Kosugi 1999), the MgO K-edge spectrum has been usually recorded for the same purpose.
Magnesium oxide (MgO, periclase) is by far the most typical model compound for Mg^{2+} in six-fold coordination; six O atoms surround the Mg absorber all at 0.21056 nm distance and in a rigorous octahedron configuration (OAV = 0.000: Boiocchi et al. 2001). The XANES spectrum of synthetic periclase shows a very strong absorption line A at 1311.3 eV followed by an equally strong doublet B and C (Fig. 1a). The IMS features are many and all rather strong, but they smear out in the energy region above 50 eV from threshold where they merge into the SS oscillations. Such a spectrum was recorded repeatedly at several facilities using different crystal monochromators and setups, as well by ELNES (Appendix 1). Moreover, it was reproduced successfully by *ab initio* theoretical MS calculations, however with best results only when clusters containing more than 100 atoms and extending to the 7^{th} coordination shell were included in the calculations (Wu et al. 1996b).
The Mg K-edge spectrum of magnesium hydroxide ($Mg(OH)_2$, brucite) is very different from those recorded both on MgO and on halides, despite brucite is very close in composition to the former compound and has a layer structure that is very similar to that of $MgBr_2$, with a hexagonal arrangement that is a derivative of that of CdI_2 provided H atoms are ignored. Indeed, the crystal structure of brucite consists of planes of equivalent edge-sharing octahedra, which have all their six O corner atoms at 0.2099 nm distances from Mg and are fairly regular in shape (OAV = 52: Zigan & Rothbauer 1967). The H atoms protrude from these planes in two opposite directions and bind them along **c** through hydrogen bonds. The brucite spectrum is completely different from that of periclase: it shows three prominent features A, B, C in the FMS region between 1309 and 1324 eV, followed upwards in the IMS region by three others that are fairly weak but well resolved. A very weak, but clearly resolved feature A' occurs at 1308.8 eV on the high-energy limb of feature A, and a second one B" is to be detected on the raising limb of feature B. Such features are poorly compatible with the little octahedral distortion determined by structure refine-

ment (see above); thus, a contribution arising from either the hydrogen bond or from far away collinear atoms should possibly be envisaged. As a matter of fact, many spectra having similarities with the brucite spectrum will be found again in most silicates (Table 1; cf. Li et al. 1999) where OH anions, together with the O anions, play an important role in the structure.

Among the published Mg K-edge spectra worth being considered in the present work for their experimental quality and for having been taken at UVSOR under the same conditions as our spectra, we should mention a magnesium hydrous carbonate studied by Aritani et al. (1998 Fig. 1). That experimental spectrum is poor of features, and all those observed are poorly resolved. The authors themselves later dismissed their spectrum because of the presence of several phases in the synthetic bulk material, as it turned out from XRD studies (Aritani et al. 2000 p. 10135).

All model compounds described so far (with the exception of majorite) have their Mg in only one type of environment, or polyhedron. This is not always the case when the Mg coordination polyhedron is not only the octahedron and the structural complexity of the material increases; indeed, most silicates possess in their structures, in addition to their intrinsic tetrahedron having different degrees of polymerization, more than one independent octahedral site, up to five or even seven.

Among the model silicate structures, magnesium monosilicate (Mg_2SiO_4 i.e., Fo_{100} or forsterite) contains Mg in two independent octahedral sites, both displaying some distortion (OAV = 95 for M1 and 90 for M2: Fujino et al.1981). Therefore, the spectrum is complex, because the two MS signals arising from these sites are distinct but largely superimposed, as demonstrated by theoretical simulations (Wu et al. 1996b, 1999); two features occur on the low energy side of edge top B, and all the IMF features are clearly doubled.

The spectrum of the synthetic solid solution intermediate between forsterite and fayalite where Mg and Fe^{2+} are in the 1:1 compositional ratio ($FeMgSiO_4$ i.e., $Fo_{50}Fa_{50}$ or "hortonolite") strongly resembles that of model forsterite but it is definitively less resolved. This suggests that Mg and Fe^{2+} are disordered over the two octahedral sites of the structure, in agreement with the similarity of their cation radii and with the HT synthesis conditions of the investigated material (Kirfel, 1996; Wu et al. 1999).

A somewhat similar spectrum is shown by the model compound $LiMgPO_4$, which has the forsterite structure (Hanic et al. 1982), but it contains Mg in one only of its two octahedral sites, the second one being taken by Li. The Mg-centered octahedron is characterized by an unusually long Mg-O bond length (0.2105 nm) and a high degree of distortion (OAV = 119.9). The Mg-XANES spectrum strongly resembles the forsterite spectrum, but with notable differences arising from the completely different distributions of the bond energies. Indeed, the occurrence of a significant shoulder at ca. 1310.9 eV on the raising limb of the first line A, and the doublet nature of the edge-top at 1315.5 (B)

and 1317.4 (C) eV stands for expansion of the Mg-centered octahedron that is definitively greater than those observed in forsterite and "hortonolite", which implies also a significant deformation. It also confirms that the local environment is significantly altered by the complete segregation of Mg and Li in their respective octahedral sites.

Among the synthetic analogues of chain silicates, monoclinic $CaMgSi_2O_6$ (i.e., Di_{100} or diopside) is the best model, because not only it contains one single tetrahedral chain, but also it has only one type of octahedral chain composed of identical, edge-linked highly regular polyhedra that host Mg (M1: OAV = 17: Cameron et al. 1973). The Mg-XANES spectrum of model diopside, synthesized hydrothermally at fairly low P (1 Kbar) and T (600 °C), looks like the brucite spectrum, although diopside is anhydrous. Indeed, the spectrum shows three major peaks in the FMS region, the middle one (B) being the most intense and blurred weak peaks in the IMS region. However the IMS regions of the two compounds are different, and the brucite spectrum appears to be more ordered than the diopside one. The spectra recorded on synthetic diopsides by Henderson et al. (1992) and Li et al. (1997) are very similar in both feature energy and intensity to ours, thus providing support to the overall good quality of Mg-XANES spectra recorded at different facilities and confirming the present one.

Further confirmation comes from the Mg-XANES spectrum of a synthetic intermediate 1:1 solid solution between diopside and "niopside", the Ni-bearing analogue end member ($Di_{50}Ni_{50}$). This spectrum is similar to that of diopside despite the higher noise, with the only exception of feature A that appears to be strongly reduced in intensity. This indicates that the octahedral M1 site hosting Mg does not undergo modification because of its substitution by Ni, which is an isovalent cation equal in size, but that the substitution differentially affects the different features, and in particular decreases line A. This being the structure produced by the longest mean free path, it also implies that the entry of Ni decreases significantly the long-range order of the entire structure. By contrast, the spectral resolution does not decrease too much, despite the much lower Mg content of this sample.

Orthorhombic $Mg_2Si_2O_6$ (enstatite) has two octahedra that both host Mg; one is rather regular (M1: OAV= 27) and the other one very irregular (M2: OAV= 140: Sasaki et al. 1982). Nevertheless, the model compound displays a spectrum that is similar to that of diopside, consisting of three intense features in the FMS region, and four weak ones in the IMS region. Note, however, that the studied spectrum, which actually is that of an enstatite-ferrosilite solid solution ($En_{80}Fs_{20}$) where the magnesian component largely exceed the ferroan one, shows a small, but evident pre-edge (labeled P in Giuli et al. 2002 Fig. 9) that decreases in intensity with increasing the substitution of Mg^{2+} by Fe^{2+} on moving across the system towards ferrosilite ($En_{40}Fs_{60}$) i.e., in the compond where the ferroan component exceeds the magnesian one (cf. also Giuli et al.

2002).
Clinoamphiboles are the model compounds for double-chain polysilicates. Their spectra should not be expected to be simple, as they present a very high degree of complexity in their large M1, M2, M3 octahedral strip, where Mg can be hosted in as many as five octahedra that would be simultaneously excited and contribute to MS pathways and to the ensuing absorption. This precarious situation becomes even worse in orthoamphiboles, because the M4 sites located sideways to the M1, M2, M3 octahedral strip have NC = 6 too, thus bringing the total number of octahedra that can host Mg and simultaneously contribute to MS up to seven.
In our synthetic analogue of tremolite (Jenkins 1987) all the five octahedra of the strip are occupied by Mg (two M1, two M2 and one M3) and are all similar in both their Mg-O distances (ca. 0.206-0.208 nm) and OAVs (from 25 to 43). The contribution to the Mg-XANES spectrum due to excess Mg substituting for Ca in M4 can be disregarded as being minor (8-10% of the site occupancy: Jenkins 1987). The same, homogeneous octahedral strip distribution is true also for richterite, which could be synthesized with no such an excess Mg in M4 (Pawley et al. 1993; Della Ventura et al. 1999). The Mg-XANES spectra of both these amphiboles consist of three major features in the FMS region, followed by three minor ones in the IMS region (Fig. 1b), which are all identical in their energies. They only differ in the relative intensity of the A and C features, the former one being fairly weak in tremolite and strong in richterite, and vice versa.
Mg-hornblende was purposely synthesized with a 10 mol% excess of the Mg-cummingtonite component to obtain the highest amphibole yield possible, and in this way the full occupancy of the octahedral strip was also reached (Jenkins et al. 1997). However, IR and MAS NMR studies showed that only the two M1 octahedra are fully occupied by Mg, whereas the remaining Mg required to fill the strip is partly disordered together with the available $^{[6]}$Al over the two M2 sites and the unique M3 site (Hawthorne et al. 2000). The Mg-XANES spectrum reflects such a situation of structural

disorder very little, with an equal intensity of features A and C. As with the pyroxenes, all amphibole Mg-XANES spectra are remarkably similar to the brucite spectrum. However, this could be expected, because they all contain a cluster of three octahedra (M3+M1+M3) having their common corner O anion with a protruding H atom, as it does in brucite. Therefore, the Mg spectral shape of amphiboles of this kind may be explained through a sort of multiplicity of brucite clusters branching out from the double-chain silicate polymer.
A synthetic "Na-cummingtonite" grown directly in a high-T furnace at room P (G. Iezzi, personal communication) is the analogue we used to model amphiboles of that family. The synthetic sample is characterized by the complete occupancy of the octahedral strip with Mg and by the presence of one additional Mg atom in one of the two M4 octahedra in alternation with one Na,

a cation that also present in the A site to compensate for the charge deficit (cf. Tropper et al. 2000). Because of such an ordering, the space group is primitive and its is different from all cummingtonite spectra either occurring in nature or obtained from these by HT-HP treatments (Yang et al. 1998). The Mg-XANES spectrum strongly resembles the tremolite one, but for the IMS region, which is much smoother than those observed in all other amphiboles and fades rapidly away.
The trioctahedral 2:1 layer silicate structure has very much in common with the amphibole structure; indeed it may be described as a derivative of it due to an infinite multiplicity that makes the brucite layer continuous (Liebau 1983). As a result, the Mg-XANES spectrum of synthetic talc, which has Mg in two independent M sites both very similar in the average bond length (0.2071 nm) and in a fairly regular octahedral configuration (OAV = 29: Perdikatsis & Burzlaff 1981), not only strongly resembles the brucite spectrum, but also the magnesiohornblende one. The major difference is in the intensity of feature B, which, however, is never as strong as that to be seen in brucite, where it probably results from the even interaction of the six corner oxygens of the octahedra by as many hydrogens all contributing to increase the strength of the Mg-O bond, while in talc only two of such corners are bound to hydrogen. Note that both the talc and the brucite spectra contain a weak feature in the energy range intermediate between the FMS region and the IMS one that makes them distinctive from monoclinic amphiboles (but not from the orthorhombic ones). Among the synthetic analogues of the micas, we had only the brittle mica kinoshitalite available for Mg-XANES recording, and such a species is by no means representative for the entire group. Therefore, we refrain from commenting its spectrum now, but we point out again that it clearly resembles those of brucite viz. magnesiohornblende except for the B peak, which is much less intense owing to the fact that only two out of the six oxygens of the octahedral layer of 2:1 phyllosilicates undergo the electrostatic strain, albeit little, induced on them by the outer hydrogens.

3.5 Five-fold coordination

No synthetic phases having Mg^{2+} in the very rare five-fold coordination (effective radius 0.066 nm: Shannon 1976) were available to serve as model compounds.

3.6 Four-fold coordination (Fig. 1c)

Tetrahedral coordination is most unusual for Mg^{2+}, which is too large a cation for it (0.057 nm effective radius: Shannon 1976). Nevertheless, it has been determined in a small number of geologically notorious minerals, all of which

exhibit structural and physical oddities that made them interesting for synthesis studies of analogues not to be found in nature (ferrites).
Magnesium aluminate ($MgAl_2O_4$, spinel) has its Mg preferentially partitioned in one only type of very regular tetrahedral site (Q.E. = 1.0000 and AV = 0.2172: Smyth & Bish 1988; but TAV = 0 according to Fischer 1967) which joins via its opposite corners the Al-centered octahedral chains. However, in spite of its simple composition, even such a normal synthetic spinel displays a temperature-dependent cation ordering inversion whereby some Mg moves to the octahedral sites and a complementary amount of Al enters the tetrahedral sites (cf. Andreozzi et al. 2000). Our model spinel was synthesized at 800 °C in the pure composition and is stoichiometric; nevertheless, it shows an inversion degree of ca. 0.20 (F. Seifert, personal communication). Its Mg-XANES spectrum is indistinguishable from those of many other spinels used as XAFS reference for four-fold-coordinated Mg, but poorly characterized in their structural arrangement (e.g., Aritani et al., 1998, 2000; cf. Appendix 1). The spectrum exhibits a sharp and strong first line A at 1310.4 eV, followed by two strong features (B and C), and by a weak shoulder in the FMS region; the IMS region comprises several broad features before smearing out in the SS region.
Åkermanite is nearly the only one, thus the most typical, of the rare silicates where four-fold-coordinated Mg occurs. The Mg cation is located in an isolated very slightly distorted tetrahedron (Q.E. = 1.0010, AV = 5.8: Smyth & Bish 1988; but TAV = 24 according to Kimata & Ii 1981) that shares its four corners with as many Si-centered tetrahedra of the Si_2O_7 disilicate groups. The Mg-XANES spectrum is remarkably similar to that of spinel, but for the sharpness of each feature, which is worse. The first feature low-energy limb is overprinted by a shoulder that points out for the occurrence of the already known A' absorption feature. This may either be due to the distortion of the tetrahedral site, albeit little, or, possibly, to a contribution of the long-range disordered structure, which is well-known to be incommensurately modulated even in the ideal composition (Seifert et al. 1987; McConnell et al. 2000).
The Mg-XANES spectrum of a synthetic Mg-Si nitride ($MgSiN_2$) semiconductor was occasionally used as the reference standard for tetrahedral Mg absorption energy because it shows a very sharp first line (Wong et al. 1997, 1999). However, all FMS and IMS features that follow in the spectrum, including the edge top, are broad and unresolved, presumably because several polymorphs coexist in that semiconductor (Bruls et al. 2000).

3.7 Minerals

Minerals differ from model compounds, including their own synthetic analogues, by not being exactly on composition and for presenting (usually, but

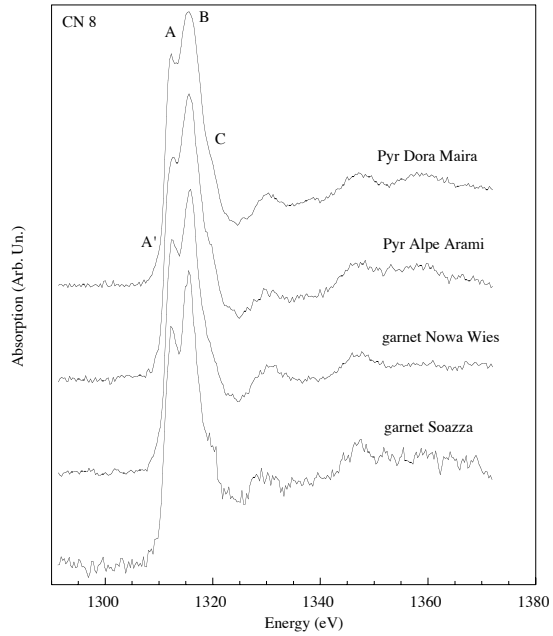

Figure 2a: *Mg K-edge XANES spectra of minerals with 8-fold coordination.*

not always) a much greater number of defects. As a result, they occasionally show deviations from the expected crystal structure due to the strain induced by the atoms substituting for those present in the ideal composition. The XAS spectra are then expected to show deviations from the model ones and these (presumably) are greatest the largest is the degree of chemical substitution for the selected element (Mg, in our case) within the various possible structural environments of the probed structure.

3.8 Twelve-fold coordination

Magnesium metal reacts readily so as to burn in an oxygen-rich atmosphere; therefore it is not a mineral, having never been found in nature so far.

3.9 Eight-fold coordination (Fig. 2a).

Natural pyrope from near Brossasco, in an area of the Dora-Maira massif the VHP formation of which is warranted by the presence of coesite inclusions (Chopin 1984), deviates very little in composition from end member pyrope

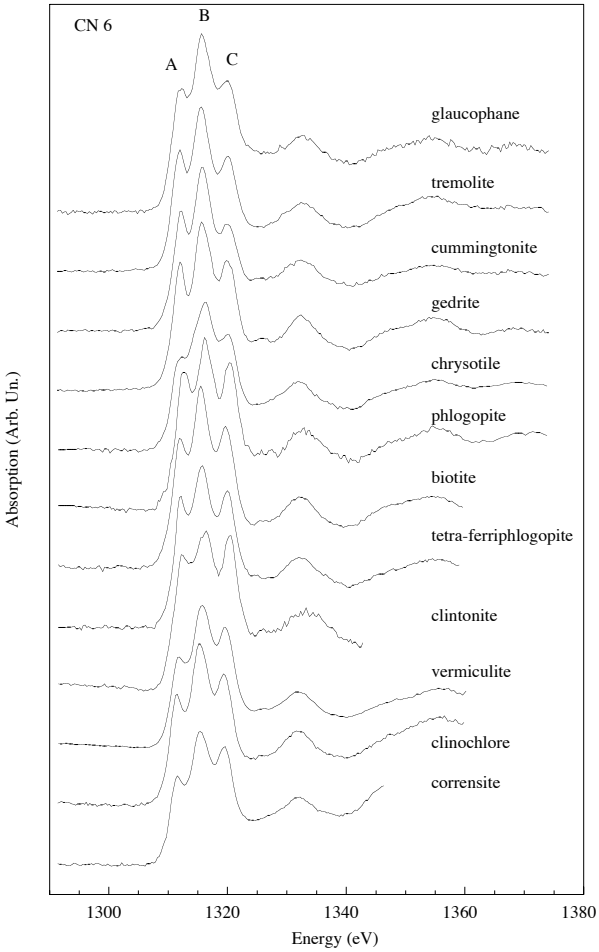

Figure 2b(1): *Mg K-edge XANES spectra of minerals with 6-fold coordination.*

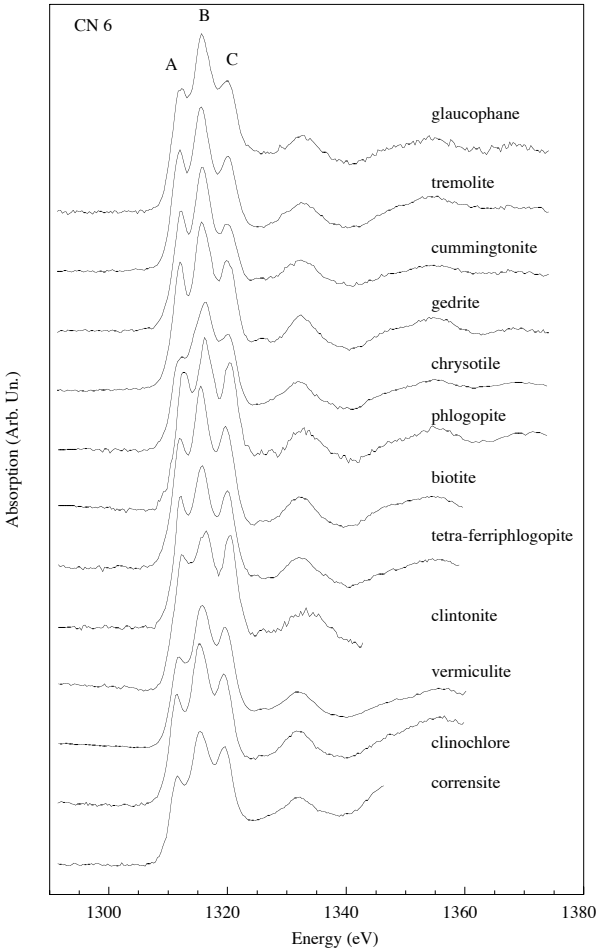

Figure 2b(2): *Mg K-edge XANES spectra of minerals with 6-fold coordination.*

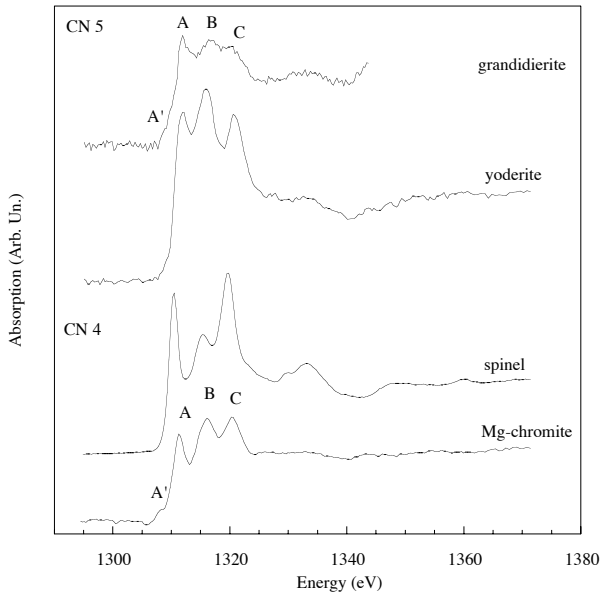

Figure 2c: *Mg K-edge XANES spectra of minerals with 5- and 4-fold coordination.*

(X = $Mg_{2.92}Fe_{0.05}Ca_{0.03}$ apfu: G. Chiari, personal communication). Consequently, it shows a XANES spectrum that is practically identical to that of model pyrope (Fig. 1a).
With increasing substitution of Mg by other cations, as in the pyrope from the Alpe Arami peridotite or in the pyrope of unknown origin studied by Li et al. (1999), features A', A, and B do not change, while C at 1319.8 eV is better resolved, and all the following ones become smooth and broad. Clearly, such a change in composition towards other pyralspite end members, as grossular and almandine, creates increasing disorder in the X site (Ungaretti et al. 1995), that results into a lesser resolution of the IMS features. Thus, it is this region of the spectrum that points out the spectroscopic signature of the intervening structural irregularity.
Such an X-site structural disorder is evidenced even better by the Mg-XANES spectra of two pyrope-almandine-grossular ternary garnets from metamorphic rocks equilibrated under eclogite facies conditions (Nowa Wies in the regional regime and Soazza in the subduction regime, respectively), where Mg^{2+} is diluted in an X site mainly containing Fe^{2+}+Ca^{2+}. Crystal structure refinements have shown (Ungaretti et al. 1995 Fig. 5) that substitutions of Fe^{2+} viz. Ca^{2+} for Mg modify the coordinates of the oxygen anions surrounding the X cation in different ways i.e., Fe^{2+} by stretching the O cage mainly along x, and Ca^{2+} along y. Consequently, these complex positional changes of the nearest neighbors to Mg reflect onto the FMS region of the Mg-XANES spectra, where all features are still strong, but blurred, not so much owing to the smaller number of Mg atoms probed, but for their almost stochastic distribution. However, it is noteworthy that, at a Mg content as low as 5.5 at% as in the Soazza garnet, the signal to noise ratio of the Mg-XANES spectrum is still meaningful and fairly well resolved.

3.10 Six-fold coordination - Figs. 2b(1) and 2b(2).

We have found no natural periclase, sellaite or chloromagnesite either pure enough or in sufficient quantity to try making a comparison with synthetic model compounds, nor does stable $MgBr_2$ occur in nature. Thus, the first spectrum of six-fold coordinated Mg in minerals we can describe here is that of brucite.
The Mg-XANES spectrum of a needle-like brucite ("nemalite") from Asbestos (Canada) is practically identical to that of synthetic model brucite, which had been recorded on a powder, made up of very fine scales (cp. Fig. 2b(1) with Fig. 1b). This is a confirmation that the procedure we followed in preparing our probed materials minimizes the experimental problems inherent in the preferred orientation of certain samples (Pettifer 1990), and allows us to present here reproducible reference spectra even for texturally difficult minerals.

Magnesite has its Mg located in a very regular octahedron (OAV = 3.55: Effenberger et al. 1981; Q.E. = 1.0010: Ross 1997), which shares each one of its six corner O with as many different Mg and C atoms. Thus, the overall structure can be described in terms of layers of corner-sharing Mg-centered octahedra alternating with planes of C-centered triangular groups. The Mg-XANES spectrum shows a very intense feature B in between two less intense ones, the first one (A at 1310.4 eV) being sharp, but weak and the third one (C) intense, but not well resolved, or actually partly covering a feature B'. A sequence of fairly intense but broad features follows in the IMS region, which eventually fades out into the SS regime.
Dolomite has its Mg at the center of an octahedral site that is even more regular than the corresponding one in magnesite (OAV = 3.1: Reeder 1983; Q.E. = 1.0009: Ross & Reeder 1992). From the structural standpoint, the major changes inevitably resulting from the presence of alternating layers of large octahedra, where Ca is segregated because of its size, and small Mg-centered octahedra are mostly transferred to the carbonate groups located in between, which undergo a rotation (ca. 6.5°: Ross & Reeder 1992) around the threefold axis where they are closest to the Ca-centered layers so as to accommodate their increased thickness; furthermore the carbonate groups acquire a very slight "aplanarity" (0.0017 nm: Reeder & Markgraf 1986), as the C atom moves back from its three O neighbors attracted by Ca. All this structural rearrangement reflects onto the Mg-XANES spectrum by generating a pattern of features decidedly different from that of magnesite: the first line A is still sharp and weak, but it is followed on the raising limb of the intense edge top B by a marked shoulder A'. Lines C and B' present in magnesite disappear altogether. Furthermore, the IMS region shows a sequence of features additional to those observed in magnesite, although weaker than these because of the halved Mg content of dolomite. On the whole, a comparison between the dolomite and magnesite spectra shows that on the long range the magnesite structure is more complex, whereas the dolomite one it is more complex on the short range.
Monticellite is the simplest Mg-bearing monosilicate with the orthorhombic forsterite structure, as the great ionic radius difference between Ca and Mg again constrains all its Mg to be segregated into one only octahedral site that is both rather complex in composition ($Mg_{.853}Fe_{.118}Mn_{.029}$: Haynes et al. 2003) and distorted (OAV = 100: Pilati et al. 1995). The Mg-XANES spectrum shows four major features essentially at the same energies as those of model compounds forsterite and "hortonolite", but all definitively broader than these. The second feature is the edge top and is skew on its high-energy side because of a shoulder, in marked contrast to the edge top of forsterite that shows shoulders on the low-energy side. Another difference is in the IMS region, the few features of which are very broad but certainly unique, in contrast with the corresponding features of all the forsterites that follow, which are always double.

The extremely pure forsterite from Afghanistan (Pilati et al. 1990) has a Mg-XANES spectrum practically indistinguishable from that of synthetic model forsterite (Fig. 1b). By contrast, other natural olivines that deviate more in composition from the end member show either broadening of their spectra or enhancing of certain fine structures that point out for changes in their local order, this being sometimes independent upon chemical composition. E.g., the Alpe Arami forsterite occurs in a garnet peridotite possibly of very deep mantle origin (Green et al. 1997) or, in any case, equilibrated at great depth (Risold et al. 2001). This olivine is compositionally nearly identical to that occurring in a spinel lherzolite nodule within the Monti Lessini basalts (Morten & Bondi 1981), which is also of mantle origin, but equilibrated at a much shallower level. Yet, there is a substantial difference between these two spectra (Fig. 2b): Alpe Arami has peaks B and C well resolved and no evident peak A, whereas Lessini is substantially identical to model forsterite in the FMS region, but for peak C that tends to disappear. The IMS regions of both samples are broader that in the model one. This is also the case with the Finero sample, a rather pure forsterite (Forbes et al. 1977-78) that occurs in a phlogopite peridotite also presumed of mantle origin, but re-equilibrated under regional metamorphic conditions during at least two pre-Alpine cycles (Lu et al. 1997) during which it even had to withstand metasomatism. The Finero Mg-XANES spectrum is indistinguishable from that of the Afghanistan one, but for a small energy shift of edge top B.

The Monroe Township (USA) "hortonolite", an olivine approaching the fayalite end member, shows an excellent Mg-XANES spectrum, however not very similar to that of the synthetic equivalent model compound. However, the Mg content is not yet so low as to significantly decrease the signal to noise nor to conceal the fine structures, so that the spectrum enhances the ordered character of the natural sample in contrast to the disorder of the synthetic one, which had been quenched from high temperature (1400 °C).

A high internal order is also the case with the Gardiner Complex, Greenland, titanian hydro-clinohumite, despite the overall structure complexity of that mineral group where as many as five independent octahedral M sites are present (cf. Ferraris et al. 2000; Friedrich et al. 2001). They are all occupied by Mg (and Fe^{2+}) in nearly the same amounts, but for the M3 site, where Mg is minor because this octahedron is the preferred site for Ti, owing to its smaller average size (0.208 nm) and lower OAV (= 53). Mg dominates in the remaining four octahedra, which are similar in pairs for average size but differ in OAV (= 77 for $M2_5$, 97 for $M2_6$, and ca. 107 for $M1_c$ and $M1_n$). It is indeed astonishing that this complex interplay of MS paths originating from different structural environments and progressing out of phase does not reflect negatively onto the observed Mg-XANES spectrum, which is well resolved and similar to that of a pure forsterite even in the occurrence of a small E feature at an energy in between the FMS and IMS regions.

Our natural diopside from Canada (Px-1), albeit slightly impure in composition, has a Mg-XANES spectrum that is even better resolved than that of model diopside. We interpret this as due to the very high long-range structural regularity of this metamorphic sample in contrast to the disorder inherent in the model synthetic one. Three features in the FMS region dominate the Mg-XANES spectrum, whereas those in the IMS region are weak to the point of being almost indistinct. However, the natural diopside recorded by Li et al. (1999) displays these IMS features with characteristics compatible with those occurring in model diopside, and so does the spectrum of a natural clinopyroxene stated to be of diopside composition (but, more properly, an augite: cf. Mottana et al. 1999), displayed by Ildefonse et al. (1995) and theoretically recalculated by Cabaret et al. (1998).

The same three major FMS features occur in omphacites, irrespectively on whether they exhibit $P2/n$ or $C2/c$ symmetry. However, these FMS spectral features become less and less intense and resolved with increasing substitution of Mg by Al, whereas the IMS ones increase. Furthermore, at a closer inspection, the Biella P-omphacite spectrum reveals a series of fine details (e.g., B' at 1314.3 eV) that can be decomposed into two sets of signals arising from Mg atoms located in two octahedral sites distinct for both average size (1.932 and 2.070 nm, respectively) and OAV (47 and 17, respectively). By contrast, C-omphacite has one only type of octahedron that is intermediate in average size (1.967 nm) between the two ones inherent in the $P2/n$ symmetry (Mottana et al. 1999, and in preparation), where the MS signals arising from Mg propagate on phase. Consequently, the Sörpollen omphacite Mg-XANES spectrum is sharp and comparatively strong, in spite of the sample very low Mg content (2.5 at%) and signal to noise ratio.

The simplest structural arrangement among amphiboles occurs in glaucophane. Its two smallest M2 octahedra are invariably centered by the two $^{[6]}$Al ($+Fe^{3+}$) atoms, thus pushing the three Mg ($+Fe^{2+}$) atoms into the two large, fairly distorted M1 sites (OAV = 79) as well as into the unique, largest and even more distorted M3 site (OAV = 85: Comodi et al. 1991). In such a three-site M1-M3-M1 fragment, each OH anion is bound by three Mg and interacts with them without having its bond energy reduced by cations outside the strip, as the A cavity is empty. The Mg-XANES spectrum (Fig. 2b(2)) differs from those of model amphiboles (Fig. 1b) not only because the higher noise due to the reduced Mg content of our sample (actually, a crossite that contains Fe in both oxidation states), but also for it shows the C feature definitively stronger than the A feature.

The Mg-XANES spectrum of an extremely pure, F-free tremolite from unknown locality with the octahedral strip consisting entirely of Mg (Welch & Pawley 1991) is identical to the model tremolite one.

Our $C2/m$ Mg- and Mn-rich cummingtonite has an Mg-XANES spectrum very similar to that of synthetic model richterite, despite its complex composition

and the large number of octahedra that may contain substantial Mg: seven (two M4, two M1, two M2, one M3) i.e., the maximum among all minerals investigated here (cf. Ghose & Yang 1987). All octahedral sites are fairly regular (OAV from 30 to 45), but the M4 sites i.e., those concentrating the little Ca and Fe cations, which are so large and severely distorted (OAV = 450) as to suggest that their actual coordination should be best indicated as being 4+1+1 (Yang et al. 1998). Contrary to our model Na-cummingtonite, there is nothing in the A cavity that may interfere with the Mg-OH bond at the very center of the 7-member octahedral strip. Consequently, the Mg-XANES spectrum of the Moravice cummingtonite is nearly identical to that of richterite in the FMS region, whereas the IMS region, although very weak, hints for the possible doubling of most features.

By contrast, the orthoamphibole anthophyllite hosts Mg preferentially in five sites of its 7-membered octahedral strip, being the two regular M2 sites (OAV = 18) partitioning the Al (+Fe^{3+}) present. The inside M1-M3-M1 three-site fragment concentrates most but not all Mg and is moderately distorted (OAV = 54 and 71), while the two outer M4 sites, where Fe^{2+} preferentially is, are very distorted (OAV = 202: Papike & Ross 1970), although not to the point of cummingtonite. The Mg-XANES spectrum of our gedrite from the type locality (Debat et al. 1971), notwithstanding the orthorhombic symmetry, closely resembles that of monoclinic glaucophane, however with a better resolution for the FMS features, and with at least one additional well-resolved, weak feature in the transition zone between the FMS and IMS regions, so that the overall spectrum has some similarity with that of talc.

As the representative for trioctahedral 1:1 layer silicates (Wicks & O'Hanley 1988), we recorded the Mg-XANES spectrum of a clinochrysotile having a platy habit that made us to morphologically mistake it for lizardite in spite of the outcrop conditions (cf. O'Hanley & Wicks 1995). Indeed, both minerals contain one sheet of octahedra (Wicks & Whittaker 1975), all identical and sharing with the tetrahedral sheet their 2 O + 1 OH proximal anions, while projecting their distal 3 OH into the interlayer. In chrysotiles curling the entire 1:1 layer solves the ensuing electrostatic strain, so that hydrogen bonding between successive layers is inhibited. In other words, the great inhomogeneity in bond energy does not translate into a substantial site distortion (OAV ca. 50: Whittaker 1956); rather it is being compensated by a differential planar stretching that induces curling into cylindrical rolls and making it possible for the mineral to develop its morphology according to fibers. Therefore, the Mg-XANES spectrum of our clinochrysotile is nearly identical to the lizardite spectrum recorded by Li et al. (1999), and both spectra strongly resemble that of brucite, but for a different peak intensity ratio.

Most trioctahedral members of the mica group are rich in Mg in their octahedral sites, but many of them also contain Fe^{2+} and other divalent cations, as well as some trivalent ones including Fe^{3+}. All these cations proxy for Mg in

the octahedra, so that only few natural specimens are known that are compositionally close to the Mg end members.
Phlogopite from Franklin (USA) practically contains only Mg, which is distributed over three translationally independent cation sites, one of them (M1) *trans*-coordinated by OH (and/or F, Cl) and the other two (M2) *cis*-coordinated and related by a mirror plane (Brigatti & Guggenheim 2002). Although structurally different, the M1 and M2 sites are nearly identical in both their moderate polyhedral distortions (OAV = 38.5 and 39.7, respectively: Hazen & Burnham 1973) and mean bond lengths (0.2065 nm: Brigatti & Guggenheim 2002 Table 1a n. 67). The phlogopite Mg-XANES spectrum consists of three features in the FMS region, which strongly resemble those occurring in talc in their width, but do not in their relative intensity, although the central feature (B) is confirmed to be the highest. The IMS region consists of several smooth and resolved, but rather broad bands declining in intensity on going to the SS region.
Note that the powder spectrum of phlogopite (Fig. 2b), as all the mica and layer silicate spectra (same figure) as well as most spectra of other layer-structured minerals, results from convolution and averaging of the contributions arising from numberless particles which all lie flat on their cleavage plane ($\approx\perp$ **c**), but are disordered in their **a** and **b** axis directions. This shows up when orientation-dependent spectra are recorded on single flakes that are progressively rotated against the horizontally-polarized synchrotron radiation: the relative intensities of the three FMS features show dramatic changes (Mottana et al. 2002 Fig. 9), with the middle one B always being the most intense one, but with A and C interchanging their intensities with increasing the rotation. This confirms the already mentioned need for a careful preparation of mineral powders before recording XANES spectra.
Indeed, this position-dependent effect may significantly interfere with the spectral changes due to the substitution of Mg by Fe^{2+} i.e., the changes that occur along the phlogopite-annite join. A biotite (actually, ferroan phlogopite) from Euganean Hills displays considerable structural differences in its octahedral sheet with respect to pure phlogopite (bond length M1 = 0.2083 nm, M2 = 0.2064; OAV M1 = 59.3, M2 = 59.0: Brigatti & Guggenheim 2002, Table 1a, n. 17). The spectrum has feature B considerably stronger than both A and C, thus strongly recalling the spectrum of brucite, although the octahedral sheet of which is entirely consisting of Mg.
Furthermore, the Tapira tetra-ferriphlogopite does not differ much from phlogopite as for its octahedral sheet occupancy, but it is very peculiar for having Fe^{3+} replacing Al in the tetrahedral layer. In order to match the increased spacing of this, the octahedral bond length increases considerably (0.2088 nm: Brigatti & Guggenheim 2002 Table 1a, n. 33). Nevertheless, the ensuing Mg-XANES spectrum is very similar to that of phlogopite, although with some intensity differences in the FMS features that are to be related not so much

to the insignificant octahedral layer compositional difference, rather to a near-next-neighbor effect arising from the Fe^{3+} located in the tetrahedral layer.
Clintonite-1M from Lago della Vacca is a brittle mica with an almost complete Si-(Al+Fe^{3+}) ordering in the tetrahedral sheet. The octahedral sheet has three independent sites (Joswig et al. 1986): M1, in the *trans*-setting, is a little larger (0.2046 nm) and more distorted (OAV = 38) than the two equivalent M2, in *cis*-orientation (0.2020 nm and 34, respectively). Fe^{2+} preferentially substitutes for Mg in M1, while Al does in M2, according to a trend that occurs also in the locally related phlogopite (cf. Alietti et al. 1997). Indeed, the Mg-XANES of clintonite shows again three FMS features as that of phlogopite, however with some fine differences, particularly in the A and B features that appear to be less resolved. In particular, edge top B is significantly broader than the corresponding ones in all micas recorded so far, and possibly double. Moreover, an additional, very weak feature occurs in the range of energy intermediate between the FMS and IMS regions.
Vermiculite is a trioctahedral layer silicate with a long-range structure that is closely related to that of talc, but with heterovalent substitutions which create charge imbalance in the 2:1 layer, thus requiring the interlayer space to be filled with water molecules plus some exchangeable cations that are distributed at random (Mathieson 1958). Mg occurs mostly in the octahedral sheet of the 2:1 layer, but also, subordinately, in the interlayer (de la Calle & Suquet 1988). We recorded the spectrum of a well-ordered vermiculite, making sure that no significant Mg other than that at the center of the octahedral sheet is present (Serratosa & Sanz 1985). Indeed, the Mg-XANES spectrum displays the same features as talc, including the small one at energy intermediate between the FMS and IMS regions, but with different relative intensities, thus suggesting a different type of layer stacking disorder (de la Calle & Suquet 1988).
Trioctahedral smectites do not differ from micas in the configuration of their octahedral sheet, since they also show one M1 site in *trans*-orientation and two M2 sites in *cis*-orientation; consequently, they also show the same types of distortion by which the octahedral sheet matches the tetrahedral sheets. Most differences lay in the interlayer, which may be exceedingly complex in smectites as a result of the need of bonding the nearby undercharged tetrahedral layers, to be compensated either by cations or by positively charged ionic solutions. In turn, this induces, or at least favors different stacking modes, with the result that smectites may exhibit a large variety of structures with different technological properties.
Montmorillonite has a fairly regular 2:1 dioctahedral layer where some Mg and Fe^{2+} cations substitute for Al and Fe^{3+} in the octahedral sheet, thus creating a charge deficit that is compensated by Ca^{2+} or alkaline cations dispersed within a network of loosely bound water molecules. The easy removal and adsorption of these makes the lattice expandable. The Mg of the octahedral sheet is very limited in amount, but it may cluster in such a way as to originate domains

of real "Mg-montmorillonite". This is probably the case with the montmorillonite of unknown origin recorded by Li et al. (1999) that shows such a good Mg-XANES spectrum. Indeed, the spectrum of our Campotamaso montmorillonite (Brigatti et al. 2000), which is rather iron-rich, is so poor as not to be worth plotting. Yet, it is consistent in its general pattern with Li et al.'s (1999) spectrum and both closely resemble that of talc.

The crystal-chemistry of Mg in the chlorite group is complicated with respect to that of 2:1 trioctahedral micas by having an octahedral interlayer that regularly alternates with the mica layer, thus creating a new series of potential Mg sites. This interlayer sheet may be compositionally similar to the M sheet so that, when both are centered by divalent cations, as in most species, one can speak of tri-trioctahedral chlorites (Bailey 1988) having a brucite-like (B) sheet and a talc-like (2:1) layer (Welch et al. 1995). Nevertheless, the two sets of octahedra always differ in their next-nearest neighbors, which are 6 OH for the B sheet and 4 O + 2 OH for the talc-like sheet, the OH dipole being always perpendicular to the sheets.

Clinochlore is the Mg-dominant member of the tri-trioctahedral chlorite subgroup, and indeed our Borgotaro sample is close to the theoretical Mg_4Al_1 octahedral composition, but for minor substitutions of iron for both Mg and Al (Brigatti et al. 2000). The talc-like sheet contains three octahedral sites nearly identical in size and OAV (0.2078 nm and ca. 30: Joswig & Fuess 1990), but of two distinct types, because Al is entirely segregated at M1 in *trans*-orientation, and Mg is ordered in the two M2 in *cis*-orientation. The brucite-like sheet also contains octahedral sites of two types i.e., two M3 and one M4, both matching the talc-sites ones in length, but somewhat more distorted (OAV ca. 50) owing to the directional hydrogen bonds they have. Thus, they show a tendency to partial ordering, in the sense that every octahedral Al is surrounded by 6 Mg octahedra (Welch et al. 1995). Despite the complex octahedral site configuration, the Mg-XANES spectrum of clinochlore is practically identical to the biotite one.

The corrensite structure could never be determined accurately, so far, but it is believed (Reynolds 1988) to consist of a perfectly ordered interstratification of chlorite-like trioctahedral sheets with either vermiculite-like sheets ("high-charge" corrensite) or trioctahedral smectite-like sheets ("low-charge" corrensite). Thus, the number of octahedra hosting Mg is large, and their sizes and distortions wide, as they both depend on those of the constituent layers. In particular, a "high-charge" corrensite such as ours from Borgotaro (Brigatti et al. 2000) should contain Mg in all four octahedral sites (Johnson 1964): they are likely to be well-ordered, because the Mg-XANES spectrum shows three major features in the FMS region that are just as sharp and well-resolved as those in the clinochlore spectrum.

3.11 Five-fold coordination (Fig. 2c).

Five-fold coordination is very unusual for Mg, as it is for most cations, but it was determined, as a single distorted trigonal bipyramidal site, in the borosilicate grandidierite by SC-XRD (Stephenson & Moore 1966) and confirmed by NMR (MacKenzie & Meinhold 1997). A further, indirect confirmation is given by the K-edge spectrum of Fe^{2+}, which substitutes for Mg in many natural samples (Farges 2001). The Mg-XANES spectrum reported by Li et al. (1999), recorded at UVSOR on a sample of unspecified origin, is superior to ours, taken at SSRL on a sample from Madagascar, for both resolution and definition of the observed features. However, our spectrum exhibits a faint first shoulder A' hinting for the possible deformation of the site owing to the concomitant presence of Fe, albeit little. Indeed, Farges (2001) warns for possible extra contributions to the pre-edge of his Fe-XANES spectra that are related to even trace amounts of Fe^{3+} occurring in any site i.e., substituting for Mg as well as Al. Nevertheless, in Li et al.'s (1999) paper we note that the first absorption line energy is given as 1310.9 eV i.e., with no shift with respect to compounds where Mg is in six-fold coordination. Moreover Li et al.'s (1999 Fig. 2) decomposition of the spectrum, using a Gaussian peak fit after subtraction of the edge background via an arctangent, evidences no faint first peak as ours, but a peak (A', according to them) intermediate between A and B and additional to those occurring in their spectra of pyrope, diopside and spinel standards. Such an A' peak is not evident in our spectrum.
Yoderite is a rare case of mineral with mixed coordination, since both Mg and Al (always together with a small but essential amount of Fe^{3+}: Fockenberg & Schreyer 1991) occur in octahedral, fairly regular sites as well as in two types of highly irregular trigonal-bypiramidal sites (Higgins et al. 1982). The yoderite Mg-XANES spectrum was recorded at UVSOR by Li et al. (1999) and deconvoluted by using the grandidierite spectrum as reference for $^{[5]}$Mg and the montmorillonite spectrum for $^{[6]}$Mg. They could confirm the occurrence of Mg in both coordination sites, thus paving the way to their following quantitative estimate of Mg distribution among the structural sites of unknown samples (Li et al. 1999 Fig. 4). Our sample, although from the same area, has a composition slightly richer in Fe (presumably Fe^{3+}) and contains a little Ca; thus Mg is distributed over the five-fold and six-fold sites in an uneven way. This reflects not so much onto the FMS region, which is strong and well resolved, but onto the IMS region of the Mg-XANES spectrum, which only shows a series of poorly resolved features.

3.12 Four-fold coordination (Fig. 2c).

The Mg-XANES spectrum of a natural spinel of unknown inversion degree and chemical composition was recorded by Li et al. (1999 Fig. 2), and appears to

be the same as that of our own spinel from Burma, which is not only highly ordered, as most natural spinels are (Schmocker & Waldner 1976), but also very pure in composition, as it contains only traces of Ni and Zn. As a matter of fact, all natural spinel spectra are practically identical to the spectra of anyone of the many synthetic spinels recorded so far (Appendix 1).
Magnesiochromite shows the normal spinel crystal structure and contains Mg^{2+} is in a highly regular four-fold coordinated site (Q.E. = 1.000: Hill et al. 1979; AV = 0.2172: Smyth & Bish 1988), thus giving rise to a well-resolved absorption edge at 1311.3 eV. The spectrum exhibits a noticeable first feature A', presumably because some of the iron present is either Fe^{3+} substituting for Cr and Al or Fe^{2+} substituting for Mg. The magnesiochromite spectrum is less suitable than the spinel one as reference for four-fold coordination, because it shows a significant noise. Indeed, the investigated mineral significantly deviates in composition from the ideal formula, and Fe^{2+} substituting for Mg induces positional disorder, reduces the intensity of the FMS features, broadens them and further decreases the signal to noise ratio in the IMS region to the point of flattening it entirely. However, magnesiochromite cannot be disregarded, as its Mg-O bond distance is significantly longer than the spinel distance: from their comparison, useful information on four-fold-coordinated Mg behavior can be derived.

4 Discussion

Three effects concur in determining shape and energy of the individual absorption features and in turn these, when taken together, determine the overall appearance of a K-edge XANES spectrum:
1. The size of the absorber atom in its excited state; in the case of Mg, which is divalent and never undergoes changes in oxidation state, size depends upon coordination and covalent fraction of the predominantly ionic Mg-to-anion bond; the Mg cation size increases from 0.057 nm for NC = 4, to 0.066 for NC = 5, to 0.0720 for NC = 6, up to 0.089 for NC = 8, to become 0.162 nm for Mg^0 in the neutral atomic state having NC = 12; consequently, the Mg-to-anion bond also increases in length, from 0.1876-0.1966 nm when in the tetrahedral geometry up to a maximum 0.2203-0.2705 nm in the cubic one, the adjustments due to bond strength being minor (in the order of 10% or less).
2. The strength of the bond in which the cation is involved depends upon the type and distribution of the ligands, as it is a function mostly of the electronegativity difference ($\Delta\chi$) between the ions involved in the bond; therefore, when these are Mg^{2+} (χ = 1.23) and O^{2-} (χ = 3.50), the bond is, on average, 75% ionic in character (Lewis' rule). However, even within the same coordination polyhedron the bond strength may show variations because the forces acting on every individual corner anion from outside the polyhedron are

different. Such forces are induced by cations attracting from the outside the Mg-bound anions so as to compensate their residual negative charge. A most conspicuous case occurs in the [Mg-O] octahedron when some of its corner oxygens are bound to an outside H by hydrogen bond: they turn to be hydroxyls and behave as such, from both the electrostatic and the stereochemical point of view. Another significant case is when different outside cations are bound to each different corner of the octahedron (where Mg ideally has the cubic $m3m$ point symmetry): their differential attractive forces induce deformation to the Mg-centered site that may lead as far as to the triclinic 1 point symmetry.

3. The overall crystal field effect i.e., the contributions of the electric fields acting on the photoabsorber atom that arise from its next-nearest neighbors of definite symmetry up to the n^{th} shell (theoretically up to infinite distance, but in practice reaching as far out as the 6^{th}-7^{th} shell: Wu et al. 1996b, 1999; Cabaret et al 1998). The underlying principle of X-ray absorption spectroscopy, according to the one-electron multiple-scattering theory (Dehmer & Dill 1975, 1976; Kutzler et al. 1980; Natoli et al. 1990, 2003) that, for the XANES portion of the XAS spectrum, has successfully superseded the single-scattering theory (Sayers et al. 1970, 1971), is that all possible multiple pathways among the atoms present in the probed cluster are touched and activated by the photoelectron emitted by the absorber. This is the peculiarity characterizing this type of spectroscopy; it implies that the entire structure over a certain mean free path is involved in the absorption process, and not only the nearest (local) environment. Unfortunately, the contribution of the crystal field is poorly known, as it varies with direction in an as yet not well-defined manner (cf. Burns 1993).

With these preliminary ideas in mind we can now proceed with discussing one after the other the results in our experimental data set (cf. Figs. 1-2).

First of all, it is clear that the energy of the edge threshold i.e., of the inflection point that records in the spectrum the beginning of the absorption process, increases with coordination. In pure Mg metal i.e., in Mg^0 in anticuboctahedral coordination (NC = 12), this energy measures the electron binding energy relative to the Fermi level in the atom, and is 1303.0 eV (Fuggle & Mårtensson 1980). However, when Mg is bound by O, as in most model compounds, the threshold energy decreases dramatically, the more so the smaller is the number of O atoms that surround Mg i.e., the smaller the Mg CN. The threshold energy can be determined easily as the energy of the maximum point in the derivative spectrum: in this way Aritani et al. (2000) determined it to be, on average, as low as 1299.0 eV for $^{[8]}$Mg, 1296.9 eV for $^{[6]}$Mg, and 1294.5 eV for $^{[4]}$Mg (but see our following *caveat* for the absolute values of these energies).

Secondly, our systematic study confirms that there is a shift with coordination in the first absorption line energy related to the transition from $1s$ to empty bound states having $3p$ character as it had been revealed by previous studies (2 eV: Ildefonse et al. 1995; ca. 4 eV: Wong et al. 1997, 1999; 2.5 eV: Li et

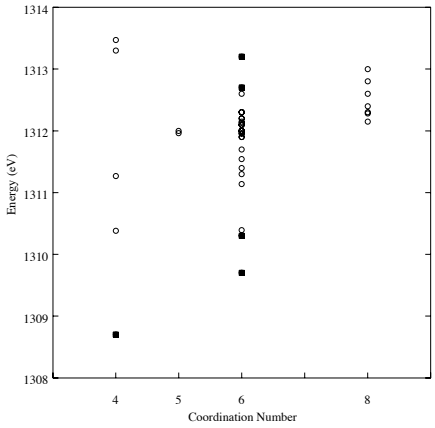

Figure 3: *Coordination-dependence of the first intense absorption line of Mg K-edge XANES spectra.*

al. 1999). In our samples we indeed measure an average positive shift, however in a very irregular way (Fig. 3). Indeed, the spread of the measured energy positions corresponding to each coordination is very high, not only when all spectra are considered, but also when our own spectra (which were homogeneously recorded albeit over a period of some years) are taken in consideration. Obviously, a meaning for such a measured variation has to be sought in structural factors inherent the various samples and not in the experimental method. Such structural factors are, mostly, related to differential characters related to the Mg-to-ligand bond even for the same coordination. Therefore, the measured positive energy shift is indeed discrete, as it occurs at steps (cf. Ildefonse et al. 1995), but it is not linear as previously believed. Coordination indeed plays a role, but it is not the dominating factor and, as it clearly appears for CN = 6, factors such as bond length and local field energy need to be taken into consideration.

Thirdly, in several spectra, whatever the Mg CN is, the first absorption line that is generated by the transition from $1s$ to the just mentioned empty $3p$ states is preceded by a small feature (A') that often almost disappears under its raising edge or, most commonly, appears as a shoulder that overlays it. For structures containing six- and eight-fold coordinated polyhedra, whenever Mg

is partly substituted by a transition element (Ti, Cr, Fe, etc.) that deforms the relevant polyhedron, this feature could be interpreted as indication of $1s \rightarrow d$ transitions that are forbidden in a regular octahedron and cube, but that become allowed because of the non-centrosymmetrical orbital character even of a non-transition atom when it is located in a deformed polyhedron (Roe et al. 1984). In other words, it may be interpreted as being due either to deformation of the first atomic cage where the photoelectron ejected by the Mg absorber undergoes its first multiple scattering interactions, following a hypothesis originally put forth and tested for $^{[6]}$Ti in minerals by Waychunas (1987). However, this interpretation cannot be extended to structures where Mg is in four-fold coordination, because the polyhedron is intrinsically non-centrosymmetrical. Indeed, in some of these compounds (e.g., spinel and $MgSiN_2$), the first absorption feature may be exceedingly strong. For them the best interpretation is the nature of exciton for that peak. By contrast, for åkermanite and the minerals with CN = 5 where Mg is in a strongly deformed site, an alternative interpretation is that feature A' may be due to extra transitions towards $3p$ empty states mixed with the empty density states of Mg, which only arise when the contributions from far-away atoms are significant. This interpretation follows the results of calculations performed *ab initio* on another atom that is not a transition element: Al in garnet (Wu et al. 1996c). In that case a feature A' was detected that arose not only in the presence of transition atoms like Fe, but also for a non-transition one like Ca, which has a large number of unfilled outer electronic states; furthermore feature A' occurred when large clusters, extending to the 4^{th} to 5^{th} shall around the photoabsorber, were included in the calculations, thus implying that not so much site distortion from centrosymmetry, but the existence of core-transitions sensitive of long-range effects are responsible for the such a feature. This finding implies also that the final state reached in the core transitions is not really a simple atomic (or molecular) state, but it is sensitive to long-range order effects too. Therefore, in natural minerals, the intensity of feature A' should increase with increasing the substitution of Mg with other cations i.e., Fe^{2+} and Ca, as in garnets. As a matter of fact, in pyrope-almandine-grossular ternary garnets, where the deformation of the cubic site does not substantially increase but until the pure almandine end member is reached (Armbruster et al. 1992), and in orthopyroxenes, where the octahedral distortion is, on average, greater in ferrosilite than in enstatite, the intensity of the A' feature decreases rather than increasing. Consequently, it is the increased Mg-Fe disorder over the sites (Kirfel 1996), which affects all XANES features by making them weaker and broader, the factor that should be considered responsible for such an as yet never pointed out nor explained anomalous feature occurring at the very beginning of the absorption process.
Fourthly, our study uncovers the presence of a systematic bias in the available experimental data. This bias concerns the energy position of the first line, thus affecting the energy calibration of the Mg-XANES spectra taken in different

laboratories. As it is to be easily seen in Figs. 1b and 1c, the $MgBr_2$ and $MgCl_2$ first absorption lines that, being very sharp, are particularly suited to serve as reference for the calibration of six-fold-coordinated Mg, and the almost as sharp first line of $MgSiN_2$ for four-fold-coordinated Mg, are shifted to lower energy by ca. 2.5 eV and ca. 2 eV, respectively, with respect to the not as sharp first lines of MgO and $MgAl_2O_4$ (spinel), these compounds being those most commonly used as reference for the same coordinations. We cannot explain the first discrepancy by assuming a systematic error in the experimental set up, since the $MgBr_2$ and $MgCl_2$ spectra have been recorded at UVSOR using the same apparatus and at the same time as the spectrum of MgF_2 (Naoe' et al. 1989), which instead appears to be totally consistent in its first line energy with the many MgO spectra taken at the same source as well as elsewhere. In our interpretation, those discrepancies arose from occasional difficulties in measuring the great difference in energy between the Mg first absorption lines and the energy of the feature used to calibrate the entire spectrum, that is stated to be that of the Al K-edge at 1559.6 eV or of a glitch occurring in the beryl monochromator crystal at about 1550 eV: indeed, a difference of as many as 250 eV is too much, in the soft X-ray energy range, to warrant for accurate results, although it is not as critical for spectra recorded in the hard X-ray range (e.g., Farges 2001).

As for the inconsistent energy value observed for the $MgSiN_2$ first line taken at SSRL (Wong et al. 1997, 1999), we reckon that it the first intense feature was wrongly interpreted as being the white line, and instead is the anomalous feature A' of unusual intensity for being produced for Mg is in a totally non centrosymmetrical site (see above). In both cases, we dare to recommend that the use for calibration of any of those three synthetic model compounds should be discontinued, and MgO and $MgAl_2O_4$ (spinel) used instead, as we always do. As a matter of fact, this is commonly being done already, not only at SSRL and UVSOR (as documented here and in many studies listed in Appendix 1), but also at other sources (e.g., Henderson et al. 1992; Ildefonse et al. 1995). Note, however, that omitting the spectra of those four compounds from the data set will decrease somewhat (but not significantly) the range of the observed energy vs. coordination shifts.

Fifthly: using a very limited data set (4 samples) Wong et al. (1999) suggested a progressive first absorption line intensity increase with coordination; by contrast, Li et al. (1999) stated, on the basis of a larger number of data (11) and of a different, more rigorous determination procedure, that the first absorption line amplitude tends to decrease, while the entire peak becomes broader. The indication to be gathered from our data set (58 samples) is not unequivocal, the more so as the amount of absorber to be considered varies widely among the different materials we probed: we remind that we took care of keeping the grain size as constant as possible, but keeping the thickness (i.e., the weight of powder) constant is impossible.

Finally, there seems to be a correlation between the energy position of line A and the average Mg-O distance of the first coordination polyhedron in most model compound we examined. This correlation is not simple, nor can be oversimplified as done by Li et al. (1999 Fig. 4). When trying to derive quantitative information on unknown samples according to the relationships they derived (Li et al. 1999 Fig. 4), we recommend to limit such a tentative correlation only to minerals and model compounds where Mg is known to be in six-fold coordination. Actually, the procedure we deem to be worth trying even for them is to determine their likely coordination first, then to evaluate quantitatively the relationships between energy and distance only for those materials the six-fold coordination of Mg in which is indubitable: only for these the number of reference data is now large enough to allow deriving a statistically significant relationship. Furthermore, the relationships between absorption energy and bond valence calculated on the basis of Brown & Altermatt's (1985) formula derived by Li et al. (1999 Fig. 5) appears not to add any significant information, at least when based on only 6 data points, as they did. The same relationships might acquire some meaning when as many as 58 pair values are taken into consideration, but it requires the evaluation of many independent sites the relative contribution of each in the absorption process is yet to be established, because the actual Mg occupancy of each site needs to be determined by other methods.

4.1 Conclusions

1. Magnesium coordination in structurally unknown materials and amorphous substances can be appreciated through XAS on the basis of a shift in the first line of the Mg K-edge spectrum: this can be certainly done for CN 4 and 8, as indicated by the best reference materials pyrope and spinel. For Mg in CN 6, a more careful analysis is required, because the energy may vary as a function not only of the ligand but also, probably, of interferences originating from local energetic effects.
2. There may be a relationship between first line intensity and coordination, but it still awaits for confirmation, as the accurate determination of the intensity of the various features present in the XANES section of an absorption edge is a matter of debate.
3. The Mg-XANES spectra of several model compounds and minerals exhibit a first, weak pre-edge feature. This feature is certainly related to a deformation of the ligand first-shell cage surrounding the Mg absorber. It can be best explained with transitions arising from high-order contributions, as it shows up when substitution of Mg by Fe and/or Ca occur that have been shown to become significant in deforming the anionic cage only when a large enough number of atoms (clusters extending to 4^{th} and 5^{th} shells) is being considered in calculations.

4. K-edge XANES spectroscopy does not probe only the immediate (local) environment of Mg absorber, but it also explores its long-range-order relationships with other atoms such as Fe and Ca substituting for it in the same structural sites. These relationships may become complex when they depend on the orientation of the samples with respect to the highly polarized synchrotron radiation.

5 Acknowledgements.

Samples were kindly made available by L. Amisano Canesi, F. Bellatreccia, R. Bocchio, M.F. Brigatti, G. Chiari, F. Demartin, S.S. Goldich, C.M. Gramaccioli, G. Iezzi, D.M. Jenkins, O. Johnsen, G. Liborio, C. Lugli, R. Pagano, G. Parodi, B.T. Poe, D. Rubie, F. Seifert, D.C. Smith, K.D. Watson, and M. Welch. The most significant portion of the experimental work was carried out at the SSRL, a facility operated by Stanford University on behalf of the U.S. Department of Energy, Office of Basic Energy Sciences. Another portion was carried out at UVSOR, a facility operated by the Institute of Molecular Science of Japan, with the friendly assistance of T. Murata to whom we express our special thanks. The access to both institutions was made possible by grants from the Italian Ministry of University, Research and Technology (COFIN99 "Layer silicates: Crystal chemistry, structural and petrologic aspects") and National Research Council (CNRC00C9DF_001). The fitting of the recorded spectra benefited of the INFN computing facilities at Laboratori Nazionali di Frascati, and of the INFM ones at Sezione di Camerino. This paper was read and criticized before submission by M.F. Brigatti and F. Seifert. We thank them for their kind attention and the two referees for their improving suggestions: all remaining errors are only due to us.

References

1. Alietti E, Brigatti MF, Poppi L Clintonite-1M: Crystal chemistry and its relationships to closely associated Al-rich phlogopite. Am Mineral **82**: 936-945 (1997).

2. Angel RJ, Finger LW, Hazen RM, Kanzaki M, Weidner DJ, Liebermann RC, Veblen DR Structure and twinning of single-crystal $MgSiO_3$ garnet synthesized at 17GPa and 1800 °C. Am Mineral **74**: 509-512 (1989).

3. Aritani H, Yamada H, Nishio T, Imamura S, Hasegawa S, Tanaka T Mg K-edge XANES study of Li- and Mn-promoted MgO. UVSOR Act Rep 1997 pp. 184-185 (1998).

4. Aritani H, Yamada H, Nishio T, Imamura S, Hasegawa S, Tanaka T, Yoshida S Formation of defects in near-surface region over Li or Mn-doped MgO studied by Mg K-edge XANES. Chem Letters **4**: 359-360 (1999).

5. Aritani H, Yamada H, Nishio T, Shiono T, Imamura S, Kudo M, Hasegawa S, Tanaka T, Yoshida S Characterization of Li-doped MgO catalysts for oxidative coupling of methane by means of Mg K-edge XANES. J Phys Chem B **104**: 10133-10143 (2000).

6. Aritani H, Yamada H, Yamamoto T, Tanaka T, Imamura S XANES study of Li-MgO and $LiLa_2O_4$-MgO catalysts for oxidation coulpling of methane. J Synchrotron Rad **8**: 593-595 (2001).

7. Armbruster T, Geiger CA, Lager GA Single-crystal X-ray structure study of synthetic pyrope almandine garnets at 100 and 293 K. Am Mineral **77**: 512-521 (1992).

8. Bauer WH Rutile-type compounds. V. Refinement of MnO_2 and MgF_2. Acta Cryst **32**: 2200-2204 (1976).

9. Bianconi A XANES Spectroscopy. Pp. 573-662 in: DC Konigsberger & R Prins (editors) X-ray absorption: principles, applications, techniques of EXAFS, SEXAFS and XANES. New York, Wiley (1988).

10. Boiocchi M, Caucia F, Merli M, Prella D, Ungaretti L Crystal-chemical reasons for the immiscibility of periclase and wustite under lithospheric P,T conditions. Eur J Mineral **13**: 871-881 (2001).

11. Bowen NL Evolution of igneous rocks. Princeton NJ, Princeton University Press(1928).

12. Bradley AM, Djajanti S, Thomson S, Howe RF Soft X-ray absorption spectroscopy of microporous materials. 1997 SSRL Act Rep pp. 7-281-7-283 (1997).

13. Bradley CR, Wroge ML, Dozier AK, Gibbons PC White lines at K edges of light atoms. Phys Rev B **31**: 5066-5070 (1985).

14. Brigatti MF, Guggenheim S Mica crystal chemistry and the influence of pressure, temperature, and solid solution on atomistic models. In: A Mottana, FP Sassi, JB Thompson Jr & S Guggenheim (editors) Micas: Crystal chemistry & metamorphic petrology. Rev Mineral Geochem **46**: 1-98 (2002).

15. Brigatti MF, Lugli C, Cibin G, Marcelli A, Giuli G, Paris E, Mottana A, Wu ZY Reduction and sorption of chromium by Fe(II)-bearing phyllosilicates: Chemical treatments and X-ray absorption spectroscopy (XAS) studies. Clays Clay Mineral **48**: 272-281 (2000).

16. Brown FC, Bachrach RZ, Lien N The SSRL grazing incidence monochromator: Design considerations and operating experience. Nucl Instr Meth Phys Sci **152**: 73-80 (1978).

17. Bruls RJ, Hintzen HT, Metselaar H, Loong CK Anisotropic thermal expansion of $MgSiN_2$ from 10 to 300K as measured by neutron diffraction. J Phys Chem Solids **61**: 1285-1293 (2000).

18. Brydson R, Sauer H, Engel W Electron energy loss near-edge structure as an analytical tool – The study of minerals. Pp. 131-154 in: MM Disko, CC Ahn, B Fultz (editors) Transmission energy loss spectrometry in materials science. Warrendale Ill, The Minerals Metals and Materials Society (1992).

19. Brydson R, Sauer H, Engel W, Zeitler E EELS as a fingerprint of the chemical co-ordination of light elements. Microsc Microan Microstr **2**: 159-169 (1991).

20. Burns RG Mineralogical applications of crystal field theory. 2^{nd} ed. Cambridge, Cambridge Univ Press (1993).

21. Cabaret D, Sainctavit P, Ildefonse Ph, Flank A-M Full multiple scattering calculations of the X-ray absorption near edge structure at the magnesium K edge in pyroxene. Am Mineral **83**: 300-304 (1998).

22. Calle C de la, Suquet H Vermiculite. In: SW Bailey (ed.) Hydrous phyllosilicates (exclusive of micas). Rev Mineral **19**: 455-496 (1988).

23. Cameron M, Sueno S, Prewitt CT, Papike JJ High-temperature crystal chemistry of acmite, diopside, hedenbergite, jadeite, spodumene, and ureyite. Am Mineral **58**: 594-618 (1973).

24. Cerino J, Stöhr J, Hower N, Bachrach RZ An ultra-high-vacuum double crystal monochromator beam line for studies in the spectral range 500-4000 eV. Nucl Instrum Meth Phys Res **172**: 227-231 (1980).

25. Chaboy J, Garcia ML, Bartolomé F, Marcelli A, Cibin G, Maruyama H, Pizzini S, Rogalev A, Goedkoop JB, Goulon J X-ray magnetic-circular-dichroism probe of a noncollinear magnetic arrangement below the spin reorientation transition in $Nd_2Fe_{14}B$. Phys Rev B: Condens Matt **57**: 8424-8429 (1998).

26. Chopin C Coesite and pure pyrope in high-grade blueschists of the western Alps: a first record and some consequences. Contrib Mineral Petrol **86**: 107-118 (1984).

27. Cliff G, Lorimer GW The quantitative analysis of thin specimens. J Microscop **103**: 203-207 (1975).

28. Comodi P, Mellini M, Ungaretti L, Zanazzi PF Compressibility and high pressure structure refinement of tremolite, pargasite and glaucophane. Eur J Mineral **3**: 485-499 (1991).

29. Davoli I, Paris E, Mottana A Synchrotron radiation XANES spectra for oxygen and magnesium in MgO (periclase). Atti Acc Lincei Rend Fis s. **8, 82**: 527531 (1988).

30. Debat P, Marre J, Perseil EA, Roux L Sur une amphibole orthorhombique "gédrite" de la vallée d'Héas (Hautes-Pyrenées). Bull Soc Franç Min Crist **94**: 446-448 (1971).

31. Dehmer JL, Dill D Shape resonances in K-shell photoionization of diatomic molecules. Phys Rev Letters **35**: 213-215 (1975).

32. Dehmer JL, Dill D Molecular effects on inner-shell photoabsorption. K-shell spectrum of N_2. J Chem Phys **65**: 5327-5334 (1976).

33. Della Ventura G, Hawthorne FC, Robert JL, Delbove F, Welch MF, Raudsepp M Short-range order of cation in synthetic amphiboles along the richterite-pargasite join. Eur J Mineral **11**: 79-94 (1999).

34. Dräger G, Frahm R, Materlik G, Brummer O On the multiplet character of the x-ray transitions in the pre-edge structure of Fe K absorption spectra. Phys Stat Sol **146**: 287-294 (1988).

35. Effenberger H, Mereitner K, Zeman J Crystal structure refinements of magnesite, calcite, rhodochrosite, siderite, smithsonite, and dolomite, with discussion of some aspects of the stereochemistry of calcite-type carbonates. Z Kristall **156**: 233-243 (1981).

36. Egerton RF, Crozier PA, Rice P Electron energy-loss spectroscopy and chemical change. Ultramicroscopy **23**: 305-312 (1987).

37. Farges F Crystal chemistry of iron in natural grandidierites: an X-ray absorption fine-structure spectroscopy study. Phys Chem Minerals **28**: 619-629 (2001).

38. Farges F, Guyot F, Andrault D, Wang Y Local structure around Fe in $Mg_{0.9}Fe_{0.1}SiO_3$ perovskite: an x-ray absorption spectroscopy study at Fe-K edge. Eur J Mineral **6**: 303-312 (1994).

39. Ferraris G, Prencipe M, Sokolova EV, Gekimyants VM, Spiridonov EM Hydroxylclinohumite, a new member of the humite group: Twinning, crystal structure and crystal chemistry of the clinohumite subgroup. Z Kristall **215**: 169-173 (2000).

40. Fischer P Neutronenbeugungsuntersuchungen der Strukuren von $MgAl_2O_4$- und $ZnAl_2O_4$-Spinellen in Abhängigkeit von der Vorgeschichte. Z Kristall **124**: 275-302 (1967).

41. Fockenberg T, Schreyer W Yoderite, a mineral with essential ferric iron: Its lack of occurrence in the system MgO-Al_2O_3-SiO_2-H_2O. Amer Mineral **76**: 1052-1060 (1991).

42. Forbes WD, Morten L, Mottana A Gigantic mineral patches in the ultramafic rocks of the Finero Complex (Central Alps). Mem Sci Geol **33**: 127133 (197879).

43. Fricke H The K-characteristic absorption frequencies for the chemical elements magnesium to chromium. Phys Rev, 2^{nd} s, **16**: 202-215 (1920).

44. Friedrich A, Lager GA, Kunz M, Chakoumakos BC, Smyth JR, Schultz AJ Temperature-dependent single-crystal neutron diffraction study of natural chondrodite and clinohumites. Am Mineral **86**: 981-989 (2001).

45. Fuggle JC, Inglesfield JE Unoccupied electronic states: Fundamentals for XANES, EELS, IPS and BIS. Berlin, Springer (1992).

46. Fuggle JC, Mårtensson N Core-level binding energies in metals. J Electron Spectrosc Rel Phenom **21**: 275-281 (1980).

47. Fujino K, Sasaki Y, Takéuchi Y, Sadanaga R X-ray determination of electron distribution of forsterite, fayalite and tephroite. Acta Crystall **B37**: 513-518 (1981).

48. Garvie LAJ, Buseck PR Bonding in silicates: Investigation of the Si $L_{2,3}$ edge by parallel electron energy-loss spectroscopy. Amer Mineral **84**: 945-964 (1999).

49. Garvie LAJ, Craven AJ, Brydson R Use of electron energy-loss near-edge fine structure in the study of minerals. Amer Mineral **79**: 411-425 (1994).

50. Gasparik T Experimental investigation of the origin of majoritic garnet inclusions in diamonds. Phys Chem Minerals **29**: 170-180 (2002).

51. Ghose S, Yang H Mn-Mg distribution in a $C2/m$ manganoan cummingtonite: Crystal–chemical considerations. Amer Mineral **74**: 1091-1096 (1989).

52. Giuli G, Paris E, Wu ZY, Berrettoni M, Della Ventura G, Mottana A Nickel site distribution and clustering in synthetic double-chain silicates by experimental and theoretical XANES spectroscopy. Phys Rev B **62**: 5473-5477 (2000).

53. Giuli G, Paris E, Wu ZY, Mottana A, Seifert F Fe and Mg local environment in the synthetic enstatite-ferrosilite join: an experimental and theoretical XANES and XRD study. Eur J Mineral **14**: 429-436 (2002).

54. Green HW, Dobrzhietskaya L, Riggs EM, Zhen-Ming J Alpe Arami: a peridotite massif from the Mantle Transition Zone? Tectonophysics **279**: 1-21 (1997).

55. Gudat W, Kunz C Close similarity between photoelectric yield and photoabsorption spectra in the soft-X-ray range. Phys Rev Letters **29**: 169-172 (1977).

56. Hanic F, Handlovic M, Burdova K, Majling J Crystal structure of lithium magnesium phosphate, $LiMgPO_4$: crystal chemistry of the olivine-type compounds. J Crystallogr Spectrosc Res **12**: 99-127 (1982).

57. Hawthorne FC, Welch MD, Della Ventura G, Liu S, Robert J-L, Jenkins DM Short-range order in synthetic aluminous tremolites: An infrared and triple-quantum MAS NMR study. Am Mineral **85**: 1716-1724 (2000).

58. Haynes EA, Moecher DP, Spicuzza MJ Oxygen isotope composition of carbonates,silicates, and oxides in selected carbonatites: constraints on crystallisation temperatures of carbonate magmas. Chem Geol **193**: 43-57 (2003).

59. Hazen RM, Burnham CW The crystal structures of one-layer phlogopite and annite. Am Mineral **58**: 889-900 (1973).

60. Heinemann S, Sharp TG, Seifert F, Rubie DC The cubic-tetragonal phase transition in the system majorite ($Mg_4Si_4O_{12}$)-pyrope ($Mg_3Al_2Si_3O_{12}$), and garnet symmetry in the Earth's transition zone. Phys Chem Minerals **24**: 206-221 (1997).

61. Henderson CMB, Charnock JM, van der Laan G, Schreyer W X-Ray absorption spectroscopy of Mg in minerals and glasses. Daresbury Ann Rept 77 (1992) .

62. Higgins JB, Ribbe PH, Nakajima Y An ordering model for the commensurate antiphase structure of yoderite. Amer Mineral. **67**: 76-84 (1982).

63. Hill RJ, Craig JR, Gibbs GV Systematics of the spinel structure type. Phys Chem Minerals **4**: 317-339 (1979).

64. Hussain Z, Umbach E, Shirley DA, Stöhr J, Feldhaus J Performance and application of a double crystal monochromator in the energy region $800 \leq h\nu \leq 4500$ eV. Nucl Instr Meth Phys Res **195**: 115-131 (1982).

65. Hutchison MT, Hursthouse MB, Light ME Mineral inclusions in diamonds: associations and chemical distinctions around the 670-km discontinuity. Contrib Mineral Petrol **142**: 119-126 (2001).

66. Ildefonse Ph, Calas G, Flank A-M, Lagarde P Low Z elements (Mg, Al, and Si) K-edge X-ray absorption spectroscopy in minerals and disordered systems. Nucl Instrum Meth Phys Res **B97**: 172-175 (1995).

67. Jenkins DM Synthesis and characterization of tremolite in the system H_2O-CaO-MgO-SiO_2. Am Mineral **72**: 707-715 (1987).

68. Jenkins DM, Sheriff BL, Cramer J, Xu Z Al, Si, and Mg occupancies in tetrahedrally and octahedrally coordinated sites in synthetic aluminous tremolite. Am Mineral **82**: 280-290 (1997).

69. Johnson LJ Occurrence of regularly interstratified chlorite-vermiculite as a weathering product of chlorite in soil. Am Mineral **49**: 556-572 (1964).

70. Joswig W, Amthauer G, Takéuchi Y Neutron diffraction and Mossbauer spectroscopic study of clintonite (xanthophyllite). Am Mineral **71**: 1194-1197 (1986).

71. Joswig W, Fuess H Refinement of a one-layer triclinic chlorite.Clays Clay Minerals **38**: 216-218 (1990).

72. Kimata M, Ii N The crystal structure of synthetic åkermanite, $Ca_2MgSi_2O_7$. N Jb Miner Mh Jg 1981 **H1**: 1-10 (1981).

73. Kinoshita T, Takata Y, Matsukawa T, Aritani H, Matsuo S, Yamamoto T, Takahashi M, Yoshida H, Yoshida T, Kitajima Y Performance of YB_{66} soft X-ray monochromator crystal at the wiggler beamline of UVSOR facility. UVSOR Act Rep 1996 pp. 198-199 (1997).

74. Kinoshita T, Takata Y, Matsukawa T, Aritani H, Matsuo S, Yamamoto T, Takahashi M, Yoshida H, Yoshida T, Ufukutepe Y, Nath KG, Kimura S, Kitajima Y Performance of YB_{66} soft X-ray monochromator crystal at the wiggler beamline of UVSOR facility. J Synchrotron Rad **5**: 726-728 (1998).

75. Kirfel A Cation distributions in olivines and clinopyroxenes. An interlaboratory study. Phys Chem Minerals **23**: 503-519 (1996).

76. Kosaka T, Yamada A, Miyaji A, Shiraishi M, Hasegawa S XANES analysis of Cu-MgO/TiO_2 bactericidal material. UVSOR Act Rep 1999 pp. 162-163 (2000).

77. Kutzler FW, Natoli CR, Misemer DK, Doniach S, Hodgson KO Use of one electron theory for the interpretation of near edge structure in K-shell X-ray absorption spectra of transition metal complexes. J Chem Phys **73**: 3274-3288 (1980).

78. Laclare JL Light source performance achievements. Nucl Instr Meth Phys Res A **467–468**: 1–7 (2001).

79. Lauterbach S, McCammon CA, Van Aken P, Langenhorst F, Seifert F Mössbauer and ELNES spectroscopy of (Mg,Fe)(Si,Al)O_3 perovskite: A highly oxidised component of the lower mantle. Contr Mineral Petrol **138**: 17-26 (2000).

80. Li D, Murata T, Peng M Na and Mg K-edge XANES of silicate minerals and glasses. UVSOR Act Rep 1996 pp 202-203 (1997).

81. Li D, Peng MS, Murata T Coordination and local structure of magnesium in silicate minerals and glasses: Mg K-edge XANES study. Can Mineral **37**: 199-206 (1999).

82. Liebau F Structural chemistry of silicates. Structure, bonding, and classification. Berlin, Springer (1985).

83. Lindner Th, Sauer H, Engel W, Kambe K Near-edge structure in electron-energy-loss spectra of MgO. Phys Rev **B33**: 22-24 (1986).

84. Lu M, Hofmann AW, Mazzucchelli M, Rivalenti G The mafic-ultramafic complex near Finero (Ivrea-Verbano Zone), II. Geochronology and isotope geochemistry. Chem Geol **140**: 223-235 (1997).

85. MacKenzie KJD, Meinhold RH MAS NMR study of pentacoordinated magnesium in grandidierite. Am Mineral **82**: 479-482 (1997).

86. Mathieson AM Mg-vermiculite: a refinement and re-examination of the crystal structure of the 14.36 Å phase. Am Mineral **43**: 216-227 (1958).

87. McConnell JDC, McCammon CA, Angel RJ, Seifert F The nature of the incommensurate structure in åkermanite, $Ca_2MgSi_2O_7$, and the character of its transformation from the normal structure. Z Krist **215**: 669-677 (2000).

88. Moore RO, Gurney JJ Pyroxene solid solution in garnets included in diamond. Nature **318**: 553-555 (1985).

89. Morten L, Bondi M Spinel lherzolite inclusions in basalts from Monti Lessini, Veneto region, northern Italy. N Jb Miner Mh jg 1981 **H 7**: 308-316 (1981).

90. Mottana A, Marcelli A, Cibin G, Dyar MD X-ray absorption spectroscopy of the micas. Pp. 119-136 in: Advances on Micas (Problems, methods, applications in Geodynamics). Accademia Nazionale dei Lincei, Roma, 2-3 Novembre 2000 (Pre-prints) (2000).

91. Mottana A, Marcelli A, Cibin G, Dyar MD X-ray absorption spectroscopy of the micas. In: A. Mottana, F.P. Sassi, J.B. Thompson Jr. & S. Guggenheim (editors) Micas: Crystal chemistry & metamorphic petrology. Rev Mineral Geochem **46**: 371-411 (2002).

92. Mottana A, Murata T, Marcelli A, Wu ZY, Cibin G, Paris E, Giuli G The local structure of Ca-Na pyroxenes. II. XANES studies at the Mg and Al K edges. Phys Chem Minerals **27**: 20-33 (1999).

93. Mottana A, Murata T, Wu ZY, Marcelli A, Paris E Detection of order-disorder in pyroxenes of the jadeite-diopside series via XAS at the Ca-Na and Mg-Al edges. J Electron Spectrosc Rel Phenom **79**: 79-82 (1996).

94. Mottana A, Paris E, Marcelli A, Wu ZY, Giuli G Crystal chemistry of olivines and garnets in alpine ultramafics: information contributed by XAFS. Mitt Österr Mineral Gesell **141**: 35-44 (1996).

95. Murata T, Matsukawa T, Naoe' S, Horigome T, Matsudo O, Watanabe M Soft x-ray beamline BL7A at the UVSOR. Rev Sci Instr **63**: 1309-1312 (1992).

96. Naoe' S, Murata T, Matsukawa T Mg K-XANES studies in magnesium halides. Physica B **158**: 615-616 (1989).

97. Natoli CR, Benfatto M A unifying scheme of interpretation of x-ray absorption spectra based on the multiple scattering theory. Pp. 11-23 in P Lagarde, D Raoux, J Petiau (editors) EXAFS and Near Edge Structure IV. J Phys (Paris) **47-C8** (1986).

98. Natoli CR, Benfatto M, Brouder C, Ruiz Lopez MZ, Foulis DL Multichannel multiple-scattering theory with general potentials. Phys Rev B **42**: 1944-1968 (1990).

99. Natoli CR, Benfatto M, Della Longa S, Hatada K X-ray absorption spectroscopy: state-of-the-art analysis. J Synchrotron Rad **10**: 26-42 (2003).

100. Nelson DO, Guggenheim S Inferred limitations to the oxidation of Fe in chlorite: a high-temperature single-crystal X-ray study. Am Mineral **78**: 1197-1207 (1993).

101. Oberti R, Ungaretti L, Cannillo E, Hawthorne FC The behavious of Ti in amphiboles: I. Four- and six-coordinate Ti in richterite. Eur J Mineral **4**: 425-440 (1992).

102. O'Hanley DS, Wicks FJ Conditions of formation of lizardite, chrysotile and antigorite. Can Mineral **33**: 753-773 (1995).

103. Papike JJ, Ross M Gedrites: crystal structures and intra-crystalline cation distributions. Am Mineral **55**: 1945-1972 (1970).

104. Parise JB, Wang Y, Gwanmesia GD, Zhang J, Sinelnikov Y, Chmielowski J, Weidner DJ, Liebermann RC The symmetry of garnets on the pyrope ($Mg_3Al_2Si_3O_{12}$) - majorite ($MgSiO_3$) join. Geophys Res Letters **23**: 3799-3802 (1996).

105. Partin DE, O'Keeffe M The structures and crystal chemistry of magnesium chloride and cadmium chloride. J Sol State Chem **95**: 176-183 (1991).

106. Pavese A, Artioli G, Prencipe M X-ray single-crystal diffraction study of pyrope in the temperature range 30-973 K. Am Mineral **80**: 457-464 (1995).

107. Pawley AR, Graham CM, Navrotsky A Tremolite-richterite amphiboles: synthesis, compositional and structural characterization and thermochemistry. Am Mineral **78**: 23-35 (1993).

108. Peng MS, Li D Na and Mg K-edge XANES study in silicate glasses. Specroscopy Spectr Anal **22**: 873-876 (2002).

109. Perdikatsis B, Burzlaff H Strukturverfeinerung am Talk $Mg_3[(OH)_2Si_4O_{10}]$. Z Kristall **156**: 177-186 (1981).

110. Pettifer RF Advances in technique and apparatus for X-ray absorption spectroscopy. Pp. 383-393 in: A. Balerna, E. Bernieri, S. Mobilio (editors) 2^{nd} Eur Conf Progr X-ray Synchrotron Rad Res Conf Proceed, 25. Bologna, Ital Phys Soc (1990).

111. Pilati T, Bianchi R, Gramaccioli CM Lattice-dynamical estimation of atomic thermal parameters for silicates: forsterite α-Mg_2SiO_4. Acta Crystall **B46**: 301-311 (1990).

112. Pilati T, Demartin F, Gramaccioli CM Thermal parameters for minerals of the olivine group: Their implication on vibrational spectra, thermodynamic functions and transferable force fields. Acta Crystall B **51**: 721-733 (1995).

113. Pouchou J Use of soft X-rays in microanalysis. Mikroch Acta [Suppl] **23**: 39-60 (1996).

114. Reeder RJ Crystal chemistry of the rhombohedral carbonates. Rev Mineral **11**: 1-47 (1983).

115. Reeder RJ, Markgraf SA High-temperature crystal chemistry of dolomite. Am Mineral **71**: 795-804 (1986).

116. Reynolds RC Mixed layer chlorite minerals. In: SW Bailey (ed.) Hydrous phyllosilicates (exclusive of micas). Rev Mineral **19**: 601-629 (1988).

117. Risold A-Ch, Trommsdorff V, Grobéty B Genesis of ilmenite rods and palisades along humite-type defects in olivine from Alpe Arami. Contrib Mineral Petrol **140**: 619-628 (2001).

118. Roe AL, Schneider DJ, Mayer RJ, Pyrz JW, Widom J, Que L Jr X-ray absorption spectroscopy of iron-tyrosinate proteins. Am Chem Soc J **106**: 1676-1681 (1984).

119. Ross NL The equation of state and high pressure behavior of magnesite. Am Mineral **82**: 682-688 (1997).

120. Ross NL, Reeder RJ High-pressure structural study of dolomite and ankerite. Am Mineral **77**: 412-421 (1992).

121. Rowen M, Rek ZU, Wong J, Tanaka T, George GN, Pickering IJ, Via GH, Brown GE First XAS spectra with a YB_{66} monochromator. J Synchrotron Rad **6**: 25-27 (1993).

122. Sasaki S, Takéuchi Y, Fujino K, Akimoto S Electron-density distributions of three orthopyroxenes, $Mg_2Si_2O_6$, $Co_2Si_2O_6$, and $Fe_2Si_2O_6$. Z Kristall **158**: 279-297 (1982).

123. Sayers DE, Lytle FW, Stern EA Point scattering theory of x-ray K absorption fine structure. Adv X-ray Anal **13**: 248-271 (1970).

124. Sayers DE, Stern EA, Lytle FW New technique for investigating noncrystalline structure: Fourier analysis of the Extended X-ray Absorption Fine Structure. Phys Rev Letters **27**: 1204-1208 (1971).

125. Schäfers F, Müller BR, Wong J, Tanaka T, Kamimura Y YB_{66}: A new soft X-ray monochromator crystal. Synchrotron Rad News **5** [2]: 28-30 (1992).

126. Schmocker U, Waldner F The inversion parameter with respect to the space group of $MgAl_2O_4$ spinels. J Phys C: Solid State Phys **9**: L235-L237 (1976).

127. Schonberger U, Aryasetiawan F Bulk and surface electronic structures of MgO. Phys Rev B **52**: 8788-8793 (1995).

128. Seifert F, Czank M, Simons B, Schmahl W A commensurate-incommensurate phase transition in iron-bearing åkermanites. Phys Chem Minerals **14**: 26-35(1987).

129. Serratosa JM, Sanz J Dehydroxilation of micas and vermiculites. The effect of octahedral composition and interlayer saturing cations. Mineral Petrogr Acta **29-A**: 399-408 (1985).

130. Shannon RD Revised effective ionic radii and systematic studies of interatomic distances in halides and chalcogenides. Acta Cryst **32**: 751-767 (1976).

131. Shiono T, Minagi T, Aritani H, Nishida T Mg K-edge XANES study of forsterite precursor prepared from heterogeneous alkoxide solution and crystallization. UVSOR Act Rep 1997 pp. 176-177 (1998).

132. Shulman RG, Yafet Y, Eisenberger P, Blumberg WE Observation and interpretation of X-ray absorption edges in iron compounds and proteins. Proc Nat Acad Sci USA **73**: 1384-1388 (1976).

133. Smith JV, Mason B Pyroxene-garnet transformation in Coorara meteorite. Science **168**: 832-833 (1970).

134. Smyth JR, Bish DL Crystal structures and cation sites of the rock-forming minerals. Boston, Allen & Unwin (1988).

135. Smyth JR, Dyar MD, May HM, Bricker OP, Acker IG Crystal structure refinement and Mossbauer spectroscopy of an ordered triclinic clinochlore. Clays Clay Minerals **45**: 544-550 (1997).

136. Stachel T Diamonds from the astenosphere and the transition zone. Eur J Mineral **13**: 883-892 (2001).

137. Takata Y, Kosugi N Mg and Al K-edge XAFS measurements with a KTP crystal monochromator. UVSOR Act Rep 1998 pp. 112-113 (1999).

138. Takata Y, Shigemasa E, Kosugi N Mg and Al K-edge XAFS measurements with a KTP crystal monochromator. J Synchrotron Rad **8**: 351-353 (2001).

139. Tanaka T, Aizawa T, Rowen M, Rek ZU, Kitajima Y, Higashi I, Wong J, Ishizawa Y Nature of the 1385.6 and 1438 eV positive glitches in the transmission function of the YB_{66} soft-X-ray monochromator. J Appl Cryst **30**: 87-91 (1997).

140. Tertian R. Mathematical matrix correction procedures for X-ray fluorescence analysis. A critical survey. X-Ray Spectrom **4**: 52-61 (1986).

141. Thomson S, Howe RF Spectroscopic studies of a magnesium substituted microporous aluminophosphate DAF-1. Pp 447-454 in: Progress in zeolite and microporous materials, pts A-C Studies in Surface Science and Catalysis 105. Amsterdam, Elsevier (1997).

142. Tombolini F, Brigatti MF., Marcelli A, Cibin G, Mottana A, Giuli G Local and average Fe distribution in trioctahedral micas: Analysis of the Fe K-edge XANES spectra in the phlogopite-annite and phlogopite-tetraferriphlogopite joins on the basis of single-crystal XRD refinements. Eur J Mineral, **14**: 1075-1186 (2002).

143. Tombolini F, Cibin G, Marcelli A, Mottana A, Brigatti MF, Giuli G A polarized XANES investigation of Mg-rich trioctahedral micas. In: A. Bianconi, A. Marcelli & N.L. Saini (editors): X-Ray and Inner-Shell Processes: 19^{th} International Conference on X-ray and Inner-Shell Processes, pp. 481-490. American Institute of Physics CP652 (2003).

144. Tropper P, Manning CE, Essene EJ, Kao LS The compositional variation of synthetic sodic amphiboles at high and ultra-high pressures. Contrib Mineral Petrol **139**: 146-162 (2000).

145. Ungaretti L, Leona M, Merli M, Oberti R Non-ideal solid-solution in garnet: crystal-structure evidence and modelling. Eur J Mineral **7**: 1299-1312 (1995)

146. Watanabe M UVSOR at IMS. Synchrotron Rad News **4** [3]: 12-17

147. Waychunas GA (1987) Synchrotron radiation XANES spectroscopy of Ti in minerals: Effects of Ti bonding distances, Ti valence, and site geometry on absorption edge structure. Am Mineral **72**: 89-101 (1991).

148. Welch MD, Barras J, Klinowski J A multinuclear NMR study of clinochlore. Am Mineral **80**: 441-447 (1995).

149. Welch MD, Pawley AR Tremolite: New enthalpy and entropy data from a phase equilibrium study of the reaction tremolite = 2 diopside + 1.5 orthoenstatite + β-quartz + H_2O. Am Mineral **76**: 1931-1939 (1991).

150. Westre TE, Kennepohl P, de Witt J, Hedman B, Hodgson KO, Solomon EI A multiplet analysis of Fe K-edge 1s $\rightarrow$ 3d pre-edge features of iron complexes. J Am Chem Soc **119**: 6297-6314 (1997).

151. Whittaker EJW (1956) The structure of chrysotile. II. Clino-chrysotile. Acta Cryst **9**: 855-861 (1956).

152. Wicks FJ, O'Hanley DS Serpentine minerals: Structures and petrology. In: SW Bailey (ed.) Hydrous phyllosilicates (exclusive of micas). Rev Mineral **19**: 91-167 (1988).

153. Wicks FJ, Whittaker EJW A reappraisal of the structure of the serpentine minerals. Can Mineral **13**: 227-243 (1975).

154. Wong J, Fröba M, Tamura E, Rowen K, Rek Z, Tanaka T Progress in 1-2 KeV spectroscopy using a YB_{66} monochromator. J Phys IV France 7 Colloque C2-511 C-512 (1997).

155. Wong J, George GN, Pickering IJ, Rek ZU, Rowen M, Tanaka T, Via GH, DeVries B, Vaughan DEW, Brown GE New opportunities in XAFS investigation in the 1-2 KeV region. Sol State Commun **92**: 559-562 (1994).

156. Wong J, Roth WL, Batterman BW, Berman LE, Pease DM, Heald S, Barbee T Stability of some soft x-ray monochromator crystals in synchrotron radiation. Nucl Instrum Meth Phys Res **195**: 133-139 (1982).

157. Wong J, Shimkaveg G, Goldstein W, Eckart M, Tanaka T, Rek ZU, Tomkins H YB_{66}: A new soft-x-ray monochromator for synchrotron radiation. Nucl Instrum Meth Phys Res A **291**: 243-249 (1990).

158. Wong J, Tanaka T, Rowen M, Schäfers F, Müller BR, Rek ZU YB_{66} - a new soft X-ray monochromator for synchrotron radiation. II. Characterization. J Synchrotron Rad **6**: 1086-1095 (1999).

159. Wu Z, Marcelli A, Mottana A, Giuli G, Paris E, Seifert F Effects of higher-correlation shells in garnets detected by x-ray-absorption spectroscopy at the Al K edge. Phys Rev B **54**: 2976-2979 (1996).

160. Wu Z, Mottana A, Marcelli A, Natoli CR, Paris E Theoretical analysis of X-ray absorption near-edge structure in forsterite, Mg_2SiO_4-Pbnm, and fayalite, Fe_2SiO_4-Pbnm, at room temperature and extreme conditions. Phys Chem Minerals **23**: 193-204 (1996).

161. Wu Z, Mottana A, Paris E, Giuli G, Marcelli A, Cibin G Order-disorder in olivine minerals by synchrotron X-ray absorption near-edge structure (XANES) spectroscopy at Mg, Fe, and Ca K edges. Lab Naz Frascati Pubbl LNF-99/019, **1-24** (1999).

162. Wu Z, Seifert F, Poe B, Sharp T Multiple-scattering calculations of SiO_2 polymorphs: A comparison of ELNES and XANES spectra. J Phys: Cond Matter **8**: 3323-3336 (1996).

163. Yang H, Hazen RM, Prewitt CT, Finger LW, Lu R, Hemley RJ High-pressure single-crystal X-ray diffraction and infrared spectroscopic studies of the $C2/m$-$P2_1/m$ phase transition in cummingtonite. Am Mineral **83**: 288-299 (1998).

164. Yoshida H, Yoshida T, Tanaka T, Funabiki T, Yoshida S, Abe T, Kimura K, Hattori T Mg K-edge XANES study of silica-magnesia. UVSOR Act Rep 1993 pp 206-207 (1994).

165. Yoshida T, Tanaka T, Yoshida H, Funabiki T, Yoshida S, Murata T Study of dehydration of magnesium-hydroxide. J Phys Chem **99**: 10890-10896 (1995).

166. Yoshida T, Tanaka T, Yoshida H, Takenaka S, Funabiki T, Yoshida S, Murata T A XANES study of the dehydration process of magnesium-hydroxide. Physica B **209**: 581-584 (1995).

167. Yoshida T, Yoshida H, Yamaguchi K, Ebitani K, Kaneda K Study of the local structure of hydrotalcite catalysts. UVSOR Act Rep 1997 pp 182-183 (1998).

168. Zigan F, Rothbauer R Neutronenbeugungsmessungen am Brucit. N Jb Miner Mh **4-5**: 137-143 (1967).

Table 1: *Mg-bearing synthetic model compounds analyzed in the present work.*

No.	Sample	Formula	Sp. Gr.	Mg#	CN	Reference
1.	Magnesium	Mg	$P6_3/mmc$	100	12	Wong et al. 1997
2.	Pyrope	$Mg_3Al_2[SiO_4]_3$	$Ia3d$	100	8	Mottana et al. 1996b
3.	Py-Maj garnet	$Mg_3(AlMg)_2[SiO_4]_3$	$Ia3d$	50	8	this study
4.	Majorite	$Mg_4Si_4O_{12}$	$I4_1/a$	100	8+6	this study
	Periclase	MgO	$Fm3m$	100	6	Rowen et al. 1993
	Periclase	MgO	$Fm3m$	100	6	Wu et al. 1996b
	Periclase	MgO	$Fm3m$	100	6	Wong et al. 1997
	Periclase	MgO	$Fm3m$	100	6	Shiono et al. 1998
	Periclase	MgO	$Fm3m$	100	6	Aritani et al.1998,2000
5.	Periclase	MgO	$Fm3m$	100	6	this study
6.	Sellaite	MgF_2	$P4_2/mnm$	100	6	Naoe' et al. 1989
	Mg-bromide	$MgBr_2$	$R\bar{3}m$	100	6	Naoe' et al. 1989
7.	Mg-bromide	$MgBr_2$	$R\bar{3}m$	100	6	Murata et al. 1992
8.	Mg-chloride	$MgCl_2$	$R\bar{3}m$	100	6	Naoe' et al. 1989
	Brucite	$Mg(OH)_2$	$P\bar{3}m1$	100	6	Yoshida et al. 1995
	Brucite	$Mg(OH)_2$	$P\bar{3}m1$	100	6	Aritani et al. 1998,2000
9.	Brucite	$Mg(OH)_2$	$P\bar{3}m1$	100	6	this study
	Mg-carbonate	$Mg_2CO_3(OH)_2$	mixture	100	6	Aritani et al. 1998
10.	Forsterite	$Mg_2[SiO_4]$	$Pbmn$	100	6	Wu et al. 1996b
11.	"Hortonolite"	$FeMg[SiO_4]$	$Pnmn$	50	6	this study
12.	Li-Mg phosphate	$LiMg[PO_4]$	$Pbmn$	100	6	this study
13.	Diopside	$CaMg[Si_2O_6]$	$C2/c$	100	6	this study
14.	Di-Ni cpx	$Ca(Mg_{.5}Ni_{.5})[Si_2O_6]$	$C2/c$	50	6	this study
15.	Enstatite	$(Mg,Fe)_2[Si_2O_6]$	$P2_1/c$	80	6	Giuli et al. 2002
	Enstatite	$(Mg,Fe)_2[Si_2O_6]$	$P2_1/c$	60	6	Giuli et al. 2002
16.	Ferrosilite	$(Fe,Mg)_2[Si_2O_6]$	$P2_1/c$	40	6	Giuli et al. 2002
	Ferrosilite	$(Fe,Mg)_2[Si_2O_6]$	$P2_1/c$	20	6	Giuli et al. 2002
17.	Tremolite	$Ca_2Mg_5[(OH)_2Si_8O_{22}]$	$C2/m$	100	6	this study
18.	Richterite	$Na_2CaMg_5[(OH)_2Si_8O_{22}]$	$C2/m$	100	6	this study
19.	Magnesiohornblende	$Ca_2Mg_4Al[(OH)_2AlSi_7O_{22}]$	$C2/m$	80	6	this study
20.	Na-cummingtonite	$NaNaMgMg_5[(OH)_2Si_8O_{22}]$	$P2_1/n$	100	6	this study
21.	Talc	$Mg_3[(OH)_2Si_4O_{10}]$	$C\bar{1}$	100	6	this study
22.	Kinoshitalite	$BaMg_3[(OH)_2Si_3AlO_{10}]$	$C2/m$	100	6	this study
	Spinel	$MgAl_2O_4$	$Fd3m$	100	4	Aritani et al. 2000
23.	Spinel	$MgAl_2O_4$	$Fd3m$	100	4	this study
24.	Åkermanite	$Ca_2Mg_2[Si_2O_7]$	$P\bar{4}2_1m$	100	4	this study
25.	Mg-Si nitride	$MgSiN_2$	?	100	4	Wong et al. 1997

No.: progressive number
Sample: name of the mineral analogue to the synthetic model compound
Formula: stoichiometry of the composition used for synthesis
Space group: determined by crystal structure refinement (see text)
Mg#: percentage occupancy in the related structural site(s)
N.C.: theoretical coordination number (as determined by the structural refinement)
Reference: published presentation of the XAS spectrum (see text)
(?): Data not found/not available.

Table 2: *Minerals analyzed in the present work.*

No.	Sample	Locality	Formula (simplified)	Sp. Gr.	Mg#	CN	Reference
26.	Pyrope	Dora-Maira, I	$Mg_3Al_2[SiO_4]_3$	$Ia3d$	97	8	Mottana et al.1996b
	Pyrope	natural	$Mg_3Al_2[SiO_4]_3$	$Ia3d$	?	8	Li et al. 1999
27.	Pyropic gnt	Alpe Arami, CH	$(Mg,Fe)_3Al_2[SiO_4]_3$	$Ia3d$	71	8	Mottana et al. 1996b
28.	Py-Alm-Grs	Nowa Wies, PL	$(Mg,Fe,Ca)_3Al_2[SiO_4]_3$	$Ia3d$	49	8	this study
29.	Alm-Py-Grs	Soazza, CH	$(Mg,Fe,Ca)_3Al_2[SiO_4]_3$	$Ia3d$	35	8	this study
30.	Brucite	Asbestos, CDN	$Mg(OH)_2$	$P\bar{3}m1$	93	6	this study
31.	Magnesite	Snarum, N	$Mg[CO_3]$	$R\bar{3}c$	99	6	this study
32.	Dolomite	Neuberg, A	$CaMg[CO_3]_2$	$R\bar{3}$	98	6	this study
33.	Monticellite	Magnet Cove,USA	$CaMg[SiO_4]$	$Pbmn$	87	6	Wu et al. 1999b
34.	Forsterite	Afghanistan	$Mg_2[SiO_4]$	$Pbmn$	99	6	Mottana et al. 1996b
35.	Forsterite	Alpe Arami, CH	$Mg_2[SiO_4]$	$Pbmn$	90	6	Mottana et al. 1996b
36.	Forsterite	Lessini, I	$Mg_2[SiO_4]$	$Pbmn$	90	6	Mottana et al. 1996b
37.	Forsterite	Finero, I	$Mg_2[SiO_4]$	$Pbmn$	90	6	Mottana et al. 1996b
	Forsterite	natural	$Mg_2[SiO_4]$	$Pbmn$	?	6	Li et al. 1999
38.	"Hortonolite"	Monroe T., USA	$(Fe,Mg)_2[SiO_4]$	$Pbmn$	38	6	this study
39.	Ti-clinohumite	Gardiner Cpl., DK	$(Mg,Fe,Ti)_9(OH)_2Si_4O_{16}$	$P2_1/b$	85	6	this study
	Cordierite	natural	$Mg_2Si_5Al_4O_{18}$	$Ccrm$	?	6	Li et al. 1999
40.	Diopside	Canada	$CaMg[Si_2O_6]$	$C2/c$	92	6	Mottana et al. 1999
	Diopside	natural	$CaMg[Si_2O_6]$	$C2/c$	?	6	Li et al. 1999
41.	P-omphacite	Biella, I	$(Na,Ca)(Al,Mg)[Si_2O_6]$	$P2/n$	41	6	Mottana et al. 1999
42.	C-omphacite	Sörpollen, N	$(Na,Ca)(Al,Mg)[Si_2O_6]$	$C2/c$	29	6	this study
	Enstatite	natural	$MgSiO_3$	$P2_1/c$	?	6	Li et al. 1999
43.	Glaucophane	Champ de Praz, I	$Na_2(Mg,Fe^{2+})_3(Al,Fe^{3+})_2[(OH)_2Si_8O_{22}]$	$C2/m$	60	6	this study
44.	Tremolite	unknown	$Ca_2Mg_5[(OH)_2Si_8O_{22}]$	$C2/m$	100	6	this study
45.	Cummingtonite	Morasice, CS	$(Mg,Mn)_7[(OH)_2Si_8O_{22}]$	$C2/m$	75	6	this study
46.	Gedrite	Gèdres, F	$Mg_5Al_2[(OH)_2Si_6Al_2O_{22}]$	$Pnma$	49	6	this study
	Lizardite	natural	$Mg_3Si_{1.83}Al_{1.17}O_5(OH)_4$	?	?	6	Li et al. 1999
47.	Chrysotile	Redwood C., USA	$Mg_6[(OH)_8Si_4O_{10}]$	$C2/m$	95	6	this study
	Talc	natural	$Mg_3Si_4O_{10}(OH)_2$	$C\bar{1}$	?	6	Bradley et al. 1999
	Talc	natural	$Mg_3Si_4O_{10}(OH)_2$	$C\bar{1}$	?	6	Li et al. 1999
48.	Phlogopite	Franklin, USA	$KMg_3[(F,OH)_2Si_3AlO_{10}]$	$C2/m$	99	6	Tombolini et al. 2003
49.	Tetra-ferriphlogopite	Tapira,BR	$K(Mg,Fe)_3[(OH)_2Si_3FeO_{10}]$	$C2/m$	91	6	Tombolini et al. 2003
50.	Biotite	Colli Euganei, I	$K(Mg,Fe,Ti)_3[(OH,F)(Si,Al)_4O_{10}]$	$C2/m$	54	6	Mottana et al. 2000
51.	Clintonite	Lago d. Vacca, I	$Ca(Mg,Al)_3[(OH)_2(Si,Al,Fe^{3+})_4O_{10}]$	$C2/m$	75	6	Mottana et al. 2000
52.	Vermiculite	Delaware, USA	$Mg_x(H_2O)_n.(Mg,Al,Fe)_2[(OH)_2(Si,Al)_4O_{10}]$	$C2/m$	?	6	this study
	Montmorillonite	natural	$Na_{0.4}(Al,Mg)_2Si_4O_{10}.nH_2O$	?	?	6	Li et al. 1999
	Hectorite	natural	$Na(Mg,Li)[(OH)_2Si_4O_{10}]$	?	?	6	Bradley et al. 1997
53.	Clinochlore	Borgotaro, I	$(Mg,Al,Fe^{3+},Fe^{2+})_5[(OH)_8Si_4O_{20}]$	$C\bar{1}$	71	6	this study
54.	Corrensite	Borgotaro, I	$Ca_{.2}(Mg,Fe^{3+},Fe^{2+},Al)_5[(OH)_5AlSi_3O_{25}]$	?	83	6	Brigatti et al. 2000
	Granddidierite	natural	$(Mg,Fe)Al_3SiBO_9$	$Pbnm$	?	5	Li et al. 1999
55.	Granddidierite	Madagascar	$(Mg_{.94}Fe_{.06})Al_3SiBO_9$	$Pbnm$	94	5	this study
	Yoderite	natural	$[6](MgAl_3)[5](MgAl)[5](Al_{.84}Fe_{.16})_2[O_2(SiO_4)_4(OH)_2]$	$P2_1/m$	?	5+6	Li et al. 1999
56.	Yoderite	Mautia Hills, TZ	$Mg_2Ca_{.2}Fe_{.5}Al_{5.3}[Si_4O_{18}(OH)_2]$	$P2_1/m$	31+21	5+6	this study
	Spinel	natural	$MgAl_2O_4$	$Fd3m$	?	4	Li et al. 1999
57.	Spinel	Burma	$MgAl_2O_4$	$Fd3m$	99	4	this study
58.	Mg-chromite	Scottie Creek,CDN	$(Mg_{.71}Fe_{.32})_{1.03}(Cr_{1.41}Al_{.52}Fe_{.07})_2O_4$	$Fd3m$	70	4	this study

Sample: IMA approved mineral name
Locality: geographical indication and country where the examined sample is from
Formula: idealized or simplified to the closest meaningful value (see text)
Space group: determined by crystal structure refinement (see text)
Mg#: effective percent occupancy of the structural site(s)
N.C.: theoretical coordination number (as determined by the structural refinement)
Reference: published presentation of the XAS spectrum (see text)
(?): Data not found/not available.

Table 3: *Mg K-edge XANES spectra of model compounds and minerals reported in the literature and not used in text, or referred to only for comparison.*

Material	origin	Simplified formula	Reference	C.N.
Magnesium	synthetic	Mg	Bradley et al. 1985	12*
Pyrope	synthetic	$Mg_3Al_2[SiO_4]_3$	Henderson et al. 1992	8
Pyrope	synthetic	$Mg_3Al_2[SiO_4]_3$	Ildefonse et al. 1995	8
Pyrope	?	$Mg_3Al_2[SiO_4]_3$	Wong et al. 1997	8
Brucite	synthetic	$Mg(OH)_2$	Shiono et al. 1998	6
Brucite	synthetic	$Mg(OH)_2$	Yoshida et al. 1994, 1998	6
Diopside	synthetic	$CaMgSi_2O_6$	Henderson et al. 1992	6
Diopside	natural	$CaMgSi_2O_6$	Ildefonse et al. 1995	6
Diopside	synthetic	$CaMgSi_2O_6$	Li et al. 1997	6
Enstatite?	synthetic	$MgSiO_3$	Shiono et al. 1998	6
Enstatite?	synthetic	$MgSiO_3$	Yoshida et al. 1994	6
Forsterite	synthetic	Mg_2SiO_4	Henderson et al. 1992	6
Forsterite	synthetic	Mg_2SiO_4	Yoshida et al. 1994	6
Forsterite	synthetic	Mg_2SiO_4	Shiono et al. 1998	6
Geikielite	?	$MgTiO_3$	Kosaka et al. 2000	6
Hydrotalcite	synthetic	$Mg_6Al_2(OH)_{16}CO_3.4H_2O$	Yoshida et al. 1999	6
Periclase	synthetic	MgO	Lindner et al. 1986	6 *
Periclase	synthetic	MgO	Davoli et al. 1988	6
Periclase	synthetic	MgO	Henderson et al. 1992	6
Periclase	synthetic	MgO	Yoshida et al. 1994, 1998	6
Periclase	synthetic	MgO	Ildefonse et al. 1995	6
Periclase	synthetic	MgO	Schonberger & Aryasetiawan 1995	6*
Periclase	synthetic	MgO	Kinoshita et al. 1997	6
Periclase	synthetic	MgO	Takata & Kosugi 1999	6
Periclase	synthetic	MgO	Kosaka et al. 2000	6
Periclase	synthetic	MgO	Mizoguchi et al. 2000	6
Periclase	synthetic	MgO	Mizoguchi et al. 2000	6*
Periclase	synthetic	MgO	Takata et al. 2001	6
Periclase-zincite s.s.	synthetic	$(Mg,Zn)O$	Mizoguchi et al. 2000	6
Åkermanite	synthetic	$Ca_2MgSi_2O_7$	Henderson et al. 1992	4
KMg-leucite	synthetic	$K_2MgSi_5O_{12}$	Henderson et al. 1992	4
Mg-Si compound	synthetic	$Mg_2Si_3O_8$	Yoshida et al. 1994	4
Mg-Si compound	synthetic	$Mg_2Si_3O_8$	Shiono et al. 1998	4
RbMg-leucite	synthetic	$Rb_2MgSi_5O_{12}$	Henderson et al. 1992	4
Spinel	synthetic	$MgAl_2O_4$	Henderson et al. 1992	4
Spinel	synthetic	$MgAl_2O_4$	Yoshida et al. 1994	4
Spinel	synthetic	$MgAl_2O_4$	Ildefonse et al. 1995	4
Spinel	?	$MgAl_2O_4$	Kosaka et al. 2000	4

(*) Electron-energy-loss near-edge structure (ELNES) spectrum. (?) Data not found/not available.

Frascati Physics Series Vol. XXXII (2003), pp. 151-162
19th INTERNATIONAL CONFERENCE ON X-RAY AND INNER-SHELL
PROCESSES – Roma, June 24 - 28, 2002

SMALL-ANGLE X-RAY SCATTERING STUDY ON THE CONFORMATION OF POLYSTIRENE IN COMPRESSED CO_2 -TOLUENE MIXTURE

Baozhong Dong, Lixia Rong, Yi Liu
Institute of High Energy Physics,
Chinese Academy of Science, Beijing 100039,China
Dan Li, Buxing Han, Zhimin Liu, Guanying Yang
Center for Molecular Science, Institute of Chemistry,
Chinese Academy of Science, Beijing 100080,China

ABSTRACT

Synchrotron radiation Small-angle X-ray Scattering (SAXS) was used to investigate the effect of dissolved CO_2 in toluene on the conformation of polystyrene (PS) in the solution. It was found that the second virial coefficient A_2 and the radius of gyration R_g decreases with the increasing of antisolvent pressure. Fractal geometry is a powerful tool for describing structure of the polymer chain. Scattering technique represents a powerful method for measuring the fractal dimensions of a microscopic structure. Self-similar structure behavior was also observed with a detailed analysis of scattering intensity. Increase of fractal dimension with the increasing of the antisolvent pressure indicates that the polymer chain changes from a swollen coil to a rather dense globule in the course of adding antisolvent CO_2.

1 Introduction

Compressed fluids, including supercritical fluids, have been used in polymer separation and purification processes such as extraction and fractionation[1], impregnation of polymers with additives, and conditioning polymer films[2,3]. CO_2 is a desirable solvent for polymer processing since it is nontoxic, nonflammable, and inexpensive. After processing, CO_2 can be removed from the polymers completely simply by decreasing the pressure.

The use of compressed CO_2 for fine particle formation is a rapidly developing field of research. [1] The gaseous antisolvent (GAS) process is one of the most important ones.[4] The possibility of obtaining solvent free microparticles with narrow size distribution makes this technology especially attractive. Dissolution of gas causes a volume expansion of the solvent and lowers solvent power, which forces the solute to precipitate. To date, GAS processes have been successfully used in the recrystallization of organic solids [5,6], the fractionation of natural products, [7,8] the preparation of ultrafine particles et al.[9−14]. We are very interested in the polymer conformation in GAS process, since the solubility of a gas in an organic solvent can be tuned by pressure and temperature, accordingly, the polymer morphology be tailored. The investigation to this problem has both practical and theoretical importance.

It is well known that small angle X-ray scattering (SAXS) is useful technique for studying polymer solutions. SAXS can provide information about apparent mean-square radius of gyration $\langle Rg^2 \rangle^{1/2}$ and the second virial coefficient (A_2), which are related with the conformation of the polymer and intermolecular interaction in the solution, respectively[15]. Some papers have been published for studying polymer solutions by SAXS in the absence of gas antisolvent[16−19].
In this work, SAXS is used to study the conformation of polystyrene (PS) chain in PS-toluene solution in the presence of antisolvent CO_2.

2 Experimental Section

Materials. The polystyrene (PS) (M_w=7.8 × 10^4) with narrow molecular weight distribution of 1.1was kindly supplied by State Key Laboratory of Polymer Science, Institute of Chemistry, Chinese Academy of Sciences. Toluene (AR grade) was produced by Beijing Chemical Factory. The PS/toluene so-

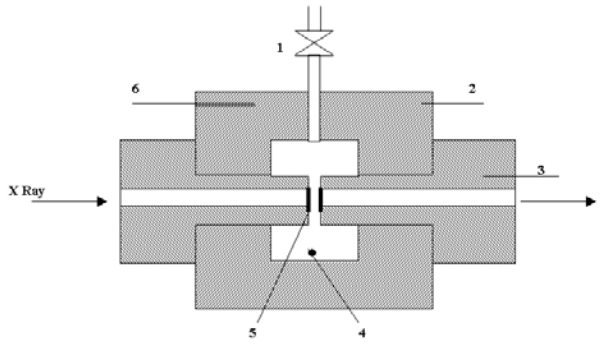

Figure 1: *Schematic diagram of the SAXS cell. 1.ball valve; 2. stainless-steel body; 3.nut; 4.stirrer; 5.diamond window; 6. thermometer probe*

lutions were prepared by gravimetric method. The original concentrations C_0 (CO_2-free) in our study were 4.6×10^{-4}, 6.9×10^{-4}, 1.07×10^{-3}, 3.2×10^{-3} and 9.2×10^{-3} g/cm^3.

SAXS Experiments. The experimental apparatus for the SAXS study was consisted mainly of a gas cylinder, a high-pressure pump, a digital pressure gauge, a high-pressure SAXS cell, a thermometer, a temperature controller, and valves and fittings of different kinds. The pressure gauge with an accuracy of °¿0.025Mpa consisted of a transducer (FOXBORO /ICT) and an indicator. The schematic diagram of the temperature-controlled SAXS cell is shown in Figure1. It was composed mainly of a stainless steel body and two diamond windows of 8 mm in diameter and 0.4 mm in thickness. The cell body was coiled with an electric heater and heat-insulate ribbon outside, which is not shown in Figure 1. The X-ray path length of the cell was 1.5 mm and the internal volume of the cell was 2.7 cm^3. There was a small magnetic stirrer in the cell to stir the fluids before the SAXS measurements, so that the equilibrium could be reached in a shorter period of time. The insulated cell was electrically heated to ±0.1 K of the desired temperature by using a temperature controller.

SAXS experiments were carried out at Beamline 4B9A at the Beijing Synchrotron Radiation Facility, using a SAXS apparatus constructed at the station. A detailed description of the spectrometer was given elsewhere[20]. The detector for SAXS data collection is image plate (IP) system Fuji BAS-2500,

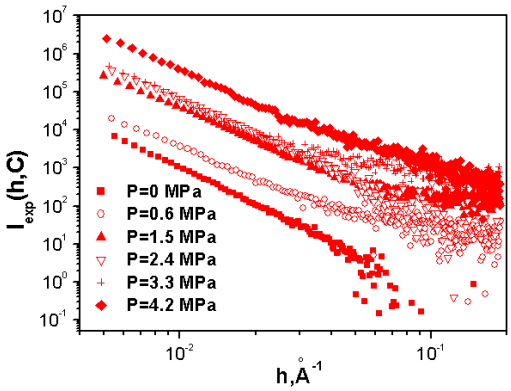

Figure 2: *Effect of antisolvent CO_2 pressure on SAXS spectra of the solution (C=.0.00046g/cm^3)*

with an active area of 400mm by 200mm and a minimum pixel size of 50 μm. The experiments had an angular resolution of better than 0.5mrad with this setting. The data accumulation time was 3 minutes. The angular range was chosen so as to provide data from h=0.005 Å^{-1} to h=0.15 Å^{-1}, where the magnitude of scattering vector $h=2\pi sin\theta/\lambda$ and θ and λ being respectively the scattering angle and incident x-ray wavelength of 1.54Å. Background scattering from the slit collimator, the solvent, and the residual air path between the vacuum chamber and the detector was measured and subtracted. It should be mentioned that for each measurement the solvent with antisolvent CO_2 at the same temperature and pressure was used as the background solvent, so that we could obtain the information of polymer chain. Excess SAXS scattering from PS solute were also corrected for incident beam decay and transmission.

Before the experiment, SAXS cell was flushed with CO_2, and then suitable amount of PS/toluene solution was filled into the cell. CO_2 was charged into the cell with stirring at the temperature of interesting. The cell was connected to the SAXS apparatus after the equilibrium was reached and the X-ray scattering was recorded.

3 SAXS Data Processing

3.1 Radius of Gyration and Second Virial Coefficient

Its scattering curve is obtained by subtracting the scattering of the solvent + antisolvent (background scattering) from the scattering of the polymer+solvent + antisolvent solution.

The scattering intensities I_{exp}(h,C) measured as a function of momentum transfer h and polymer concentration C of the polymer, usually expressed in g/cm^3, may be treated according to Zimm and Flory and Bouche [15]

$$\frac{KC}{I_{exp}(h,C)} = \frac{1}{M_w I_n(h)} + 2A_2 Q(h)C + ... \tag{1}$$

where K is the optical constant, A_2 is the second virial coefficient, M_w is molecular weight of the dissolved polymer, and I_n(h) is the single particle scattering function. Q(h) and I_n(h) are normalized in such a way that $I_n(0)=1$ and $Q(0)=1$. The first term in right side of equation (1) is merely due to intramolecular interference, whereas the higher term reflect the influence of the intermolecular interference.

To a first approximation, we only consider the first two terms of the right side in equation (1). From equation (1), if $h \sim 0$, we can also obtain the equation[15]

$$\lim_{c\to 0} \frac{KC}{I_{exp}(h,C)} = \frac{1}{M_w}(1 + 2A_2 M_w C) \tag{2}$$

or

$$\frac{1}{M_w C} = -2A_2 + \frac{K}{I_{exp}(0,C)} \tag{3}$$

K and A_2 can be obtained from the slope and intercept of $1/M_wC$ vs. $1/I_{exp}(0,C)$ plot. If C°˙0, we can obtain the equation [15]

$$\lim_{c\to 0} \frac{KC}{I_{exp}(h,C)} = \frac{1}{M_w I_n(h)} = \frac{1}{M_w}(1 + \frac{< R_g^2 >}{3} h^2) \tag{4}$$

The initial slopes of equation (4) vs. h^2 yield the mean square radius of gyration <Rg^2>.

3.2 Fractal Dimension

The concept of fractal geometry is an useful tool to describe the polymer sructure[21,22]. SAXS technique represents a powerful method for measuring the fractal dimensions of a microscopic structure[23]. A characteristic feature of the small-angle scattering from fractal scatterers is that when $hl \gg 1$,

$$I(h)\ h^{-\alpha} \tag{5}$$

where l is the average diameter of a scatterer, and α are positive constant. In this case, the fractal dimension can be determined from the slope of $ln(I_h)$ vs $ln(I_h)$ curves.

Two kinds of fractal disordered solid or liquid systems have been studied by small-angle scattering: These fractal systems are called mass-fractals and surface fractals[24]. For mass fractals $0 < \alpha < 3$, while $3 < \alpha \leq 4$ for surface fractals. Thus small-angle scattering determinations of the α can be used to distinguish between mass and surface fractals in a monodisperse system of scatterers.

Mass fractals are aggregates of primary particles or submits. The distributions of mass $M(r)$ in a mass fractal has the property that the mass inside a spherical surface of radius r is given by

$$M(r) = M_0 r^{D_m} \tag{6}$$

where D_m is the mass fractal dimension. For mass fractals that are connected solids (i.e. , not made up of isolated points), the meaningful values of D_m fall in the interval $1 \leq D_m < 3$ and $D_m = \alpha$

Surface fractals, on the other hand, consist of one or more fractal surface that have a fractal dimension D_s. When the area is measured by covering the surface with the smallest possible number $N(r)$ of balls with radius r and thus with a cross-sectional area πr^2, the measured area $A(r)$ can be written

$$A(r) = A_0 r^{2-D_s} \tag{7}$$

where A_0 is a constant, and D_s is the fractal dimension of the surface fractal. The meaningful values of D_s lie in the interval $2¡=D_s¡3$ and $D_s=6\text{-}\alpha$.

4 Results and Discussion

In this work, We determined scattering intensity at original PS concentrations of 4.6×10^{-4} g/cm^{-3}, 6.9×10^{-4} g/cm^3, 1.07×10^{-3} g/cm^3, 3.2×10^{-3}g/cm^3, and 9.2×10^{-3} g/cm^3 and the different antisolvent CO_2 pressures. As examples, Figures 2 shows double logarithm plot of scattering intensity I_{exp}(h,C) versus scattering vector h at $C_0=4.6\times10^{-4}$ g/cm^3 and different antisolvent CO_2 pressures, with I_{exp}(h,C) being the scattered intensity due to the PS solute.
The scattering intensity increases with the increasing of antisolvent pressure. We have known that the X-ray scattering is due to the contrast provided by the difference in electron densities in the solute and solvent. The increasing of the scattering intensity may result from the aggregation of the polymer chain.

Figure 3 shows double logarithm plot of I_{exp}(h,C) versus h for PS/toluene solutions of different original concentrations at 2.4 MPa. The magnitude of the polymer concentration effect depends on the shape and charge of the particle and the solvent. No general function exists which would allow prediction of the magnitude of the concentration effect. From figure 3, we can say that concentration has large effect on the scattering of polymer solution.
To use equation (3) to get A_2 and K at different antisolvent pressures, the double logarithm scattering intensity plots of I_{exp}(h,C) vs. h at different concentrations were obtained using the experimental data. The concentration C has been corrected for the volume expansion. The data were extrapolated to h=0, and the values of I_{exp}(0,C) were obtained. Figure 4 shows the $1/M_wC$ vs. I_{exp}(0,C) curves which are linear in the concentration range studied in this work. This verifies that we can get reliable results although we only considered the first two terms in the right side of equation (1). Thus K and A_2 at different antisolvent pressures were easily obtained from slope and intercept of $1/M_wC$ vs. I_{exp}(0,C) curves, and the results are listed in Table 1.
The second virial constant A_2 is related with the solvent power of the solvent for the polymer. As expected, A_2 depends on the partial pressure of antisolvent CO_2. A_2 decreases with increasing antisolvent pressure, which indicates that the solvent power of toluene to PS decreases with adding of antisolvent CO_2.
To calculate the mean square radius of gyration <Rg^2> using equation (4), the data for $KC/I_{exp}(h,C))_{C=0}$ are required. To do this, KC/I_{exp}(h, C) is plotted against C. KC/I_{exp}(h, C) vs C curves were extrapolated to zero concentration and $(KC/I_{exp}(h,C))_{C=0}$ was obtained. $(KC/I_{exp}(h,C))_{C=0}$ vs h^2 curves are

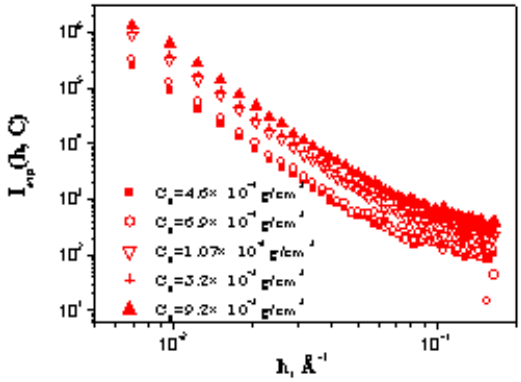

Figure 3: *Effect of original solution concentration (C_0) on SAXS spectra of the solutions at antisolvent CO_2 pressure of 2.40MPa.*

Table 1: *Values of K, A_2 ,and $\langle Rg^2 \rangle^{1/2}$ of PS at different pressures*

Pressure MPa	**K cm^{3}mol/g^2**	**A_2 cm^{3}mol/g^2**	**$\langle Rg^2 \rangle^{1/2}$Å**		D
0	34.72	0.00051	95.5	3.12	2.88
0.6	22.00	0.00048	92.8	2.53	2.53
1.5	17.85	0.00044	89.0	2.74	2.74
2.4	15.36	0.00038	86.3	2.80	2.80
3.3	13.35	0.00034	78.4	2.93	2.93
4.2	11.97	0.00030	71.3	2.98	2.98

linear, as shown in Figure 5. Thus $\langle Rg^2 \rangle^{1/2}$ can be evaluated from their slopes as can be known from eq. (4). The results are given in Table 1.

As shown in Table 1, $\langle Rg^2 \rangle^{1/2}$ decreases with increasing pressure. It indicates that the PS chain experience shrinking in the course of adding antisolvent CO_2. Toluene is a good solvent for PS and the coil expanded due to prevailing intersegmental repulsion; after adding CO_2, the solvent power of the solvent is reduced and PS chain is shrunk due to prevailing intersegmental attraction.

Using eq. (5) to obtain the fractal dimension D of the PS/toluene solutions at different antisolvent pressures, the plots of ln I_{exp}(h,c) vs ln h at C_0=4.6×10^{-4} g/cm^3 were obtained and shown in figure 6. The α can be determined from the slope of ln I_{exp}(h,c) vs ln h curves. The α and D of PS/toluene solutions at different antisolvent pressures are listed in Table 1. These results are a clear indication for self-similar structures, which is frequently called

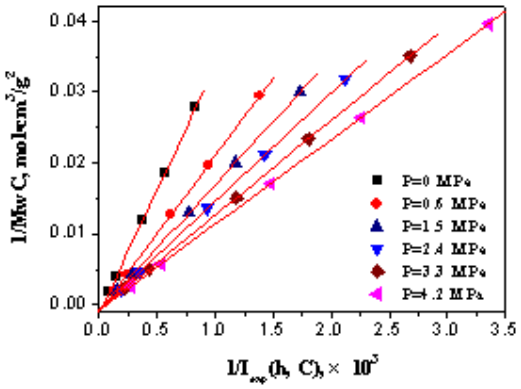

Figure 4: *Plots of $1/M_w$ against $1/I_{exp}(0,C)$ at different antisolvent pressures.*

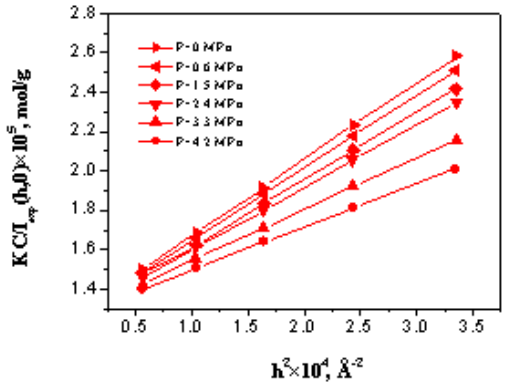

Figure 5: *Plots of $(KC/I_{exp}(h,0)$ against h^2 for PS in toluene at different antisolvent CO_2 pressures.*

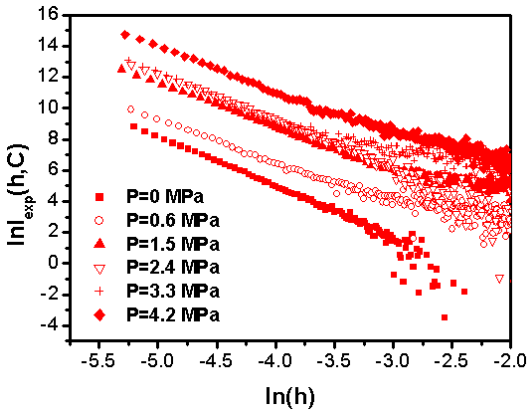

Figure 6: *Plots of ln $I_{exp}(h,C)$ vs ln(h)at different antisolvent CO_2 pressures for PS/toluene solutions (C_0 =0.00046 g/cm^3)*

fractals with the values of D=2.88, 2.53, 2.74, 2.80, 2.93, and 2.98. A fractal dimension of 2.53∼2.98 is characteristic of a polymer chain that has an internal structure between a hard sphere(D=3.0) and a fully swollen randomly coiled macromolecule in a thermodynamically good solvent (D=2.0)[25]. As can be seen from Table 1, the fractal dimension increases with increasing antisolvent CO_2 pressure, indicating collapse of polymer chain from a coil to a rather dense globule form in the course of adding antisolvent CO_2.

5 ACKNOWLEDGMENT

This work was supported by the National Basic Research Project-Macromolecular Condensed State and the National Natural Science Foundation of China(29633020, 29725308).

References

1. McHugh, M. A., and Krukonis, V. J., Supercritical Fluids Extraction Principles and Prantice, 2nd Ed., Stoneham, MA: Butterworth-Heinemann, 1994, pp 189.

2. Li, D., and Han, B. X., Macromolecules 33, 4555-4560 (2000).

3. Arora, K. A., Lesser, A. J., McCarthy, T. J., Macromolecules 32, 2562(1999).

4. Eckert, C. A., Knutson, B. L., Debenedetti, P. G. , Nature 383, 313(1996).

5. Gallagher, P. M., Coffey, M. P., Krukonis, V. J. , J. Supercrit. Fluids 5, 130(1992).

6. Robertson, J., King, M. B., Swcille, J. P. K., Merrifield, D. R., Buxton, P. C., Proceedings of the 4^{th} International Symposiums on Supercritical Fluids, 1997, pp 47.

7. Shishikura, A. Proceedings of the 4^{th} International Symposiums on Supercritical Fluids, 1997, pp 51.

8. Catchpole, O. J., Hochmann S., Anderson, S. R. J., High Pressure Chemical Engineering, Ph. Rudolf von Rohr and Ch. Trepp (Eds.), 1996, pp 309.

9. Reverchon, E., Della Porta, G., Sannino, D., Ciambelli, P., Powder Technology 102, 127(1999).

10. Reverchon, E., J. Supercrit. Fluids 15, 1(1999).

11. Dixon, D. J., Johnston, K. P., J. Appl. Polym. Sci. 50, 1929 (1993).

12. Mawson, S., Johnston, K. P., Betts, D. E., McClain, J. B., DeSimone, J. M., Macromolecules 30, 71(1997).

13. Luna-Barcenas, G., Kanakia, S. K., Sanchez, I. C., Johnston, K. P., Polymer 36, 3173(1995).

14. Yeo, S.-D., Debenedetti, P. G., Radosz, M., Giesa, R., Schmidt, H.-W., Macromolecules 28, 1316(1995).

15. Glatter, O., and Kartky, O., Small Angle X-ray Scattering, academic press, New York, 1982.

16. McClain, J. B., Londino, D., Combes, J. R., Romack, T. J., Canelas, D. A., Betts, D. E., Wignall, G. D., Samulski, E. T., DeSimone, J. M., J. Am. Chem. Soc. 118, 917(1996).

17. Hayashi, H., Hamada, F., Nakajima, A., Macromolecules 7, 959(1974).

18. Yoon, D. Y., Flory, P. J., Macromolecules 9, 294(1976).

19. Hyman, A. S., Macromolecules 8, 849(1975).

20. Liu, Y., Dong, B. Z., Wang, J., Ding Y. F., Wu Z. H., High Energy Physics and Nuclear Physics, 26, 87(2002).

21. Mandelbrot, B. B., The Fractal Geometry of Nature, Freeman: New York, 1983

22. Sander, L.M., Nature 322,789(1986)

23. Vicsek, T., Fractal Growth Phenomena, Singapores: World Scientific, 1989, pp. 72

24. Pfeifer, P., and Obert, M., In The Fractal Approach to Heterogeneous Chemistry, edited by D. Avnir, pp. 11-43. Chichester, England: Wiley

25. Stauffer, D., Coniglio, A., Adam, M. Adv. Polym. Sci. 44, 103(1982).

Frascati Physics Series Vol. XXXII (2003), pp. 163-171
19th INTERNATIONAL CONFERENCE ON X-RAY AND INNER-SHELL
PROCESSES – Roma, June 24 - 28, 2002

STUDIES OF VALENCE BAND STRUCTURE OF LITHIUM COMPOUNDS BY XAS AND XPS

Y. Iwata, K. Maeda, M. Fujita, J. Tsuji
Division of Electronics and Applied Physics,
Osaka Electro-Communication University,
18-8 Hatsu-cho, Neyagawa, Osaka 572-8530, Japan
D. Sawa
SR Center, Ritsumeikan University,
1-1-1 Noji-Hagashi, Kusatsu, Shiga 525-8577, Japan
N. Ozawa, T. Yao
Graduate School of Energy Science, Kyoto University,
Yoshida, Sakyo-ku, Kyoto 606-8501, Japan
K. Kojima, S. Ikeda
SR Center, Ritsumeikan University,
1-1-1 Noji-Hagashi, Kusatsu, Shiga 525-8577, Japan
K. Taniguchi
Division of Electronics and Applied Physics,
Osaka Electro-Communication University,
18-8 Hatsu-cho, Neyagawa, Osaka 572-8530, Japan

ABSTRACT

In this work, the Li-XAS (X-ray Absorption Spectra) and Li-XPS (X-ray Photoelectron Spectroscopy) spectra of various lithium compounds are measured and studies from the viewpoint of industrial materials that are compound of the lithium atom. The obtained spectra are compared with the theoretical spectra by means of the molecular orbital calculation and discussed. It is clarified that the energy position of a first sharp peak shifts to higher energy side depending on the decrease of the electronegativity or solubility.

1 Introduction

The materials composed of the lithium atom mainly are applied to the industrial application as rechargeable lithium ion batteries, lithium polymer batteries

and glass materials. For the investigation of the characterization of those materials, EXAFS (Extended X-ray Absorption Fine Structure) and XPS (X-ray Photoelectron Spectroscopy) spectra are used as one of the analysis method. By those analyses, the informations of the local structure and the valence band structure in the materials are obtained. For example, in the case of the rechargeable lithium ion battery, the EXAFS spectra of various transition metals (Mn, Co and Ni) in the positive electrode materials were measured, and the conformational change due to the charge and discharge cycles was investigated [1, 2, 3, 4]. And in also the carbon materials of the negative electrode, its conformational change was investigated by means of the C K-edge XANES spectra [5, 6]. Valence band structure for the positive electrode materials was investigated by XPS method [7, 8]. However it is difficult to observe the Li 1s peak in the positive electrode materials by XPS. This is because the Li 1s peak overlaps the background of the 3p peak of the transition metal in the positive electrode materials. When the Mg-Kα line is used as the excitation source in XPS measurement, the photoionization cross section of the transition metal 3p electron is higher than that of the Li 1s electron. In addition, the energy shift of the peak due to the structural change is too small to be observed, though the valence band structure of the occupied level can be observed directly in XPS.

In this work, the Li-XAS (X-ray Absorption Spectra) and Li-XPS spectra of various lithium compounds (lithium halides, Li_2O, Li_2S, LiOH-H_2O, Li_2CO_3, Li_2SO_4 and $LiNO_3$) are measured and studied from the viewpoint of industrial materials. The obtained spectra are compared with the theoretical spectra by means of the molecular orbital calculation and discussed. From the discussion of the charge transfer of the Li atom in the compounds, the ionic bonding strength of each compound can be found.

2 Experimental

Li-XPS spectra are measured by ESCA 1000 (SHIMAZU). The experimental spectra are obtained with 0.1 eV step and 60 sec/point. Mg-Kα (1253.6 eV) line as the excited source is selected. Mg-Kα is operated by 10 kV as applied voltage and 30 mA as emission current. The energy in spectra are calibrated by C-1s (285 eV) peak. The measurement samples (lithium halides, Li_2O, Li_2S, LiOH-H_2O, Li_2CO_3, Li_2O_4 and $LiNO_3$) are powders bought from Wako

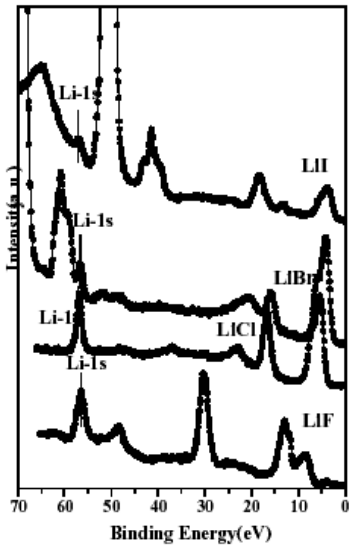

Figure 1: *The XPS spectra of various lithium halide.*

Chemical and those are mounted on an indium sheet.

3 Experimental Results

The XPS spectra of lithium halides are shown in Fig. 1.

In four spectra, the binding energy position of the Li-1s peak shift. The ionic bond strength between lithium atom and halogen atom is very strong. The energy of the peak shift depends on the electronegativity of the halogen atom bonding to the lithium atom. The energy position of Li-1s in LiF, LiCl, LiBr and LiI is 56.4 eV, 56.9 eV, 57.0 eV and 57.3 eV, respectively. For lithium halide, the Li-1s peak of LiF is seen at higher energy side than them of the other lithium halides. In the meantime, the electronegativity of fluorine atom is the highest in the halogen atoms. The relationship between the energy position of the Li-1s and the electronegativity of the halogen atom is shown in Fig. 2. The relation between energy position of Li-1s and the lithium halide is linear.

In Li-XAS (X-ray Absorption Spectroscopy) spectra measured by Tsuji et al [9]. The energy position of peak "a" of LiF, LiCl, LiBr and LiI-2H_2O is 61.9 eV, 60.8 eV, 60.5 eV and 60.1 eV, respectively, In Li-XAS spectra, the

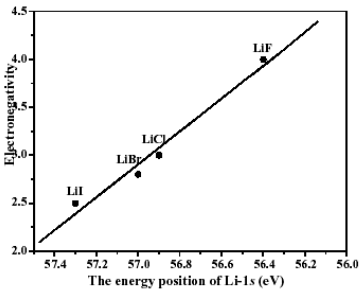

Figure 2: *Relation between Li-1s peak energy and electronegativity of halogen atom.*

relationship between the energy position of each peak and the electronegativity of the halogen atom is approached a linear.

The XPS spectra of Li_2O and Li_2S are shown in Fig. 3. In these compounds, the Li-1*s* peaks shift. The binding energy shift of these peaks of Li_2O and Li_2S depends on the electronegativity of the oxygen atom and sulfate atom bonding to the lithium atom. The energy position of each peak of Li_2O and Li_2S is 57.3 eV and 56.0 eV, respectively. The Li-1s peak of Li_2O is seen at the higher energy side than it of Li_2S. The electronegativity of the oxygen atom is higher than that of the sulfate atom.

The XPS spectra of LiOH-H_2O, Li_2CO_3, Li_2SO_4 and $LiNO_3$ are shown in Fig. 4. In those compounds, the Li-1s peak shifts. The shift of the peak can be discussed simply in electronegativity because of the crystal structure of all lithium halides is NaCl-type. However crystal structure of each oxygen acid lithium compounds is different, Li_2SO_4-monoclinic, LiOH-H_2O-monoclinic, Li_2CO_3-monoclinic and $LiNO_3$-trigonal system. It is difficult to discuss a peak shift by only the oxidation number of oxygen acid ion because the crystal structure of each compound is different. However it may be available to discuss about the solubility. The energy position of Li-1s peak of $LiNO_3$, Li_2SO_4, LiOH-H_2O and Li_2CO_3 are 56.3 eV, 55.7 eV, 55.5 eV and 55.4 eV, respectively. For the oxygen acid lithium compound, the energy position of the Li-1s peak of $LiNO_3$ is the higher energy than that of the other oxygen acid lithium compounds. The solubility of $LiNO_3$ is also higher value than that of the other oxygen acid lithium compounds. The relationship between the en-

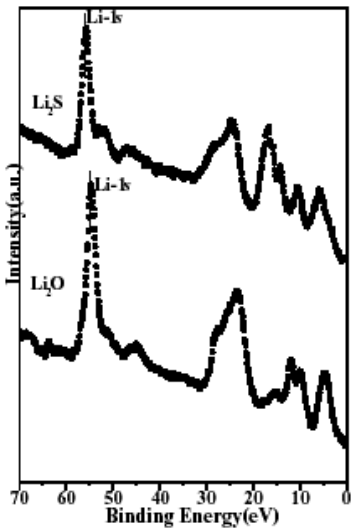

Figure 3: *The XPS spectra of Li_2O and Li_2S.*

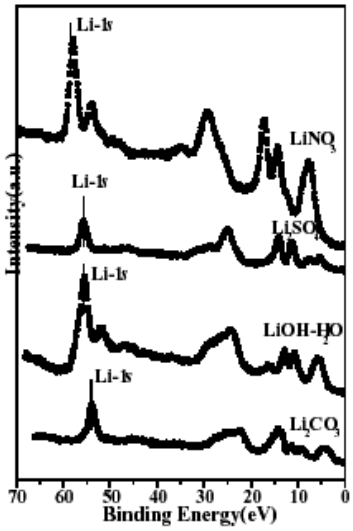

Figure 4: *The XPS spectra of oxygen acid lithium compounds.*

ergy position of each Li-1s peak and the solubility of each compound is shown in Fig. 5. The relation between energy position of Li-1s and the solubility is linear.

The relationship between the energy position of the core exciton peak and the solubility of each compound is shown in Fig. 6. The same result is got with the Li-XAS and Li-XPS. In the oxygen acid lithium compounds, it is found that the energy shift of the Li-1s peak in XPS spectra depends on the solubility of each compound. And the result can be also applied to the core exciton peak of the Li-K x-ray absorption spectra, except for $LiNO_3$.

4 DV-Xα molecular orbital calculation

For lithium halides, Li_2O and Li_2S, DV-Xα molecular orbital calculation is carried out and XPS spectra obtained in this studies are compared with the theoretical spectra. In the calculation, ($LiX_6Li_{12}Li_6$) cluster (X=F, Cl, Br and I) is used (see Fig.7 (a).). The crystal structure of LiX is NaCl-type structure and symmetry orbital used as O_h. The length of a-axis is 0.40173 nm (LiF),

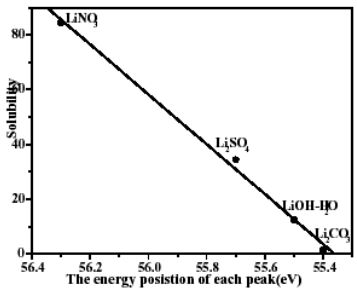

Figure 5: *Relation between Li-1s peak energy and solubility of oxygen acid lithium compounds.*

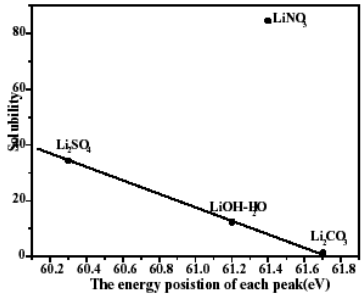

Figure 6: *Relation between first peak energy and solubility of oxygen acid lithium compounds.*

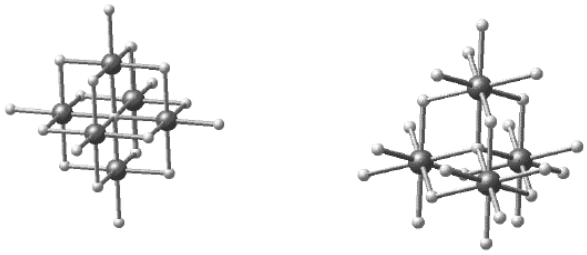

Figure 7: *The schematic drawing of the cluster used in the calculation; (a) ($LiX_6Li_{12}Li_6$) (X=F, Cl, Br,I) and (b) ($LiY_4Li_6Li_{12}$) (Y=O or S).*

0.51396 nm (LiCl), 0.55013 nm (LiBr) or 0.600 nm (LiI). The ($LiY_4Li_6Li_{12}$) (Y=O or S) cluster is used in the calculation of Li_2O and Li_2S (see Fig.7 (b).). The crystal structure of Li_2O and Li_2S is anti-fluorite-type and symmetry orbital used T_d. The length of the a-axis is 0.4619 nm (Li_2O) or 0.5708 nm (Li_2S). Li is put lithium in the solid as precisely as possible. The theoretical spectrum is allow the photoionization cross section. The theoretical spectrum shift to correspond to the experiment spectrum.

4.1 The calculation results

The theoretical spectra of the lithium halides are shown in Fig. 8. The theoretical spectra of Li_2O and Li_2S are shown in Fig. 9. The Li-1s peak in the theoretical spectra shifts as well as the experimental spectra. The ion bonding

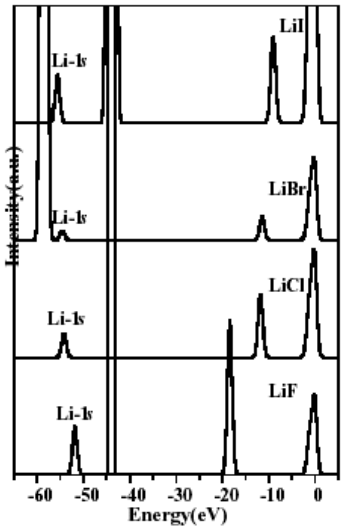

Figure 8: *The theoretical spectra of various lithium halide.*

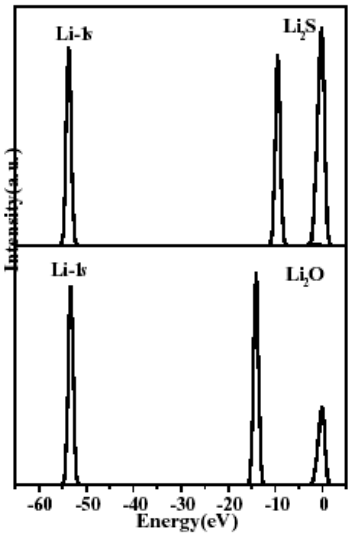

Figure 9: *The theoretical spectra of Li_2O and Li_2S.*

strength between the lithium atom and halogen atom, and the lithium atom and oxygen atom or sulfate atom is very strong. The energy shift of the Li-1s peak depends on the electronegativity of the coordination atom bonding to the lithium. The relationship between the energy position of the Li-1s peak in the theoretical spectra and the electronegativity of bonding lithium is shown in Fig.10. The energy position of each Li-1s peak of LiF,LiCl,LiBr and LiI is -51.9 eV,-54.2 eV, -54.6 eV and -55.6 eV, respectively. And the energy position of each Li-1s peak of Li_2O and Li_2S is -53.3 eV and -53.7 eV, respectively. In the comparison with Fig. 2 (experimental) and Fig. 10 (theoretical), the inclination of the linear in Fig. 2 is similar to that in Fig. 10.

As a result, it is deduced that the theoretical calculation result reproduces the electronic structure in the lithium halides. The charge transfer of each compounds obtained by the theoretical calculation is shown in the Table 1.

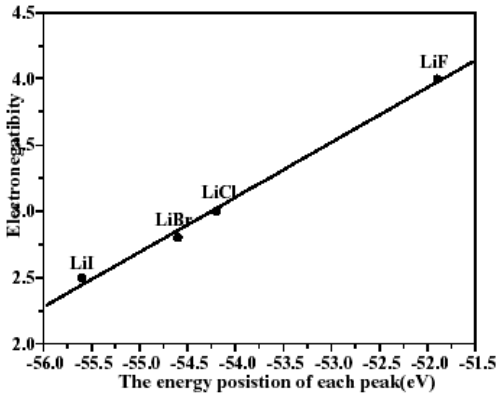

Figure 10: *Relation between Li-1s peak of the theoretical energy and solubility of halogen atom.*

5 Conclusion

In this studies, the XPS spectra of lithium halide, Li_2O, Li_2S and the other lithium compounds ($LiOH{\bullet}H_2O$, Li_2CO_3, Li_3PO_4, $Li_2SO_4{\bullet}H_2O$ and $LiNO_3$) are measured.

The measured XPS spectra are compared with the theoretical spectra calculated by the molecular orbital calculation and studied by using the results of the previous measured Li-XAS. From the discussion of the in the compounds, the ionic bonding strength of each compound can be found. In the future, the molecular orbital calculation of the oxygen acid lithium compounds should be carried out and the charge transfer should be discussed.

Table 1: *The charge transfer of the Li atom*

	LiF	LiCl	LiBr	LiI	Li_2O	Li_2S
Li	0.66237	0.25005	0.12033	0.26017	0.56017	0.06638

References

1. I. Nakai, K. Takahashi, Y. Shiraishi, T. Nakagome, F. Izumi, Y. Ishii, F. Nishikawa and T. Konishi, J. Power Sources **68**, 536 (1997).

2. A. N. Mansour, J. McBreen, C. A. Melendres, J. Electrochem. Soc. **146**, 2799 (1999).

3. B. Ammundsen, M. S. Islam, D. J. Jones and J. Roziere, *J. Power Sources* **81**, 500 (1999).

4. J. M. Rosolen and M. Abbate, Solid State Ionics **139**, 83 (2001).

5. J. R. Dahn, J. N. Reimers, T. Tiedje, Y. Gao, A. K. Sleigh, W. R. McKinnon and S. Cramm, Phys. Rev. Lett., **68** 835(1992)

6. G. Sandi, K. Song, K. A. Carrado and R. E. Winans, Carbon **36**, 1755 (1998).

7. V. R. Galakhov, E. Z. Kurmaev, St. Uhlenbrock, M. Neumann, D. G. Kellerman and V. S. Gorshkov, Solid State Communs **99**, 221 (1996).

8. J. C. Dupin, D. Gonbeau, H. Benqlilou-Moudden, Ph. Vinatier and A. Levasseur, Thin Solid Films **384**, 23 (2001).

9. J. Tsuji, K. Kojima, S. Ikeda, H. Nakamatsu, T. Mukouyama and K. Taniguchi, Journal of Synchrotron Radiation, **8** 554 (2001).

10. K. Taniguchi and J. Tsuji, Functionally Intelligent Materials of Interface Regions, 113 (2000).

Frascati Physics Series Vol. XXXII (2003), pp. 173-178
19th INTERNATIONAL CONFERENCE ON X-RAY AND INNER-SHELL
PROCESSES – Roma, June 24 - 28, 2002

SULFUR K-EDGE XANES STUDY IN IRON SULFIDE.

A.N. Kravtsova, I.E. Stekhin, A.V. Soldatov
Faculty of Physics, Rostov State University, 344090, Rostov-on-Don, Russia
X. Liu, M.E. Fleet
Dept. of Earth Sciences, University of Western Ontario,
London, Ontario, Canada N6A 5B7

ABSTRACT

The S K-edge XANES spectra for FeS (NiAs-type; B8 structure) and for hypothetical FeS (NaCl-type; B1 structure) have been calculated using ab initio full multiple scattering theory. It is found that a good agreement between theoretical and experimental spectra is reached for large cluster of 9 shells for NaCl-type structure of FeS, although a comparatively small cluster of 4 shells appears sufficient for NiAs-type structure of FeS. The comparison of XANES spectra for two phases of iron sulfide is discussed.

1 Introduction

X-ray absorption near-edge structure (XANES) spectroscopy is now a familiar technique for investigation of local and electronic structures of metal sulfides. In particular, XANES region gives information on the lower part of the conduction

band of 3d transition metal sulfides. In present research we study two phases of iron sulfide by XANES spectroscopy.

Iron sulfide has long attracted attention as a transition metal compound with a range of interesting properties. It has hexagonal NiAs-type structure at ambient pressure and temperature. One of the main interests of previous investigations was to establish a model of the band structures of the compound in order to understand its optical, electrical and magnetic properties.

Sugiura and co-workers[1,2,3] ere the first to record the S K-edge and the Fe K-edge absorption spectra of iron sulfides. The first multiple scattering calculation of the S K-edge absorption spectrum of FeS was performed by Kitamura et al [4]. The Fe K-, Fe $L_{2,3}$ and S K X-ray absorption edges have been recorded and are discussed in the terms of the calculated band structures by Womes et al [5]. The S K-edge XANES of the 3d transition monosulfides VS, CrS, MnS, FeS, CoS, NiS were recently investigated by Zajdel [6] and compared with linear muffin-tin orbital (LMTO) numerical calculations. The experimental S K-edge XANES spectra of synthetic niningerite ($Mg_{1-x}Fe_xS$) were presented by Farrell [7]). It was found that iron sulfide changes its structure from NiAS-type (B8 structure) to NaCl-type (B1 structure) influenced by MgS matrix. And solid solution $Mg_{1-x}Fe_xS$ has homogenous rocksalt (B1) structure when x=0-0.68. If x¿0.68 there are two-phase mixtures of $Mg_{0.32}Fe_{0.68}S$ (B1) and FeS (B8). The S K-edge XANES spectrum of the hypothetical cubic (B1) FeS phase has been derived from the spectrum of $Mg_{0.375}Fe_{0.625}S$. At present investigation we calculated the S K-edge XANES spectra of iron sulfide in both B8 and B1 phases in order to establish the changes observing in XANES spectrum when the transition from B8 to B1 phase takes place.

2 Experiment and method of calculation

Sulfur K-edge XANES spectra for $Mg_{1-x}Fe_xS$ were collected at the Canadian Synchrotron Radiation Facility, Aladdin storage ring (University of Wisconsin at Madison, Wisconsin)[7]. The computer code G4XANES and the algorithm of the total multiple scattering method[8] were used to calculate the S K-edge XANES spectra of iron sulfide in both B1 and B8 phases. To estimate phase shifts, we utilized the crystalline muffin-tin potential constructed by means of the Mattheiss scheme with mutually touching spheres. The exchange part of this potential was calculated in the Xα model with the exchange constant equal

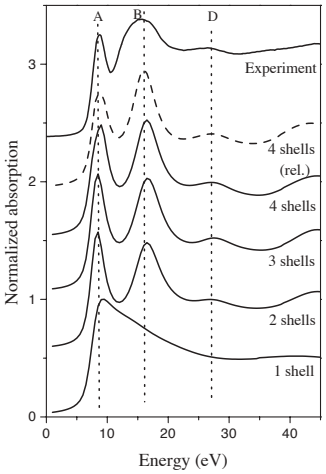

Figure 1: *Comparison of experimental S K-XANES for FeS (B8 phase) with theoretical XANES spectra for different cluster sizes. The theoretical spectra were calculated taking into account all of the broadening factors and Fermi distribution, and the relaxed spectrum was calculated in the Z+1 approximation (dashed line).*

to 0.9. The atomic charge densities were found by the Dirac-Slater method. Phase shifts with the orbital angular momentum up to 3 were taken into account in our calculations. In order to compare the theoretical spectra obtained from the projected density of states and dipole transition matrix element with experimental XANES, one must take into account the Fermi distribution function and three main factors that cause the broadening of the spectra. These factors are: (1) the width of the core hole states, which is 0.59 eV for the S K-edge XANES; (2) the mean free path of the photoelectron function[9]; (3) the experimental energy resolution - 0.9 eV.

3 Discussion

The first step in multiple scattering analysis is to determine the minimum cluster size that would reproduce all the peculiarities of the experimental XANES spectrum. The comparison of experimental XANES with the multiple scattering calculations of the XANES S K spectra in FeS (NiAs-type; B8 structure) for clusters of different sizes are shown in Fig.1. The spectra were ligned rela-

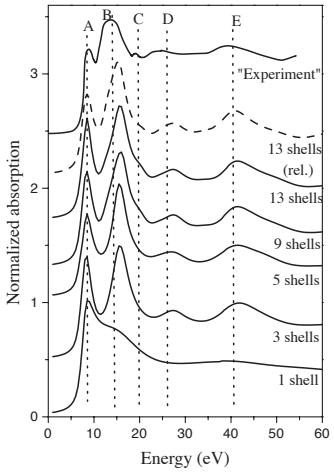

Figure 2: *Comparison of experimental S K-XANES of rocksalt FeS (B1 phase) with theoretical XANES spectra for different cluster sizes. Dashed line correspond to fully relaxed potential calculation.*

tive to the position of peak A. The energy scale is utilized for convenience in comparing the experimental data with calculated spectra, were the zero value of the muffin-tin energy is chosen as the origin of the coordinates. The XANES spectrum consists of a single broad maximum and differs considerable from the experimental spectrum in the case of the cluster consisting of a single coordination shell, where the central sulfur atom is surrounded by six iron atoms. In cluster including two coordination shells we already can see all main details of experimental spectrum, but the peak A is more intensive than peak B while from experimental spectra we can notice that peak B is more extensive than A. The structure of theoretical spectrum consisting of 4 shells agrees well with experimental one. Further increase of the cluster size does not lead to any changes in the spectrum shape. Therefore, the XANES spectrum for the S K-edge in FeS (B8) results from the multiple scattering of an excited photoelectron inside a relatively small cluster of 4 shells (37 atoms). We have calculated XANES spectra in both ground state potential and relax potential (i.e., taking into account the presence of the core hole created by electronic transition). The theoretical S K-edge XANES spectra calculated in both the ground state (unrelaxed) and the Z+1 approximation (fully relaxed) do not differ significantly

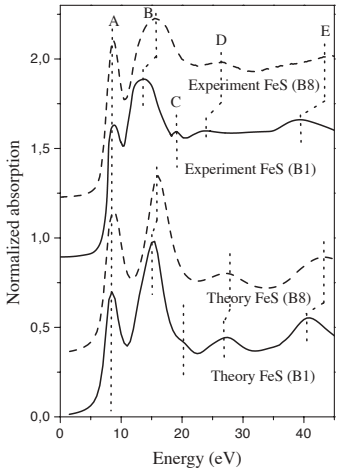

Figure 3: *Comparison of experimental S K-XANES for both rocksalt (B1) FeS and NiAs-type structure (B8) FeS with theoretical relaxed spectra. Dashed lines correspond to B8 structure of FeS, solid lines - B1 structure.*

(although the spectrum calculated in Z+1 approximation agrees slightly better with experimental one in intensity). Figure 2 compares the experimentally derived S K-edge XANES spectrum of FeS (rocksalt; B1 phase) with theoretical spectra calculated for different cluster sizes. The spectra were aligned relative to the position of peak A. The shape of XANES spectrum consisting of one shell doesn't agree with the shape of experimental XANES. The addition of next shells reproduces all details (A, B, D, E) of experimental spectra with the exception of feature C. The theoretical spectrum reproduces the peak C only when the number of coordination shells in the cluster reaches nine shells. Thus, good agreement between theoretical and experimental spectra of NaCl-type of FeS takes place only for large cluster including at least 147 atoms. The calculation taking into account fully relaxed potential does not differ from XANES calculated in ground state potential (Fig.2). The comparison of Figs.1 and 2 shows that good agreement between theoretical and experimental spectra is reached for comparatively small cluster of 4 shells for NiAs-type structure of FeS, although a large cluster of 9 shells appears sufficient for NaCl-type structure of FeS. In Fig. 3, we compare the experimental S K-edge XANES spectra for B1 and B8 phases of $Mg_{1-x}Fe_xS$. The theoretical simulations for these

phases of iron sulfide are also shown in figure 3. One can see that the intensity of peak A of B1 phase spectrum is smaller as compared with the spectrum of B8 phase of FeS. The same behavior is observed in the theoretical spectra. Peak B of B1 phase shifts in the high-energy direction relatively to B8 phase. This displacement occurs in both experimental and theoretical spectra. The experimental XANES spectrum of B1 phase has a peak marked as C, but this detail is absent in experimental spectrum of B8 phase. The same behavior is observed for the theoretical XANES spectra. The features D and E of B1 phase spectrum moves to the long-wave region as compared with B8 phase spectrum details both in theoretical and experimental spectra.

Thus, the structure of $Mg_{1-x}Fe_xS$ solid solution was analyzed. It is known that FeS has hexagonal NiAs-type structure at ambient pressure and temperature. It was found that in solid solution iron sulfide changes its structure from NiAs-type (B8 structure) to NaCl-type (B1 structure) under the influence of Mg matrix. The results of theoretical investigation confirm the existence of cubic NaCl-type phase of FeS in $Mg_{1-x}Fe_xS$ solid solution.

References

1. C. Sugiura et al. Phys. Rev. B **10**, 338 (1974).
2. C. Sugiura. J.Chem. Phys. **74**, 215 (1981).
3. C. Sugiura. J.Chem. Phys. **80**, 1047 (1984).
4. M. Kitamura et al. Solid State Comm. **67**, 313 (1988).
5. M. Womes et al. J. Phys. Chem. Solids. **58**, 345 (1997).
6. P. Zajdel et al. J. Alloys Compounds **286**, 66 (1999).
7. S.P. Farrell et al. Solid State Comm. **113**, 69 (2000).
8. S. Della Longa et al. Comput. Mater. Sci. **4**, 199 (1995).
9. J.E. Muller et al. Solid State Comm. **42**, 365 (1982).

Frascati Physics Series Vol. XXXII (2003), pp. 179-187
19th INTERNATIONAL CONFERENCE ON X-RAY AND INNER-SHELL
PROCESSES – Roma, June 24 - 28, 2002

PHOTOEMISSION STUDY OF Ba^{2+} AND Nd^{3+} SUBSTITUTION FOR Ca^{2+} IN THE BSCCO (2212) SUPERCONDUCTING SYSTEM

Kamlesh Kumari, R.K. Singhal, K.B. Garg
Department of Physics, University of Rajasthan, Jaipur- 302004, India
M. Heinonen, J. Leiro
Applied Materials Science Lab, Department of Physics,
University of Turku, 20014 Turku, Finland
Anurag Gupta and S.K. Agarwal
National Physical Laboratory, CSIR Complex,
Pusa Road, New Delhi 110012, India

ABSTRACT

Photoemission measurements have been made on the BSCCO(2212) superconducting system to understand the effect of substitution of trivalent impurity (Nd) for divalent Ca and the effect of substitution of Ba for Ca. The two systems have been characterized by XRD and resistivity measurements. The measurements are made on the Bi 4f, Sr 3d, Ca 2p, Cu 2p, Ba 3d and O 1s core levels. The spectra show some notable changes in their binding energies and fine structure resulting from the substitution. The results are discussed in terms of their valence and hole density.

1 Introduction

A lot of substitutional studies at different cationic sites have been made to understand the basic mechanisms that govern the superconducting properties

of copper oxides [1, 2, 3, 4, 5, 6, 7]. A widely observed effect with respect to the incorporation of the 3d element is the suppression of Tc with increasing impurity concentration [6, 7, 8]. Our own study on Co-doped BSCCO results in decrease of Tc with increasing Co concentration [9]. The doping of Y at Ca site decreases the Tc as well as the Cu valence [10]. Also, it has been found that rare earth ions doping in Sr site of Bi 2201, is accompanied by incorporation of extra oxygens and enhancement of T_c upto 30 K [11]. By substituting rare earth elements for Ca in Bi-2212, a transition from superconductor to insulator is found to occur with progressive substitutions of rare earths and this transition has been attributed to a decrease in the carrier concentration [12, 13, 14]. Generally, there may be two reasons for superconductor to insulator transition. First, the substitution of trivalent impurity for divalent Ca kills holes and decreases the carrier concentration and second is the substitution of ion having different ionic radius than Ca, inducing pressure effects, thus changing the superconducting properties. It is very interesting to study these two effects separately taking the other as constant. Here, we report a systematic study of the XPS spectra on $Bi_2Sr_2Ca_{1-x}Nd_xCuO_8$ (x= 0.05, 0.2), where the ionic radius of Nd is same as Ca and the valence of Nd is 3+, higher than the Ca and $Bi_2Sr_2Ca_{1-x}Ba_xCuO_8$ (x= 0.05, 0.2) where the valence of Ba is same but the ionic radius of Ba is higher than that of Ca.

2 Experimental

The samples of Nd and Ba doped BSCCO(2212) were prepared by solid state reaction method in a microprocessor controlled furnace (with temperature accuracy of $\pm 1^oC$ at 1000^oC). The starting materials were Bi_2O_3, $SrCO_3$, $CaCO_3$, Nd_2O_3, $BaCO_3$ and CuO powders with the purity of >99.99%. The powders were mixed well and calcined in air at 800^oC for 12 hours. The mixing and calcination were repeated at 810^oC and 815^oC to ensure complete reaction. The reacted powder was then pressed into pellets and heated at 860^oC for 48 hours followed by quenching to liquid nitrogen temperature.

The samples are characterized by XRD and resistivity measurements. The samples were found to be nearly single phase but few impurity peaks were seen in the high doped samples. The resistivity of the samples were measured by four probe method in the temperature range 25-300 K.

The valence band and core level photoemission studies were carried out on

in-house x-ray photoelectron spectrometer. The spectra were taken with non-monochromatic but monoenergetic Al K_α radiation (resolution $\sim$ 0.9 eV and pass energy 35 eV). Energy scale and resolution calibration were made using sputter cleaned gold (Au 4f line at 84.0 eV). The vacuum was 5×10^{-10} torr both in the preparation chamber and measuring chamber. Fresh surfaces needed for the measurements were obtained by mechanically scraping the sample surface in UHV. Scraped and cleaved surfaces showed similar results, so the spectra were taken on scraped surfaces. Scraping was done several times until there was no change in the amount of oxygen and carbon, which indicates surface contamination. No shift due to charging was observed in any of the core-levels recorded.

3 Results and Discussion

From the resistivity measurements, the onset Tc, is found to be nearly same for all the samples ($\sim$90 K). DTc is nearly same for pristine, low Nd doped compound (Nd=0.05) and high Ba doped compound (Ba=0.2), less for low Ba doped compound (Ba=0.05) and large for high Nd doped compound (Nd=0.2). The normal state resistivity also changes with doping. The compound with low Nd doping (Nd =0.05) shows an increase in normal state resistivity and the compound with high Nd doping (Nd=0.2) further show an increase in the normal state resistivity which is evident from the hole quenching by Nd^{3+}. The low Ba doped compound (Ba=0.05) shows a decrease in the normal state resistivity. The normal state resistivity of high Ba doped compound (Ba=0.2) increases as compared to low Ba doped compound but is still lower than the pristine sample.

X-ray photoemission studies have been carried out on the core level electron states of Bi, Ca, Sr, Cu and oxygen and the valence band in the $Bi_2Sr_2Ca_{1-x}Nd_xCuO_8$ (x= 0.05, 0.2) and the $Bi_2Sr_2Ca_{1-x}Ba_xCuO_8$ (x= 0.05, 0.2) systems.

3.1 Bi 4f Core level

Fig. 1(left) shows the Bi 4f core level spectra for various doping concentrations of Ba and Nd. For pure Bi2212, the lower binding energy (LBE) peak is at 158.4 eV and higher binding energy (HBE) peak is at 159.1 eV. The origin of

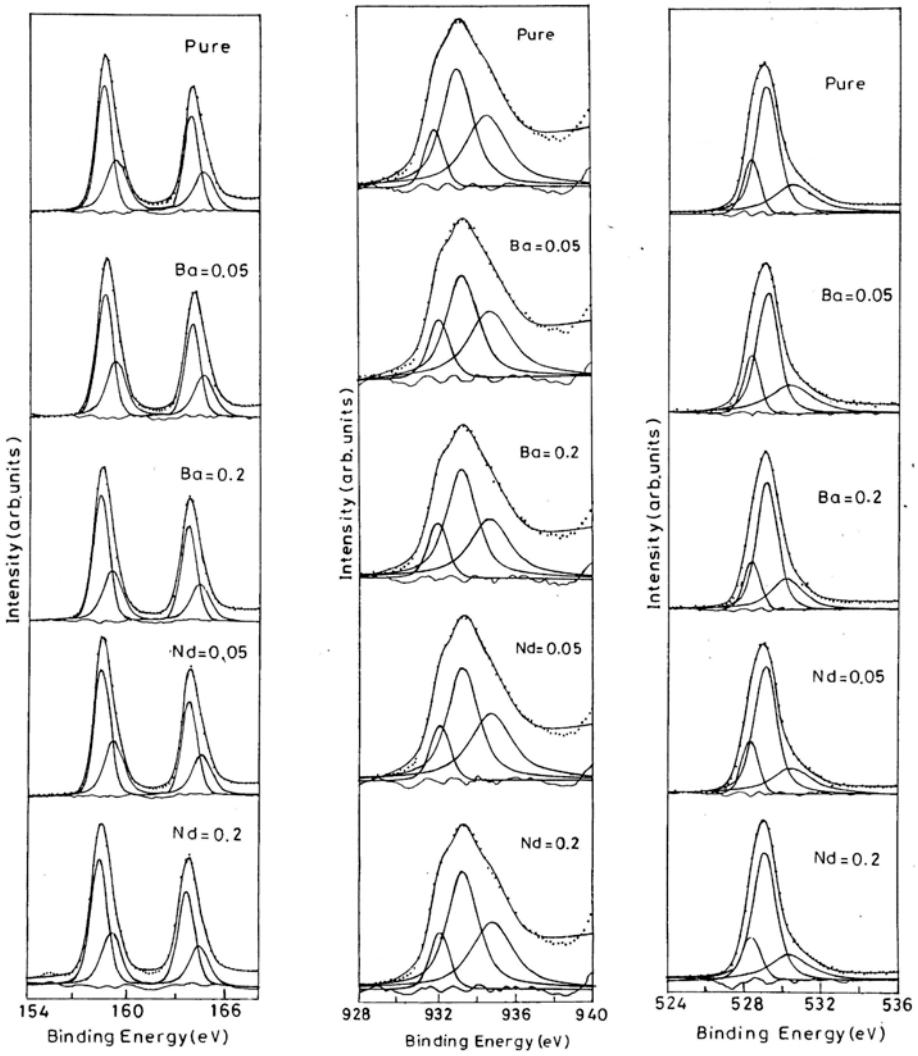

Figure 1: *Bi $4f_{7/2}$ XPS spectra of BSCCO (2212) for different Ba and Nd doping concentrations (left), Cu 2p spectra of BSCCO (2212) for different Ba and Nd doping concentrations (middle) and O 1s XPS spectra of BSCCO (2212) for different Ba and Nd doping concentrations (right)*

the LBE is due to Bi in the Bi-O sheet and the HBE is due to Bi situated between the Bi-O and Cu-O sheets [15]. The LBE peak which appears at 158.4 eV confirms Bi to be at oxidation state of 3+, as we know that for Bi_2O_3, the peak appears at this energy i.e.158.5 eV.

The HBE components are separated by 0.7 eV from the corresponding LBE components. In the case of pure BSCCO(2212) sample (x=0), the intensity contribution from the LBE peak is 71 % of the total intensity, which shows that Bi going to the Bi-O layers is 71 % of the total Bi and Bi going between Bi-O and Cu-O layers is 29%. However, no appreciable shift in the binding energy of LBE and HBE is observed with progressive Ba and Nd doping concentrations. This shows that the average valence of Bi is 3+ and does not change with Ba and Nd doping. There is no systematic change in the ratio of the intensities of the components (ILBE/IHBE) with Ba and Nd doping. Hence, the chemical bond nature of Bi was not affected by Ca site doping. This can be easily understood since Bi lies far away from the superconducting Cu-O_2 planes hardly affecting its chemical bonding.

3.2 Cu 2p core level

The Cu 2p spectra of Ba and Nd doped BSCCO (2212) samples show well-screened spin-orbit split main lines $2p_{3/2}$ (~933 eV) and $2p_{1/2}$ (~953 eV) with their respective satellites at ~9eV from each of them. The main peak, in general, represents the $2p^3d^{10}L$ and $2p^3d^{10}L^2$ final states while the satellite represents the $2p^3d^9$ multiplet final states, where 2p denotes a core hole state and L signifies charge transfer from oxygen ligands to the Cu^{2+} ions. The broad Cu $2p_{3/2}$ main line shows a shoulder at lower binding energy. The Cu $2p_{3/2}$ main line has been deconvoluted and shown in figure 1 (middle). The main peak consists of three components, the central dominant peak at 933.2 eV is due to $2p^3d^{10}L$ final state and the higher binding energy peak at 934.7 eV is due to $2p^3d^{10}L2$ final state which corresponds to Cu being in valence state higher than 2+. Many authors have attributed this to a trivalence state of Cu [16]. The LBE peak at 932 eV shows the presence of Cu^{1+} ($2p^3d^{10}$) and this may originate from some other phase present in the sample in very small amount. The binding energies of the three peaks and their relative area have been shown in the Table 1.

3.3 O 1s Core level

Figure 1(right) shows the O 1s spectra of Ba and Nd doped BSCCO (2212) samples. The spectra consist of three peaks at binding energies at ∼528.3 eV, ∼529.1 eV and ∼530.4 eV in all the samples. The lower binding energy peak at 528.3 eV has its origin from the oxygen atoms from the Sr-O or Cu-O layers [16] and is responsible for superconductivity. The energies and their weightage are given in the Table 1. The peak at energy 529.1 eV has its origin from Bi-O planes and the peak at energy 530.4 eV may arise due to the extra oxygen intercalated between the Bi-O layers [17] or may be due to surface degradation or grain boundary contamination.

Let us first confine attention to the Cu 2p results with reference to the pristine and low doped compounds in Table 1. The observed decrease in the relative area of III peak (originating due to the presence of itinerant holes) with increasing Nd shows that the density of holes decreases with doping Nd. The decrease in the density of holes is due to the hole quenching by the Nd^{3+}. On the other hand, we observe an increase in the relative area of III peak with low Ba doping implying that there is an increase in the density of holes. However, there is a decrease in the relative area of III peak with both high Ba and Nd doping. These two compounds do not appear to be single phase and hence we do not discuss them any further.

These results are also confirmed by the O 1s spectra where we observe three peaks out of which the first peak, which is at 528.3 eV is due to itinerant holes in the samples. Hence, the relative area of first peak is a measure of itinerant holes in the samples. From the Table 1,we observe that there is a decrease in the relative area of this peak for Nd doped compounds and also for heavy Ba doped compound. However, for low Ba doping it shows an increase, indicating a possible increase in number of itinerant holes in it. This may be responsible for the observed decrease in DTc.

The Ca 2p spectra and Sr 3d spectra have been deconvoluted and show two doublets corresponding to the two lattice sites which appears due to their site interchangeability which has been reported by many authors [9, 15, 18]. The two doublets observed are positioned at 344.82 eV and 345.75 eV in the spectra of Ca 2p and 131.9 eV and 132.9 eV in the spectra of Sr 3d. With both Ba and Nd doping, these components are found to shift to the high binding energies and thus indicate that Ca and Sr become more ionic in character as

Table 1: *Binding Energies of three deconvoluted peaks for Cu $2p_{3/2}$ and O 1s and their relative weightage*

	Cu $2p_{3/2}$ (eV)			O 1s (eV)		
Sample	I Peak	II Peak	III Peak	I Peak	II Peak	III Peak
Pure	932.00	933.19	934.71	528.3	529.1	530.5
	11.64%	47.62%	40.73%	15.3 %	58.15%	26.53%
Ba=0.05	932.11	933.33	934.74	528.3	529.1	530.4
	15.26%	43.72%	41.02%	16.58%	53.97%	29.44%
Ba=0.2	932.11	933.32	934.78	528.3	529.1	530.14
	13.8%	48.49%	37.71%	15.3%	58.57%	26.07%
Nd=0.05	932.06	933.25	934.69	528.3	529.1	530.5
	12.68%	46.97%	40.35%	15.4%	59.65%	24.91%
Nd=0.2	932.07	933.25	934.78	528.3	529.1	530.4
	12.36%	49.18%	38.46%	15.4%	59.9%	24.7%

observed in [9]. For pure sample, Ca going at the Sr site is 46% and at the Ca site it is 54 % whereas Sr going at the Sr site is 71% and at the Ca site it is 29%. With Ba and Nd doping, the relative site occupancy of Sr ion at the Sr site increases to 75 % for both the dopings. We can say on this account that Ba and Nd ion preferentially occupies Ca site, thus lowering the probability of Sr ion to occupy Ca site.

The Ba 3d core level spectra also show two peaks at 778.3 eV and at 779.1 eV. Since Ca and Sr are interchangeable in their lattice sites and Ba has been doped for Ca, Ba can also go to both the lattice sites. Hence, the two peaks can be attributed to two lattice sites of Ba. With high Ba doping, the binding energy of the peaks shifts to higher binding energy side. For low Ba doping (Ba=0.05) Ba going at the Ca site is 59 % and for high Ba doping Ba going at the Ca site is 53%.

4 Summary

The BSCCO (2212) superconductor with Ba and Nd doping have been studied using Photoemission measurements. Bi spectra shows no shift in binding energy and confirms Bi to be in a valence state of 3+. The Cu 2p and O 1s spectra show that low Ba doping results in decrease in the transition width ΔT_c as

compared to all the other studied samples. Nd doping, as expected leads to deterioration in the superconducting behaviour of the samples.

5 Acknowledgements

The research work has been partially supported by the UGC, New Delhi. One of us (KBG) is thankful for the TRIL program of International Center for theoretical Physics (ICTP), Trieste for a partial support for completion of the work.

References

1. A.V. Narlikar, C.V. Narasimha Rao and S.K. Agarwal, in: Studies of High Temp. Superconductors I, Ed. A.V. Narlikar (Nova Science, New York 1989), 341.

2. G. Hilscher, P. Rogl, E. Gratz, H. Muller and P. Fischer Physica C **158** (1988); G.Hilscher S. Pollinger, L.H.. Greene, G. W. Hull and W.R. McKinnon, Physica C **167** (1990) 472.

3. M. Tarascon and B.G. Bagley: in Chemistry of Superconducting Materials, Ed. T.Vanderah (Noyes, Park Ridge, NJ, 1990)

4. E. Wang, J.M. Tarascon, L.H. Greene, G. W. Hull and W.R. McKinnon, Phys. Rev. B **41** (1990), 6582.

5. S. Yamagata, K. Adachi, M. Onoda, H. Fujishita, M. Sera, Y. Ando and M. Sato, Solid State Comm. **74** (1990), 177.

6. K.V.R. Rao, K.B. Garg, S.K. Agarwal, V.P.S. Awana and A.V. Narlikar, Physica C **192** (1992) 419.

7. A. Maeda, T. Yabe, S. Takebayashi, M. Hase and K. Uchinokura, Phys. Rev. B **41** (1990) 4112.

8. N.L. Saini, B.R Sekhar, P. Srivastava, K.B. Garg, P. Filip, K. Mazenec, J. Rusek and P. Kuirek, J. Mat. Science and Engineering B **15**, 9 (1992).

9. N.K. Man, Kamlesh Kumari, S. Venkatesh, T.D. Hien, N.K. Sinh, N.X. Phuc and K.B. Garg, Int. J. Mod. Phys. B.**13** (1999) 1655.

10. B.R. Sekhar, N.L. Saini, P.Srivastava and K.B. Garg, J. Phys. Chem. Solids **55**, (1994) 49.

11. W.A. Groen et al, Solid State Comm. **72** (1989) 697.

12. H. Yamanaka, H. Enomoto, J.S. Shin, T. Kishimoto, Y. Takano, N. Mori and H. Ozaki. Jpn. J. App. Phys. **30** (1991) 645; Y.Shichi, Y. Inoue, F. Munakata and M. Yamanaka, Phys. Rev. B **42** (1990) 939.

13. Mahmoud Khaled, P. Srivastava, B.R. Sekhar, K.B. Garg, S.K. Agarwal, A.V. Narlikar and F. Studer, J. Phys. Chem. Solids **59**, (1998) 777.

14. B.R. Sekhar, P. Srivastava, N.L. Saini, K.V.R. Rao, S.K. Sharma and K.B. Garg, Physica C **206** (1993) 139.

15. S. Kohiki, T.Wada, S. Kawashima, H. Takagi, S. Uchida and S. Tanaka, Phys. Rev. B **38** (1988), 7051; S. Kohiki, T. Wada, S. Kawashima, H. Takagi, S. Uchida and S. Tanaka, Phys. Rev. B **38** (1988), 8868.

16. Biju R. Sekhar, Ph.D thesis, University of Rajasthan, Jaipur, India, November 1992.

17. P. Srivastava et al, Materi. Sci. Eng. B **22** (1994) 217.

18. F.U. Hillebrecht, J. Fraxedas, L. Ley, H.J. Trdahl, J. Zaanen, W. Braun, M. Mast, H. Peterson, M. Schaible, L.C. Bourne, P. Pinsukanjana, A. Zettl, Phys. Rev. B **39** (1989) 236.

Frascati Physics Series Vol. XXXII (2003), pp. 189-212
19th INTERNATIONAL CONFERENCE ON X-RAY AND INNER-SHELL PROCESSES – Roma, June 24 - 28, 2002

THE PIXE (Proton Induced X-Ray Emission) ANALYTICAL TECHNIQUE TO DETECT INSOLUBLE ATMOSPHERIC MICROPARTICLES ARCHIVED IN THE EPICA DOME C ICE-CORE (Antarctica): PALEOCLIMATIC IMPLICATIONS.

Federica Marino
Dip. di Scienze dell'Ambiente e del Territorio (DISAT), Univ. di Milano-Bicocca, Piazza della Scienza 1, 20126 Milano, Italy.
Dip. di Scienze della Terra, Università di Siena, Via del Laterino 8, 53100 Siena, Italy.
Valter Maggi
Dip. di Scienze dell'Ambiente e del Territorio (DISAT), Univ. di Milano-Bicocca, Piazza della Scienza 1, 20126 Milano, Italy.
Grazia Ghermandi
Dip. di Ingegneria Meccanica e Civile, Univ. di Modena e Reggio Emilia, Via Vignolese 905, 41100 Modena, Italy.
Daniele Ceccato
INFN-LNL Univ. di Padova, V.le Università 2, 35020 Legnaro (PD), Italy.
Rodolfo Cecchi
Dip. di Ingegneria Meccanica e Civile, Univ. di Modena e Reggio Emilia

ABSTRACT

Particle Induced X-Ray Emission (PIXE), is a technique for multielemental analysis based on a technique of nuclear physics.

The preliminary results obtained by application of PIXE in detecting elemental composition of insoluble particles in ice cores samples, has resulted in the improvement of this analysis technique for obtaining new information in the interpretation of ice core paleo-environmental records.

Natural mineral aerosol (dust) is an active component of the climate system and plays multiple roles in mediating physical and biogeochemical exchanges between the atmosphere, land surface and ocean, because of its potential in ocean fertilization and chemical equilibrium. Changes in the amount of

dust in the atmosphere are caused both by changes in climate (precipitation, wind strength, regional moisture balance) and changes in the extent of dust sources by either anthropogenic or climatically induced changes in vegetation cover. Variations in the concentration and chemical composition of aerosols deposited in remote areas vary as a result of the distance from source and the efficiency by which particles are transported in the atmosphere (e.g., size of the polar vortex, intensity of atmospheric circulation, relative contribution of the different aerosol sources to the polar regions) and removed by deposition. The study of compositional and temporal fluctuations of atmospheric aerosols during different climatic conditions offers a unique way of assessing their link to the environmental changes.

Here we present the records of insoluble (terrigenous) silicon (Si), iron (Fe) and titanium (Ti) of mineral particles from the Dome C ice core (75°06' S, 123° 24' E, 3233 m a.s.l), obtained within the framework of the European Project for Ice Coring in Antarctica (EPICA). More than 200 samples covering the last 220 kyrs were analysed using the PIXE technique, which has for the first time been applied to the investigation of the mineral content of Antarctic ice cores. Measurements were made exclusively on the insoluble fraction obtained by filtration of the samples. The data presented in this paper includes the first continuous record of silicon from a deep ice core, which represents a good proxy for continental dust. The mineral fraction of the particle mass determined from the PIXE measurements is highly correlated with the total dust mass (determined by Coulter©Counter). The concentrations of Si, Fe and Ti with respect to the total mass reflect the average abundances of these elements in the Upper Continental Crust.

The principal variations during the different climatic periods are very coherent between the PIXE analysis and total dust mass, and show increasing concentrations during glacial stages 2, 4, and 6 and very low particle content during both the Holocene and stage 5e interglacials. Such differences are due mainly to the increase of atmospheric dynamics during cold stages. However, some differences exist between the Holocene and the LGM periods. As a hypothesis, these variations could reflect differences in atmospheric processes affecting particles during transport, or can be explained in terms of either or both the variability of or variability at the dust source regions.

1 Introduction

Proton Induced X-ray Emission (PIXE) is a relatively new technique.

PIXE was first introduced at the Lund Institute of Technology in 1970, following the advent of lithium drifted Si(Li) detectors in the late 1960s. It was

this detector technology which stimulated the development of PIXE and other energy dispersive spectroscopic techniques. Like other spectroscopic techniques used for elemental analysis, PIXE is based upon the physics of the atom, rather then its chemistry. It involves the exitation of the atoms in the sample to produce characteristic X-ray and a means of detection (Johansson et al.,1995). A beam of protons or, on occasion, heavier ions, accelerated to an energy of a few mega-electron-volts excites characteristic X-ray in the atoms of a specimen. The X-ray spectrum is recorded in energy-dispersive mode by a semiconductor X-ray detector. The proton beam is used to eject inner-shell electrons from atoms in a solid specimen (target). When the resulting vacancies are filled by outer-shell electrons, characteristic X-rays whose energies identify the particular atom, are emitted. A typical PIXE spectrum consists of characteristic X-ray peaks superimposed on a background due to bremsstrahlung radiations and nuclear reactions induced by the beam. The area of each peak is related directly to the concentration of the corresponding element in the specimen. The PIXE technique allows fast (10-20 minutes), non-destructive, highly sensitive simultaneous determinations of a wide group of elements with atomic number ranging from 12 to 85, without large variations in sensitivity among different elements. Given its main capabilities, PIXE has proven a useful tool for the study of trace element distribution in the ecosystem, both in terms of pollution measurement monitoring as well as for geochemical and geophysical studies (Ghermandi, 2000). The insolubile atmospheric dust represents an important fraction of the total mass of atmospheric aerosols (Pye, 1987), and provides one of the most important paleoclimatic information archives.

Dust is recognized as a major component of the tropospheric aerosol assemblage. The global annual input of mineral aerosol to the atmosphere is estimated to be of the order of 1 to 2 billion metric tons per year, representing about half of the total production of tropospheric aerosols by both natural and antrophogenic sources (IPCC, 1994; Duce, 1995).

Although mineral dust is composed of relatively large particles with a mass median diameter of 1.5-3 μm, it can be transported over very long distances. For instance, dust raised over tropical and subtropical arid and semi-arid areas, can be found over remote areas (i.e. Antarctica). This is because, unlike other tropospheric aerosol species, dust is raised rapidly by wind events to altitudes of several kilometers above source regions and is mainly transported above the atmospheric boundary layer (Bergametti, 1992; Prospero, 1996).

The role of mineral aerosol in climate dynamics is quite complex and not yet fully understood, but the concentration of dust in the atmosphere (i.e. atmosphere dust loading) influences the climate system through affecting radiative forcing, through chemical reactions with other atmospheric constituents, and through acting as a source of nutrients to biological systems (Kohfeld & Harrison, 2001; Duce, 1995; Dentener et al., 1996; Kumar et al., 1995; De Baar et al., 1995).

The continental particulate material deposited on ice sheets is derived by atmospheric transport, and is thus of purely aeolian origin (Pye, 1987). Dust is generated from aeolic erosion of the continental surfaces in source regions, lifted from the surface into the atmosphere, transported by winds, and then deposited either by settling (dry deposition) or by being washed out (wet deposition) of the atmosphere (Harrison et al., 2002). Of all the dust archives, ice cores provide one of the most detailed and best preserved sources of paleoclimatic information (Delmonte et al., 2002). The total amount of dust present in the core provides a record of dust deposition rates through time.

Ice core records from Greenland and Antarctica, spanning several climatic cycles, show that aeolian deposition rates and particles concentration at high latitudes were higher during the cold stages than during the warm stages. In the last 420kys, the last two glacial/interglacial periods, the dust concentration in atmosphere rise and drop many time; The cold Marine Isotopic Stage (MIS) 10 to MIS 2 (also Last Glacial Maximum – LGM) represent periods with a large amount of dust, and the warm stages as MIS 11, MIS 9, MIS 7.5, MIS 5.e (also Eemian), and the Holocene are characterized by low concentrations (20 to 50 time less than the cold stages) (Petit et al., 1981, 1990, 1999; Hammer at al., 1985; Taylor et al., 1993; Steffensen, 1997).

The mineralogy, chemistry and isotopic composition of the particulate matter can be used to identify the source areas from which the aeolian material is derived or to reconstruct the atmospheric circulation regime during transport.

Dust constituents are mainly minerals, pollens, spores, organic fly ash and, from marine environment, diatoms and sea salts (Maggi, 1997). Volcanic ash and tephra was observed as glass shard or single mineral crystals. Because the volcanic particles should be concentrated in narrow ash layers, and the sea-salt reacts in the atmosphere with soluble compounds, the composition of the insoluble dust can be considered similar to the composition of the mineral particles, so the atmospheric dust should represent the mean composition of the surface deflation areas. (Royer et al., 1983).

Dust stable isotope (mainly neodymium and strontium) measurements was performed for the determination of the source areas of the atmospheric dust reaching Vostok and Dome C in East Antarctic Plateau (Figure 1), indicate the South Southern America (Patagonia) as the mainly source area (Basile et al, 1997; Delmonte et al., 2002). Total and soluble composition has been done for many heavy metals such as Cr, Ni, Cd, Pb, V etc., but normally the total soluble element fractions were detected (Barbante et al., 2001; Planchon et al., 2001).

However, less information is available on the elemental composition of the insoluble fraction of dust flying from the source areas. Two order of problems arise for the measurements of the insoluble dust element content: i) the difficulty of separating soluble and insoluble fractions without include disturbances in the measurement precedure (i.e filter by filtration), ii) the low quantities of

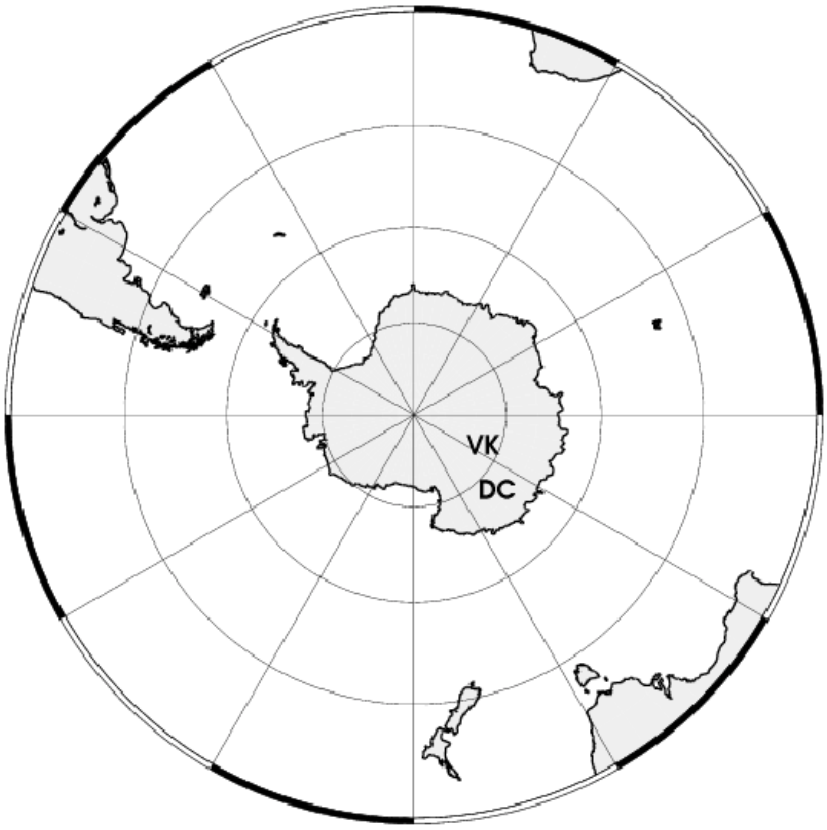

Figure 1: *Map of Antarctica and sourrounding continents with localization of EPICA Dome C (DC) and Vostok ice cores (VK).*

insoluble particles that can be collected (ppb to ppt) using a reasonable amount of ice.

This work presents the first record of PIXE measurements of insoluble dust elemental composition (Si, Fe, Ti) from the upper 2200 m depth of the EPICA (European Project for Ice Coring in Antarctica) Dome C (75°06'S; 123°21'E) ice core, that span the last 220 kyrs using the EDC1 timescale (Schwander, personal communication). For the first time, the record of three insoluble elements, Si, Fe and Ti, originating from continental mineral dust with very low reactivity with soluble atmospheric compounds, are reported.

2 Materials and Methods

2.1 Ice-Core Sampling

EPICA (European Project for Ice Coring in Antarctica) is a multinational European plan for deep ice core drilling in Antarctica, to address critical environmental issues of global relevance. It will play a major part in the international effort to understand climate change. EPICA aims to reconstruct high resolution histories of past changes in climate, atmospheric composition and ice cover in Antarctica spanning several glacial/interglacial cycles. A total of about 200 ice samples from depths of 100 m to 2200 m of the EPICA Dome C ice-core (75°06'S; 123°21'E; Fig.1) were analysed. The time period covered by the core spans about 220 kyr (Schwander, personal communication). The resolution (time frequency) of sampling along the core for PIXE analysis was variable with mean values of about one sample per 230 years for the Holocene period, one sample per 300 years for the LGM period, one sample per 860 years for Stage 3, one per 1,5 kyrs for Stage 4 and 5 and one sample per 4 kyrs for Stage 6.

The 2200 m EPICA ice core was cut into about 4000 sections (bags) of 55 cm length; 200 of these sections, distributed along the core (at intervals ranging from 2.5 m to 5 m), were sampled with clean procedures (Delmonte et al., 2002) in the clean, cold laboratory of the Laboratoire de Glaciologie et Géophysique de l'Environnement (LGGE), in Grenoble (France). The samples were transferred to Modena (Italy), sealed in plastic bags to avoid any possibility of contamination and kept frozen (-30°) until required for PIXE target preparation and melted immediately before target preparation.

2.2 PIXE Analysis

Particle Induced X-Ray Emission (PIXE) has been proven a very useful technique for the study of trace element distribution in ecosystems. The major features of this technique are multielement analysis and high sensitivity. Addi-

tional advantages are the speed of analysis of a wide variety of samples (Ghermandi, 2000).

However, it must be stressed that adequate sample preparation procedures and suitables measurements conditions are required in order to make full use of PIXE capabilities.

Since solid targets have to be exposed to the particle beam, thin targets are preferable, in order to minimize matrix effects. The optimum sensitivity of PIXE is obtained in the analysis of trace elements in a matrix of light elements and with thin samples of low mass. Since the concentrations of trace elements in polar snow and ice are very low and range from ppm (mg/kg) to fractions of ppt (ng/kg), it follows that extreme care must be taken in sample treatment and target preparation to avoid any possibility of contamination (Ghermandi et al., 1996). Therefore it should be emphasised that no pretreatment (i.e. preconcentration or precipitation with carbamates or addition of chemical substances) has been used in this work.

PIXE targets were prepared by filtering each melted sample (a volume of about 20 ml for samples in the upper 580 m and 3-8 ml for deeper samples), through a Nuclepore membrane (polycarbonate (PC) 1 mg cm^{-2}, pore size 0.45 μm). Nuclepore polycarbonate (PC) membranes are preferable for size selectivity, even if they generally may contain traces of Cr, Fe, and sometimes Br in variable amounts. This contamination is negligible in comparison with the Cr and Fe concentrations in suspended particles; the possible release of these elements (mainly Cr) from the membranes into the soluted filtrate was evaluated by filtration of blank samples. The diameter of the filtration area was about 1 cm. All operations were performed inside a custom-made class 100 clean plastic bench which ran continuously located inside a clean laboratory at the Department of Mechanics and Civil Engineering, University of Modena and Reggio Emilia (Modena, Italy). All apparatus in contact with samples was previuosly cleaned by successive immersions in three 0.1% HNO_3 solutions acidified with ultrapure HNO_3 and a final immersion into deionized water.The PIXE analyses were carried out using the 2 MeV AN 2000 Van de Graaff accelerator at the National Laboratories of Legnaro (Istituto Nazionale di Fisica Nucleare (INFN), Padua, Italy). Working conditions were follows: proton beam, 1.8 MeV; angle to target, 135°; current on target, 15-35 nA; detector, Si(Li) Link (resolution 150 eV at 5.9 KeV, solid angle 0.0198 sr) with funny filter (hole 7.06% of total area); total charge on target, 15 μC, resulting in a dead time <10%. To obtain a homogeneous circular beam spot on the target, the beam was diffused through a Ni foil, 450 μg cm^{-2}, and then collimated to a diameter of 1.5 cm; the proton beam area (1,77 cm^2) was larger than the sample area. A more detailed description of the PIXE experimental set-up is presented elsewhere (Cecchi et al., 1987; Ghermandi, 2000).The PIXE experimental chamber was calibrated by analyzing a series of polycarbonate foils coated with known Cu concentrations. Extremely accurate blanks are prepared in order to quantify

any spurious additions to the samples during target preparation operations. The average blank concentration calculated from the analysis of some Nuclepore polycarbonate filters was subtracted from each sample.

Blank values, very similar to those measured by Laj et al.(1997), are also very similar to those measured by inductively coupled plasma mass spectrometry (ICP-MS) in Nuclepore polycarbonate filters (Berg et al., 1991).

Comparison between PIXE and other analytical techniques, i.e. IC – Ion chromatography (Sellegri et al., in press) and ICP-AES – Inductively Coupled Plasma Atomic Emission Spectroscopy (Menzel et al., 2002), has shown that the different methods usually agree to within 15% or better.

X-ray counts were directly registered using a multichannel analyser and PIXE spectra were fitted using a commercial software. The software used for PIXE spectra analysis and element concentration evaluation is GUPIX98 (Gupix Software, Maxwell et al., 1989, 1995), which also estimate errors (typically <15%) and detection limits tens to 0.1 ng m^{-3}.

Element concentration uncertainties were of the order of 5-10% of the concentration, depending on the elements. The overall measurement error was higher when the mass of the material was close to the detection limit. Part of the measured uncertainty was due to the fluctuating proton beam intensities, but it is greatly reduced when considering the relative variations of each element with respect to others. A more detailed description of analytical procedures and sample preparation can be found elsewhere (Ghermandi et al., 1996; Laj et al., 1997).

As mentioned above, Proton Induced X-ray emission allows multielement determination of trace concentrations suitable for a wide group of elements with atomic number (Z) from 12 to 85, without large variations in sensitivity among different elements. It offers its maximum sensitivity in two atomic number regions: 20<Z<35 and 75<Z<85 (Ghermandi, 2000).

But for the purpose of this study we focused on iron, silicon and titanium, which dominate the analyzed mass with this method and which are the most significant components found in the continental crust (Taylor and McLennan, 1985; Wedephol, 1995).

3 Discussion

Examples of PIXE spectra, obtained in this work (EPICA sample 3402, filter and blank filter) are shown in Figure 2. It should be noticed that the bremsstrahlung background of the blank sample is quite smooth and agrees well with the minima between the peaks in the spectrum of the sample. In particular, the elemental lines due to impurities in the blank filter are rather low, i.e. they usually amount to no more than a few percent of the respective aerosol signal. This reflect the low impurity level in the filters.

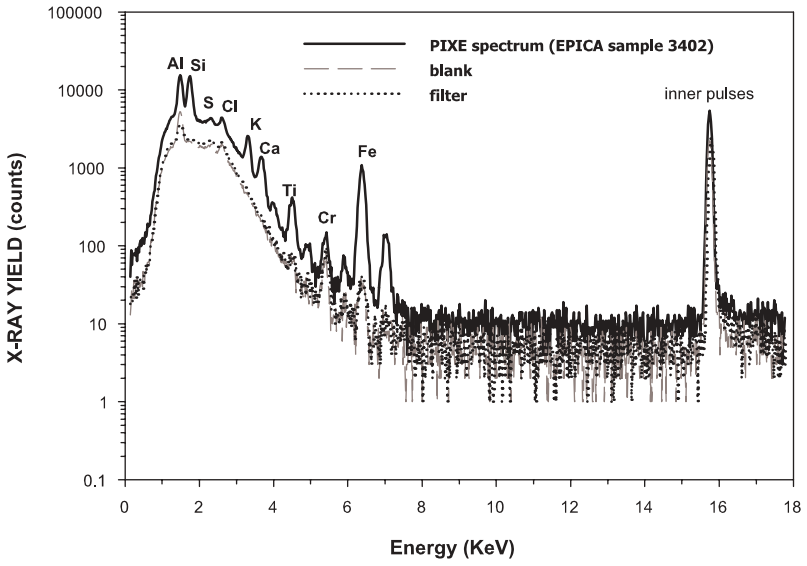

Figure 2: *PIXE spectra of an EPICA sample (bag 3402) and comparison of the spectra with a filter and a blank filter.*

The most high peaks on the right part of the spectrum (Fig. 2) represent an inner signal produced by a pulse generator applied to the experimental set-up for monitoring dead time losses. Consequently, it should be noticed that this peak produced clearly the same signal in the three different spectra (sample, blank and filter). As mentioned above, PIXE allows simultaneous analysis of all the elements in a sample having atomic number greater than 12. A practical problem, however, is that some emission lines of a given element appear at the same or almost the same energy as the lines from other elements, producing complicated spectra in which the clear separation of lines sometimes becomes difficult. Obviously, the higher the number of elements one wishes to detect, the higher the difficulty and the lower the resolution achieved. Nevertheless, one can identify from 10 to 15 different elements simultaneously with acceptable accuracy.

In this work we focused on silicon (Si), iron (Fe) and titanium (Ti) which are typical element constituents of the continental upper crust (Wedepohl, 1995). Table 1 show the correlation matrix between the dust mass concentration (Delmonte, personal communication) and the main continental crustal elements (CCE) made by PIXE measurements. In the context of CCE abundances, Si, Fe, Ca, Ti are quite well correlated, but large differences arise in correlation between Al and other elements. As correlation for Al are generally below 0.76, although with a major correlation to the Si (0.80), and low correlation to the dust mass (0.54), thus reduces the representativity of the Al as reference element for this work. It is not clear why the Al does not fit with the dust mass and other elements (except Si); by contrast, Si and other elements are quite well correlated, also with the dust mass. This should help to increase confidence in the PIXE technique for this type of analysis. Nevertheless, further work is needed on Al analysis. Ca represents one of the most used markers for the continental sources (as Ca^{++}) but this ion is related to the soluble fraction (Rotlisberger et al., 2002). The soluble/insolube fractionation in the atmospheric calcium are not well understood. Furthermore, few works have been done, and normally without definitive results (Laj et al. 1997). The correlations between Si, Fe and Ti represent the higher values (more than 0.90), and have also a good correlation with dust mass although, lesser, but in any case significant (Table 1); for this reason we use only these three elements for the discussion.

Silicon is the most abundant continental crust element, with large differences in the relative abundances in different rocks (Taylor & MacLennan, 1985; Deer et al., 1993; Wedepohl, 1995). The presence of silicon is related also to the growth of diatoms in the oceans (Brzezinski et al., 2003). Iron, from mineral sources also, represents one important element that control oceanic productivity, acting as a source of nutrients to biological systems and sequestrating carbon from the atmosphere (Boyd et al., 2002; Martin et al., 1994; Coale et al., 1996). Titanium is the typical rock element, found in most of the silicates,

Table 1: *Correlation matrix between the crustal origin elements measured by PIXE, and the dust mass conentration measured by Coulter © Counter, as discussed on the text.*

	Al	**Si**	**Ca**	**Ti**	**Fe**	**dust mass**
Al	1.00	.80	.70	.76	0.75	0.54
Si		1.00	.90	0.92	0.99	0.86
Ca			1.00	0.84	0.90	0.78
Ti				1.00	0.91	0.80
Fe					1.00	0.89
dust mass						1.00

and practically in all the clays and mica minerals which represent most of the aeolian dust (Wadepohl, 1995; Deer et al., 1993).

The relationship between element concentrations and insoluble particles are strictly related to the nature of the atmospheric dust, especially to the source areas. Insoluble particles are composed mainly of crustal minerals, mostly aluminosilicates, and, in minor quantities, volcanic shards and meteoric debris. Silicates are the most abundant family of crustal minerals (Deer at al., 1993).

Si, Fe and Ti records (Figure 3) show the typical features with high concentration levels during the cold stages and low or very low concentrations during warm stages. Because of the thinning of the ice with the depth, the samples during the Holocene represent around 200-300 years, while these during the MIS 6 around 4000 years. In fact the cold stages, LGM, MIS 4 and MIS 6, represent the major features in the records, as in the case for the total dust mass (Figure 3). This relationship can be observed in Figure 4 where the Si/Fe and Fe/Ti ratios show a good correlation. Quite less correlated is dust/Si, but this might be related to the different techniques used for measurements. Some differences arise when the mean elemental concentrations are compared with mean dust mass concentration for the different climatic periods (Table 2). The glacial stages, LGM and MIS 6, present a very similar concentration of Si and Ti, and around 50% difference for the Fe (LGM higher than MIS 6). Despite of the high mass of dust, the MIS 6 concentration is around 30% of the LGM one. The interpretation of this behaviour is very difficult because of the absence of mineral types identification, but it is possible to relate this pattern to changes in the composition of the mineral assemblage (i.e. silicates, carbonates, no Si-Fe-Ti minerals, organics).

The element relationships between climate periods showns a good correlation especially in the cold stages (Figure 5), due mainly to the high con-

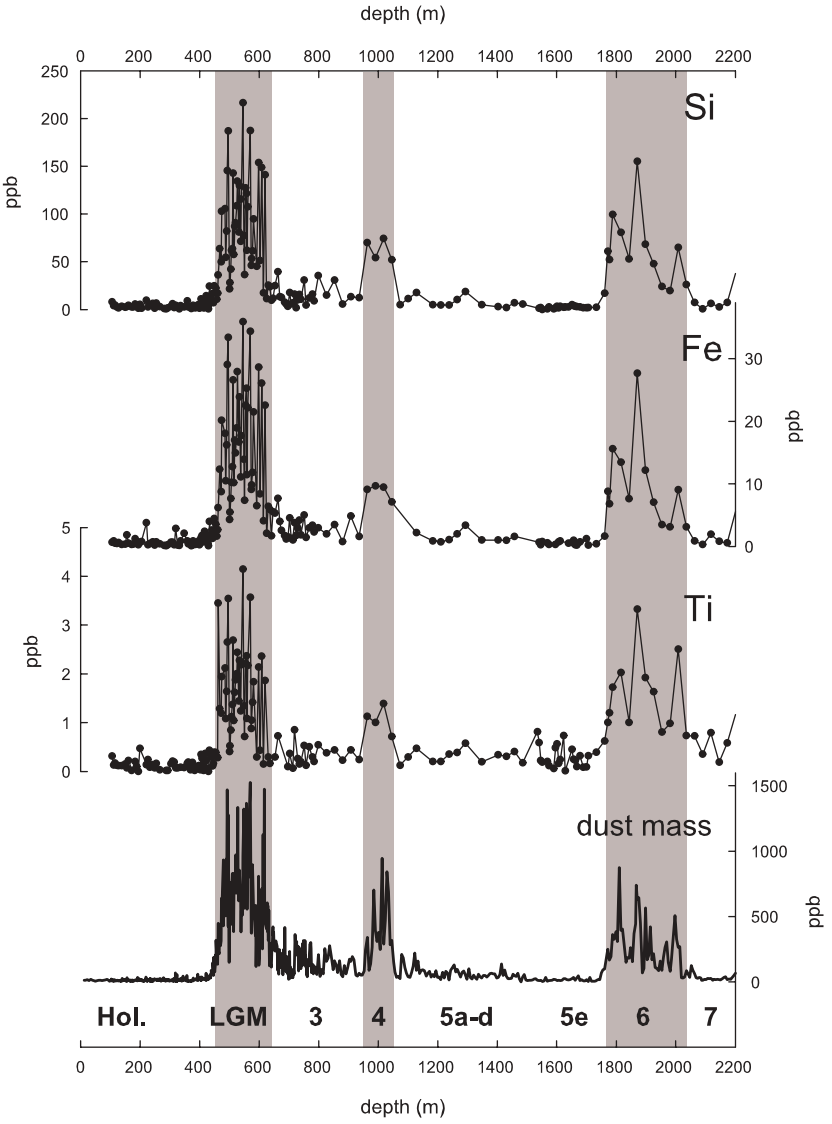

Figure 3: *Silicon (Si), iron (Fe) and titanium (Ti) records from EPICA ice core, obtained by PIXE measurements, in comparison with dust mass concentration (Delmonte et al., personal communication). The grey shade areas represent the cold periods and at the bottom row are shown the nomenclature used on the discussion. (Hol. = Holocene; LGM = Last Glacial Maximum; 3, 4, 5a-d, 5e, 6, 7 = number of Marine Isotopic Stages-MIS; The MIS 5e is alone because represent the last interglacial, Eemian).*

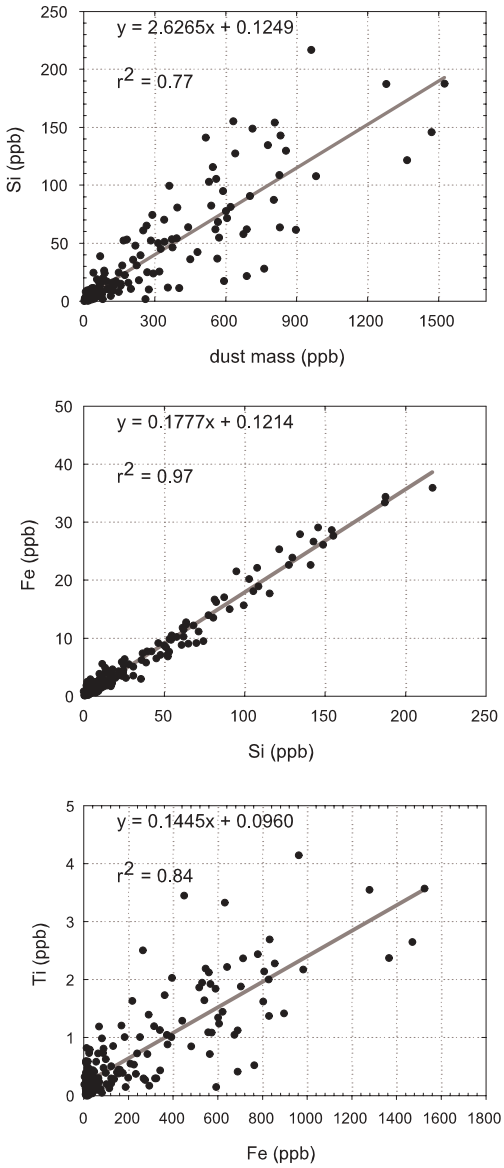

Figure 4: *Correlation between a) dust concentration (Delmonte et al., personal communication) and Si, b) Si and Fe, and c) Fe and Ti. The r^2 coefficients are all very high, except the dust-Si one, related to an higher scattering due to the use of two different analytical techniques (see the text).*

Table 2: *Average of Si, Fe and Ti element concentrations of principal climatic periods and the dust mass concentration (ds = standard deviation) for the last 220 kyrs.(a) PIXE samples only.*

	Average Si (ppb)	ds	**Average Fe (ppb)**	ds	**Average Ti (ppb)**	ds	**DUST MASS ppb (a)**	ds
Holocene	**3.6**	2.3	**0.75**	0.78	**0.14**	0.10	**16**	6
LGM-Stage 2	**93.7**	49.3	**17.22**	8.90	**1.69**	0.93	**733**	287
Stage 3	**13.0**	8.9	**2.58**	1.28	**0.33**	0.20	**139**	68
Stage 4	**62.7**	11.1	**8.85**	1.18	**1.06**	0.28	**327**	51
5e	**2.3**	1.2	**0.59**	0.31	**0.26**	0.19	**16**	9
Stage 6	**61.9**	38.3	**9.72**	7.04	**1.56**	0.79	**276**	182

centrations of samples that reduces the relative scattering of the data. In fact Si/Fe, Fe/Ti and Si/Ti are all well correlated in the LGM. In the MIS 6, the lower correlation could be related to the minor number of samples analyzed. Moreover, the angular coefficients of the LGM and MIS 6 regressions lines are very close for each couple of elements (Figure 5). These data could indicate that no changes occur in source areas during the cold stages in the last 220 kyrs, as previously suggested by the dust isotopic fingerprint (Basile et al., 1997). The warm periods show more scattered Si, Fe, and Ti data, mainly because of their low concentration. The element ratios for the main interglacial periods, Holocene and MIS 5e (Eemian), present a very low correlation, and, in some cases, no correlation at all (Figure 6). Better relationships could be obtained using more sample to perform measurements with more significativity.

The Fe/Si, Ti/Si and Ti/Fe ratios permit the evaluation of the evolution of the dust, mainly during the cold stages. Different type of minerals present different ratios between the major elements (i.e. Si, Fe and Ti). The upper continental crust element ratios are shown in table 3 (Wedephol, 1995). Therefore it should be emphasized that this values refer to the upper continental bulk rock, without soils and surface weathering that characterize the main aeolian deflation areas (Arimoto, 2001; Harrison et al, 2001; Kohfeld and Harrison, 2001). During cold periods, high atmospheric turbulence affects the dust tra-

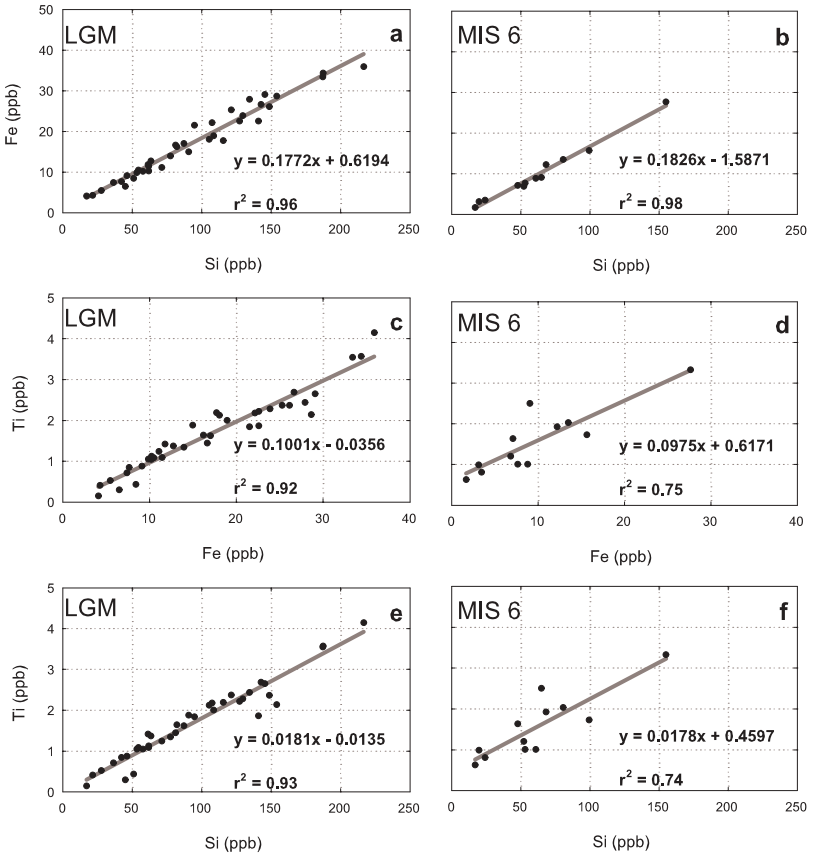

Figure 5: *Correlations between the Si, Fe and Ti elements for the two main cold stages, the Last Glacial Maximum (LGM) and the Marine Stage 6 (MIS 6). The better correlation during the LGM is probably due to the large amount of data that reduce the scattering.*


0.2
0.0
0
1.0
0.8
0.6
0.4
0.2
0.0
0
2

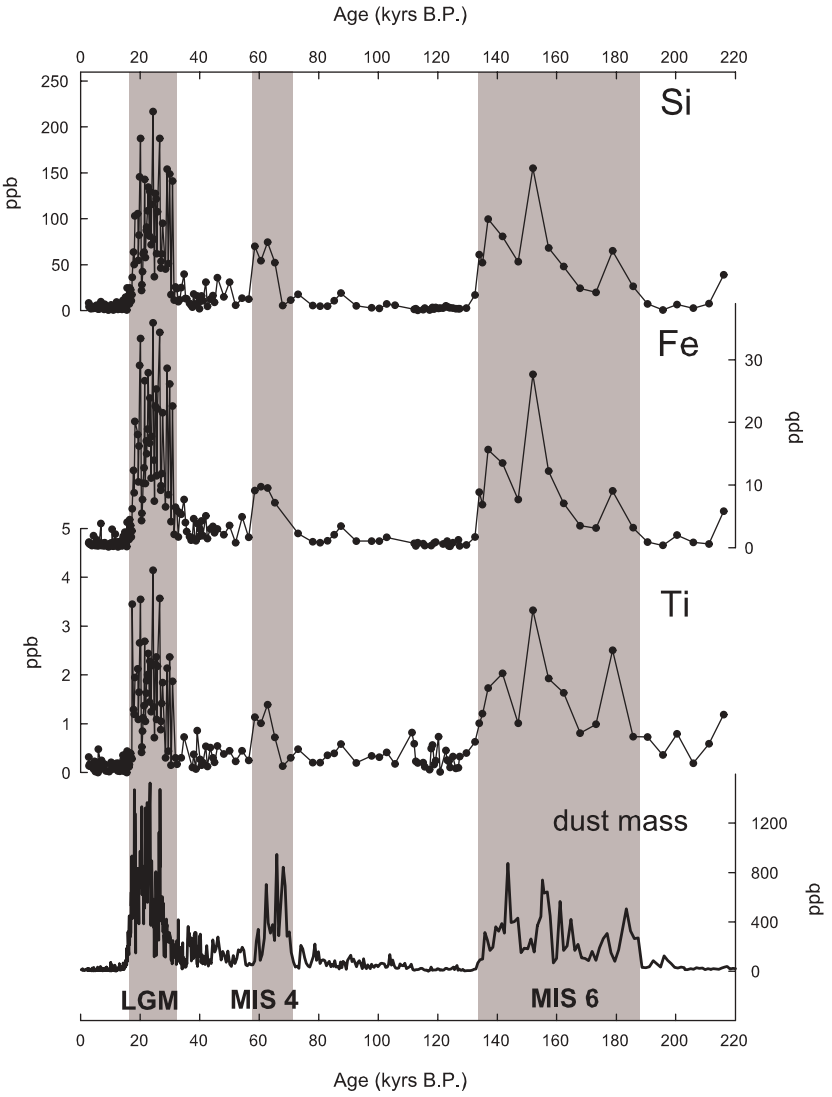

Figure 7: *Records of silicon (Si), iron (Fe), titanium (Ti) and dust mass concentration (Delmonte et al., personal communication) using the new EPICA timescale (Schwander, personal communication). The grey shaded areas represent the cold stages shown on the bottom row (LGM – Last Glacial Maximum; MIS 4 - Marine Isotopic Stage 4; MIS 6 – Marine Isotopic Stage 6).*

Table 3: *Element ratios (Fe/Si, Ti/Fe, Ti/Si) on principal climatic periods and the continental crustal element ratios for comparison (Wedepohl, 1995).*

	Fe/Si	**Ti/Si**	**Ti/Fe**
Crust	**0.15**	**0.01**	**0.09**
Holocene	0.21	0.038	0.182
LGM-Stage 2	0.18	0.018	0.098
Stage 3	0.20	0.025	0.128
Stage 4	0.14	0.017	0.120
5e	0.26	0.117	0.449
Stage 6	0.16	0.025	0.161

jectories and increases the travel distance of particles from the source areas to DC. The transport efficiency of dust microparticles is strongly related to shape, size and density (i.e. weight); the crystal abitus and density are strongly related to the mineral typology of the particles. For this reason the long range transport can select particles with low density and more aerodynamic shape. Also well known is the effect of the enhanced atmospheric turbulence during cold periods on the dust size distribution (i.e. mode) (Delmonte et al., 2002). The strong selection of dust during long distances transport from the surrounding continents (i.e. South America) to Antarctica, depends on the type of minerals. As a result the major part of particles with high weight and/or low aerodynamic characteristics are normally removed during the first hundred kilometers by scavenging. Within some thousand kilometers, this kind of selection is probably much reduced, so differences in dust transport from 5000 to (i.e) 8000 km cannot affect the mineralogy.

As an additional hypothesis, the differences on element ratios might be related to changes in the sources areas. The increasing deflation areas, due to the expansion of sandurs (planes from glacier rivers) and the continental shelf exposure from sea level decrease are, with the reduced vegetation cover, the main changes of the continental areas. So the larger surfaces available to the wind erosion increase the dust atmospheric concentration load with a mean value of elemental ratios close to the upper continental composition (Wedepohl, 1995). During the warm periods, most of the areas previously affected by wind erosion was covered by water (rise of the sea level) and vegetation, and consequently the surface areas are characterized by soil formation and evolution. For these reasons the amount of dust in the atmosphere drops and the elemental ratios are affected by the extension of soil covering and weathering due to pedological processes. These changes infer a variation in the typology of aeolian dust and at the least the elemental composition of the atmospheric dust.

4 Conclusions

The Proton Induced X-ray Emission technique represents a strong tool for measurements of atmospheric dust, both for climatic and environmental purposes. An important advantage of the technique is in allowing the analysis of low concentration of particles collected from Antarctic ice core samples.

The record of Si, Fe and Ti show a very close relationship with the dust mass concentration revealing a good proxy for continental contribution on the aerosol load. The element ratios permit the evaluation not only of the concentration of dust but also the characterization of the variability of the continental sources, mainly due to the soil and vegetation evolution.

Differences of element concentrations between cold and warm periods can be related mainly to changes in source areas or atmospheric circulation. In fact changes in wind trajectories can explain the variability in size distribution of the dust (Delmonte et al., 2002), but not the variability in mineral composition. However, changes on the deflation surfaces of source areas, for weathering, soil changes and vegetation cover, are the most likely hypothesis to explain these element differences (Arimoto, 2001; Harrison et al, 2001; Kohfeld and Harrison, 2001).

Here we have shown that PIXE technique provides a clear record of Si concentrations in atmospheric dust. This is of particular importance because of the high abundance of Si in the continental crust (28.8%), compared to that of Al (7.9%) (Wedepohl, 1995).

The very successful application of the PIXE analytical system in the insoluble atmospheric dust measurements along deep ice core, lead to further development of this technique. The next step will be the increase of number of elements to include in the climatic and environmental discussions. Further mineralogical studies will be needed to quantify the contribution of each element and the interplay between them all.

References

1. Arimoto R. (2001). *Eolian dust and climate: relationships to sources, tropospheric chemistry, transport and depositino.* Earth-Science Reviews 54, 29-42.

2. Barbante C., Turetta C., Capodoglio G., Cescon P., Hong S., Candelone J-P., Van de Velde K., Boutron C.F. (2001). *Trace element determination in polar snow and ice. An overview of the analytical preocess and application in environmental and paleoclimatic studies.* Environmental Contamination in Antarctica-A Challenge to Analytical Chemistry, S. Caroli, Cescon P.

and D.W.H. Walton, editors, Elsevier Science B.V., pp. 55-86.

3. Basile I., Grousset F.E., Revel M., Petit J.R., Biscaye P.E., Barkov N.I. (1997). *Patagonian origin of glacial dust deposited in East Antarctica (Vostok and Dome C) during glacial stages 2,4 and 6.* Earth Planet. Sci. Lett. 146: 573-589.

4. Berg T., Royset O., Steinnes E. (1991). *Blank values of 30 elements in 19 filter materials determined by ICP-MS.* Norw. Inst. For Air Res., Lillestrom.

5. Bergametti G. (1992). *In: Enciclopedia of Earth System Science.* Vol. 1, Academic Press, San Diego, 171-182.

6. Boyd P.W. (2002). *The role of iron in the biogeochemistry of the Southern Ocean and equatorial Pacific: a comparison of in situ iron enrichments.* Deep-Sea Research II 49, 1803-1821.

7. Brzezinski M.A., Dickson M-L, Nelson D.M., Sambrotto R. (2003). *Ratios of Si, C and N by microplankton in the Southern Ocean.* Deep-Sea reasearch II, 50, 619-633.

8. Cecchi R., Ghermandi G., Calvelli G. (1987). *Ultratrace PIXE analyses in water with low selective metal preconcentration at various pH.* Nucl. Instrum. Methods Phys. Res. B, 22, 460-468.

9. Coale K.H., Johnson K.S., Fitzwater S.E., Gordon R.M., Tanner S., Chavez F.P., Ferioli L., Sakamoto C., Rogers P., Millero F., Steinberg P., Nightingale P., Cooper D., Cochlan W.P., Kudela R. (1996). *A massive phytoplankton bloom induced by an ecosystem-scale iron fertilization experiment in the equatorial Pacific Ocean.* Nature 383, 495-501.

10. De Baar H.J.W., Jong J.T.M.D., Bakker D.C.E., Loscher B.M., Veth C., Bathmann U., Smetacek V. (1995). *Importance of iron for plankton blooms and carbon dioxide drawdown in the Southern Ocean.* Nature 373: 412-415.

11. Deer F.R.S., Howie R.A. and Zussman J. (1993). *An introduction to the Rock-Forming Minerals.* Longman, White Plains, N.Y., pp.696.

12. Delmonte B., Petit J.R., Maggi V. (2002). *Glacial to Holocene implications of the new 27000-year dust record from the EPICA Dome C (East Antarctica) ice core.* Climate Dynamics 18, 647-660.

13. Dentener F.J., Charmichael G.R., Zhang Y., Lelieveld J., Crutzen P.J. (1996).*Role of mineral aerosol as a reactive surface in the global troposphere.* J. Geophys. Res. 101 (D17), 22869-22889.

14. Duce R.A. (1995). *In: Aerosol Forcing of Climate.* Charlson, R.J. and Heintzenberg, J. (eds.), Wiley, New York, 43-72.

15. Ghermandi G., Cecchi R., Laj P. (1996). *Procedures of target preparation to improve PIXE efficiency in environmental research.* Nuclear Instruments and Methods in Physics Research B 109/110, 63-70.

16. Ghermandi G. (2000). *Proton –induced X-ray Emission in Environmental Analysis.* Encyclopedia of Analytical Chemistry, R.A. Myers (Ed.), John Wiley & Sons Ltd, Chichester, pp.3197-3227.

17. Hammer C.U., Clausen H.B., Dansgaard W., Neftel A., Kristinsdottor P., Johnson E. (1985). *Continuous impurity analysis along the Dye 3 deep core.* In: Langway, J.C.C., Oeschger H., Dansgaard W. (eds.), Greenland Ice Core: Goephysics, Geochemistry, and the Environment. Geophys. Monogr., AGU, Washington, DC, pp. 90-94.

18. Harrison S.P., Kohfeld K.E., Roelandt C., Claquin T. (2001). *The role of dust in climate changes today, at the last glacial maximum and in the future.* Earth-Science Reviews 54, 43-80.

19. IPCC -Intergovernmental Panel on Climate Change (1994). *Radiative forcing of climate chnge and an evaluation of the IPCC 1992 emission scenarios 1994.* Houhton, JJ.T. Filho, L.G.M. Bruce, J.P. Lee, H. Callandar, B.T. Hailes, E.F. Harris, N. and K. Maskell. Cambridge Univ. Press, Cambridge, UK, pp.200.

20. Johansson S.A.E., Campbell, J.L. & Malmqvist, K.L., (1995). *Particle Induced X-ray Emission (PIXE).* Jhon Wiley & Sons, Inc., New York.

21. Kohfeld K.E. & Harrison S.P. (2001). *DIRTMAP: the geological record of dust.* Earth-Science Reviews 54, 81-114.

22. Kumar N., Anderson R.F., Mortlock R.A., Froelich P.N., Kubic P., Ditrich-Hannen B., Suter M. (1995). Increased biological productivity and export production in the glacial Southern Ocean. Nature 378: 675-680.

23. Laj P., Ghermandi G., Cecchi R., Maggi V., Riontino C., Hong S., Candelone J-P., Boutron C. (1997). *Distribution of Ca, Fe, K, and S between solubile and insolubile material in the Greenland Ice Core Project ice core.* J. Geophys. Res. Vol. 102, No C12, 26615-26623.

24. Maggi V. (1997). *Mineralogy of atmospheric microparticles deposited along the Greenland Ice Core Project ice core.* J. Geophys. Res. Vol. 102, No C12, 26725-26734.

25. Martin J.H., Coale K.H., Johnson K.S., Fitzwater S.E., Gordon R.M., Tanner S.J., Hunter C.N., Elrod V.A., Nowicki J.L., Coley T.L., Barber R.T., Lindley S., Watson A.J., Van Scoy K., Law C.S. (1994). *Testing the iron hypothesis in ecosystems of the equatorial Pacific Ocean.* Nature, 371, 123-129.

26. Maxwell J.A., Campbell J.L., Teesdale W.J. (1989). *The Guelph PIXE Software Package.* Nucl. Instrum. Methods Phys. Res. B, 43, 218-230.

27. Maxwell J.A., Teesdale W.J., Campbell J.L. (1995). *The Guelph PIXE Software Package 2.* Nucl. Instrum. Methods Phys. Res. B, 95, 407-421.

28. Menzel N., Schramel P., Wittmaack K. (2002). *Elemental composition of aerosol particulate matter collected on membranes filters: A comparison of results by PIXE and ICP-AES.* Nucl. Instrum. Methods Phys. Res. B, 189, 94-99.

29. Petit J.R., Briat M., Royer A. (1981). *Ice age aerosol content from East Antarctic ice core samples and past wind strength.* Nature 293, 391-394.

30. Petit J.R., Mounier L., Jouzel J., Korotkevich Y.S., Kotlyakov V.I., Lorius C. (1990). *Pleoclimatological and chronological implications of the Vostok core dust record.* Nature 343, 56-58.

31. Petit J.R., Jouzel J., Raynaud D., Barkov N.I., Barnola J.M., Basile I., Bender M., Chappellaz J., Davis M., Delaygue M., Delmotte G., Kotlyakov V.M., Legrand M., Lipenkov V.Y., Lorius C., Pepin L., Ritz C., Saltzman E., Stievenard M. (1999). *Climate and atmospheric history of the past 420,000 years from the Vostok ice core, Antarctica.* Nature 399 (6735), 429-436.

32. Planchon F.A.M., Boutron C.F., Barbante C., Wolff E.W., Cozzi G., Gaspari V., Ferrari C.P., Cescon P. (2001). *Ultrasensitive determination of heavy metals at the sub-picogram per gram level in ultraclean Antarctic snow samples by inductively coupled plasma sector field mass spectrometry.* Analytica Chimica Acta 450, 193-205.

33. Prospero J.M. (1996). *In: Particle Flux in the Ocean.* Ittekot, V., Schafer, P., Honjo, S. and Depretis, P.J. (eds.). Wiley, New York, 19-52.

34. Pye K. (1987). *Aeolian Dust and Dust Deposits.* Academic, San Diego, California, pp.334.

35. Röthlisberger R., Mulvaney R., Wolff E.W., Hutterli M.A., Bigler M., Sommer S., Jouzel J. (2002). *Dust and sea salt variability in central East Antarctica (Dome C) over the last 45 kyrs and its implications for southern high-latitude climate.* Geophysical research Letters, Vol. 29, No 20, 1963.

36. Royer A., De Angelis M. and Petit J.R. (1983). *A 30,000 year record of physical and optical properties of micro-particle from an East Antarctic ice core and implications for paleoclimate reconstruction models.* Clim. Change, 5, 381-412.

37. Sellegri K, Laj P., Peron F., Dupuy R., Legrand M., Preunkert S., Putaud J.P., Cachier E., Ghermandi G. (in press). *Mass balance of free atmospherical aerosol at the Puy de Dome(France) in winter.* Journal of Geophysical Research – Atmosphere.

38. Steffensen J.P. (1997). *The size distribution of microparticles from selected segments of the Greenland Ice Core Project ice core representing different climatic periods.* J. Geophys. Res. 102, 26755-26763.

39. Taylor K.C., Hammer C.U., Alley R.B., Clausen H.B., Dahl-Jensen D., Gow A.J., Gundestrup N.S., Kipfstuhl J., Moore J.C., Waddington E.D. (1993). *Electrical conductivity measurements from the GISP2 and GRIP Greenland ice cores.* Nature 366, 549-552.

40. Taylor S.R. & McLennan S.M. (1985). *The Continental Crust:its Composition and Evolution.* Blackwell Scientific Publications, p.312.

41. Wedepohl K.H. (1995). *The composition of the continental crust.* Geochimica et Cosmochimica Acta, Vol. 59, No. 7, 1217-1232.

Frascati Physics Series Vol. XXXII (2003), pp. 213-221
19th INTERNATIONAL CONFERENCE ON X-RAY AND INNER-SHELL PROCESSES – Roma, June 24 - 28, 2002

COMPARATIVE STUDY OF THE ELECTRONIC STRUCTURE OF NATURAL AND SYNTHETIC RUBIES USING X-RAY ABSORPTION AND EDAX ANALYSIS

P. Parikh, D. M. Bhardwaj
Department of Physics, University of Rajasthan, Jaipur- 302004, India
R. P. Gupta
Central Electronics and Engineering Research Institute, Pilani-333031, India
N. L. Saini
INFM Unit, Dipartimento di Fisica, Universita di Roma La Sapienza, Roma, Italy
S. Fernandes
Gem Testing Laboratory, Jaipur-302003, India
R. K. Singhal, D. C. Jain and K. B. Garg
Department of Physics, University of Rajasthan, Jaipur- 302004, India

ABSTRACT

We have studied the Cr-K-edge XANES and EXAFS in natural Indian rubies (from different sources) and a synthetic ruby. Weight % of various constituents in them is determined using EDAX measurements. Putting the results together from the different techniques we are able to demonstrate their feasibility in quantitative study of precious stones.

1 Introduction

Ruby belongs to the corundum class of crystals having the chemical formula Al_2O_3. Corundum in purest form is colorless, rare and with tetragonal structure. The oxygen atoms occupy nearly hexagonal closed packed configuration with their cations between these planes in octahedral coordination. For every three octahedra, two distorted cations are occupied by aluminum atom in an

ordered arrangement; thus each aluminum atom is surrounded by six oxygen atoms. The same corundum structure is seen in Cr_2O_3, V_2O_3, Ti_2O_3, Fe_2O_3 etc. Some of these, when mixed with Al_2O_3, the position of Al atom in the lattice is replaced by Cr^{+3}, V^{+3}, Ti^{+3}, Fe^{+3} ions.

When Al atom is replaced by Cr atom the red color ruby results in [1]. Transition metal causes color because of their unpaired electrons and variable valence. Ruby occurs as mineral in a wide variety of quality spread all over the world e.g. Burma, India, Thailand, Nigeria, Sri Lanka, Kenya, etc. Synthetic ruby due to the low cost mass production is also available. Therefore, there is a commercial demand to distinguish a precious natural ruby from the artificial (synthetic) ruby. Some of the known methods for identification of gemstones utilize the knowledge of refractive index (RI), specific gravity (SG), double refraction (DR), hardness, color, luster, spark and appearance [2]. To determine chemical composition techniques like Spectrophotometry, Fourier Transform infrared (FTIR), Nuclear Magnetic Resonance (NMR), X-ray Diffraction (XRD) and trace element analysis etc are also employed [3]. In many cases, however, these methods are not adequate, as the synthetic rubies resemble the natural one very closely in physical properties as well as in chemical composition. Since elemental contents in natural rubies also vary from one source to another [4], it is always difficult to know precisely the difference in composition of natural and synthetic rubies. None of the conventional techniques can provide exact compositional data due to presence of many elements in a gem in traces. These impurities although present in traces but may sometimes greatly influence the appearance of gems.

X-ray absorption spectroscopy is a powerful and versatile technique to study electronic structure and near-neighbor environment around a given cation. Furthermore, being a microscopic probe, it measures the local density of unoccupied state of a particular symmetry. The position and the shape of the pre-peak, the absorption edge, the principal absorption maximum (PAM) and the other features in the XANES region give reliable information about valence state of absorbing ion and symmetry of surrounding near neighbors [5]. EXAFS, on the other hand, provides structural information on the local atomic environment of the absorbing species [6].

Table 1: *EDAX: Natural (Indian) and Synthetic (flame fusion) Ruby in weight%.*

	Ruby samples		
Constituents	Nat.Ind.(M.P.)	Nat.Ind.(Karnat.)	Synth.(Fl. Fus.)
Na_2O	0.020	0.025	0.020
MgO	0.20	0.21	-
Al_2O_3	74.65	75.21	97.23
SiO_2	3.43	3.35	0.52
CaO	0.032	0.005	-
TiO_2	0.016	0.02	0.01
Cr_2O_3	0.56	0.62	0.76
Fe_2O_3	1.13	1.53	0.07
Others	19.966	19.44	1.39

2 Experimental

Samples studied in this paper -natural rubies are from two different Indian sources (Karnataka and Madhya Pradesh) and synthetic ruby is from Verneuil's flame fusion process. In the present study we report the results of our investigations on the comparative study of the electronic structure of synthetic (flame fusion) and natural rubies from two different Indian sources. The Energy Dispersive X-ray Analysis (EDAX) was done at CEERI, Pilani to find weight % of various atomic components non destructively.

The XAFS measurements were performed at the beamline BM32 of ESRF, France. We have recorded all the spectra at room temperature over a wide range of energy. Detection was carried out in fluorescence mode. EXAFS analysis has been done using the ATOMS 3.0, FEFF 8.0 and UWXAFS 3.0 program packages [?]. The absorption edge was determined by the first derivative of first rise of the absorption spectrum after pre-edge baseline subtraction. The isolated EXAFS was normalized to the edge step and converted to wave number scale by AUTOBK program. The Fourier transform was performed on k^3– weighted EXAFS oscillation in the range 3.00 to 10.50 $Å^{-1}$ using a Hanning window and analyzed using the FEFFIT program. The fit is performed on data in k, R- space as fitting in R-space gives the most satisfactory results.

3 Results and Discussion

3.1 EDAX Measurements

We discuss the XANES and EXAFS results along with those obtained from EDAX. EDAX measurements are given in table 1 and show the main impurities present in the three samples. A glance at it shows that the Cr content is highest in synthetic ruby followed by the natural sample at from Karnataka and natural sample from M.P in that order.

3.2 Cr-K-edge XANES

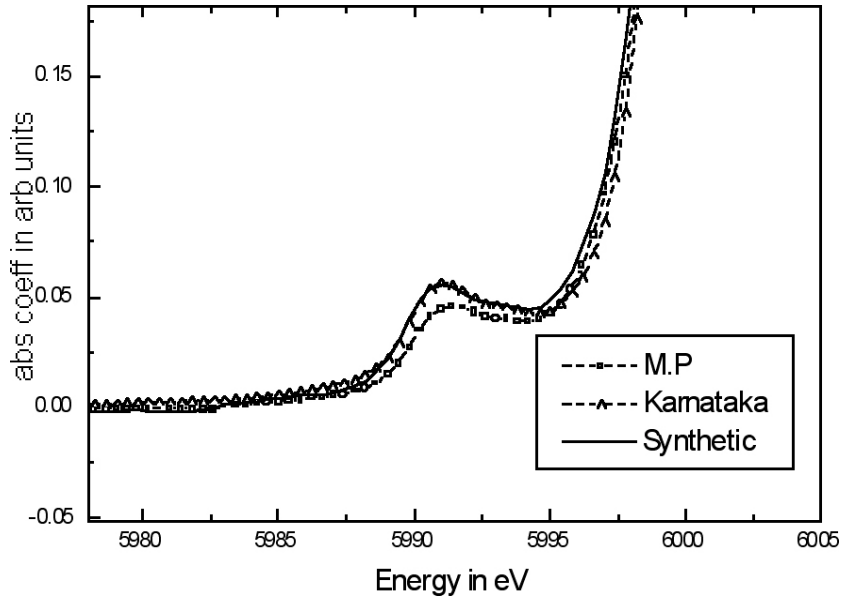

Figure 1: *The Cr-K- pre-edge peak spectra for Indian (M.P and Karnataka) and synthetic (flame fusion) rubies.*

Let us now turn our attention to the XANES results. Figs.1 and 2 show the pre-peak and the Cr-K-edge XANES spectra for the two rubies from Indian sources (Madhya Pradesh and Karnataka) and a synthetic ruby (flame fusion)) respectively. The pre-edge peak (Fig 1) has been associated mainly with the direct quadrupole transition 1s to the empty Cr *3d* states [8, 10]. This feature

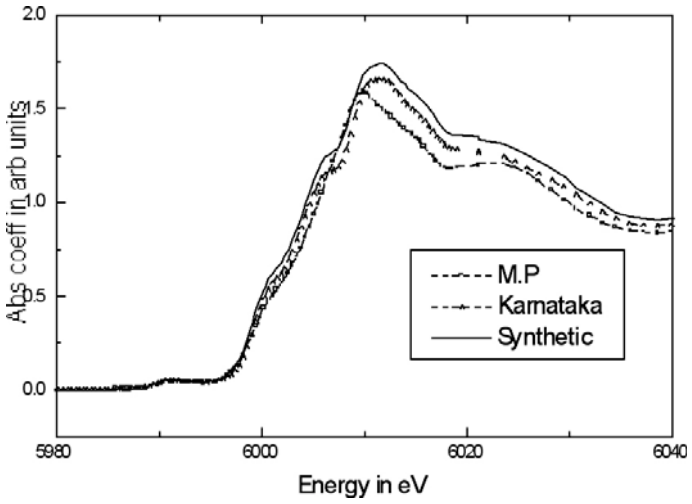

Figure 2: *Cr-K-edge for XANES spectra for natural natural Indian (M.P and Karnataka) and synthetic (flame fusion) rubies.*

represents the transition probability of the Cr *1s* electron into empty t_{2g} and e_g states that are originated by the Cr *3d* and O *2p* states under the influence of the octahedral ligand field [8, 9]. This crystal field splits the *3d* states into t_{2g} and e_g bands with a separation of ∼1.79 eV [11]. The transition probability thus also depends upon how much chromium replaces aluminum at tetrahedral site. The intensity of pre-peak also depends on the density of d states. The intensity of the pre-peak is high in natural ruby from Karnataka and synthetic ruby and low in the natural ruby from M. P. which is in agreement with the Cr content in these (table1). The position of pre-edge peak (fig 1) appears at ∼ 5991.00 eV in all the samples as 3d level is a core level and is unaffected by the outside environment. The position of the absorption edge, determined by the first derivative of the spectra, is found to be at the same ∼ 5999.4 eV for all the three rubies.

Some other features are also observed just before and after the principal absorption maximum due to as shake-in and shake-off structures when a second electron is ejected rather than excited. The partition of kinetic energy between the two ejected electrons shows up as a step followed by the continuum, instead of peaks.

Now we come to the main peak (Fig 2), known as principal absorption maximum (PAM), arising due to 1s-> 4p dipole transition. The position of the main peak (PAM) also shows the valence of the absorbing ion. The PAM is found at 6011.38 eV for the Indian ruby from Karnataka and the synthetic ruby (flame fusion) and at 6009.78 eV for the Indian ruby from M.P. This indicates that the effective valence of Cr is less in case of ruby from M.P than the two other samples. The intensity of main peak (PAM) depends upon partial density of 4p states [5]. The density of the 4p states is highest in synthetic ruby followed by the Karnataka ruby and the M.P ruby in the same order as Cr_2O_3 contents (table 1). The XANES features from multiple scattering afterwards are almost same as the crystal structure of all the samples and the plane of measurements is same.

3.3 Cr-K edge EXAFS

Fig 3 represents the k^3 weighted experimental and fitted Fourier transformed χ (k) spectra in r space and fig 4 represents the filtered back Fourier transformed $k^3\chi$(k) vs. k ($Å^{-1}$) spectra for the natural and the synthetic rubies. The EXAFS fitting has been done for only first two shells from 1.25 Å to 2.9 Å in r-space, as the system is complex and the information on site geometry of most impurities is unknown to permit any reliable analysis for the higher shells. The first two shells in the r-space were fit then back-Fourier transformed (Fig 4). The agreement between experiment curves and fitting is quite nice. The Cr-O distance and coordination numbers for each shell and other structural factors such as Debye Waller factor σ^2 and amplitude reduction factor $S_0{}^2$ for the fittings are shown in table 2.

The EXAFS (table 2) clearly show that there are two distances for the first shell. The Cr-O(1) shorter distance pertains to Cr replacing Al at the tetrahedral sites. The longer Cr-O(2) distance to replacing Al at octahedral sites. The $S_0{}^2$ and Debye Waller factors for all the fittings are quite reasonable vindicating the good quality of fittings. The amount of Cr at the tetrahedral site is higher in the Karnataka ruby and a little less in the case of synthetic ruby while it is substantially less in case of M.P ruby. This is what we have observed by the way of intensity of pre-peak in Fig 1. Further a glance at table 1 shows that Cr content is maximum in the synthetic case followed by Karnataka and M.P ruby in that order. Since intensity of a transition is proportional to both

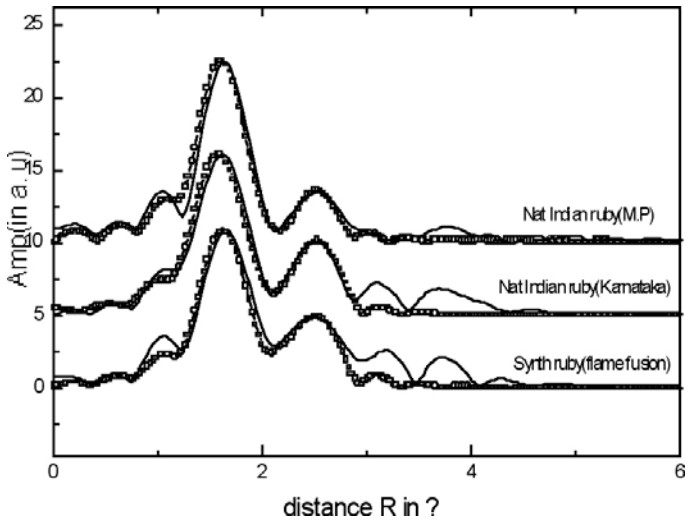

Figure 3: *The k^3-weighted Fourier transformed spectra, exp.(-) and fitted (circle) for natural and synthetic rubies.*

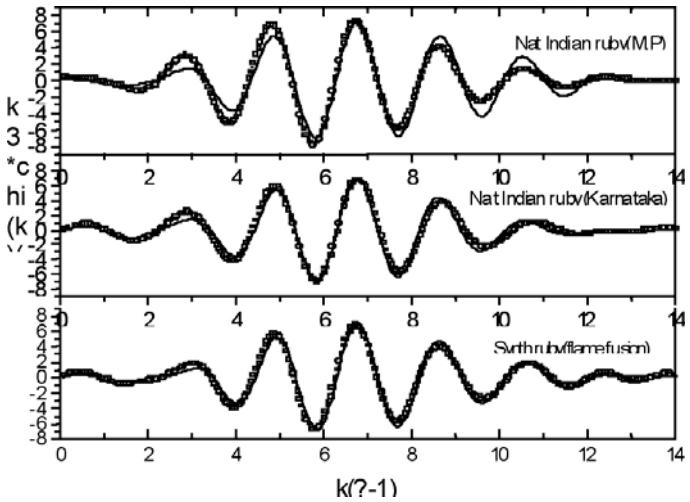

Figure 4: *The k^3-weighted filtered χ (k) vs k spectra;exp (-) and fitted (circle) for natural and synthetic rubies.*

Table 2: *Cr-O distance and related parameters obtained from the EXAFS analysis for first shell fit.*

Ruby source	Tetrahedral site Cr-O(1) (Å)	Cr-O(1) (n1)	Octahedral site Cr-O(2) (Å)	Cr-O(1) (n2)	S_0^2	σ^2(Å^2)
Nat.Ind. M.P.	1.95	2.49	2.06	3.00	0.716	0.0008
Nat.Ind. Karnat.	1.92	3.0	2.04	2.95	0.756	0.0008
Synth. Fl. Fus.	1.94	2.95	2.06	3.00	0.726	0.0008

transition probability and density of states. These results would predict higher intensities of the pre-peaks in synthetic and the Karnataka rubies and a lower intensity in case of M.P ruby.

4 Summary

We have made EDAX, XANES and EXAFS measurements (Cr-K-edge) on three ruby samples from different sources, two natural and one synthetic. EDAX gives us the Cr content and concentrations of other impurities in them. From XANES and EXAFS we are able to quantitatively estimate the Cr-O distances and Cr population at the octahedral and tetrahedral sites. The results from three measurements show a good agreement. In conclusion, we have shown how these techniques can be used to study precious stones.

5 Acknowledgements

One of us (PP) is thankful to the UGC and the Government of Rajasthan for granting TRF. Thanks also to the ESRF staff for helping in doing the XANES & EXAFS studies. KBG is thankful for the TRIL program for the partial support.

References

1. Hughes, W. Richard. RUBY & SAPPHIRE, RWH. Publishing & Boulder, Colorado, USA, 1997.
2. Read, P.G. Gemmology. Butterworth-Heinemann, (1997).
3. Moroz. I., Inessa et al. Australian Gemmologist (1999) **20**, 315-320.
4. Muhlmeister Sam, Emmanuel Fritch et al. Gems & Gemology 1998.
5. Azaroff, L.V. and Pease, D.M. (1974) X-ray Spectroscopy (New York: McGraw Hill) 288.
6. Durham P.J., Pendry J.B. and Hodges, C.H. (1982) Comput. Phys. Commun.**25**, 193.
7. Raval, B., Newville, M., Cross, J. O. and Bouldin, C.E. Physica B **145** (1995) 208.
8. Rehr, J., Zabinsky, S.I. and Albers, R.C. Phys. Rev. Lett. **69** (1992) 3397.
9. Stern, E.A. Phys. Rev. B **48** (1993) 9825.
10. Booth, C. H., Bridges, F., Kwei, G. H., Lawrence, J. M., Cornelius, A. L, and Neumeier, J. J. Phys. Rev. B **57** (1998) 10440.
11. Goldman, D. S., Rossman, G..R., Parkin, K. M., Phys. Chem. Mineral. **3** (1978) 225.

Frascati Physics Series Vol. XXXII (2003), pp. 223-228
19th INTERNATIONAL CONFERENCE ON X-RAY AND INNER-SHELL
PROCESSES – Roma, June 24 - 28, 2002

THE LOCAL GEOMETRICAL STRUCTURE OF Zn_7-METALLOTHIONEIN-2 PROBED BY XANES SPECTROSCOPY.

Grigory Smolentsev, Alexander Soldatov
Department of Physics, Rostov State University, Rostov-Don, 344090, Russia
Martin Stillman
Department of Chemistry, University of Western Ontario,London, Ontario N6A 5B7, Canada

ABSTRACT

We have applied multiple scattering theory and molecular dynamic calculation of the protein geometry to simulate the Zn X-ray absorption near edge structure (XANES) spectra of rabbit liver Zn_7-metallothionein-2. Our method is sensitive to the radial distribution and bond angles of about 20 atoms surrounding each zinc ion. This allows to determine an average Zn-S distance and to choose the best model for local geometry of the active site from the comparison of theoretical and experimental spectra. Calculations were performed for the 3 published models obtained by NMR for Cd-MT with reduced metal-sulfur bond lengths and model generated by molecular dynamic technique. It has been found that the model obtained using molecular dynamic is most realistic. The calculated average Zn-S bond length is about 2.35 Angstrom, which consistent with previous EXAFS study.

1 Introduction

The study of metal-thiolate clusters in metallothioneins (MT) is a key step in solving problems of heavy metals carriage and storage and in general to gain an understanding of the relationship between protein structure and function. The properties of metallothioneins with different metals such as Zn, Cd, Cu, Co, Hg and Ag are widely studied [1]. The rat liver Cd_5Zn_2-MT protein has been crystallized [2] and is found to adopt two separate metal binding domains (named a (C-terminus) and b (N-terminus). The b domain contains M_3Cys_9 cluster, whereas the a domain contains M_4Cys_{11} cluster (M=Cd, Zn or Co). X-ray diffraction and NMR provides the standard structural probe to measure the atomic positions in proteins. Cd_7-MT has been described structurally by the analysis of NMR spectra and to date three sets of data are available [3, 4, 5] in Protein Data Bank (PDB). Cd_5Zn_2-MT has been investigated using X-ray diffraction [6]. Nowadays methods of structure determination such as X-ray diffraction and NMR reach limit in atomic resolution where the positions of single atoms in a protein molecule can be determined with precision about several tenths of Angstrom. On the other hand, analysis of XANES (x-ray absorption near edge structure) and EXAFS (extended x-ray absorption fine structure) can provide information on the geometry with subatomic resolution [7, 8]. XANES spectroscopy is complementary to EXAFS spectroscopy because the XANES experiment is particularly sensitive to the bond angles and positions of about 20 neighboring atoms surrounding each metal ion. This contrasts the case of the EXAFS experiment, which provides excellent bond lengths but almost no information on angular distribution of neighboring atoms. We have applied the multiple scattering theory to simulate the XANES spectra of several alternative geometry models of the Zn-site and chosen from them the best model for local geometry of the active site.

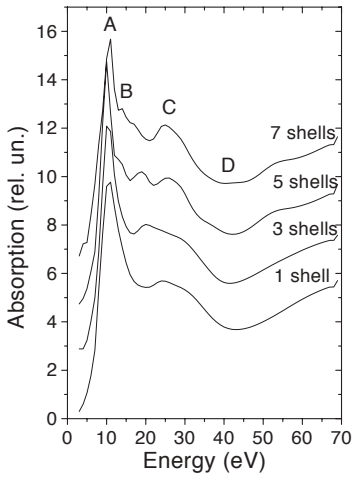

Figure 1: *Calculated Zn K-edge XANES generated within the clusters of 1, 3, 5 and 7 shells*

2 Method of calculation

The XANES simulations make use of the one-electron full multiple scattering formalism [9] included in G4XANES computer package [10]. The calculations have been performed in the real space for 7 shell clusters in the same manner as in previous work [11]. For a chosen protein model seven XANES spectra for all non-equivalent metal centers have been calculated and averaged with the same weight. A broadening Lorentzian function has been applied to the calculated XANES to take into account core hole lifetime (1.4 eV), the experimental resolution (1.5 eV) and an energy dependent factor representing photoelectron lifetime due to inelastic scattering by valence electron [12].

3 Results and Discussion

Our method of local geometrical structure probe is based on comparison of experimental and theoretical spectra, calculated for different protein models. To

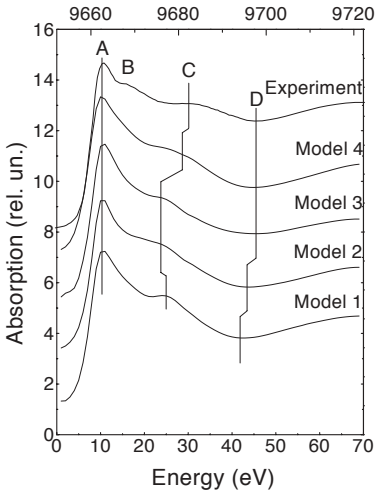

Figure 2: *Experimental and theoretical Zn K-edge XANES calculated for the different models.*

date there is no structural data on Zn_7-MT in PDB. Only 3 sets of NMR data on the structure of Cd_7-MT are available [3, 4, 5]. Messerle et al. [13], using proton NMR, found that the three-dimensional structures of the Zn- and Cd-proteins were very similar and concluded that the connectivities between metal and cysteine sulfurs were the same. Therefore, we assumed that the protein structures around the metal atoms in both Zn-MT and Cd-MT have the same bond angles and distances in amine residues. To take into account changes in metal arrangement when Cd atoms substituted by Zn, we have contracted proportionally all metal- sulfur distances. Thus we obtained three models of the metal- thiolate clusters on the basis of PDB data (model 1 [3] - PDB identification 1MHU, 2MHU, model 2 [4] - 1MRB, 2MRB and model 3 [5]- 1MRT, 2MRT) Moreover we have constructed fourth model using molecular modeling and molecular dynamic (MM2-MD) techniques [14], modified to include the effects of terminal and bridging sulfurs on the metal-sulfur bond length.

The important step in the multiple scattering analysis is the determination of the minimum size of a cluster of neighboring atoms around the absorbing Zn sufficient to obtain all spectral details. In fig.1, the results of the multiple scattering calculations of the XANES spectra for the first absorbing center in model 1 generated within the clusters of 1, 3, 5 and 7 shells are shown. Additional atoms included in the 7-shells cluster do not change the spectrum significantly. Therefore all subsequent calculations were performed using 7 shells cluster. As one can see (fig.1), peaks A and C appear just as in the 1-shell cluster. Whilst the position of peak A does not change significantly when other shells are added into the calculation, the position of peak C depends on the number of shells included, because it mixes with other peaks arising from the scattering within outer shells. Therefore, the relative energy separation between peak A and the position of minimum D has been used for the determination of the average metal-sulfur distance, while the energy of peak C has been used as a criterion to find the best model of outer shell geometry. The energy of the maximum of A is separated from minimum D by 34 eV in the experimental spectrum. In the theoretical spectrum this value is equal to 29 eV when the average Zn-S distance is set to 2.50 Angstrom (value proposed for Cd-MT) and 34 eV when the Zn-S bond length is set to 2.3 Angstrom. Best agreement between theoretical and experimental results is reached when Zn-S bond length is 2.35 Angstrom. This correlates well with the previous EXAFS data [15] and with our results of MM_2-MD calculations.

In fig.2 we present theoretical XANES for the four models described above and experimental spectrum. As one can see, the position of peak C depends on the model chosen. The calculations using model 4 reproduce its position most accurately. On this basis, we propose that model 4 of the active site geometry is the most realistic. More precise structural information can be obtained using Monte Carlo search techniques of a geometrical model, which gives the best fit to the experimental spectra [16]. Peak B, which is not reproduced in our

calculations, may be used as a criterion in this calculation. But this technique is very time consuming, especially for systems with more than one non-equivalent absorbing center.

References

1. M.J. Stillman, Coord. Chem. Review **144**, 461 (1995).
2. W.F. Furey *et al*, Science **234**, 704 (1986).
3. B.A. Messerle *et al*, J. Mol. Biol. **214**, 765 (1990).
4. A. Arseniev *et al*, J. Mol. Biol. **201**, 637 (1988).
5. P. Shultze *et al*, J. Mol. Biol. **203**, 251 (1988).
6. A.H. Robbins *et al*, J. Mol. Biol. **221**, 1269 (1991).
7. S.S. Hasnain *et al*, J. Synchrotron Rad. **6**, 852 (1999).
8. F. Boffi *et al*, J. Synchrotron Rad. **8**, 196 (2001).
9. P. Durham *et al*, Comput. Phys. Commun. **25**, 193 (1982).
10. S. Della Longa *et al*, Comp. materials science **4**, 199 (1995).
11. S. Della Longa *et al*, Eur Biophys. J. **27**, 541 (1998).
12. J.E. Muller *et al*, Solid State Commun. **42**, 365 (1982).
13. B.A. Messerle *et al*, J. Mol. Biol. **225**, 433 (1992).
14. D.A. Fowle *et al*, J. Biomol. Struct. Dyn. **14**, 393 (1997).
15. D.T. Jiang *et al*, J. Am. Chem. Soc. **116**, 11004 (1994).
16. M. Benfatto *et al*, J. Synchrotron Rad. **8**, 1087 (2001).

Frascati Physics Series Vol. XXXII (2003), pp. 229-239
19th INTERNATIONAL CONFERENCE ON X-RAY AND INNER-SHELL
PROCESSES – Roma, June 24 - 28, 2002

EFFECT OF THE SURFACTANTS ON THE LOCAL ATOMIC STRUCTURES OF CERIUM OXIDE NANOPARTICLES

Zhonghua Wu, Jing Zhang, Zhongjun Chen, Ziyu Wu*
Beijing Synchrotron Radiation Laboratory,
Institute of High Energy Physics
Chinese Academy of Sciences,
P.O. Box 918, Bin 2-7, Beijing 100039, P. R. China
Lin Guo
School of Material Science and Engineering,
Beijing University of Aeronautics and Astronautics,
Beijing 100083, P. R. China

ABSTRACT

In this paper, cerium oxide nanoparticles coated, respectively, with sodium bis(2-ethylhexyl) sulfosuccinate (AOT) and cetyltrimethyl ammonium bromide (CTAB) were prepared using chemical method (emulation method), and the naked ones without surfactant were prepared by using precipitation method. The particle size were found to be 2∼3 nm by using transmission electron microscope (TEM) and x-ray diffraction (XRD). X-ray absorption spectra at the Ce L_3 edge were collected at extended x-ray absorption-fine-structure (EXAFS) station (beam line 4W1B) of Beijing Synchrotron Radiation Facility (BSRF). Mixed valence of Ce^{3+} and Ce^{4+} was detected by x-ray absorption near-edge-structure (XANES) spectra. The local atomic structures of these nanoparticles were obtained by a detailed EXAFS data analysis. We found that a core-shell model can describe these nanoparticles. The core part with Ce^{4+} characteristic is almost the same with bulk CeO_2. The shell part of surfactant-coated nanoparticles with Ce^{3+} characteristic is similar to the structure of Ce_2O_3, while for the naked nanoparticles without surfactant, there still are 8

O atoms surrounding Ce with Ce-O bond length of 2.634 Å. There are about 7 O atoms surrounding the near-surface cerium atoms in AOT- and CTAB-coated nanoparticles. Their Ce-O bond lengths (respectively, 2.504 Å and 2.628 Å) for AOT- and CTAB-coated cerium oxide nanoparticles are different because of the different environment. Effect of surfactant on the local atomic structures of cerium oxide nanoparticles was discussed.

1 INTRODUCTION

Because of the special properties and potential application, the fabrication, structural characteristic and property measurement of nano-structural materials attract widely scientist's interesting. Cerium oxides have been widely studied due to their complex electron structures [1−5]. For the nano-structural cerium oxides, because of the quite small particles size and quite large ratio of surface to volume as well as the possible amorphism, the other techniques can usually not provide the details of the local atomic structures. X-ray absorption fine structure (XAFS) technique is a powerful tool to study the local atomic and electronic structures. In this paper, by comparing the XAFS spectra of the naked cerium oxides nanoparticles and those coated, respectively, by surfactants sodium bis(2-ethylhexyl) Sulfosuccinate (AOT) and Cetyltrimethyl Ammonium Bromide (CTAB), we hope to predict the effect of surfactants on the local atomic structures of cerium oxide nanoparticles.

2 EXPERIMENTAL

Two kinds of cerium oxide nanoparticles coated, respectively, with surfactant AOT ($C_{20}H_{37}NaO_7S$) and CTAB ($C_{16}H_{33}(CH_3)_3NBr$) were prepared by using the microemulsion method. Another naked cerium oxide nanoparticles was prepared by using precipitation method. The details of sample preparation can be found in references [6−8]. X-ray diffraction (XRD) patterns of the three samples and the bulk CeO_2 were shown in Fig. 1. The particle sizes were evaluated to be about 2∼3 nm for the three kinds of nanoparticles. Similar particle sizes were confirmed by transmission electron microscopy (TEM) as shown in Fig.2 for AOT-coated cerium oxide nanoparticles.

The cerium L_3-edge XAFS spectra were collected at ambient temperature with transmission mode at EXAFS station of Beijing Synchrotron Radiation Laboratory (BSRF). Samples were homogeneously smeared on Scotch adhesive tape. Several layers were folded to reach the optimum absorption thickness ($\Delta\mu$d ≈1.0, $\Delta\mu$ is the absorption edge step, d is the physical thickness of the sample). The storage ring was run at 2.2 GeV with the electron current about

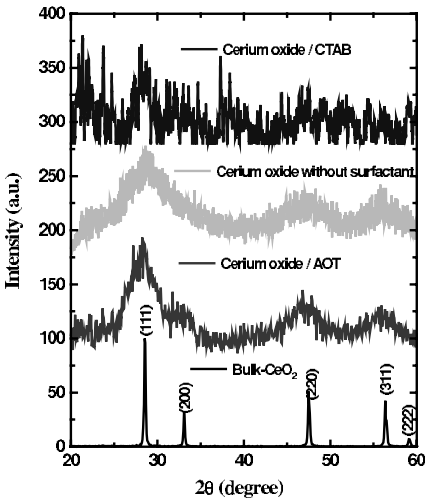

Figure 1: *X-ray diffraction patterns for bulk-CeO_2, cerium oxide nano-particles without surfactant and with surfactants (AOT and CTAB).*

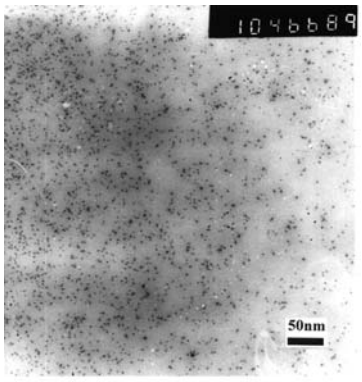

Figure 2: *Transmission electron micrograph of AOT-coated cerium oxide nanoparticles.*

80 mA. Higher harmonics were eliminated by detuning the double crystal Si (111) monochromator. The incident and transmission x-ray intensities were, respectively, detected by ion chambers that were installed in front of and behind the sample. Energy resolution ($\Delta E/E$) is about 2×10^{-4}. The absorption spectra were collected from 200 eV below the absorption threshold to over 500 eV above the threshold until the L_{II} absorption edge appears. The XANES spectra of the three-cerium oxide nanoparticles were shown in Fig.3. For comparison, the XANES spectra of Ce L_3-edge of bulk CeO_2 (quadrivalent Ce^{4+}) and bulk $Ce(NO_3)_36H_2O$ (trivalent Ce^{3+}) were also shown in Fig.3. Four XANES features [1)] were, respectively, denoted as A, B, C, and D. Features A and B are the characteristic of Ce^{4+} while feature C coincides with the main peak of Ce^{3+}. It can be concluded that the AOT- and CTAB-coated nanoparticles contain a Ce^{3+} component, besides the Ce^{4+} one. However, it almost only contains the Ce^{4+} component in the naked cerium oxide nanoparticles. Probably, this can be attributed to the difference of the starting materials, for example, $Ce(NO_3)_36H_2O$ for AOT- and CTAB-coated nanoparticles and $Ce(SO_4)_24H_2O$ for the naked ones.

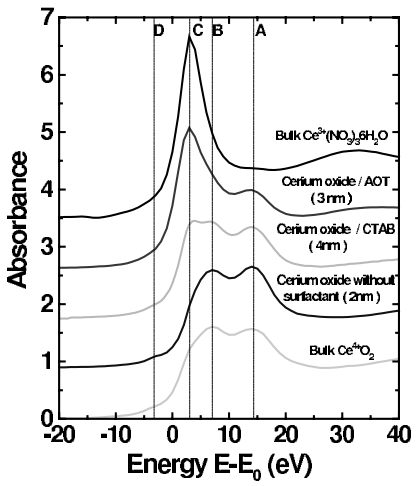

Figure 3: *XANES spectra of Ce-L_3 absorption for the three kinds of cerium oxide nanoparticles. For comparison, those of bulk CeO_2 and $Ce(NO_3)_36H_2O$ are also shown in this figure.*

3 DATA ANALYSIS AND RESULTS

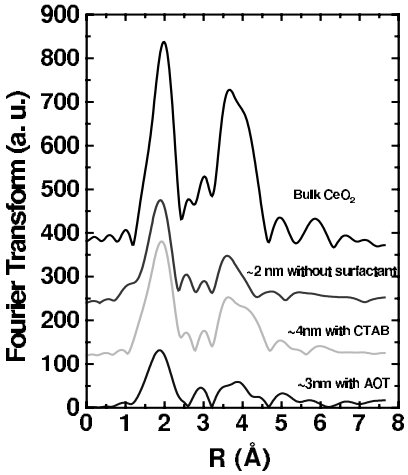

Figure 4: *Fourier transform spectra of Ce-L_3 absorption with k^3-weight for the bulk-CeO_2 and the cerium oxide nanoparticles without surfactant and with surfactants (AOT and CTAB).*

The XANES features were fitted by using four Gaussian- broadened Lorentzian functions [9–10]. An arctan function was used to simulate the absorption background. The spectroscopic valences [9] were calculated to be about 3.48, 3.54, 3.49, and 3.51, respectively, for AOT-coated, CTAB-coated, the naked nanoparticles, and bulk CeO_2. The corresponding f-electron counts are 0.52, 0.46, 0.51, and 0.49, respectively.

Multielectron excitation [11–18] affects seriously the EXAFS signal at the L_3-edge of Ce-absorption. After removing of the multielectron excitation effect, the absorption curves were transferred to k space using the formula: $k=(2m(E-E_o)/h^2)^{1/2}$. The post-edge absorption background was fitted and subtracted by using spline function. Then, EXAFS functions were Fourier- transformed to R space with k^3-weight. Hanning windows were used in the Fourier transform and filter process. The Fourier transform and filter regions are, respectively, about 7.8 $Å^{-1}$ and 1.5 Å. More than seven fitting parameters are allowable. The Fourier- transform spectra and the near-neighbor coordination EXAFS functions were, respectively, shown in Fig. 4 and 5.

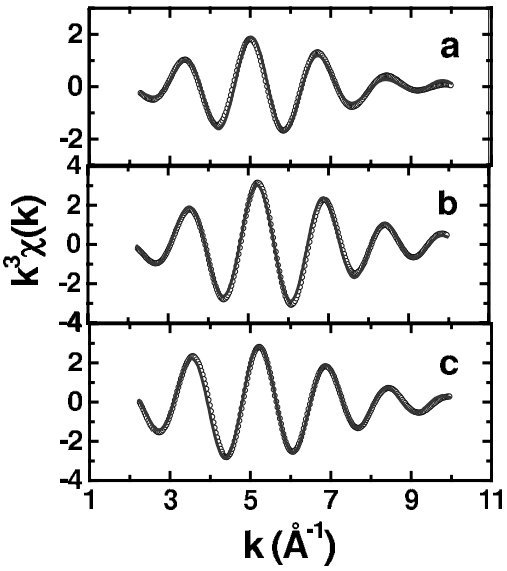

Figure 5: *EXAFS curves of Ce L_3-edge with k^3-weight, in cerium oxide nanoparticles coated by surfactant AOT (a), surfactant CTAB (b), and without surfactant (c). Symbols are experimental values, solid line are the fitting ones.*

A single-shell fitting cannot give the robust parameters, so two sub-shells (core-shell model) was used to describe the local atomic structures in the three kinds of nanoparticles. Bulk CeO_2 was used as the reference sample to get the amplitude and phase shift of Ce-O bond. The conventional EXAFS formula was used to fit the experimental signals. The first sub-shell was found to have the same structural parameters (8×2.343 Å) as the bulk CeO_2 [19] for the three kinds of nanoparticles. Evidently in the three samples, the first sub-shells are corresponding to the core part of the nanoparticles, which gives the x-ray diffraction patterns as shown in Fig.1. The core parts are less affected by the surfactants (AOT and CTAB). The second sub-shells are used to describe the local atomic structures at the shell-parts (surface) of the nanoparticles. We expect that the shell-part can represent the effect of surfactants (AOT and CTAB) on the nanoparticles. In addition, it also reflects the difference between the two cases with and without surfactants. The fitting results were given in table 1.

Table 1: *Oxygen coordination parameters around Ce in naked cerium oxide nanoparticles (without surfactant) and those coated, respectively, by surfactant sodium bis(2-ethylhexyl) sulfosuccinate (AOT) and Cetyltrimethyl ammonium bromide (CTAB).*

Samples	N	R (Å)	^{2} (Å^2)	(eV)
Bulk-CeO_2	8.0	2.343	0.0	0.0
Cerium oxide	4.10.3	2.3430.010	0.00170.0020	0.01.0
coated by AOT	3.40.4	2.5040.020	0.00250.0020	6.81.0
Cerium oxide	6.50.4	2.343 (fix)	0.00540.0020	0.21.0
coated by CTAB	1.40.8	2.6280.020	0.00780.0030	3.32.0
Cerium oxide	6.80.4	2.343(fix)	0.00720.0030	0.91.0
without surfactants	1.21.0	2.6340.0020	0.00530.0030	2.82.0

4 DISCUSSION

Cerium oxide nanoparticles were well described by two sub-shells. The first sub-shell is almost the same with the bulk CeO_2. We attribute this sub-shell to the contribution of the core-parts. Eight oxygen atoms surround the central cerium atom in the core part and the cerium presents Ce^{4+} characteristic. Another sub-shell describes the contribution of the shell-parts. The obtained coordination numbers as shown in Table 1 are nominal coordination numbers. The composition (α) of the core part can be evaluated according to α=N_{nom}/N_{true}. Here, N_{nom} is the nominal coordination number as listed in Table 1, N_{true}=8 is the real coordination number in core part as bulk CeO_2. From the composition (β=1-α) of the shell-part, the real coordination number of shell-part can be evaluated according to N_{true}=N_{nom}/β. Finally, the composition of the core-part was evaluated to be about 51% (AOT), 81% (CTAB) and 85% (naked), respectively. The second sub-shells are mainly the contribution of the shell part (surface) of the nanoparticles. The real coordination number in the shell part were evaluated to be about 7 for AOT- and CTAB-coated CeO_2 nanoparticles, and 8 for naked ones. That is to say, there are about 7 oxygen atoms around cerium in an average distance of 2.504 Å in the shell part of AOT-coated nanoparticles. Similarly, seven oxygen atoms surround central cerium atom with an average bond length of 2.628 Å in the shell part of CTAB-coated nanoparticles. But, eight oxygen atoms surround central cerium atom with an elongated Ce-O bond length (2.634 Å) in the shell-part. These imply that the shell part of AOT-coated nanoparticles is similar with Ce_2O_3 [20] (averagely, 7 O at 2.5047 Å). Partial cerium presents Ce^{3+} characteristics in the two surfactant-coated oxides that just originate from the shell part of the nanoparticles.

On the basis of the shell-core model, we can explian the phenomen of the XANES spectra. Comparing with the pure Ce^{4+} compound CeO_2 and the pure Ce^{3+} compound $Ce(NO_3)_36(H_2O)$, obviously, the two kinds of cerium oxide nanoparticles are the mixtures [21-24] of the Ce^{3+} and Ce^{4+}. This is agreement with the EXAFS results. We believe there are some vacancies or distortation in the interface between the surfactant and the nanoparticles. It is the surfactants (AOT and CTAB) that limits the particle size, which made the shell part of the nanoparticles have to distort or create vacancies to decrease the formation energy of the nanoparticles. For the two kinds of nanoparticles with different surfactants AOT and CTAB, their shell parts show the same Ce^{3+} characteristic and coordination numbers, but the Ce-O bond lengths are quite different. Although the total average bond length (7.5×2.416 Å) in AOT-coated nanoparticles is larger than that (7.9×2.394 Å) in CTAB-coated nanoparticles, the bond length of shell part is smaller in the former (7.0×2.504 Å) than in the latter (7.0×2.628 Å). In the same time, we also found that the latter has larger Debye-waller factor than the former. This is agreement with XRD prediction. For naked cerium nanoparticles, their bond length (8.0×2.634 Å) at shell part is the greatest among the three, while the total average bond length (8.0×2.387 Å) is the smallest. Assuming the nanoparticles take a spherical shape and have uniform mass density, and D is the diameter of the nanoparticle, then the thickness (δ) of the shell-part of the nanoparticles can be approximately evaluated as δ=D(1-$\alpha^{1/3}$)/2. The naked nanoparticles have thinner shell thickness ($\delta\approx$0.5Å), because they are not affected by the surfactant. But in the surfactant-coated nanoparticles, the shell thickness is, respectively, 0.6Å (CTAB) and 2.0Å (AOT).

5 CONCLUSION

Two components of Ce^{3+} and Ce^{4+} exist in the surfactant-coated nanoparticles. The Ce^{3+} components probably come from the starting materials $Ce(NO_3)_36H_2O$. The composition of Ce^{3+} was evaluated to be about 48% (AOT) and 19% (CTAB), respectively. However, for the naked cerium oxide nanoparticles, the Ce^{3+} component is negligible.

XAFS results were well explained by a core-shell model, i.e., these nanoparticles are consisted of two parts (the core part and the shell part). The core parts have the same structures as bulk CeO_2 and present Ce^{4+} characteristic, the shell parts presents Ce^{3+} characteristic (AOT- and CTAB-coated nanoparticles) or Ce^{4+} characteristic (the naked nanoparticles without surfactant).

Surfactants (AOT and CTAB) mainly affect the Ce-O bond length and thickness of shell part. For AOT-coated nanoparticles, the Ce-O bond length and thickness of shell part are, respectively, 2.504 Å and 2.0 Å. For CTAB-

coated nanoparticles, are 2.628 Å and 0.6 Å. For naked nanoparticles, are 2.634 Å and 0.5 Å. The total average bond lengths over core and shell parts are, respectively, 2.387Å (naked nanoparticles), 2.416 Å (AOT-coated nanoparticles) and 2.394Å (CTAB-coated nanoparticles).

References

1. Bianconi, A., Marcelli, A., Dexpert, H., Karnatak, R., Kotani, A., Jo, T., Petiau, J. *Phys. Rev.* B, **35,** 806-812 (1987).

2. Soldatov, A. V., Ivanchenko, T. S., Kotani, A., Bianconi, A. *Physica B,* **208-209**, 53 (1995).

3. Soldatov, A. V., Ivanchenko, T. S., Della Longa, S., Kotani, A., Iwamoto, Y., Bianconi, A. *Phys. Rev.* B, **50,** 5074-5080 (1994).

4. Dexpert, H., Karnatak R. C., and Esteva, J. M., Connerade, J. P., Gasgnier, M., Caro, P. E. and Albert, L. *Phys. Rev*. B, 36, 1750-1753 (1987).

5. Beaurepaire, E., Kappler, J. P., Malterre D. and Krill, G. *Europhys. Lett.* **5,** 369-374 (1988).

6. Malterre, D. *Phys. Rev.* B, **43,** 1391-1398 (1991).

7. Wu, Z. H., Zhang, J., Benfield, R. E., Ding, Y. F., Grandjean D., Zhang, Z. L, and Ju, X., *J. Phys. Chem. B*, **106**, 4569-4577 (2002).

8. Wu, Z. H., Benfield, R. E., Guo, L., Li, H. J., Yang, Q. L., Grandjean D., Li, Q. S, Zhu, H. S., *J. Phys.: Condensed Matter,* **13,** 1-15 (2001).

9. Nachimuthu, P., Shih, W. C., Liu, R. S., Jang, L. Y., and Chen, J. M. *J. Solid State Chem.*, **149,** 408-413 (2000).

10. Capehart, T. W., Mishra, R. K., Fuerst, C. D., Meisner, G. P., Pinkerton, F. E. and Herbst, J. F. *Phys. Rev.* B, **55,** 11496-11501 (1997).

11. Vandormael, D., Grandjean, F., Briois, V., Middleton, d. P., Buschow, K. H. J., Long, C. J. *Phys. Rev.* B, **56,** 6100-6106 (1997).

12. Kodre, A., Arcon, A., Hribar, M., Štuhec, M., Villain, F., Drube, W., Tröger, L. *Physica* **B**, **208&209,** 379 (1995).

13. Fonda, E.; Andreatta, D.; Colavita, P. E. and Vlaic, G., *J. Synchrotron Rad.*, **6,** 34-42 (1999).

14. Li, G., Bridges, F., and Brown, G. *Phys. Rev. Lett.*, **68,** 1609-1612 (1992).

15. Mukoyama, T., and Ito, Y. *Nucl. Instrum. Meth. Phys. Res.* B, **87,** 26-33 (1994).

16. Chaboy, J., Marcelli, A., and Tyson, T. A. *Phys. Rev.* B, **49,** 11652-11661 (1994).

17. Benfield, R. E., Filipponi, A., Bowron, D. T., Newport, R. J. and Gurman, S. J. *J. Phys.: Condens. Matter,* **6,** 8429 (1994).

18. D'Angelo, P., Di Cicco, A., Filipponi, A. and Pavel, N. V. *Phys. Rev.* A, **47,** 2055-2063 (1993).

19. Filipponi, A., Tyson, T. A., Hodgson, K. O. and Mobilio, S. *Phys. Rev* A, **48,** 1328-1338 (1993).

20. Whitfield, H. J., Roman, D., Palmer, A. R. *J. Inorg. Nucl. Chem.*, **28,** 2817 (1966).

21. Baernighausen, H., Schiller, G., *Journal of the Less-common Metals*, **110,** 385 (1985).

22. Zhou, Y. C., and Mohamed, N. R. *Acta Materialia*, **45,** 3635 (1997).

23. Tschopea, A., Birringera, R. *Nanostruct. Mater.*, **9,** 591 (1997).

24. Palmqvist, A. e. C., Wirde, M., Gelius, U. and Muhammed, M. *Nanostruct. Mater.,* **11,** 995 (1999).

25. Pfau, A., Schierbaum, K. D. *Surface Science*, **321,** 71 (1994).

INSTRUMENTATION AND TECHNIQUES

Frascati Physics Series Vol. XXXII (2003), pp. 243-253
19th INTERNATIONAL CONFERENCE ON X-RAY AND INNER-SHELL
PROCESSES – Roma, June 24 - 28, 2002

THE DAΦNE-LIGHT FACILITY

Emilio Burattini, Francesca Monti
Università degli Studi di Verona, strada LeGrazie 15, I-37138 Verona
Fabio Belloni, Gianfelice Cinque*, Sultan Dabagov, Antonio Grilli,
Augusto Marcelli, Elisabetta Pace, Massimo Piccinini, Agostino Raco
INFN-Laboratori Nazionali di Frascati, via Fermi 40, I-00044 Frascati
Paolo Calvani, Mariangela Cestelli Guidi, Alessandro Nucara
Università di Roma La Sapienza*, piazzale Aldo Moro 5, I-00185 Roma*

ABSTRACT

The new Synchrotron Radiation facility at Frascati exploits the intense photon emission from DAΦNE, the 0,51 GeV storage ring circulating over 1 A of electrons. Among the three beamlines commissioned, the Synchrotron INfrared Beamline At Daϕne (SINBAD) is fully operational by a brilliant SR beam spanning the entire IR. Recently, the soft X-ray beamline has been characterized and, once implemented the double-crystal monocromator, X-ray Absorption Spectroscopy is applied on material standards in the distinguishing energy region below 4 keV. An UltraViolet line, dedicated to photobiology dosimetry, has also given first results on cell irradiation in the UVB band.

*Corresponding author: fax +39 06 9403 2597, e-mail cinque@lnf.infn.it

1 The DAΦNE Synchrotron Radiation source

The 97,7 m long DAΦNE electron storage ring is parasitically used for Synchrotron Radiation purposes: since its unique characteristics of energy, 0,51 GeV, and circulating current, routinely over 1 A, it provides an intense photon emission spectrally peaked in the low energy range. Some machine parameters [1)] are reported in Table 1.

Table 1: *DAΦNE electron ring parameters (December 2002 set-up).*

Energy, GeV	0,51
Max current, A	1,82
Number of bunches	47
Injection time, min	3
Horizontal emittance, m·rad	$0{,}8{\cdot}10^{-6}$
Energy spread, %	0,04
At bending magnet: β_x, m β_y, m	9,1 3,6
At wiggler: β_x, m β_y, m	2,4 2,2

1.1 The IR source

An arc of few degrees from a DAΦNE bending magnet (BM) provides the IR emission fan: its critical wavelength, about 60 Å, does not affect the IR intensity since the asymptotic spectral emission at long wavelengths. Moreover, the large electron beam emittance is not relevant in the IR domain where the intrinsic divergence of the SR dominates. The characteristics of the SR from the BM source are presented in Table 2 according to a nominal circulating current of 1 A. The spectral flux [2)] from the dipole is plotted in Figure 1.

Table 2: *Bending Magnet and Synchrotron Radiation parameters.*

BM radius, m	1,54
BM field, T	1,2
BM angle, rad	0,8
SR critical energy, eV	208
SR Flux at critical energy, ph/s·mrad at 0,1% b.w.	$8{,}2{\cdot}10^{12}$

Table 3: *Wiggler and Synchrotron Radiation parameters.*

W Magnetic field at the center gap, T	1,8
Number of poles	$\frac{1}{2}$ +5+ $\frac{1}{2}$
Period length, m	0,64
W length, m	1,92
K value	107,6
SR critical energy, eV	311
SR divergence at critical energy, mrad	±0,65
SR Flux at critical energy, ph/s·mrad at 0,1% b.w.	$4{,}9{\cdot}10^{13}$

1.2 The X-ray source

One of the 6-pole equivalent planar insertion devices installed on the electron ring for vertical beam compaction is the X-ray source. This wiggler (W) forces the emission of a wide electromagnetic radiation fan mostly polarized in the horizontal plane. The electron trajectory in the magnet (max displacement ∼34 mm) gives a deflection angle larger than the SR divergence (K ∼108); the typical SR continuous spectral distribution has a critical wavelength of circa 4 Å. By 1 A of circulating current an intense flux of soft X-rays is present well beyond one decade from the critical energy. The characteristics of the SR beam from the wiggler (nominal current 1 A) are presented in the Table 3, while the spectral flux [2)] produced is also shown in Figure 1.

2 The IR beamline

Since the 2001, SINBAD operates in parasitic mode – in the near-, mid- and far-IR domain – also as SR facility opened to European Union users in the frame of TARI program.

The front end collects the SR fan under a solid angle of 45 × 18 mrad^2: four remotely controlled slits define both beam size and (linear or circular) IR polarization. The ∼25 m long IR beamline is made by a complex optics [3)] under Ultra High Vacuum (Figure 2) till the CVD diamond wedged window at the second optical focus. Schematically, the SR is firstly focused (by an ellipsoidal mirror) since the intrinsic IR divergence, and successively collimated (by a toroidal mirror) towards the experimental area. By this system, the IR beam is transferred as a plane wave and finally refocused into a spot area of less

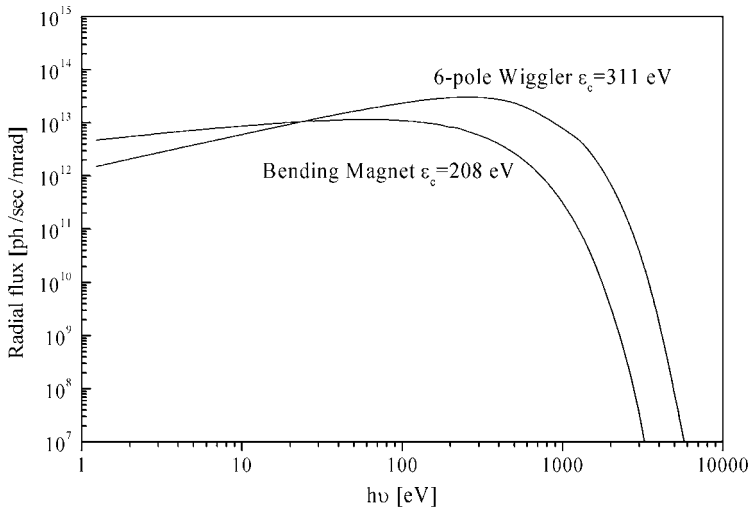

Figure 1: *Estimated spectral flux of the Synchrotron Radiation from dipole and wiggler sources of DAΦNE at 1 A.*

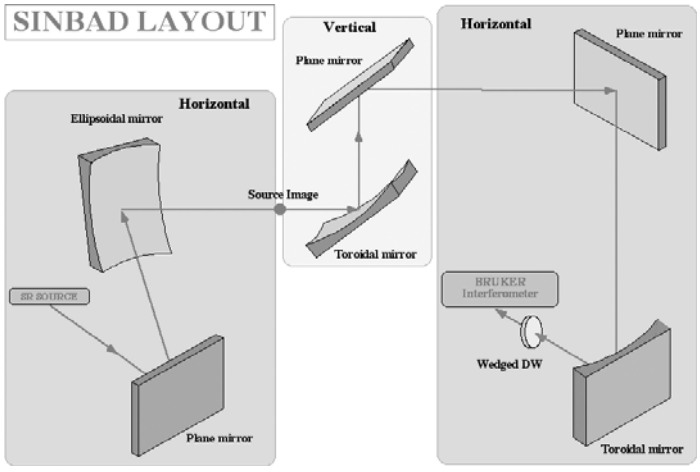

Figure 2: *SINBAD optical system. The IR SR beam is reflected by six Au-coated mirrors till the CVD diamond window at the interferometer pupil.*

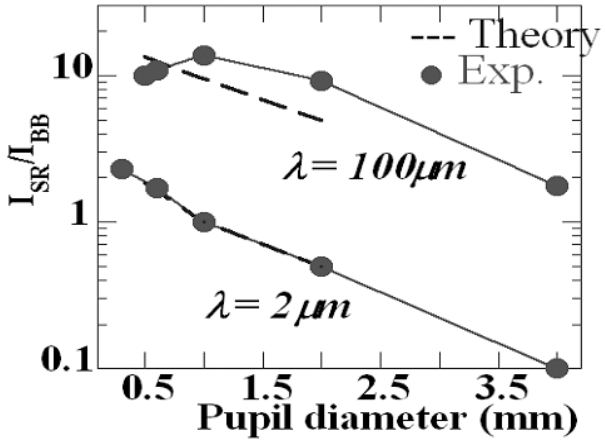

Figure 3: *Experimental intensity ratio, between SR and black body (BB), versus diameter aperture at sample position in the far- (100 μm) and the mid-IR (2 μm). The dashed lines give the Actual Brilliance Ratio between the SR (at 1 A of circulating current) and the BB.*

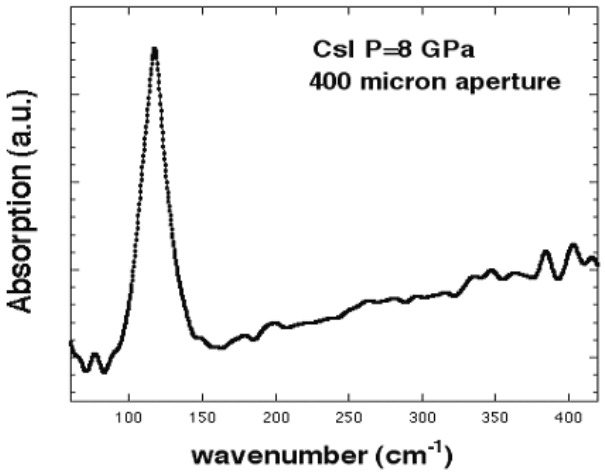

Figure 4: *Far-IR absorption spectra recorded at SINBAD with resolution of 8 cm^{-1} in a diamond anvil cell containing a CsI powder under high pressure. The peak is due to the CsI tranverse optical phonon, shifted towards higher frequencies and much better resolved with respect to zero pressure.*

than 2 mm^2. Here is the pupil of a Michelson interferometer, modified to work under vacuum, which allows both transmission and reflectivity experiments on solid samples. The instrument range is 10-5000 cm^{-1} wavenumber (1000-2 μm), covered by different detectors and beamsplitters with a max resolution of 0,5 cm^{-1}. An IR microscope is also available, in parallel to the previous instrument, for working in the near- and mid-IR range.

The SINBAD performances [4] are given in terms of intensity ratio between the SR IR with respect to a black body (BB): the figure of merit $I_{SR}(\omega)/I_{BB}(\omega)$ is thus plotted versus the pupil diameter at the sample position and compared to the ray-tracing calculations of the Actual Brilliance Ratio (data normalized to 1 A in Figure 3). At 100 the μm $I_{SR}(\omega)/I_{BB}(\omega)$ ratio is about 2 for a full aperture ($\sim$ 4 mm), while it approaches a maximum value of 20 for d = 1 mm, in good agreement with theoretical estimates. Thanks to this significant brilliance gain, the first experimental results have been obtained by SR in the far-IR domain on materials inside a Diamond Anvil Cell (DAC). In the small opening window available (<400 μm), the CsI powder has been investigated at high pressure to detect the transverse optical phonon (see Figure 4). At SINBAD, a high SR linear polarization has been also measured, reaching an 80% degree in the mid-IR with full open slits. First observations of the SR above the orbit indicate over 80% of circularly polarized light by selecting 50% of the total flux available.

3 The soft X-ray beamline

In the energy region around few keV DAΦNE insertion devices represent a high flux and horizontally wide SR sources accessing a niche of research and technological applications rarely covered by other facilities.

The front-end of the X-Ray beamline ($\sim$4 m from the mid source) accepts about 15 mrad of the photon fan in the orbit plane. After the shielding walls, the X-ray beamline develops in a tunnel (experimental area) where a set of both horizontal-vertical slits ($\sim$10 m aside the wiggler, Figure 5) selects the overlap of two radiation lobes from the structured wiggler source. A beam size of 20 $\times$ 50 mm^2 (v $\times$ h), corresponding to circa 5 mrad in horizontal and the full SR vertical divergence, enters into the next mirror chamber where the Au-coated Si-mirror (80 cm long) deflects horizontally half of the SR fan by 4,4^o inward the UltraViolet line. The actual X-rays proceed through the

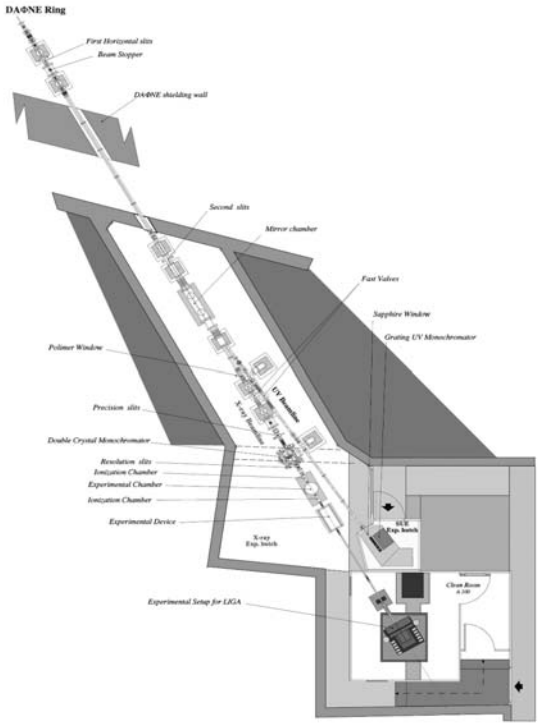

Figure 5: *Lay-out of X-Ray beamline and UltraViolet branch line.*

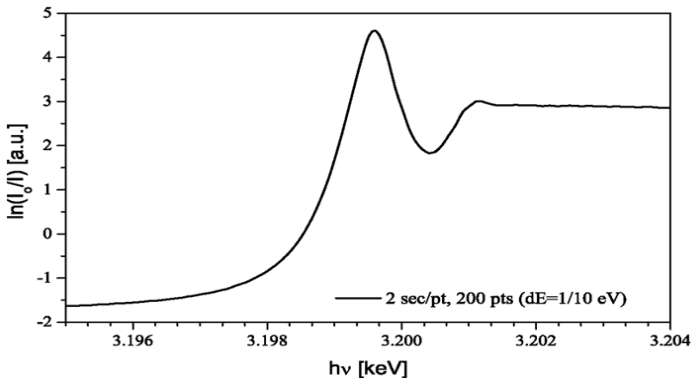

Figure 6: *K-edge of argon gas measured in transmission; the spectrum is a single scan acquired parasitically in circa 20 minutes (average current 700 mA).*

straight section where an 1100 Å thick polymide window guarantees both the machine UHV environment and a high transmittance (>80 % at the oxygen K-edge). A last set of submillimetric resolution slits defines the beam entering the monochromator, at most 15 × 24 mm^2 (v × h). The beamline is endowed with a double-crystal monochromator (by Toyama) in the "boomerang" geometry, to ensure a fixed beam exit at all energies. Working with Bragg's angles from 15^o to 75^o, the equipment of Si(111), α-Quartz(10-10) and KTP(001) crystals allow covering the energy spectrum above 1,2 keV with max resolution $\Delta E/E=10^{-5}$ (and always $<10^{-3}$). Immediately after, a multipurpose cylindrical experimental HV chamber includes two ionisation chambers (IC) to detect inward and outward signals in X-ray Absorption Spectroscopy (XAS) on thin samples. Standard kapton windows allow transmission measures down to the P K-edge, and ultra-thin polyamide films are implemented below the 2 keV range. In cascade, a Clean Room (class A 100) is present to apply lithographic and micro-engineering techniques on soft X-ray photoresists by an upgrading remotely controlled stepper device. Investigations on policapillary systems are in due course in order to provide a SR microbeam for spectroscopy applications.

The X-ray beamline has been characterized on performing XAS on material standards: XANES technique was applied in the range 2 - 4 keV, i.e. more than 10 times the wiggler critical energy, using Si(111) crystals for monochromatization. Transmission spectra were acquired parasitically in runs of circa 20 min, constraining the actual measure time to 1-3 s per point, and using gas ionization chambers. Energy calibration was obtained using as reference the Rydberg-like peak of the Ar K-edge (see Figure 6). Pure 2 μm Cd and 1 μm Ag metal foils were analysed and their three L-edges spectral region measured in a single scan (2 keV): low resolution EXAFS spectra were acquired to test both monochromator and IC sensitivity (e.g. the L_I-edge "white line"). XANES spectra were measured on thin samples in the low energy side of the available spectral range. In particular Cl was perfectly detected in a KCl solution deposited on paper filter, as well as K in a thin mica layer (Figure 7). Further XANES acquisitions were successfully carried on lighter elements like S and P. Planned up-grade on both the detection equipment will open the spectral range toward lower energy side of soft X-rays (e.g., down to Na K-edge), while improvements on the monochromator system should extend the upper limit toward 6 keV.

4 The UV beamline

The SR photon beam from the W is splitted (Figure 5) by a grazing incidence Au-coated mirror (θ_i=40 mrad, cut-off energy ~800 eV).

About 3 mrad^2 of UV radiation are carried to an experimental hutch now dedicated to the Solar Ultraviolet Experiment (SUE) of photobiology. SUE involves a systematic investigation of the biological effects induced on cultures of human cells and progenies by the B band of the UV (280 - 320 nm). This experiment has a large impact on evaluating the incidence of skin cancer in humans due to an increase of UVB radiation reaching the earth surface when the stratospheric ozone layer reduces. The use of highly monochromatic photons at DAΦNE is unique since the optimal matching between the continuous SR spectral emission and the range of interest. After a sapphire window and some optics in air, a grating monochromator (Jobin-Yvon) selects the photons in the spectral range between 2 and 6 eV: by a bandwidth better than 0,3%, the monochromatic beam enlights the cell on teflon cylinders. The UV beam homogeneity at sample position has been tested using radiographic plates, scanned by a microdensitometer and, within small stochastic fluctuations, it is below 10%. Dosimetry and spectral intensity (from 20 to 40 J/m^2) have been checked by an absolute Si photodiode (Hamamatsu Photonics pre-calibrated by NIST). The exposure time at each irradiation dose was given by monitoring the electron ring current. On the monochromator entrance slits (mirror system focus) the radiant power measured in the spectral band 200 - 1200 nm per e^- current unit is 1.50 mW/A, in accordance with theoretical estimates, while at the monochromator exit slits (zero diffraction order) this value reduces to 0.42 mW/A.

The first experimental results on irradiation of human hybrid cell line CGL1 (HeLa-x human skin fibroblast) are shown in the Figure 8: they concern the cell survival fraction as function of both released dose and SR wavelength. The interesting threshold effect in the narrow energy range investigated is going to be clarified with both longer acquisition (data under analysis) and finest wavelength scanning planned in the next months.

Concerning vacuum and security systems, all beamlines are monitored and controlled by a dedicated software code [5)] developed under LabView and interfacing FieldPoint hardware (National Instrument).

Since the beginning of 2002, a SR Scientific Committee is in charge of

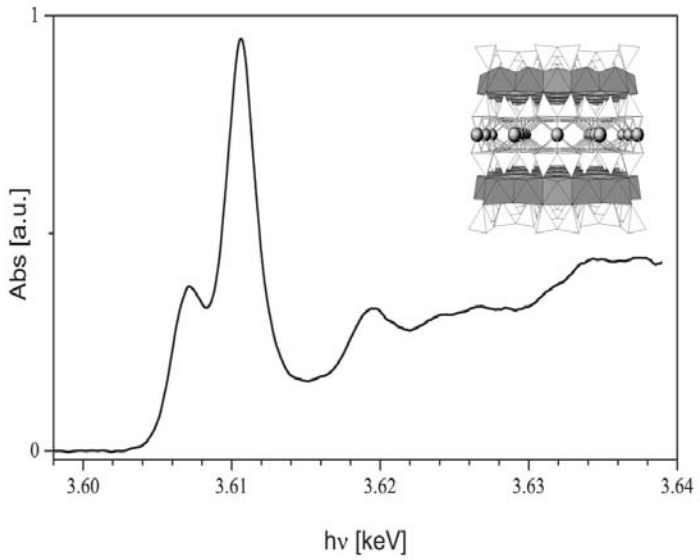

Figure 7: *K-edge XANES spectra of potassium in a 40 μm thick foil of a natural biotite (mica) measured in transmission; this single scan was acquired in a parasitic run of 20 minutes (average current 800 mA). In the inset a pictorial view of mica atoms and structure.*

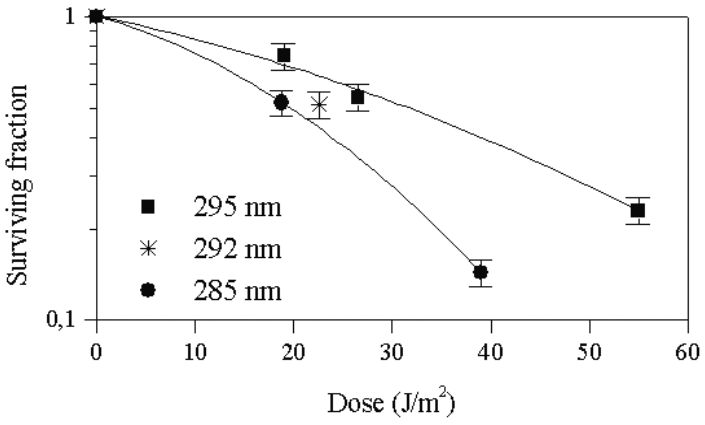

Figure 8: *Preliminary results at three different wavelengths of the cell survival fraction versus exposure dose of monochromatic UVB radiation.*

evaluating new scientific proposals at the DAΦNE-Light EU facility. On this regard, future developments of the Laboratory are planned in the VUV and soft X-ray domain using another BM source. They consist in the construction of two new beamlines covering, respectively, the 5-150 eV and 60-1000 eV energy ranges.

5 Acknowledgments

SUE experiment is financed by INFN "Gruppo V" and is a collaboration with Daniela Bettega, Paola Calzolari and Lucia Tallone from INFN "Sezione di Milano". The DAC implementation and the IR measurements under high pressure are due to the help of Paolo Postorino and Andrea Sacchetti from the Università di Roma *La Sapienza*. We also acknowledge the Electronic Pool of the Laboratori Nazionali di Frascati, in particular Ubaldo Denni and Giuseppe Papalino, for technical support.
A special thanks to Giannantonio Cibin for his substantial help to this manuscript.
Work partially supported by TARI contract HPRI-CT-1990-00088.

References

1. S. Guiducci *et al*, The DAΦNE Project Team, internal note LNF-90 / 031; S. Guiducci *et al*, in: Proc. PAC 2001 (Chicago USA, 2001) **353**; M. Preger, private communication for the December 2002 configuration.
2. I. Titkova, M. Zobov and S. Dabagov, internal note LNF-03 / 002(IR).
3. A. Marcelli *et al* The Beamline SINBAD at DAΦNE, in Infrared Synchrotron Radiation, (Ed. Composizioni Bologna, 1998), Il Nuovo Cimento D **20**, 463;
4. A. Marcelli *et al*, Synch. Rad. News **16**(2), 28 (2003);
5. E. Pace *et al*, Proceedings Int. Conf. on Computing in High Energy and Nuclear Physics (Ed. Scientific Press, Beijing, 2001).

Frascati Physics Series Vol. XXXII (2003), pp. 255-274
19th INTERNATIONAL CONFERENCE ON X-RAY AND INNER-SHELL
PROCESSES – Roma, June 24 - 28, 2002

DAΦNE BENDING MAGNET AND WIGGLER RADIATION

Emilio Burattini
INFN - Laboratori Nazionali di Frascati, I-00044 Frascati, Italy
Dipartimento di Informatica, Università di Verona,
I-37134 Verona, Italy

Irina V. Titkova *
Joint Institute for Nuclear Research, 141980 Dubna, Russia

Sultan B. Dabagov
INFN - Laboratori Nazionali di Frascati, I-00044 Frascati, Italy
RAS - P.N. Lebedev Physics Institute, 119991 Moscow, Russia

ABSTRACT

DAΦNE is a special kind of accelerator dedicated to the production of Φ-mesons, coming from the annihilation of electrons and positrons at the Φ-resonance energy. However, due to the high circulating current, DAΦNE represents also an intense source of synchrotron radiation in the infrared and soft X-ray domains. In this work the main characteristics of synchrotron radiation from DAΦNE's wigglers and dipole magnets are estimated for a parasitic regime of operation. Calculations of synchrotron radiation properties for two lattices have been compared and discussed.

1 Introduction

DAΦNE optics have been chosen to satisfy high intensity and high luminosity requirements of large high energy detectors. In order to achieve the highest

possible luminosity at low energy of accumulation (E=0.51 GeV) a double ring scheme has been chosen [1-4]. However, beam-beam interaction that is severe at low energy, sets a limit to the maximum achievable luminosity. Actually the radiation damping is a strong parameter to determine the luminosity. For the DAΦNE Main Ring both radiation damping and noise are weak so that, to increase the radiated energy four wigglers have been installed in the Main Ring lattice. These wigglers are used also for the emittance control, which is a crucial parameter for the beam-beam interaction.

However, these devices are also intense sources of synchrotron radiation (SR). DAΦNE wigglers are placed in the dispersion region for the emittance control (mainly to increase emittance) and beta functions were chosen to improve the luminosity. To optimize radiation parameters wigglers locations have low betas and zero dispersion functions. As a consequence SR emitted by DAΦNE wigglers in parasitic mode is determined by the parameters of the storage ring selected to optimize the high energy detector.

The main goal of this manuscript is to estimate SR characteristics and parameters of the DAΦNE wiggler and dipole magnet in two different parasitic regime comparing also the brightness associated to these experimental lattices, e.g., KLOE and DEAR experiments.

2 Bending Magnet Radiation

The angular distribution of radiation emitted by electrons following a circular trajectory in a horizontal plane, as in bending magnet, is [5]

$$\frac{d^2F}{d\omega d\Omega} = \frac{3r_e mc^2\gamma^2}{4\pi^2 c}\left(\frac{\omega}{\omega_c}\right)^2\left(1+\gamma^2\theta_y^2\right)^2\left[K_{2/3}^2(\xi)+\frac{\gamma^2\theta_y^2}{1+\gamma^2\theta_y^2}K_{1/3}^2(\xi)\right] \quad (1)$$

where ω_c is the critical photon frequency, θ_x and θ_y are the observational angles in the horizontal and vertical directions (Ω is a solid angle) respectively, r_e – classical electron radius, $K(\xi)$ are modified Bessel functions of the second kind, and $\xi \equiv \frac{\omega}{2\omega_c}\left(1+\gamma^2\theta_y^2\right)^{\frac{3}{2}}$. The two terms in the square bracket correspond to the horizontally and vertically polarized radiation. In the middle plane the second term vanishes and the polarization is purely linear. Out of the orbital plane both terms contribute and polarization becomes elliptical. It is interesting to study the spatial distribution for the two polarization modes.

Not only the intensities are very different but also the spatial distributions are different. The spatial distribution of the σ-mode is mainly oriented in the forward direction while the π-mode has no intensity in the direction of the orbit $\theta_y = 0$ and radiation is emitted into two lobes at finite angles.

Integrating (1) over all frequencies and keeping in mind that $\hbar\omega_c = \frac{3}{2}\hbar c\frac{\gamma^3}{\rho}$ [6], where ρ is a bending radius, we obtain the angular distribution of the SR:

$$\frac{dF}{d\Omega} = \frac{21}{48}\frac{r_e mc^2\gamma^5}{\rho(1+\gamma^2\theta_y^2)^{\frac{5}{2}}}\left[1+\frac{5}{7}\frac{\gamma^2\theta_y^2}{\left(1+\gamma^2\theta_y^2\right)}\right]$$

The quantity F is the radiation energy per unit solid angle from a single electron and single pass. The average radiation power is therefore $P_\gamma = \frac{F}{T_{rev}}$, where $T_{rev} = \frac{2\pi\rho}{c}$ is a revolution time, or [5]:

$$\frac{dP_\gamma}{d\Omega} = \frac{21}{32}\frac{P_\gamma\gamma}{2\pi\left(1+\gamma^2\theta_y^2\right)^{\frac{5}{2}}}\left[1+\frac{5}{7}\frac{\gamma^2\theta_y^2}{\left(1+\gamma^2\theta_y^2\right)}\right]$$

As SR is emitted over a wide range of frequencies, it is of great interest to know the exact frequency distribution of the radiation. It is also useful to integrate over all angles of emission to obtain the total spectral photon flux. Actually we can integrate (1) with respect to the emission angles and obtain the frequency spectrum of the radiation:

$$\frac{dF}{d\omega} = \int\limits_{-\infty}^{\infty}\frac{d^2F}{d\omega d\Omega}d\Omega = 2\pi\int\limits_{-\infty}^{\infty}\frac{d^2F}{d\theta_y d\omega}d\theta_y$$

The emission angle θ_y appears in (1) in a rather complicated way. Replacing the modified Bessel's functions by Airy's functions

$$Ai(z) = \frac{\sqrt{z}}{\sqrt{3}\pi}K_{1/3}(\xi), \quad Ai^{'}(z) = -\frac{z}{\sqrt{3}\pi}K_{2/3}(z)$$

and with $z = \eta^{2/3}\left(1+\gamma^2\theta_y^2\right), \quad \eta = \frac{3\omega}{4\omega_c}$, we can write:

$$\frac{d^2F}{d\omega d\Omega} = 4r_e mc\gamma^2\left[\eta^{\frac{2}{3}}Ai^{'^2}(z) + \gamma^2\theta_y^2\eta^{\frac{4}{3}}Ai^2(z)\right]$$

Now the spectral power distribution can be expressed by Airy's function:

$$\frac{d^2P}{d\omega d\Omega} = \frac{9}{2\pi}\frac{P_\gamma\gamma}{\omega_c}\left[\eta^{\frac{2}{3}}Ai^{'^2}(z) + \gamma^2\theta_y^2\eta^{\frac{4}{3}}Ai^2(z)\right] \ ,$$

where $P_\gamma = \frac{2}{3} r_e mc^3 \frac{\gamma^4}{\rho^2}$. To obtain the photon frequency spectrum, we may integrate over all angles of emission, accomplished by an integration along the orbit that contribute with a factor 2π, over the angle θ_y. The resulting SR spectrum is [5,6]:

$$\frac{dP}{d\omega} = \frac{P_\gamma}{\omega_c} \frac{9\sqrt{3}}{8\pi} \frac{\omega}{\omega_c} \int_{\frac{\omega}{\omega_c}}^{\infty} K_{5/3}(x)\, dx \tag{2}$$

Of more practical use are the spectral photon flux per unit angle of deflection in the bending magnet and the photon flux per unit solid angle into a frequency bin $\frac{\Delta\omega}{\omega}$ and for a circular beam current I:

$$\frac{dN_{ph}}{d\theta_x} = \frac{dP}{d\omega} \frac{\Delta\omega}{2\pi\hbar\omega}, \quad \frac{dN_{ph}}{d\theta_x d\theta_y} = \frac{d^2F}{d\omega d\Omega} \frac{I}{e} \frac{\Delta\omega}{\omega} \frac{1}{\hbar} \tag{3}$$

that, using expressions (1) and (2), can be rewritten in the following:

$$\begin{aligned} &\tfrac{dN_{ph}}{d\theta_x} = C_\Psi I E \tfrac{\Delta\omega}{\omega} \tfrac{9\sqrt{3}}{8\pi} \tfrac{\omega}{\omega_c} \int_{\frac{\omega}{\omega_c}}^{\infty} K_{5/3}(x) dx, \\ &\tfrac{dN_{ph}}{d\theta_x d\theta_y} = C_\Omega E^2 I \tfrac{\Delta\omega}{\omega} \left(\tfrac{\omega}{\omega_c}\right)^2 \left(1+\gamma^2\theta_y^2\right)^2 \left(K_{2/3}^2(\xi) + \tfrac{\gamma^2\theta_y^2}{1+\gamma^2\theta_y^2} K_{1/3}^2(\xi)\right) \end{aligned} \tag{4}$$

where

$$\begin{aligned} C_\psi &= \tfrac{4\alpha}{9mc^2 e} = 3.967 \cdot 10^{16} \text{ ph/(s·rad·GeV·A)}, \\ C_\Omega &= \tfrac{3\alpha}{4\pi^2 e (mc^2)^2} = 1.3273 \cdot 10^{16} \text{ ph/(sec mrad}^2 \text{ GeV}^2 \text{ A)}. \end{aligned}$$

The bending magnet energy spectrum is smooth and broadband falling off exponentially above the critical energy $\epsilon_c \equiv \hbar\omega_c = 3\hbar c\gamma^3/2\rho$, where ρ is a magnet bending radius. In practical units the critical energy and critical wavelength are given by

$$\epsilon_c\,[keV] = 0.665 B\,[T]\, E^2\,[GeV], \qquad \lambda_c\,[A^\circ] = 18.64/B\,[T]\, E^2\,[GeV] \ ,$$

where B is the bending magnet magnetic field and E is the electron energy.

3 Wiggler Radiation

Wigglers are insertion devices that modify the electron trajectory. In fact the wiggler magnets induce electrons to oscillate in the orbital plane with deflection

larger than the natural emission angle of the SR. The resulting emission spectra is a broadband fan-shaped beam of photons. It is usual to consider the wiggler emission similar to that produced by an individual bending magnet, but $2N$ times as intense due to repetitive electron bending over the length of a $2N$-pole wiggler:

$$\frac{d^2F}{d\omega d\Omega} = 2N\ \frac{3r_e mc^2\gamma^2}{4\pi^2 c}\left(\frac{\omega}{\omega_c}\right)^2\left(1+\gamma^2\theta_y^2\right)^2\left[K_{2/3}^2\left(\xi\right)+\frac{\gamma^2\theta_y^2}{1+\gamma^2\theta_y^2}K_{1/3}^2\left(\xi\right)\right] \tag{5}$$

where N is a number of wiggler periods and a field strength corresponds to the wiggler field amplitude.

In reality there is always an interference structure, more or less smoothed depending by the radiation frequency and by additional parameters such as the angular acceptance, beam emittance, energy spread, etc.

In a wiggler, radiation from different periods interferes incoherently. The harmonic peaks are spaced so closely that they blur together. Usually different experimental stations may share a wiggler fan characterized by an horizontal angular extent $2K/\gamma$, where K is the wiggler strength parameter e.g., the ratio between the radiation fan angle and the characteristic radiation cone aperture $1/\gamma$ and in practical units

$$K \equiv 0.934 B_0\left[T\right]\lambda_w\left[cm\right],$$

where B_0 is the wiggler magnetic field and λ_w is the wiggler period. A wiggler is an insertion devices characterized by $K >> 1$.

The spectral and angular properties of the radiation emitted in wiggler were presented in [7]. Let briefly describe these features.

The angular distribution of radiation emitted by electrons following a sinusoidal trajectory into the wiggler can be calculated using the equation of the energy radiated per unit bandwidth and per unit solid angle for a relativistic electron with arbitrary trajectory [8]:

$$\frac{d^2F}{d\omega d\Omega} = \frac{3r_e mc^2}{4\pi^2 c}\left|\int_{-\infty}^{\infty}\frac{\vec{n}\times\left[\left(\vec{n}-\vec{\beta}\right)\times\dot{\vec{\beta}}\right]}{\left(1-\vec{n}\ \vec{\beta}\right)^2}\exp\left(i\omega\left(t-\frac{\vec{n}\ \vec{r}}{c}\right)\right)dt\right|^2 \tag{6}$$

where $\vec{n}$ is a unit vector describing the observation direction, $\vec{r}$, $\vec{\beta}$, $\dot{\vec{\beta}}$ are the electron position, velocity and acceleration. According to Fig.1 the components of $\vec{n}$ are given in term of $(\theta_x,\, \theta_y)$ as follows:

$$n_x = \theta_x,\; n_y = \theta_y,\; n_z = 1 - \frac{1}{2}\left(\theta_x^2 + \theta_y^2\right), \quad \theta_x, \theta_y,\; \theta_z << 1 \tag{7}$$

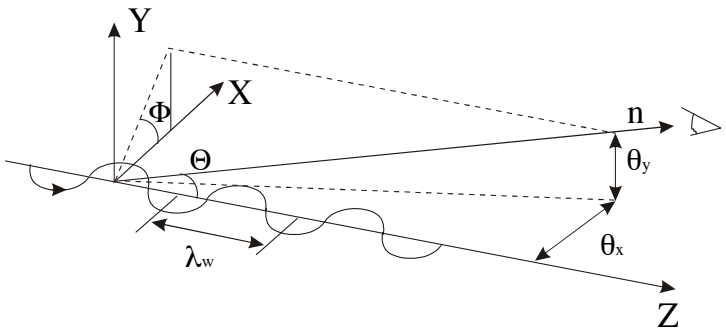

Figure 1: *Definition of angles for the SR emission.*

In the case of a sinusoidal magnetic field variation $B_y = B_0 \cos\left(k_w z\right), \quad k_w = \frac{2\pi}{\lambda_w}$ the equations of electron motion in the wiggler are given by [5]:

$$\begin{aligned} x &= \tfrac{K\lambda_w}{2\pi\gamma} \cos k_w z \\ z &= \left(1 - \tfrac{K^2}{4\gamma^2}\right) ct + \tfrac{K^2\lambda_w}{16\pi\gamma^2} \sin 2k_w z \end{aligned} \tag{8}$$

In wiggler there are two emission points per period (Fig.2) and $\theta_x = -\frac{K}{\gamma} \sin k_w z$.

If we define $\alpha = \frac{\gamma\theta_x}{K}$ (the ratio between the horizontal emission angle and the deflection angle of the trajectory) and for two emission points we have:

$$k_w z_1 = -\arcsin\alpha, \quad k_w z_2 = \pi - k_w z_1$$

According to (3) the equation for the phase of emission can be written as $e^{i\delta}$, where $\delta = \omega\left(t - \frac{\vec{n}\,\vec{r}}{c}\right)$. Combining expressions (7) and (8) we get the following expression:

$$\delta = \frac{\omega}{\omega_1}\left(\frac{2\pi z}{\lambda_w}\right) - 2\alpha\frac{K^2}{A}\cos kz - \frac{K^2}{4A}\sin 2kz \;,$$

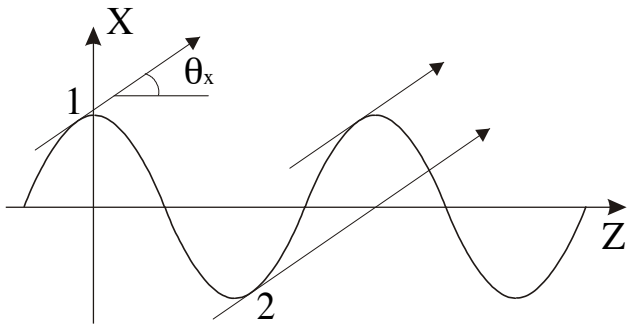

Figure 2: *Source points for the SR emission in the horizontal plane.*

where $\omega_1 = \frac{2\pi c}{\lambda_w} \frac{2\gamma^2}{1+\frac{K^2}{2}+\gamma^2\left(\theta_x^2+\theta_y^2\right)}$ is the wiggler fundamental frequency and $A = 1 + \frac{K^2}{2} + \gamma^2\left(\theta_x^2 + \theta_y^2\right)$. The expression in square bracket in (1) can be rewritten for wiggler period as follows:

$$\left[P_x^2 + P_y^2\right] = \left(e^{i\delta_1} - e^{i\delta_2}\right)^2 K_{2/3}^2(\xi) + \left(e^{i\delta_1} + e^{i\delta_2}\right)^2 \frac{\left(\gamma\theta_y\right)^2}{1+\left(\gamma\theta_y\right)^2} K_{1/3}^2(\xi) \ ,$$

where P_x, P_y are amplitudes of the polarization in the orbit plane and in the direction perpendicular to it and δ_1, δ_2 are the phases of the two source points. The different signs for P_x and P_y is because the horizontal component is proportional to $\dot{\beta}_x$. In fact, with respect to the nominal point of emission $\dot{\beta}_x$ (and P_x) is symmetric in z and changes sign as a function of the polarity of the wiggler poles. On the other hand $\dot{\beta}_z$ is asymmetric and remains the same for all poles. For any combination of the two poles the circular polarization rate becomes zero, irrespective of the angle of emission.

For all wiggler periods equation (5) can be written as the product of an integral and a function that contains the interference between periods: $\frac{\sin^2 N\pi\frac{\omega}{\omega_1}}{\sin^2 \pi\frac{\omega}{\omega_1}}$. Summing all the expressions, the angular distribution of the radiation becomes [7,9]:

$$\frac{d^2F(\omega)}{d\omega d\Omega} = \frac{3r_e mc^2\gamma^2}{4\pi^2 c}\left(\frac{\omega}{\omega_c}\right)^2\left(1+\gamma^2\theta_y^2\right)^2 * \\ * 4\left[\sin^2\frac{\Delta}{2}K_{2/3}^2(\xi) + \cos^2\frac{\Delta}{2}\frac{\gamma^2\theta_y^2}{1+\gamma^2\theta_y^2}K_{1/3}^2(\xi)\right]\frac{\sin^2 N\pi\frac{\omega}{\omega_1}}{\sin^2\pi\frac{\omega}{\omega_1}},$$

where $\Delta = \frac{\omega}{\omega_1}\left(\pi + 2\arcsin\alpha + 3\frac{K^2}{A}\alpha\sqrt{1-\alpha^2}\right)$. For nonzero horizontal observation angle θ_x, the electron effective radius of curvature at the trajectory locations, contributes to the observed radiation decreases and the off-axis critical energy becomes $\epsilon_c(\theta_x) = \epsilon_c(0)\sqrt{1-(\theta_x\gamma/K)^2}$.

In practical units, according to the expression (3) for wiggler, we can write

$$\frac{dN_{ph}}{d\Omega} = C_\Omega E^2 I\frac{\Delta\omega}{\omega}\left(\frac{\omega}{\omega_c}\right)^2\left(1+\gamma^2\theta_y^2\right)^2 * \\ *4\left[\sin^2\frac{\Delta}{2}K_{2/3}^2(\xi) + \cos^2\frac{\Delta}{2}\frac{\gamma^2\theta_y^2}{1+\gamma^2\theta_y^2}K_{1/3}^2(\xi)\right]\frac{\sin^2 N\pi\frac{\omega}{\omega_1}}{\sin^2\pi\frac{\omega}{\omega_1}} \quad , \qquad (9)$$

$$\frac{dN_{ph}}{d\theta_x} = \int_{-\infty}^{\infty}\frac{dN_{ph}}{d\Omega}d\theta_y,$$

where α is a fine structure constant.

The factors $\left\{\sin^2\frac{\Delta}{2},\ \cos^2\frac{\Delta}{2}\right\}\frac{\sin^2 N\pi\frac{\omega}{\omega_1}}{\sin^2\pi\frac{\omega}{\omega_1}}$ are fast oscillating in contrast to the functions $K_{2/3}^2(\xi)$, $K_{1/3}^2(\xi)$. Maxima and minima of the σ-component and those of the π-component alternate each other in the spectral distribution: in any direction we have neighboring frequencies at which either a σ- or a π-component is emitted. The SR brightness of a wiggler can be approximated by the following expression [10]:

$$B = \frac{dN_{ph}/d\theta_x}{(2\pi)^{\frac{2}{3}}\left[\left(\sigma_x^2 + a^2 + \sigma_x'^2L^2/12\right)\left(\sigma_y^2 + \sigma_y'^2L^2/12\right)\left(\sigma_y'^2 + \sigma_R'^2\right)\right]^{\frac{1}{2}}} \qquad (10)$$

where σ_x, σ_y, σ_x', σ_y' are the sizes and divergence of electron beam, a is the amplitude of the electron sinusoidal motion, L is a length of wiggler, σ_R' is the vertical opening of the radiation.

Table 1: *Circulating beam parameters.*

Energy, MeV		510
Circulating current, A		1.0
Horizontal emittance, mrad		10^{-6}
Energy spread, %		0.04
Twiss functions at the source point for dipole (DEAR experiment[11)])	β_x, m	5.6
	β_y, m	6.16
	α_x	-2.204
	α_y	3.6649
	D_x, m	1.1053
	D_y, m	0
	$D_x^{'}, m$	-0.33077
	$D_y^{'}, m$	0
Twiss functions at the source point for wiggler(DEAR/KLOE experiments)	β_x, m	3.947 / 2.161
	β_y, m	1.191 / 0.88
	α_x	-0.089 / -1.466
	α_y	-0.063 / -0.2
	D_x, m	2.426 / 1.716
	D_y, m	0.0
	$D_x^{'}, m$	-0.05 / -0.1
	$D_y^{'}, m$	0.0
Coupling, %		0.2

4 The Main Ring Parameters

For the calculations of the DAΦNE SR characteristics of bending magnets and wigglers the SynRad computer code [11)] was used. This code, developed at Stanford University, has been used to characterize bending magnets, wigglers and undulators. With SynRad the wiggler SR emission is calculated according to the formula (5). For the investigations of the interference structure of wigglers (formula (9)) a new computer code was implemented. Convenient algorithm for calculations of the modified Bessel's functions $K_\nu(x)$ of fractional order and the integral $\int_x^\infty K_\nu(\eta)\, d\eta$ is given in [12)]:

$$K_\nu(x) = h \left(\frac{e^{-x}}{2} + \sum_{r=1}^{\infty} e^{-x \cosh(rh)} \cosh(\nu r h) \right),$$

$$\int_x^\infty K_\nu(\eta)\, d\eta = h \left(\frac{e^{-x}}{2} + \sum_{r=1}^{\infty} e^{-x \cosh(rh)} \frac{\cosh(\nu r h)}{\cosh(rh)} \right),$$

Table 2: *Dipole parameters.*

Type	electro-magnet
Bending radius, m	1.4
Magnetic field, T	1.2
Bending angle, rad	0.8
Magnetic rigidity, Tm	1.701

Table 3: *Wiggler parameters.*

Construction	rectangular
Magnetic field at the gap center,T	1.8
Number of poles	6
Period length, mm	640
Wiggler length, m	1.92
Gap, mm	40
K-value	107.6

where h is some suitable interval, ($h = 0.5$).

The circulating beam parameters considered are summarized in Table 1 [1–3].

The dipole magnet parameters used in calculation are presented in Table 2 [1]. The wiggler parameters used in calculation are presented in Table 3 [13,14].

5 DAΦNE Bending Magnet SR

According to the data from Table 1, 2 the sizes and divergence of electron beam at the source point are $\sigma_x = 2407.38\mu m$, $\sigma_y = 111\mu m$, $\sigma_x^{'} = 1031.27\mu rad$, $\sigma_y^{'} = 68.45\mu rad$. Parameters of dipole magnets are summarized in Table 4. Note that all calculations were made for a circulating current of 1 A. The angular photon flux, the angular and spatial flux density from a DAΦNE dipole are presented in Fig.3, 4. The angular distribution curves for three different frequencies ω are shown in Fig.5. In Table 5 the total flux for both polarization modes and for different observation angles are presented. The expressions for the photon flux are useful also to calculate the spectral distributions of the photon beam divergence. Photons are emitted into a narrow angle and we may

Table 4: *SR parameters from DAΦNE dipole magnet.*

Photon critical energy, keV	0.2079
Critical wavelength, Å	59.71
Total flux at the critical wave length, ph/(s·mrad·0.1%b.w.)	$8.172 \cdot 10^{12}$
Total power, kW	0.5287
Angular power, W/mrad	0.67
Power density at the source point, W/mm^2	1.424

Table 5: *Radiated flux into the σ- and π-mode.*

Vertical observation angle , ψγ	*Vertical opening angle, mrad*	*σ-mode, ph/(s·mrad²)*	*π-mode, ph/(s·mrad²)*	*Total flux, ph/(s·mrad²)*
0.0	*0.649*	$5.02 \cdot 10^{12}$	*0.0*	$5.02 \cdot 10^{12}$
0.25	*0.793*	$4.64 \cdot 10^{12}$	$1.88 \cdot 10^{11}$	$4.83 \cdot 10^{12}$
0.5	*1.42*	$3.60 \cdot 10^{12}$	$5.25 \cdot 10^{11}$	$4.12 \cdot 10^{12}$
0.75	*3.59*	$2.22 \cdot 10^{12}$	$6.24 \cdot 10^{11}$	$2.84 \cdot 10^{12}$
1	*12.9*	$1.01 \cdot 10^{12}$	$4.20 \cdot 10^{11}$	$1.23 \cdot 10^{12}$

represent the narrow angular distribution by a Gaussian distribution with an effective width of $\sqrt{2\pi}\sigma_\theta$. The angular divergence of the forward lobe of the photon beam or for a beam polarized in the σ-mode is

$$\sigma_\theta\,(mrad) = \frac{C_\psi}{\sqrt{2\pi}C_\Omega}\,\frac{1}{E}\,\frac{S\,(x)}{x^2 K_{2/3}^2\,(x/2)}\ ,$$

where $x = \omega/\omega_c$ and $S(x)$ is the universal function of the SR spectrum. The photon beam divergence for low photon energies compared to the critical photon energy is independent by the particle energy and is inversely proportional to the cubic root of the bending magnet radius and photon energy. The photon beam divergence from DAΦNE dipole magnet is shown in Fig.6.

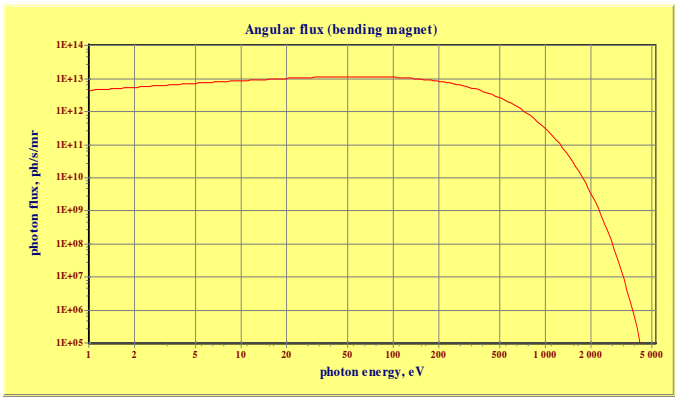

Figure 3: *Angular photon flux from a DAΦNE dipole magnet.*

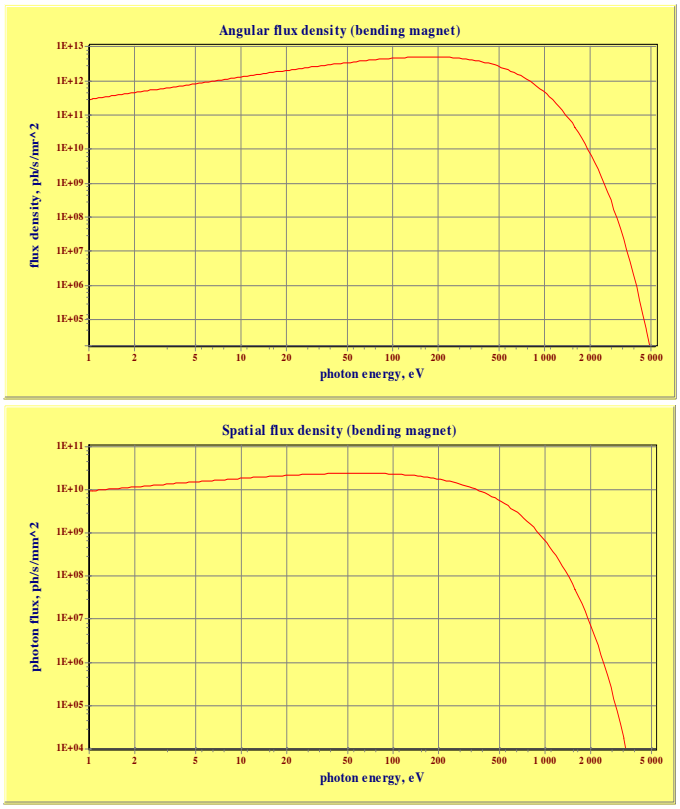

Figure 4: *Angular and spatial flux density from a DAΦNE dipole magnet.*

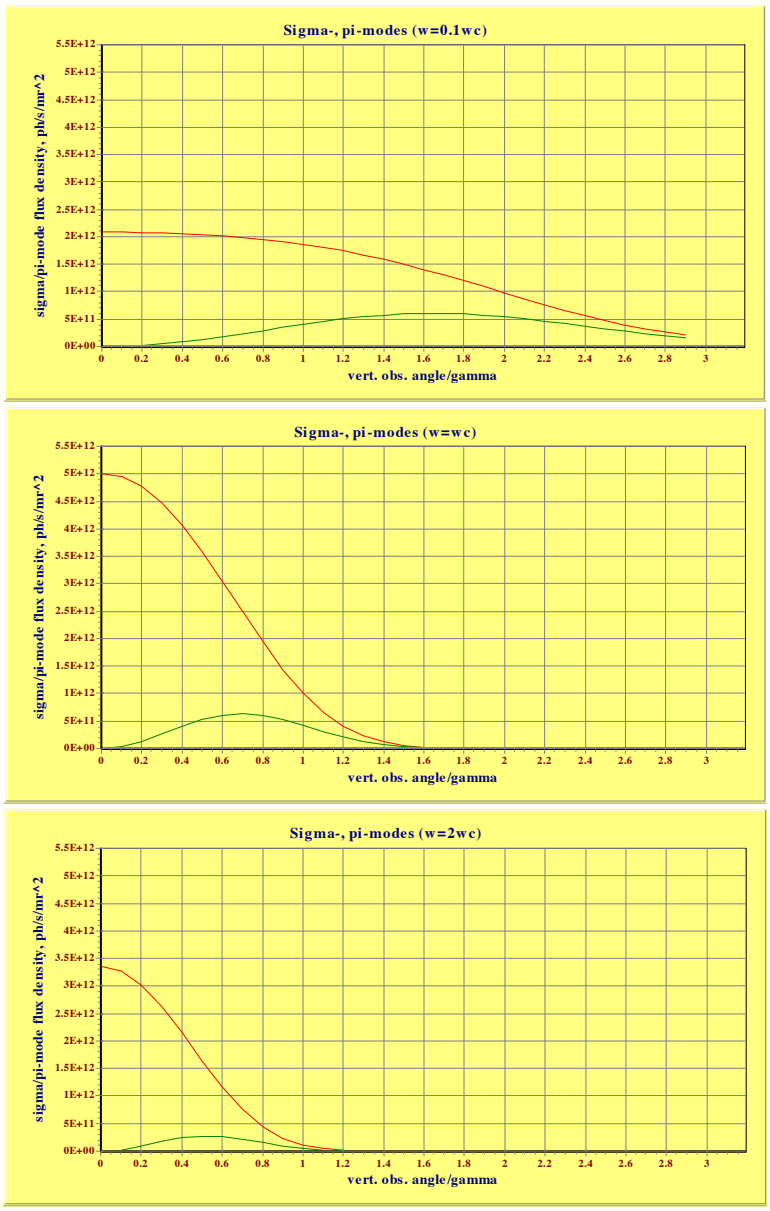

Figure 5: *Angular distribution for both polarization modes at different frequencies* ω=$0.1\omega_c$, ω_c, $2\omega_c$.

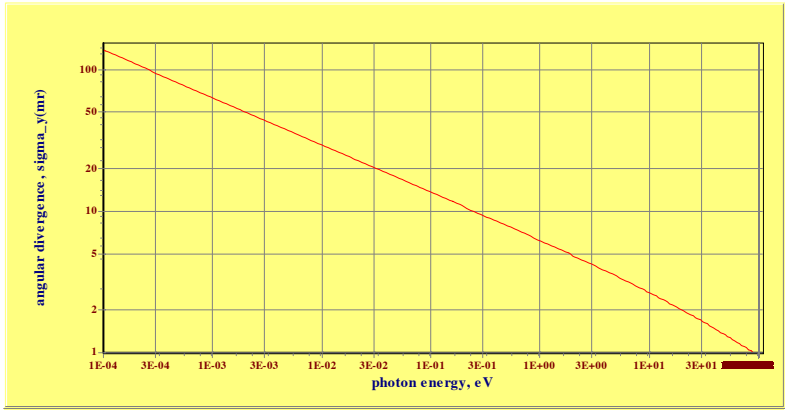

Figure 6: *Photon beam divergence from a DAΦNE dipole magnet.*

6 DAΦNE Wiggler SR

As a first step we calculated the characteristics of wiggler emission using the SynRad code (the distribution of the radiation was calculated using the equation (5)) for the DEAR lattice configuration. According to data from Table 1 and 3 beam sizes at the source point are: $\sigma_x = 2211.04\mu m$, $\sigma_y = 48.81\mu m$, $\sigma_x^{'} = 505.73\mu rad$, $\sigma_y^{'} = 41.06\mu rad$. The maximum path displacement inside the wiggler is 21.97 mm while the maximum angle deflection is 107.9 mrad. The characteristics of the parameters of the DAΦNE wigglers (at a circulating current of 1 A) using the parameters for the DEAR configuration are summarized in Table 6.

Table 6: *SR parameters for a DAΦNE wiggler in the DEAR configuration.*

Photon critical energy, keV	0.31134
Critical wavelength, Å	39.823
Vertical cone, μrad	650
Angular flux at the critical wavelength, ph/(s·mrad·0.1%b.w.)	$4.9{\cdot}10^{13}$
Flux density at the critical wavelength, ph/(s·mrad^2·0.1%b.w.)	$3.01{\cdot}10^{13}$
Brightness at the critical wavelength, ph/(s·mm^2·mrad·0.1%b.w.)	$4.44{\cdot}10^{7}$
Total radiation power, kW	1.025
Power density at the source point, kW/mm^2	1.512

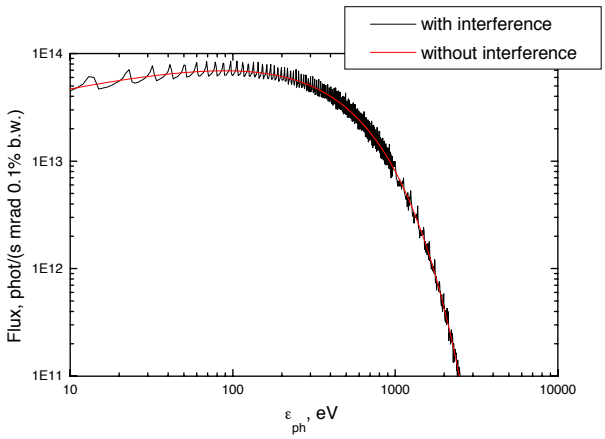

Figure 7: *Angular flux from a DAΦNE wiggler.*

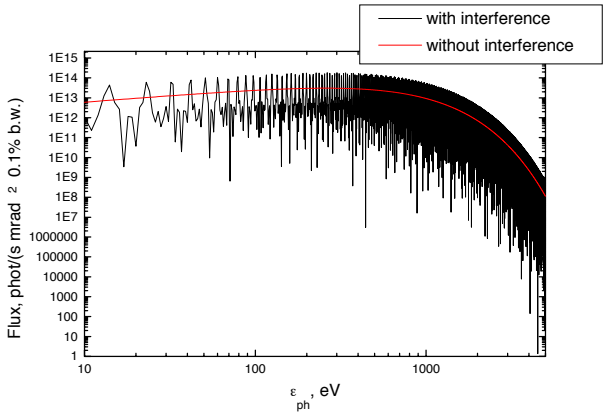

Figure 8: *Angular flux density from a DAΦNE wiggler.*

The SR characteristics were calculated according to formula(9). Comparison is shown in Figs.7 and 8. In the high frequency limit it can be seen that the angular flux tends to the result obtained by a standard wiggler type calculation without interference phenomena [15].

According to equation (3) we calculated the angular flux density for a slit of 15×4 mm^2. The distance between the wiggler and the slit was set to 18 m as a consequence the angular sizes of the slit are: $\theta_x = 53.086 \div 53.914$ mrad, $\theta_y = 0 \div 0.222$ mrad. Calculations for radiation with different critical wavelengths are presented in Fig.9. The maximum flux density is $2.9208 \cdot 10^{13}$ ph/(s·mrad^2), the minimum is $2.8038 \cdot 10^{13}$ ph/(s·mrad^2).

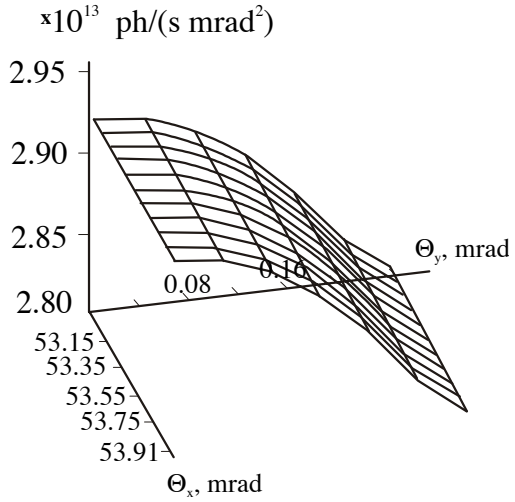

Figure 9: *Angular flux density for a slit at 18 m from the source.*

This calculation is valid when the detector is placed far from the source, namely, when the angular sizes of the wiggler is much less then γ^{-1}. In this case the distance between the wiggler and and observer has to be $R >> L_w \gamma \sin\theta_x$, where L_w is the length of the wiggler. The angular flux and the angular flux density calculations according to the equation (9) are shown in Fig.10 and Fig.11. The angular flux density is presented as function of the horizontal angle of observation when the vertical angle is zero and as function of the vertical angle in the orbital plane (θ_x=53.414 mrad). A strong interference pattern can be distinguished.

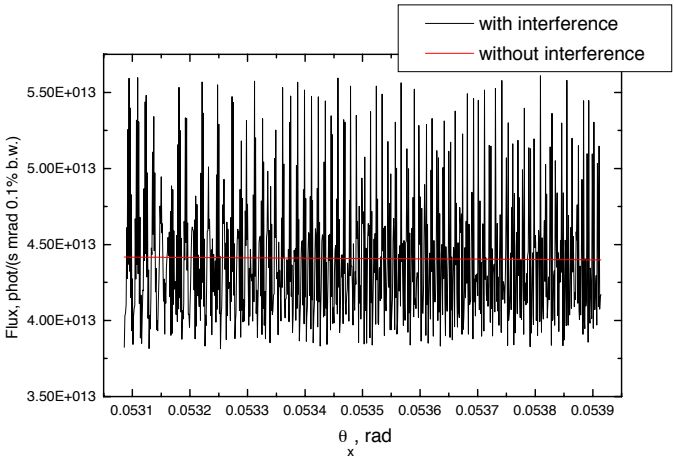

Figure 10: *Angular flux for a slit placed at 18 m from the source.*

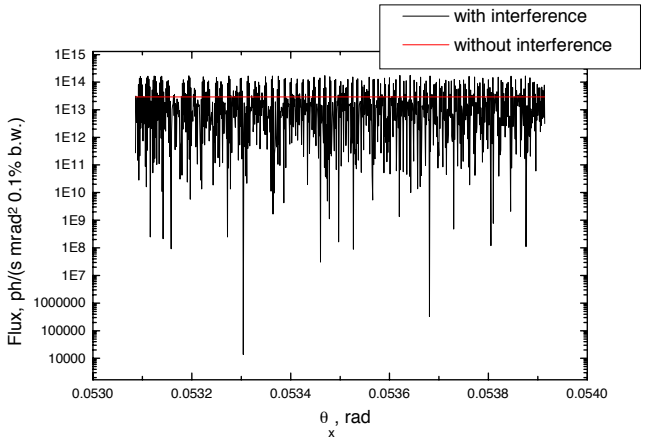

Figure 11: *Angular flux density for the a slit as function of* θ_y *(*θ_x*=53.414 mrad) (top) and as a function of* θ_x *(*θ_y*=0) (bottom).*

According to Eq.(10) the wiggler brightness depends on the size and the divergence of electron beam. In Fig.12 the brightness for two operational configurations are compared. The Twiss-parameters of these calculations correspond to KLOE and DEAR experiments. Comparison between the results shows that the KLOE configuration is preferable in term of brightness.

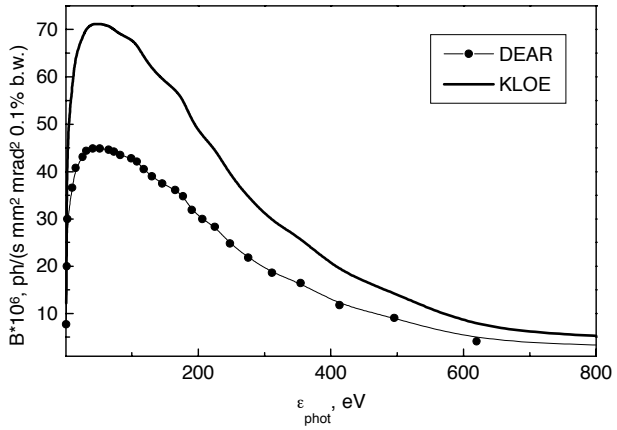

Figure 12: *Brightness comparison for the wiggler emission for the two experimental configurations.*

7 Conclusions

In this manuscript we discussed the main characteristics of the SR emission for both dipole magnet and wiggler sources. The angular photon flux and the photon beam divergence for dipole magnets and the angular flux and the angular flux density for wigglers have been calculated using the SynRad computer code. This code does not take into account the radiation interference structure that may be not negligible also in the case of the wiggler emission. To improve the analysis a new computer code taking into account interference phenomena has been implemented. Preliminary results have been presented and discussed.

Brightness for two Main Ring configurations have been calculated and the results show how the KLOE lattice is better for SR applications. To still improve the results a more careful analysis of the lattice functions is required, in particular to optimize the wigglers operation to achieve an intense and stable

SR source also in parasitic operation sharing the ring lattice configurations optimized for high energy experiments.

8 Acknowledgements

We thank M. Zobov for the information on the DAΦNE parameters. A special thanks is due to A. Marcelli for many stimulating discussions.

References

1. M.E. Biagini, S. Guiducci et al, *DAΦNE Lattice Update*, Proc. of **EPAC'92**, 424.
2. M.E. Biagini, *DAΦNE Status Report*, Proc. of **EPAC'92**, 60.
3. M. Bassetti, M.E. Biagini et al., *DAΦNE Main Ring Optics*, Proc. of **EPAC'98**, 879.
4. M. Bassetti, Proc. of V Int. Conf. on High Energy Accelerators, (1999) 709.
5. H. Wiedemann, *Particle Accelerator Physics*, V.**2**, Springer-Verlag 1993.
6. A.Hofmann, *Characteristics of Synchrotron Radiation*, CAS, **CERN 98-04**.
7. R.P. Walker, *Interference Effect in Undulator and Wiggler Radiation Sources*, Nucl. Instr. Meth. **A335** (1993) 328.
8. J.D.Jackson, *Classical Electrodynamics*, 1975, 674 p.
9. V. Ya. Epp, G.K. Razina, *Radiation in a Wiggler with Sinusoidal Magnetic Field*, Nucl. Instr. Meth. **A307** (1991) 562.
10. R.P. Walker, **SST/M-TN-89/24**, July 1989.
11. http://coherent.stanford.edu/He-Web/PC-programs.html
12. V.O. Kostroun, *Simple Numerical Evaluation of Modified Bessel Function Kν(x) of fractional order and the integral* $\int_x^\infty K_\nu(\eta)\,d\eta$, Nucl. Instr. Meth. **A172** (1980) 371.

13. S. Sanelli, H. Hsieh, *Design of the 1.8 Tesla Wiggler for the DAΦNE Main Rings*, Proc. of **EPAC'92**, 1391.

14. H. Hsieh, M. Modena et al, *The 1.8 Tesla Wiggler for the Main Rings of DAΦNE, the Frascati Φ-Factory*, Proc. of **EPAC'94**, p.2247.

15. I. Titkova, M. Zobov, and S. Dabagov, *Synchrotron Radiation from DAΦNE Bending Magnet and Wiggler*, Preprint **LNF-03/002(IR)**, 18 Feb. 2003.

Frascati Physics Series Vol. XXXII (2003), pp. 275-279
19th INTERNATIONAL CONFERENCE ON X-RAY AND INNER-SHELL PROCESSES – Roma, June 24 - 28, 2002

ELEMENTAL MAPPING OF MULTICELLULAR TUMOR SPHEROIDS BY SYNCHROTRON RADIATION MICROPROBE

Gianfelice Cinque
INFN - Laboratori Nazionali di Frascati, via Fermi 40, I-00044 Frascati
Emilio Burattini*and Francesca Monti
Università degli Studi di Verona, Facoltà di Scienze MM.FF.NN., strada Le Grazie 15, I-37134 Verona
Giuseppe Bellisola, Giulio Fracasso and Marco Colombatti
Università degli Studi di Verona, Facoltà di Medicina e Chirurgia, P.le A.L. Scuro, I-37134 Verona
Alexandre Simionovici
ESRF, 6 rue J. Horowitz, F-38043 Grenoble Cedex

ABSTRACT

Multicellular spheroids are used in pre-clinical studies to optimize new anti-tumoral therapies inasmuch as they maintain both architecture and functions of human micrometastasis [1]. Immunotoxins, obtained by a chemical (or genetical) link of a carrier molecule to a natural toxin, are capable of selectively killing tumor cells [2]. The carrier provides recognition and binding to the cell membrane, while the associate toxin leads to cell death through a cytotoxic action. Unlike chemotherapy, immunotoxins can kill both proliferating and resting tumor cells, but the clinical success depends largely on their diffusion within the tissues. The coupling of X Ray Fluorescence (XRF) technique with Synchrotron Radiation microbeam (μSR) allows the non-destructive analysis of biomedical materials together with their mapping with micrometric resolution [3, 4]. Here, we studied the distribution of transition metals within

*also at INFN - Laboratori Nazionali di Frascati, via Fermi 40, I-00044 Frascati.

spheroids grown under different conditions of treatment by complete, and incomplete, immunotransferrin molecules.

1 Multicellular Tumor Spheroids and ImmunoTransferrin

Multicellular tumor spheroids from the human breast carcinoma cell line MCF7 were grown in monolayer cultures according to the protocol of Yuhas and coworkers [5]. The selected vehicle molecule was the human transferrin because of the high number of receptors on MCF7 cell membrane. Ricin Toxin A-chain is the highly toxic subunit of the heterodimeric toxin obtained from seeds of *Ricinus communis* plant [1]. Spheroids between 200 and 300 μm in diameter ($\sim 10^7$ cells) were incubated during the last 24 h with immunotransferrin, ricin, or transferrin alone at the highest molar concentration preventing any organic matrix disgregation (i.e. 10^{-9}, 10^{-9} and 10^{-11} M, respectively). All spheroids, included mock-treated samples for control, were washed twice in physiological solution and fixed by paraformaldehyde solution. Spheroids were placed into ultra pure quartz capillaries (10 μm thick from HilgenbergFigure 1) and filled up with a 10% acryl amide solution; gel polymerization was achieved *in situ*, and the samples were storage at 4^o C until irradiation.

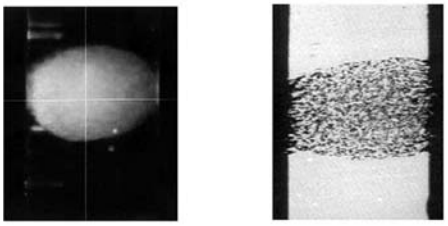

Figure 1: *A spheroid inside the capillary as seen by the microscope at the ID22 sample holder (left), and from an inverted optical microscope in transmission (right).*

2 Synchrotron Radiation microprobe X-Ray Fluorescence

Spectroscopy experiments were carried out using the X Ray microbeam at the beamline ID22 [6] of the European Synchrotron Radiation Facility. The

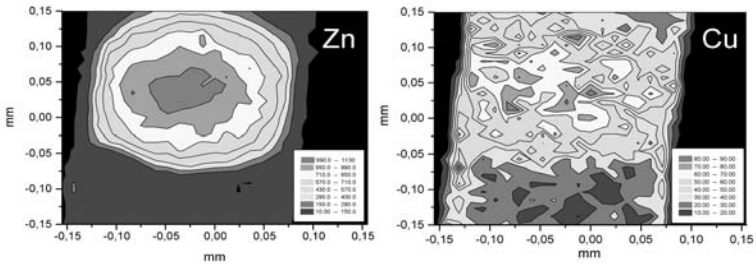

Figure 2: *Trace element distribution by micro X-ray fluorescence of an untreated spheroid. The elemental maps are normalized to an average photon flux of* $2{\cdot}10^9 ph/sec$ *and to 50 s of acquisition time per pixel.*

multielemental analysis was performed by a 15 keV monochromatic photon beam focused by a Au/Si Fresnel Zone-Plate ($M = 1/100$) into a 10 μm pinhole (beamspot dimensions 1 μm × 10 μm (v × h). The samples were scanned into over regions of 400 μm × 400 μm (v × h). By a final flux of about $10^9 ph/sec$, an X Ray Fluorescence collection time of 50 sec was necessary per point using a Si(Li) detector (Eurisys Mesures, ΔE=137 eV fwhm at Mn K_α) at 2-4 cm from the sample in the classical 90^o configuration.

The Immunotoxin here used is a chemical cross-link of human Transferrin, containing $2Fe^{++}$ per molecule, to Ricin A-chain, the last already known to contain traces of Fe, Cu, Zn, Cd, Co and Pb. The trace elements finally detectable by XRF were K, Ca, Fe, Cu, Zn, and Pb; their relative concentration maps are given as gray scale contour plots of their fluorescence signal, since the direct proportionality between the two under a thin sample analysis [3)]. The lightest element distribution was not considered since the strong fluorescence absorption by the organic matrix.

3 μSR-XRF Elemental Maps

Concerning the untreated spheroid in Figure 2, Zinc and - to a lesser extent - Copper maps reveal the spheroid shape and thickness as crossed by the SR beam: naively, in the 2-D projections the fluorescence signal increases on going inward the sample material.

A more careful analysis, consisting in normalizing the XRF signals to the material thickness, i.e. using both an ellipsoidal shape that fits the spheroid

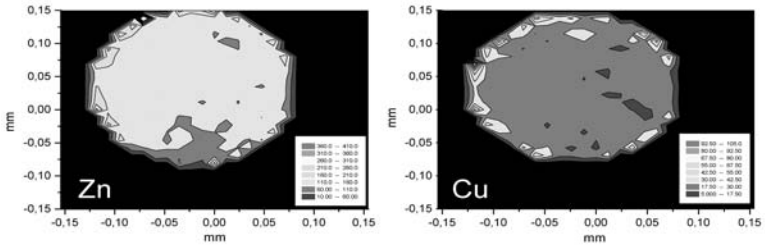

Figure 3: *Trace element distribution by μSR-XRF of an untreated spheroid after normalization to an ellipsoid shape, fitting the spheroid, and a tubular one, fitting the capillary.*

dimension and another tubular shape that fits the capillary envelope, demonstrated that Zn and Cu were homogeneously distributed within the untreated spheroid tissue (Figure 3). As a matter of fact, these metals were found to be useful tracers of the cells present within the spheroid, although some Cu was also present in the capillary walls. The distribution pattern of Fe and Pb in the ful-immunotoxin treated sample is shown in Figure 4. The distribution of Zinc is not reported because substantially unchanged from before, i.e. Zn mostly accumulated within the spheroid independently from the treatment type. Copper fluorescence could be still correlated to the spheroidal shape. Unexpectedly, the Fe - as well as the Pb - map did not resembled any spheroid shape like that indicated by the Zn distribution. Such a scenario, common to all different samples and treatments, reveals that neither the accumulation of

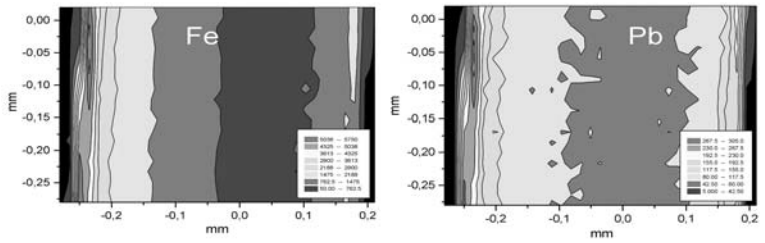

Figure 4: *Trace element distribution by micro X-ray fluorescence of a spheroid treated by immunotoxin. Maps are normalized to an average photon flux of* $2{\cdot}10^9 ph/sec$ *and to 50 s of acquisition time per pixel.*

transferrin, related to the Fe signal, nor that of Ricin, possibly related to Pb, were detectable.

Notice that the low doses of antitumor drug used in this investigation are those applied in the clinics. After this preliminary investigation, to our knowledge the first applying μSR-XRF to follow the diffusion of drugs in a three dimensional models of tumors, future quantitative analysis can be devised, e.g. by labelling vector and toxin molecules with different and naturally non-occurring elements. The use of bi-functional chelating agents could provide many atoms per molecule, thus bringing to a clear recognition of the immunotoxin transport by SR microprobe and XRF mapping within the *in vitro* micrometastasis.

4 Acknowledgments

We acknowledge the European Synchrotron Radiation Facility for provision of synchrotron radiation facilities, in particular for the use of beamline ID22, and the European Molecular Biology Laboratory Grenoble Outstation for support (experiment LS995). Work partially supported by AIRC, Miur and Fondazione Cariverona.

References

1. G. Fracasso and M. Colombatti, Crit. Rev. Oncol/Hemathol., **36**, 159-178 (2000);
2. M. Colombatti *et al*, Cancer Res. **50**, 1385-1391 (1990);
3. C.J. Sparks, in Synchrotron Radiation Research, (Eds.H. Winich and S. Doniach, Plenum Press-New York, 1980), 459;
4. K.W. Jones, Synchrotron Radiation-Induced X-ray Emission, in Handbook of X-Ray Spectrometry, (Eds: R.E. Van Grieken and A.A. Markowicz, Marcel Dekker Inc.-New York, 2001), 411-452;
5. J.M. Yuhas, A.O. Martinez, A.J. Ladman, Cancer Res., **37**, 3639-3643, (1977);
6. S. Bohic *et al*, in Proceedings SRI2000, Nucl. Instr. and Meth. A **30-33** (2001).

Frascati Physics Series Vol. XXXII (2003), pp. 281-294
19th INTERNATIONAL CONFERENCE ON X-RAY AND INNER-SHELL PROCESSES – Roma, June 24 - 28, 2002

FEATURES OF X-RAY SCATTERING IN A NANOTUBE LAYER

Sultan B. Dabagov, Antonio Grilli
INFN - Laboratori Nazionali di Frascati, I-00044 Frascati (RM), Italy
Alexander V. Okotrub
SB RAS - Nikolaev Institute of Inorganic Chemistry, 630090 Novosibirsk, Russia

ABSTRACT

New coherent effects of radiation scattering in capillary nanostructures have been recently discussed theoretically. In this work we present and discuss the observation of angular anisotropy in the X-ray scattering inside a thin layer formed by multiwall carbon nanotubes.

1 Introduction

Propagation of x-ray and neutron through microcapillaries has been intensively investigated in the last 20 years [1, 2] due to the high transmission efficiency of the radiation by the internal hollow part of microcapillaries, but also, due to the possibility to characterize new optical elements capable to deflect or bend intense radiation beams. These researches shown, in addition to the relevance of

the capillary optical systems, that capillaries represent a fine tool to investigate fundamental dispersion features of x-ray radiation by a surface [3, 4, 5].

In microcapillaries the sizes of channels for radiation propagation are much larger than the effective wavelength of the radiation and the process dispersion is described within the framework of surface (superficial) channeling. Capillary optics manufacturing technology allows us to reach extremely small channel diameters, actually, the last (fifth) generation of these optics achieved submicron channel diameters. The last reports show that capillary optical elements with an inner channel diameter of a few tens of nanometers can be obtained with the existing technologies [6].

Simultaneously, design and test of new natural systems composed by many channels capable to guide radiation continued since the mid 80's. The first manuscript on the new crystalline structures [7] presently well-known as carbon nanotubes was published more than ten years ago [8]. Just from the beginning films of oriented carbon nanotubes represented a field of interest for the development of new electronic emitters, nanodevices, etc. [9]. The discovery of carbon nanotubes suggested also their use as collimators for hard x-ray radiation and charged particles beams or for channeling of charged particles, x-rays and neutrons [10, 11, 12, 13, 14]. Features of nanotube morphology, e.g., the presence of inner cavity, address the possibility to achieve an efficient transmission of x-ray, thermal neutron and charged particle beams. Actually, nanotubes may be considered as nanoscale capillaries. However, for carbon nanotubes, the effective wavelength of x-radiation becomes comparable with the diameter of channels and the description of the propagation as a reflection of photons from the internal surfaces of the tube walls is not consistent. Hence, instead of superficial effects of radiation scattering we deal with bulk features of radiation interaction with the system [15].

To understand the propagation nature and the scattering of soft x-rays inside channels of extremely small diameters is a nontrivial problem. The present investigations is probably the first experimental evidence of the influence of the nanotube alignment on the angular dependence of x-ray fluorescence of carbon.

2 Basic Principles

As mentioned above, a nanotube can be considered as a capillary of very small inner diameter and wall thickness. However, there is a strong difference be-

tween a typical glass capillary and a nanotube from the point of view of radiation propagation inside these structures. First of all, the dielectric parameter as a function of the distance from the center of glass microcapillary channel varies with a step-law from zero in the inner hollow cavity to a constant value defined by the substance, for the channel wall. On the contrary, for a nanotube channel we observe a continuous change of the dielectric parameter value. However, the main difference is associated to the large difference in channel diameters that makes different the propagation character of the radiation inside microcapillaries and nanotubes. Indeed, radiation transmission by a cavity is defined as the ratio between the transverse wavelength of the radiation and the channel diameter $\lambda_\perp/d$. When this ratio is quite small, $\lambda_\perp/d \ll 1$, we can neglect wave features in the propagation process in the framework of the ray optics approximation. The same approach is not valid if $\lambda_\perp/d \simeq 1$ e.g., when the diffraction angle becomes comparable to the Fresnel angle $\theta_c = \frac{\omega_0}{\omega}$(the critical angle of total external reflection), where $\omega_0 = \left(\frac{4\pi e^2}{m_0}N_e\right)^{1/2}$ is a plasmon energy, N_e, e and m_0 are the electron density of matter, charge and mass of electron, respectively, ω is an energy quantum of radiation. This last condition occurs in nanosize channels and as a consequence nanochannels behave as radiation waveguides as demonstrated in Fig. 1.

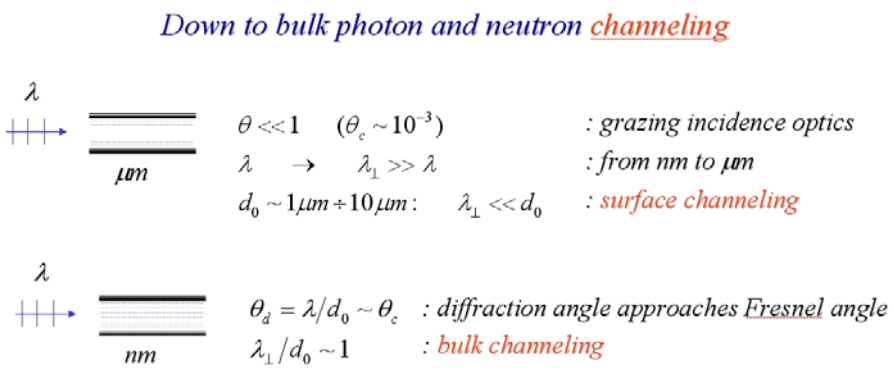

Figure 1: *Changes in the propagation character of the radiation inside micro- and nanochannels.*

The main characteristic of the propagation of radiation is correlated to the electron density $N_e\left(\vec{\mathbf{r}}\right)$, which is position dependent. We may determine

the density using an atomic potential approximations, the most simple of which is a Molier approximation [16]. The use of a typical procedure for averaging interaction potential results in the following expression for a bent nanotube:

$$\langle N_e(r)\rangle \approx \frac{r_{curv} N_a Z}{\pi a^2} \sum_i \alpha_i \beta_i^2 \int_0^\pi d\theta \; K_0\left(\frac{\beta_i \rho}{a}\right), \qquad (1)$$

$$\rho^2 = r^2 + r_{curv}^2 - 2 r r_{curv} \cos\theta,$$

where r_{curv} is the radius of nanotube bending, N_a is the atomic density, a is the screening radius of carbon atomic form-factor, and $Z = 6$. Evaluation of this relation gives estimation for the plasmon energy dependence presented in Fig. 2. As expected, the behaviour has a deep maximum in the wall, while is a smooth continuous function crossing a nanotube cavity. Propagation of polychromatic radiation through a straight nanotube is accompanied by a continuous energy filter: the effective width of nanotube channel as wider as higher photon energy.

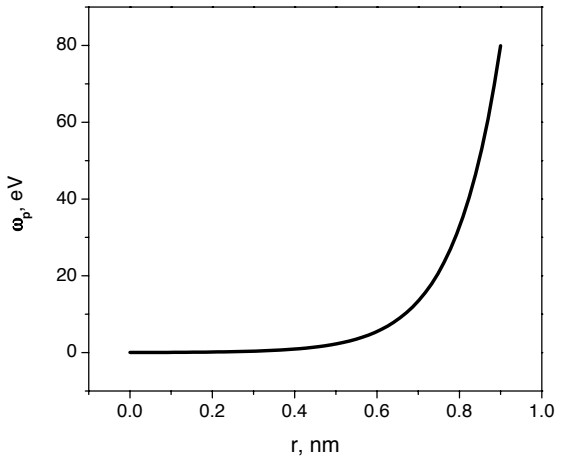

Figure 2: *Plasmon nanotube energy vs position inside a channel*

As follows from the analysis of the main parametes that defines the propagation characteristics of the radiation through a nanotube, the transverse

wavelength $\lambda_\perp$ of the radiation is independent by the projectile energy but is a function of the electron density of the nanotube. The density difference at the nanotube axis and inside the nanotube wall determines the transverse wavelength which is just a few nm.

Additionally to radiation channeling, the tunneling probability through the wall ($\propto \exp\left(-\frac{\Delta d}{\lambda_\perp}\right)$) is quite high for a single wall nanotube due to the small thickness of the wall. This effect is suppressed in multi wall nanotube. However, the diffraction of the radiation in multilayer wall system can not be neglected.

3 Characterization of Carbon Nanotube Layers

At present many techniques may produce layers of oriented nanotubes. Mostly aligned multiwall carbon nanotubes have been synthesized using zeolite-supported catalysts [17], lithographyc techniques [18, 19], and mixtures of ferrocene and fullerene C_{60} or hydrocarbons compounds [20, 21, 22]. The nanotube structure and the orientation character change following the synthesis conditions. It should be underlined here that, nanotubes composed by one layer are often bent and this contributes to the no ideality of the film structure. A simple explanation of the formation of the nanotube structures is illustrated in Fig. 3.

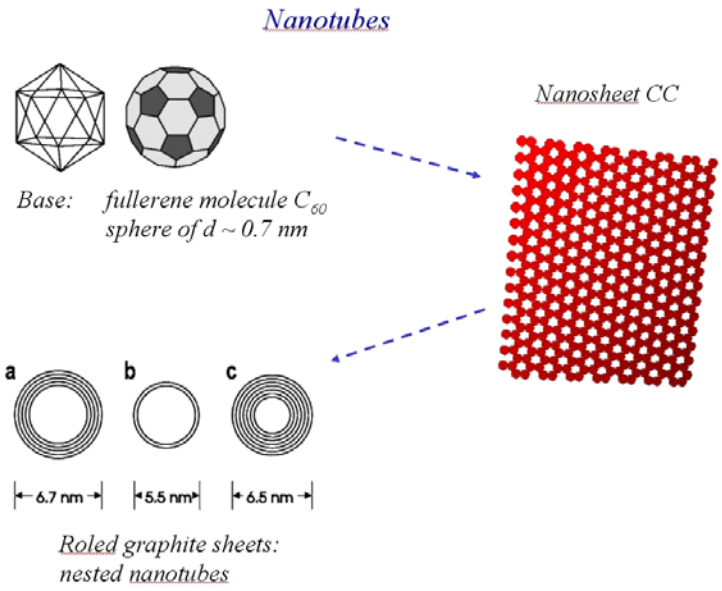

Figure 3: *Nanosheets and nanotubes derived by fullerene molecules.*

In our case a film of vertically aligned nanotubes on a Si substrate was prepared by thermal chemical vapor deposition (CVD) of ferrocene/fullerene mixture. The horizontal CVD apparatus consists of a stainless steel gas flow reactor of 1 m length and 3.4 cm diameter and a tubular furnace with a heating length of 30 cm. The reactor is fitted with a removable quartz tube 3 cm in diameter. A ceramic boat with a mixture of fullerene C_{60} and ferrocene $Fe(C_5H_5)_2$ taken in the ratio of (1:1) was placed inside the quartz tube under the Si plate of size 4×10 mm^2. The pyrolysis was performed at 950° C and atmospheric pressure in an argon flow (3 l/min).

The material produced was characterized by a scanning electron microscope (SEM) with a resolution of ~ 10 nm. Fig. 4 shows a SEM image of aligned carbon nanotube bundles deposited perpendicularly to the substrate surface. The mean length of nanotubes coincides with the thickness of a layer and is about 10 μm. The bundles are rather closely packed in the film and their density was estimated about 1000 pieces per μm^2. For a second sample the layers of the oriented nanotubes were destroyed by pressing nanotubes

onto a substrate surface. Due to the fact that nanotubes in the layer were quite long and defective, in the second investigated sample, nanotubes were mainly parallel to the layer surface.

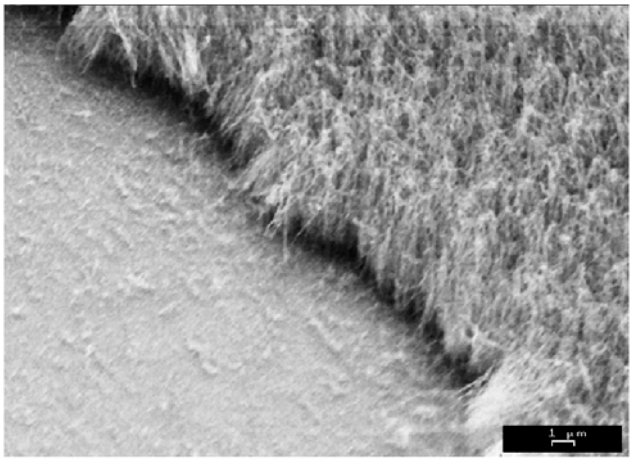

Figure 4: *SEM image of the carbon nanotube forest grown on a Si substrate.*

As the TEM images show, multilayered carbon nanotubes, characterized by external diameter of $100 \div 200$Å, and diameter of an internal cavity of $50 \div 70$ Åmay support the growth of film structures that range from 5 up to 25 layers. Defects and bends of nanotubes are formed during growth, at destruction of a film or during the preparation of a sample for electron-microscopic measurements. In each layers the nanotubes are linked enough to form a sheaf of hundreds separate nanotubes, whose internal cavity is filled in part by metal iron.

From the SEM analysis we observed that nanotubes are most ordered in an internal part of a film. In the beginning of the growth process the silicon surface with deposited iron particles acts as the catalytic surface capable to support the alignment of carbon nanotubes. Then, a simultaneous growth does not allow tubes to be significantly bent. The external area of a film with thickness of $0.1 \div 0.2$ μm is probably the most disordered region due to the final contribution of the growing process, e.g., when the fullerene concentration is low.

4 X-Ray Emission Measurement and Discussion

The angular dependence of the x-ray fluorescence from nanotube films was measured using a laboratory spectrometer. Fig. 5 shows the scheme of the experimental apparata placed in the spectrometer chamber operating in a vacuum of $2 \cdot 10^{-6}$ Torr. The sample 8 mm long and about 2 mm wide was placed on the rotatable axis providing an angular range α, between the sample surface and the optical axis of spectrometer from 60° to 100°. The position of the copper anode of the x-ray tube and the entrance slit was fixed. The angle β between the radiation source (the anode surface is about 6 mm wide) and the rotating axis was 20°. A gas proportional counter with methane pressure of 0.2 atm was placed beyond the slit. A counter window was made from polypropylene film of 1 μm thickness. At anode voltage of 2.3 kV and current of 100 mA the maximal counter charge was $\sim$ 3000 impulses/sec. The total intensity at the maximum accounted for $\sim$ 60000 impulses.

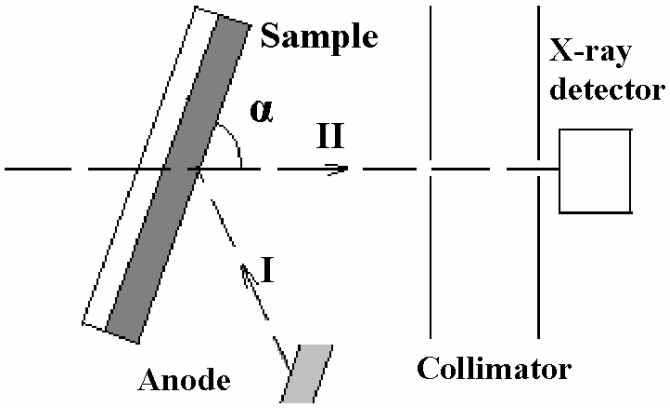

Figure 5: *Layout of a scattering experiment. In the scheme the sample is set in a position near to the x-ray tube. X-ray incident(II) and x-ray fluorescence beams are also outlined(I).*

X-ray fluorescence of a carbon atom does no show any angular dependence due to the localization and symmetry of the inner 1s-level. However, in crystals the probability of radiation emission is determined by the distribution of electrons in the valence band and may have a complex angular dependence. For

example, in the emission x-ray spectra of graphite, the contribution of π and σ components is varied depending on angular orientation of the detector [23]. The shape of the C K_α-spectrum of graphite is changed monotonously with a take-off angle of radiation and an integral intensity of a spectrum almost constant.

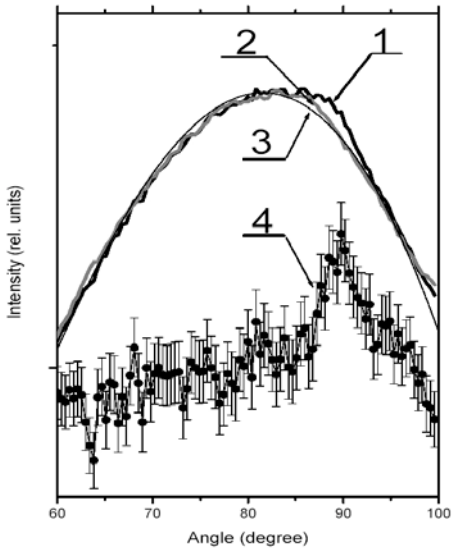

Figure 6: *The angular dependence of the x-ray fluorescence measured for a film of aligned carbon nanotubes (curve 1) and for a disordered distribution with vertical nanotube orientation (curve 2). Curve 3 is the angular dependence of the x-ray fluorescence described by the Eq.(2). In the bottom the difference multiplied by five, between curves 1 and 2.*

To detect effects due to channeling in carbon nanotubes the x-ray fluorescence from aligned nanotube film is compared to the emission of disordered nanotube film. The vertical orientation of carbon nanotubes in the second sample was destroyed by applying a pressure to the film. Indeed, after the treatment SEM analysis has shown an orientation almost parallel to the film surface. The angular dependence of the intensity of the x-ray fluorescence measured for both nanotube samples, aligned and disordered (curves 1 and 2, respectively) are compared in Fig. 6. Intensity is normalized to the maximum

at about 85°. All curves show a similar angular dependence increasing at angles from 60° up to 85°. The sample of aligned carbon nanotubes is characterized by additional small feature around 90°. For the disordered film the angular dependence of the X-ray fluorescence intensity can be described with the geometrical parameters of the incoming beam and the emitted fluorescent beams. The measured intensity fits the following expression

$$I = I_0 \sin\alpha \cos(\alpha - 20^\circ) \exp\left(\frac{-\eta \cos(\alpha - 20^\circ)}{\sin\alpha}\right) , \qquad (2)$$

where I_0 is the initial radiation intensity, η is the cumulative factor included the absorption and the density of the sample. The formula takes into account the change of the measured area with an angle α and the absorption of the incident radiation and fluorescence when the sample thickness is larger than the characteristic absorption depth of the exciting radiation. The behaviour (2) is represented by curve 3 in Fig. 3. The angular behaviour of the radiation intensity is a strong function of η and using this parameter to fit curve 3, we obtain a maximum at 82°.

The experimental angular dependence of the fluorescence emission is in good agreement with simulations and doesn't show features in the angular range near to the normal. The excitation of carbon x-ray fluorescence in nanotubes occurs through all the depth of a layer. However, the contributions of the radiation emitted by the deeper layers tend to decrease. On the other hand, the absorption of C K_α-radiation in a carbon layer is negligible. Therefore the contribution to the spectrum is given by the entire sample.

The difference between curves 1 and 2, multiplied by five is represented by the curve 4 in Fig. 3. The intensity of this curve is estimated to be about 0.4% of the total x-ray fluorescence intensity. Despite the large signal/noise ratio curve 4 exhibits a clear maximum at 90° with a width of about 6°. This feature can be interpreted as due to the interaction with carbon nanotubes oriented in the direction of the radiation. The width is then determined by the deviation of carbon nanotubes from the ideal vertical alignment. X-ray fluorescence from carbon nanotubes significantly misaligned, which mainly occurs near to the sample surface, contribute to the diffuse halo. The complex form of curve 4 is actually determined by a combination of different phenomena of dispersion of the radiation from oriented nanotubes. We shall try to evaluate these contribution from the major factors of dispersion in the total angular

distribution of the radiation behind the investigated structure.

Let us suppose that the angular distribution of the x-ray fluorescence from carbon nanotubes is isotropic so that we may estimate the mean angular deviation $\langle \Delta\theta \rangle$ of the x-ray fluorescence after traversing of a carbon layer. It may be calculated considering the complex mechanism of the scattering in the inner cavity and from the walls of nanotubes $\langle \Delta\theta \rangle_{chan}$ as well as by the diffuse scattering occurring in the space between separate nanotubes $\langle \Delta\theta \rangle_{diff}$. Hence, we can determine that

$$\langle \Delta\theta \rangle = \langle \Delta\theta \rangle_{diff} + \langle \Delta\theta \rangle_{chan} \tag{3}$$

The first term of the Eq.(3) depends by the texture of the nanotube's forest and by the mean distance between separate nanotubes or bundles of nanotubes tight attached to each other in the forest, i.e. $\langle \Delta\theta \rangle_{diff} = \langle \Delta\theta \rangle_{text} + \langle \Delta\theta \rangle_{pass}$. The latter can be easily estimated from geometrical parameters while the microscopic pictures of the samples allow texture parameters to be defined. The analysis shows that for a layer thickness of 10 μm, the mean distance between separate nanotubes or bundles of nanotubes is about 100 Å. Moreover, we can evaluate also the mean angular deviation in the angular orientation of the forest of nanotubes of about $20^\circ \div 30^\circ$. Thus, for our samples the term $\langle \Delta\theta \rangle_{pass}$ corresponding to the straight ray propagation (without reflection "on a gleam", i.e., free propagation in a space between nanotubes) between the nanobundles in the carbon layer, is a few mrads (less than 1^0) order from below. This value is lower than the angular divergence of an x-ray beam channeling in a nanotube. However, this factor has a small influence, i.e. the density of rays following a "straight propagation" is quite small. It is also reasonable, that the angular width of the dispersion due to the nanolayer texture $\langle \Delta\theta \rangle_{text}$ can be estimated with the same method, e.g., analyzing the layer micropicture and the angular orientational disorder of nanotubes within the layer. Disorder may be estimated by the mean deviation value of the angular orientation of nanotubes that is about $20^\circ \div 30^\circ$.

The second term of the expression (3) is the term that describe the radiation scattering inside the oriented channels of the layer. Following the definition of the scattering in channeling phenomena (see [24]), with a simple model we can write the following equation for the average angle of scattering in a nanotube ($e = \hbar = c = m_0 = 1$)

$$\langle \Delta\theta \rangle_{chan} \sim \frac{1}{r_0 N_0} \int_{\omega_{\min}}^{\omega_{\max}} d\omega \; \frac{N_{ph}\left(\omega\right)}{\omega} \int_0^{r_0} dx \; \omega_0\left(x\right) \;\; , \qquad (4)$$

where r_0 is an internal radius of the "hollow" part of nanotube, ω and $N_{ph}\left(\omega\right)$ correspond to the emitted photon energy and the number of photons, $\omega_0\left(x\right) = \sqrt{4\pi\rho\left(x\right)}$ is the energy of nanotube plasmon with a density of $\rho\left(x\right) = \frac{e^2}{m_0} N_e\left(x\right)$ [11, 12]. From the expression (4) we can estimate that $\langle \Delta\theta \rangle_{chan} \leq \omega_{0\,\max} r_0/10 \approx 6^\circ \div 10^\circ$ at the given values of $\omega_{0\,\max} \simeq 100 \div 150$ eV and $r_0 \simeq 20 \div 30$ Å, that is in good agreement with the experimental data. Actually small angles of dispersion are affected by the interaction between x-ray quanta and electrons of the nanostructured media, which in nanotubes form axially symmetrical channel with smoothly varying density of the electronic cloud. Moreover it is also necessary to take into account the tunnel effect of quantum transition between channels in film formed by multiwall nanotubes. In the investigated samples the walls thickness has a range $\Delta d \sim 25 \div 65$ Å of the order or less than the transverse wavelength of the radiation $\lambda_\perp \sim 50 \div 100$ Å. Therefore, the probability of tunneling into the neighbour channels, $\propto \exp\left(-\Delta d \;/\; \lambda_\perp\right)$, is large enough. However, the process of tunneling is accompanied also by small-angle diffraction. The presence of a set of ordered walls introduces diffraction dispersion of x-ray and the first maximum mainly determined by diffraction, is observed at angles close to the angles of channeling.

A significant portion of the radiation mainly scattered at the condition of channeling by the hollow part of the nanotubes, is not guided due to the distributed disorder of the nanosystem orientation. In other words, a large angular width of the orientation distribution of the nanotubes leads to a fast dechanneling of the radiation due to the increase of the "reflection angles" from nanotube walls. Then the scattering of this dechanneled fraction of the beam is dominated by diffusion phenomena in the nanotube forest and explains also the weak peak in the angular distribution of the emerging radiation.

5 Conclusion

Modern technological manufacture processes addressed in the last years the scientific relevance of systems formed by layers of focusing nanotubes. The question about the possible use of hollow channels in nanostructures, discussed theoretically in the last years appears now feasible. However, the quality of

these films is still far from ideal in order to be used as devices with defined crystal directions. Nevertheless, it is now possible start preliminary investigations about the structural effects of radiation dispersion in carbon nanotubes. In these systems the observed effects on the micron scale are due to the small sizes of the channels.

In this manuscript we tried to characterize orientational effects due to x-ray scattering in the forest of the nanotube bundles. Moreover, with sensitive x-ray fluorescence experiments we detected small scattering features in the range of the angles close to normal from a film of aligned multiwall carbon nanotubes. We have also shown that the width of the reflection curves is defined by the deviation in the angular orientation of the nanolayer texture. As a consequence the distribution of the carbon K_α-radiation has a maximum along the inner cavity of carbon nanotubes.

References

1. M.A. Kumakhov, *Radiation of Channeling Particles* (Energoatomizdat, Moscow: 1986).

2. M.A. Kumakhov, *Kumakhov Optics and Application* (SPIE, Washington: 2000) Proc. of SPIE **4155**.

3. S.B. Dabagov, Research Report of FIROS (Nalchik-Moscow, 1992) (in Russian).

4. S.B. Dabagov, and M.A. Kumakhov, Proc. of SPIE **2515** (1995) 124; S.B. Dabagov, M.A. Kumakhov, and S.V. Nikitina, Phys. Lett. **A203** (1995) 279.

5. G. Cappuccio, S.B. Dabagov, A. Pifferi, and C. Gramaccioni, Appl. Phys. Lett. **78** (2001) 2822.

6. 17th International Congress on X-ray Optics and Microanalysis, Sept. 22-26, 2003 Chamonix, France.

7. S. Iijima, Nature **354** (1991) 56.

8. R. Saito, G. Dresselhaus, and M.S. Dresselhaus, *Physical Properties of Carbon Nanotubes* (Imperial College Press, London: 1998).

9. L. Langer, V. Bayot, E. Grivei et al. Phys. Rev. Lett. **76** (1996) 479.

10. V.V. Klimov, and V.S. Letokhov, Phys. Lett. A **222** (1996) 424.

11. G.V. Dedkov, Nucl. Instr. Meth. **B143** (1998) 584.

12. N.K. Zhevago, and V.I. Glebov, Phys. Lett. **A250** (1998) 360.

13. E. Burattini, S.B. Dabagov and F. Monti, Nuovo Cimento **117B** (2002) 769; S.B. Dabagov, in: *X-Ray and Inner-Shell Processes*, Eds. A. Bianconi, A. Marcelli, and N.L. Saini, AIP Conference Proc. **652** (NY: 2003) 89.

14. S. Bellucci, and S.B. Dabagov, J. Phys.: Cond. Matt. **15** (2003) 3171.

15. S.B. Dabagov, Physics-Uspekhi **173** (No.10) (2003).

16. D. S. Gemmel, Rev. Mod. Phys. **129** (1974) 46.

17. W.Z. Li, S.S. Xie, L.X. Qian et al. Science **274** (1996) 1701.

18. J.I. Sohn, S. Lee, Appl. Phys. **A74** (2002) 287.

19. M. Terrones, N. Grobert, J. P. Zhang et al. Chem. Phys. Letters **285** (1998) 299.

20. M. Mayne, N. Grobert, M. Terrones et al. Chem. Phys. Letters **338** (2001) 101.

21. N. Grobert, W.K. Hsu, Y.Q. Zhu et al. Appl. Phys. Lett. **75** (1999) 3363.

22. B.C. Satishkumar, A. Govindaraj, C.R. Rao, Chem. Phys. Letters **307** (1999) 158.

23. Chr. Beyreuther, R. Hierl, G. Wiech, Berlichte der Bunsen-Gesselschaft für Phys. Chem. **79** (1975) 1081.

24. S.B. Dabagov, Rad. Eff. Def. Solids **25** (1993) 103.

Frascati Physics Series Vol. XXXII (2003), pp. 295-301
19th INTERNATIONAL CONFERENCE ON X-RAY AND INNER-SHELL
PROCESSES – Roma, June 24 - 28, 2002

DEVELOPMENT OF SUPERCONDUCTING SERIES-JUNCTION DETECTORS FOR APPLICATION TO XRF

A. Kagamihata, M. Kurakado, S. Kamihirata, and K. Taniguchi
Division of Electronics and Applied Physics,
Osaka Electro-Communication University, Osaka 572 -8530, Japan

ABSTRACT

We have developed a superconducting series-junction detectors capable of two-dimensional position resolution. The position dependence of the pulse height of the detectors is corrected making use of the incident position information obtained by the detectors themselves. It has been shown that the correction of position dependence is useful for improving the energy resolution of the superconducting series-junction detectors.

1 Introduction

Semiconductor detectors are useful for material analysis using radiations, e.g., X-rays and charged particles. The energy resolution of semiconductor detectors is, however, not sufficiently high for many applications. We are studying superconducting series-junction detectors for X-ray analysis. Superconducting

tunnel junction (STJ) detectors have the possibility of ultrahigh energy resolution [1]. Actually, single-junction detectors have shown about one order higher energy resolutions than semiconductor detectors for low energy X-rays [2, 3, 4, 5]. A single-junction detector consists of an STJ and it directly absorbs radiations. The area and the thickness of a single junction are usually of the order of 100×100 μm^2 and 100 nm, respectively. To improve the detection efficiency of STJ detectors, we are developing series-junction detectors.

2 Series-junction detectors

Series-junction detectors consist of STJs connected in series. One of the main principles of series-junction detectors is the efficient excitation of electrons (quasiparticles) by phonons, and another one is the effective capacitance. Radiations are absorbed by the single-crystal substrate of the series junctions. The energies of the radiations are converted to non-thermal high-energy phonons, which break Cooper-pairs in the STJs and thereby excite electrons beyond the energy gap of the superconductor. The excitation efficiency of electrons by high-energy phonons ($\Omega \geq 2\Delta$) is high. The mean energy ϵ required to excite an electron is about 1.7Δ [1]. Here, Ω is the energy of a phonon and 2Δ is the gap energy of the superconductor. The excited electrons, i.e., quasiparticles, in the superconductors can pass through the tunnel barrier and can contribute to signal charge. Therefore, the thickness of a series-junction detector is given by the thickness of the substrate.

When signal charge Q is produced by a radiation in a series-junction detector, Q gives rise to signal voltage $Vs = Q/C_{eff}$, where C_{eff} is $C + nC'$, C is the electric capacitance of an STJ, n is the number of junctions in series, and C' is the input capacitance of the amplifier connected to the detector. It should be noted that the effective capacitance [6, 7] is not equal to the usual electric capacitance ($=C/n + C'$). The effective capacitance C_{eff} of an optimized series-junction detector is proportional to the root square of total junction area S, i.e., $S^{1/2}$, enabling large-area detectors, whereas C_{eff} of a single junction detector is almost proportional to S.

3 Two-Dimensional Position Resolution

In our cases, the substrate is usually 400-μm-thick sapphire, i.e., single-crystal Al_2O_3. The detection efficiencies of series-junction detectors are three orders higher than those of single-junction detectors and can be comparable to those of semiconductor detectors. One of the merits of series-junction detectors is the flexibility in the choice of a single-crystal substrate. Substrates including high atomic-number materials will be useful for high-energy X-rays and even for γ-rays. However, the height of signals from series-junction detectors depends on the incident position of radiations, which degrades their energy resolutions. We have developed series-junction detectors having two-dimensional position resolution and a method of correcting the position dependence.

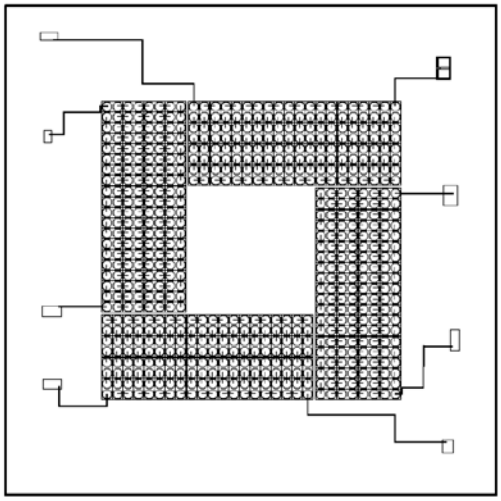

Figure 1: *Structure of α series-junction detector*

In Fig . 1, a series-junction detector developed for two-dimensional position resolution is shown. Two-dimensional position detection was performed with a detector that is constructed of 4 series junctions. Figure 1 shows the structure of the detector. Each series junction consists of 160 STJs: The diameter of each STJ is 110 μm. The layer structure of the STJs is, from bottom to top, 200 nm Nb/70 nm Al/AlO_x/70 nm Al/150 nm Nb. The setup of the mea-

surement is shown in Fig. 2. The detector was irradiated by a particles (5.486 MeV: 85%;5.443 MeV: 13 %) from ^{241}Am through 5 holes in a collimator, as can be seen in Fig. 2.

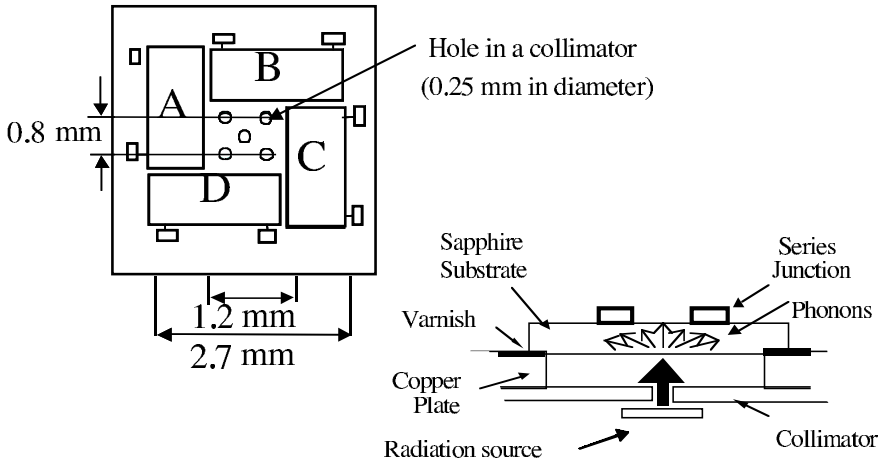

Figure 2: *Setup of α particle measurements with α series-junction detector*

The intensity of the available ^{241}Am source was only about 1000 Bq and the active area was about 7 mm in diameter, therefore the source was closely attached to the collimator resulting in a loose collimation of α particles. Pulse-height spectra obtained with each series junction are shown in Fig. 3. Positions (X, Y) were measured using the signal height ratios, $V_C/(V_A+V_C)$ and $V_D/(V_B+V_D)$. Here, V_A, V_B, V_C, and V_D are heights of signals from the four series junctions. $V_C/(V_A+V_C)$ and $V_D/(V_B+V_D)$ are shown in Fig. 4. Two-dimensional position resolution is obtained with four series junctions (A-C and B-D), as shown in Fig. 5. The rotated image is caused by the rotated distribution of the series junctions on the chip (see Fig. 1). In the correction of the position dependence, the asymmetry was not a serious problem.

4 Correction of Position Dependence

Even though the statistics was poor, correction of the position dependence of the signal height Z ($=V_A+V_B+V_C+V_D$) was carried out making use of the position resolution. Figure 6 (a) shows the original spectrum of Z; the total count is only 3690 and the count rate was about 0.2 cps with the weak α source.

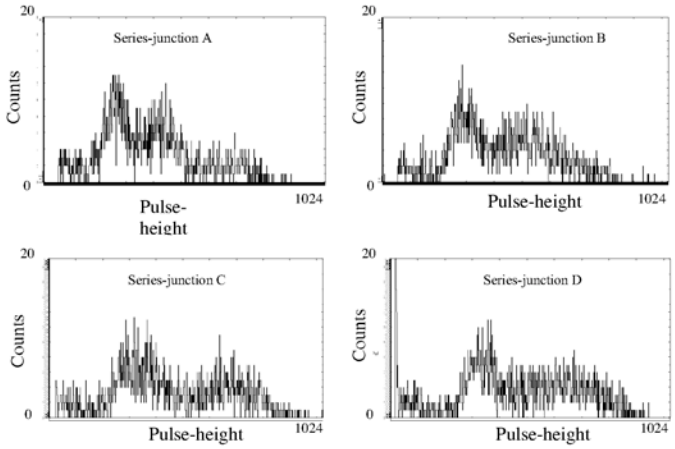

Figure 3: *Pulsed height spectra obtained with each series-junction detector*

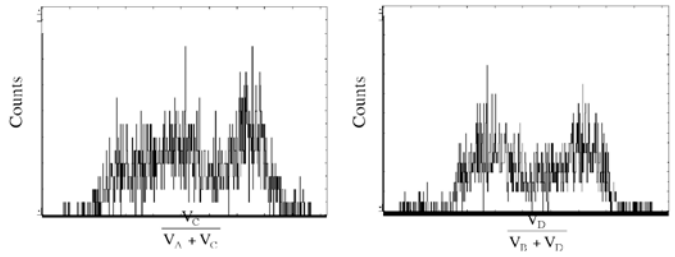

Figure 4: *One dimensional position spectra:* $V_C/(V_A+V_C)$ *and* $V_D/(V_B+V_D)$ *versus counts.*

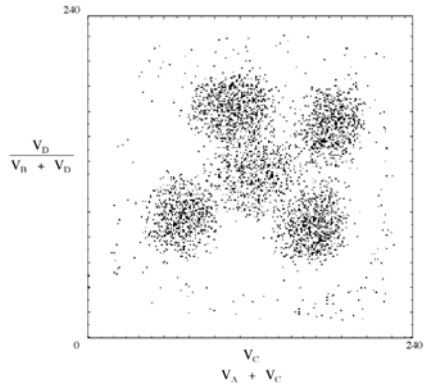

Figure 5: *Measured two dimensional incident position of α particles.*

Figure 6 (a) shows the original spectrum, and (b) the corrected spectrum. The original spectrum separated into two peaks. The separation may be attributed to the preamplifiers; three kinds of preamplifiers were used for the measurement, resulting in additional position dependence. The position dependence includes the different characteristics of the amplifiers. The energy resolution of (b) is 0.79 %, about 13 times better than that of (a). The resolution of 0.79 % corresponds to 47 eV for 5.9 keV X-rays. Assuming that the total data area is 1.5×1.5 mm^2, the position resolution applied to the correction of the position dependence corresponds to 50 μm. Two-dimensional position resolution and correction of the position dependence of the pulse height of series-junction detector were demonstrated for the first time.

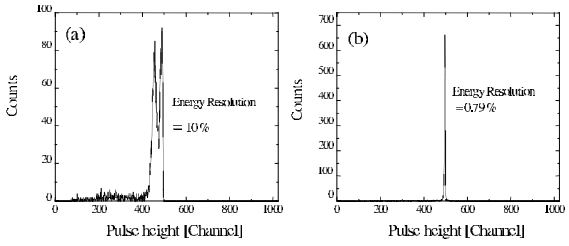

Figure 6: *Pulsed height spectra obtained with series-junction detector shown in Fig. 1 before (a) and after (b) correction of position dependence.*

Even though the precision of the correction method was restricted by the statistics of the data, i.e., low total count, it was shown that the correction of position dependence is useful for improving the energy resolution of the superconducting series-junction detectors. The superconducting series-junction detector will be applied to the X-ray fluorescence analysis.

References

1. M. Kurakado, Nucl. Instrum. Methods **196**, 275 (1982).
2. C. A. Mears, S. E. Labov, M. Frank, M. A. Lindeman, L. J. Hiller, H. Netel and A. T. Barfknecht, Nucl. Instrum. Methods A **370**, 53 (1996).
3. M. Frank, L. J. Hiller, J. B. le Grand, C. A. Mears, S. E. Labov, M. A. Lindeman, H. Netel, D. Chow and A. T. Barfknecht, Rev. Sci. Instrum. **69**, 25 (1998).
4. P. Verhoeve, N. Rando, A. Peacock, A. van Dordrecht, A. Poelaert and D. J. Goldie, IEEE Trans. Appl. Supercon. **7**, 3359 (1997).
5. G. Angloher, P. Hettl, M. Huber, J. Jochum, F. V. Feilizsch and R. L. Mossbauer, J. Appl. Phys. **89**, 1425 (2001).
6. M. Kurakado, A. Matsumura, T. Takahashi, S. Ito, R. Katano and Y. Isozumi, Rev. Sci. Instrum. **62**, 156 (1991).
7. M. Kurakado, D. Ohsawa, R. Katano, S. Ito and Y. Isozumi, Rev. Sci. Instrum. **68**, 3685 (1997).

Frascati Physics Series Vol. XXXII (2003), pp. 303-313
19th INTERNATIONAL CONFERENCE ON X-RAY AND INNER-SHELL
PROCESSES – Roma, June 24 - 28, 2002

NOVEL HIGH FLUX X-RAY SOURCE: A LABORATORY SYNCHROTRON

O.V. Mikhin, V.D. Gelver, A.V. Priladyshev
Institute for Roentgen Optics,123060 Moscow, Russia
UNISANTIS S.A., 1213 Geneva, Switzerland

S.B. Dabagov
INFN-Laboratori Nazionali di Frascati, I-00044 Frascati, Italy
RAS – P.N. Lebedev Physics Institute, 119991 Moscow, Russia

ABSTRACT

A novel x-ray laboratory system optimized for diffraction studies of protein crystals and macromolecules as well as for phase contrast analysis and other applications is described. The system is based on a micro-focus X-ray source of 10W power and provides the minimum focal spot size of $\sim$10 μm and the flux of $\sim 4.5 \times 10^{12}$ ph/sec at the Cu $K_\alpha-$line.

1 Introduction

Achievements in X-ray optics stimulated interest to creation of new radiation sources, which in a combination with optics enables considerably to improve the results of measurements in X-ray optics. In particular, the big progress is observed in the technology of capillary optical elements that, in turn, allows X-ray bunches to be rather effectively operated [1)]. These optical elements consist of many thousands hollow tapered tubes (channels) that condense the radiation

by multiple reflections from the inner channel surface. The main parameter, in most cases, is the density of a beam of radiation that can be raised on some orders by the use of capillary optical samples [2–4]. Due to this fact the given optics is widely used in various laboratories operating both with traditional sources of radiation and with synchrotron radiation sources [5]. However, it is necessary to note, that the basic advantage of capillary optics, most likely, is the fact that it provides essential increase of the efficiency of desktop X-ray sources. Quite big angular aperture and opportunity of turn of a radiation bunch through large angle with simultaneous focusing in a spot of small diameter allow the density of radiation comparable with that from synchrotron sources to be reached on traditional laboratory sources of X-radiation.

In the given work the study of a new X-ray source representing a micro focus tube in combination with capillary optics is resulted. The first data allow us to conclude, that by correct optimization of parameters of a tube and optics it is possible to create a powerful source of X-radiation. The new source, despite of high density of radiation on an output, is compact and can be quite well attributed to the class of desktop X-ray sources.

2 Micro Focus X-ray Source

It is obvious that the increase of radiation density can be received by means of optics. However, as the analysis shows, a source already defines a certain limit, which can be realized in a specific experiment. Therefore in order to improve radiation characteristics it is necessary to optimize not only parameters of optics, but also of a source. One of the most important characteristics of a source is the size of a focal spot. Its reduction provides essential increase of overall source performance, some problems with a heat-conducting path become simpler and the efficiency of the optics sharply rises.

As the first step an X-ray micro focus generator has been developed on the base of transmission anode X-ray tube with a point focus. For the purpose of adjustment the generator provides voltage on the tube within the range of about 40 kV and current of about 500 μA, maximum tube power is about 10 W. The source contains an electromagnetic system allowing electron beam formation inside the tube. The system comprises a focusing coil to ensure electron beam compression into a spot with diameter of down to 10 μm on the target and also two deflecting windings. One of them is used for electron beam alignment in two mutually perpendicular directions. The results obtained by a Cu anode X-ray tube will be presented below.

To assess the tube focal spot size, a polycapillary pillar (straight collimator system) was used with a channel diameter of 2 μm. An image was registered with the help of a 2D X-ray visualizer with a spatial resolution of 2 μm. The

experiment's block scheme is shown in Fig. 1.

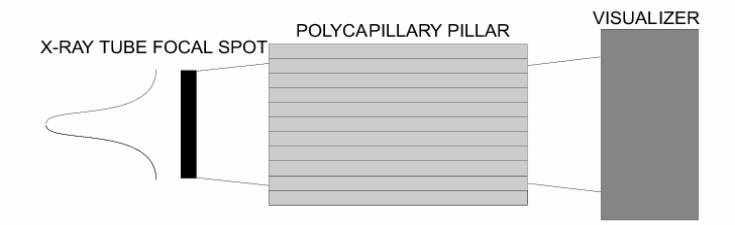

Figure 1: *The block diagram of tube focal spot size assessment experiment.*

To calibrate the system the polycapillary pillar was replaced with a thick-wall monocapillary (single capillary) with 18 μm diameter of hole; image was registered at the exit in the same experimental geometry conditions. The images obtained are shown in Figs. 2 and 3.

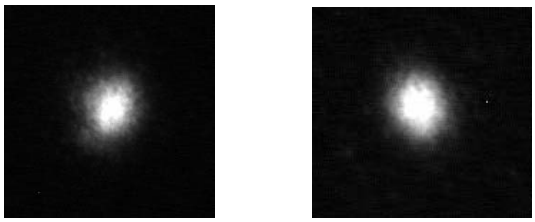

Figure 2: *Image of X-ray tube anode.* *Figure 3:* Image at the exit of 18 μm.

Analysis of the images has shown that the focal spot size of the tube is much less than 18 μm.
More accurately, the focal spot size was measured with the help of extended collimator, consisting of two polished glass plates, 70x70 mm in size. In this case, the distance between closely jammed plates makes ˜ 1μm. In order to increase the slit size and, respectively, the flux of quanta passing through the obtained gap, the 5 μm-thick foil strips were placed between the plates. The central plate part was grinded to prevent X-ray total external reflection and to reduce the inlet angular acceptance of a collimator (Fig. 4).

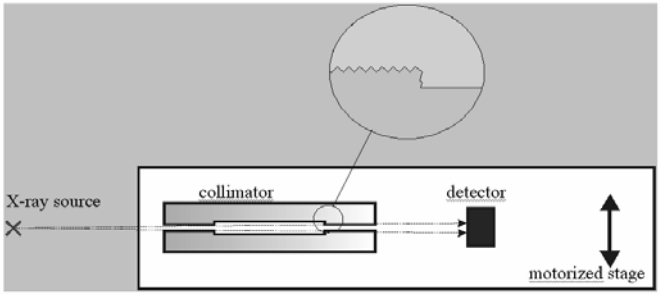

Figure 4: *Block-diagram of collimator for measuring X-ray focal spot size.*

In our experiment, the collimator was placed on a special holder movable in three orthogonal directions. The step of scanning was 2μm. This ensured precise alignment of the collimator respect to the X-ray focal spot. X-radiation was registered with the help of a semiconductor detector. Measurements were done under the following X-ray source mode of operation: 40 kV voltage, and 250 μA current. Results of the measurements are given on Fig. 5.

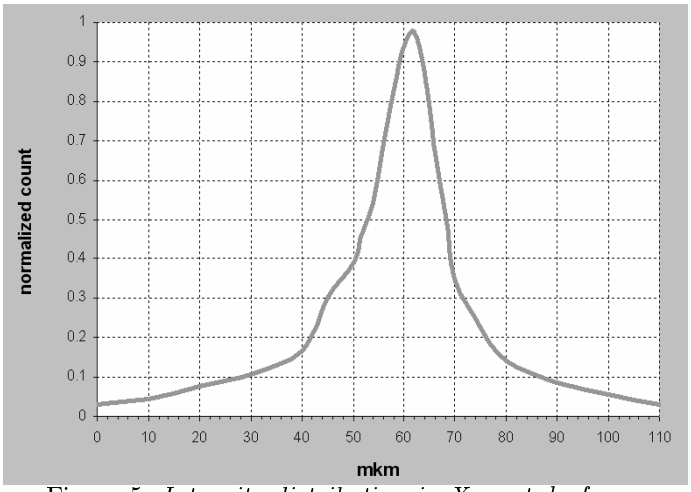

Figure 5: *Intensity distribution in X-ray tube focus.*

The obtained diagram shows that the focal spot size measured at half maximum of the curve (FWHM) less than effective size of the collimator slit. Asymmetric nature of the curve can be explained by the fact that the flux density of electrons hitting the X-ray tube anode has uneven distribution.

3 Integral Tube Flux Study

Integral X-ray flux measurements were done using a semiconductor Amptek XR-100T detector installed at 1 m distance from the source of radiation. To reduce the X-ray flux at the detector's inlet, a diaphragm was installed having a hole of 100 μm in diameter. In addition, in order to suppress Cu K_β rays, a 10 μm-thick nickel filter was placed behind the diaphragm. Experiments were performed at 40 kV voltage of the X-ray source. The results of measurements are presented in Fig. 6. It is seen from the diagram, that at 10 W in power, the source emits 4.5×10^{12} monochromatic photons per second.

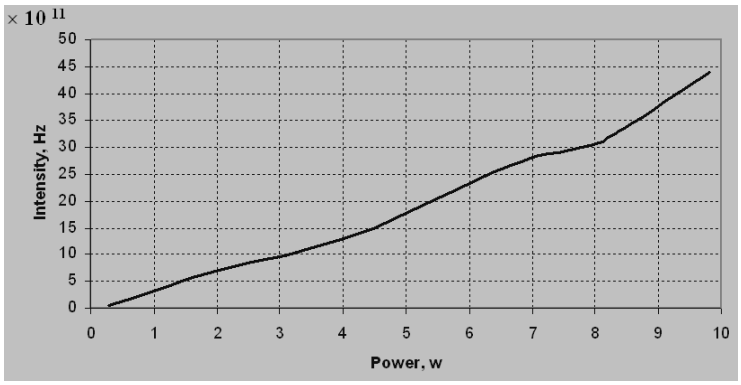

Figure 6: *Integral intensity of the X-ray source.*

For any type of radiation the most important characteristics is temporal flux stability. Study of this parameter was done in the same way as in the previous experiment. The results of measurements are given in Fig. 7.

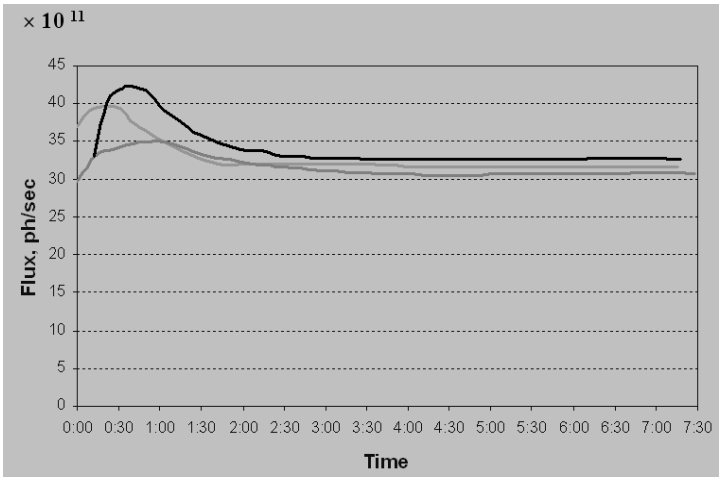

Figure 7: *Investigation of the source's long-term stability.*

These experiments have proven that after the system warming-up, deviations from the mean value do not exceed 0.8 % for 5 hours of operation. Maximum temperature on the housing surface is about 40^o C.

4 Phase Contrast Analysis by Micro Focus Tube

The above described X-ray tube will have a wide range of applications. We used it in a set of applications, but the most attractive result was obtained in phase-contrast analysis experiment.

Obviously, the first very simple idea is to use it for microscopic studies. Herein, the contrast resolution can be significantly improved due to the small source size. Moreover, it is particularly convenient, because in such a system with transmission anode configuration any object can be placed very close to the anode, thus ensuring the maximum magnification of the object under the study.
In addition, radiation goes to a semi-sphere permitting a concurrent investigation of several objects.

The system was used for phase-contrast imaging in weak absorption objects. In this instance, an improvement in the clarity of X-ray image, providing greater definition of weakly absorbing features in a fish body, was obtained (Fig. 8).

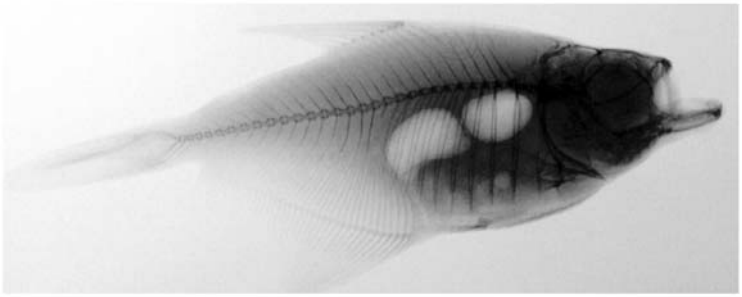

Figure 8: *X-ray image of a fish body.*

5 Half-lens parameters

To achieve maximum density of quasi-parallel radiation for a narrow beam, we have used a half-lens (polycapillary half lens), which was optimized to obtain the best correlation between the capture angle (acceptance) and the exit diameter. To satisfy this requirement, it is necessary to have a half-lens with minimum focal length. Thus, the half-lenses with the focal lengths of about 3 mm and less were fabricated. Transmission of the central part (300 μm) of the developed half-lenses approaches 35-40%.
In order to measure the beam divergence, a diaphragm with 0.3 mm diameter was installed at the half-lens exit and aligned to obtain the maximum X-ray flux. Then the X-ray beam passed a Si monochromator, plane (400), mounted on a motorized θ-2θ goniometer that allowed a rocking curve to be taken. The obtained curves are given in Fig. 8.

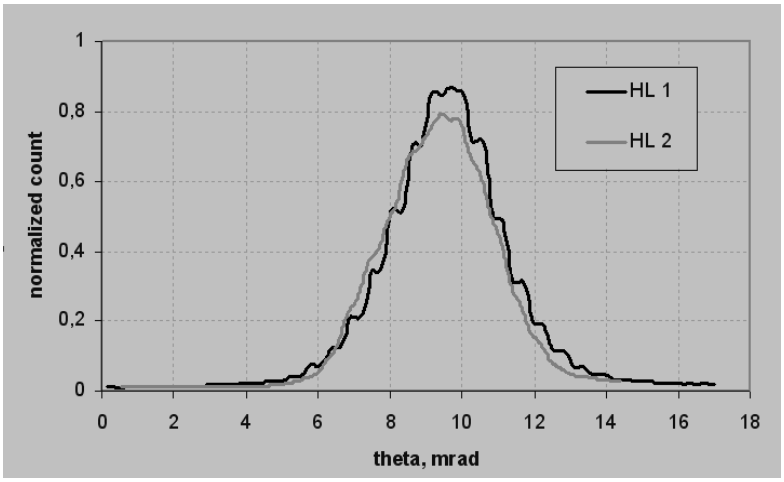

Figure 9: *Angular divergence of radiation transmitted by a polycapillary half-lenses.*

Analysis of these curves allows us to define the divergence of quasi-parallel beam to be of the order of 3.5 mrad.

6 Flux Measurements for Micro Source & Optics Assembly

The first tests of a new micro focus source have shown perspectives of research continuation. However, as follows from the simple analysis, irrespective of absolutely new solutions there is a certain limit of an ability of any source that is impossible to overcome by only physical principles. Obviously thus, that for improvement of source characteristics, application of a certain optics is necessary. In our case the combination of the offered new source (microfocus X-ray source) with the capillary lens (the half-lens) optimized for a concrete source was investigated.

The system flux was measured using a semiconductor Amptek XR-100T detector. As above mentioned, at the exit of half-lens a diaphragm of 0.3 mm in diameter was installed as well as a 9 μm-thick Ni filter to obtain monochromatic radiation. Further along the beam path, at a distance of 45 mm from the lens exit, an acrylic resin disperser was installed. This method allowed us to avoid saturation on the detector due to extremely high flux of radiation. The detector with 1 mm diaphragm at the inlet was placed at 35 mm distance from the point where X-rays hit the disperser. The disperser plus detector system with the

same geometry was calibrated to determine a conversion rate. Measurements were done with the source of 10 W power. It was shown that under the given parameters, , the half-lens forms a flux with intensity of $2x10^8$ ph/sec at the exit of $\emptyset 300$ μm diaphragm, and makes $2.8x10^9$ ph/sec/mm^2 for 1 mm^2 area.

As seen this is a record flux for desktop (laboratory) sources comparable with those obtained at synchrotron facilities.

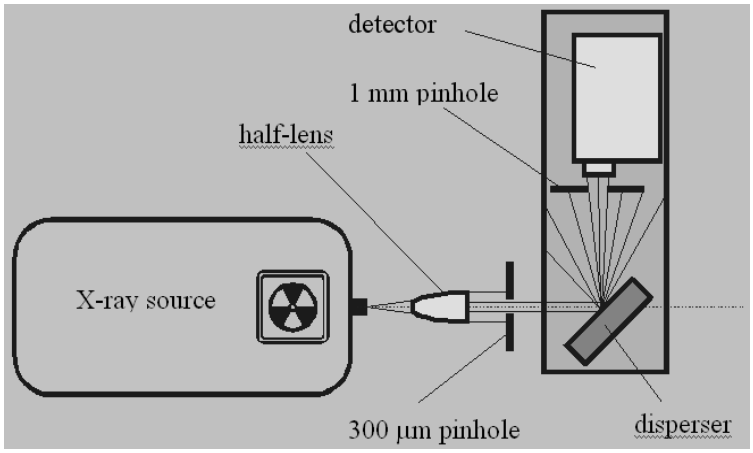

Figure 10: *Scheme of experiment for the flux measurement for an assembly of point source and half-lens.*

7 Conclusion

A micro focus generator has been created featuring a transmission anode with about 10 μm focal spot and 10 W power, i.e. the electron beam density on the anode makes 10^7 W/cm^2. This is an unprecedented density for a transmission type of anode by order higher than that at the rotation anodes [7].

The micro focus source has a wide range of applications. In particular, it was used for phase-contrast imaging of biological objects. In this instance very good results were obtained. The development of this new technology has the potential to provide new applications in medical, industrial and biological environments.

Moreover, the importance of this source of X-radiation will be increased by its combination with definite optics. For instance, we have used a micro focus source-polycapillary half-lens system for protein crystal studies that generally

require high-intensity beams from tens to several hundreds microns in diameter [8]. A quasi-parallel beam of about 20 μm in diameter and 3x10^{10} ph/sec/mm^2 flux density was obtained by means of the half-lens. It is important that the system permits using tubes with various anode materials that is convenient for express protein crystal investigations.

Figure 11: *Picture of a prototype of "Laboratory Synchrotron".*

Thus, on the basis of micro focus source and polycapillary optics, a unique source has been created that has no analogies in the world. With its help, an unprecedented quasi-parallel flux of monochromatic X-radiation with density varying from 3×10^9 ph/sec/mm^2 to 3×10^{10} ph/sec/mm^2 in dependence on the beam size was detected. The obtained fluxes largely exceed the fluxes obtained at rotation anodes and are comparable with the fluxes usually obtained at synchrotron workstations. This source was named a "Laboratory Synchrotron" [9] (see Fig. 11). There is also another point to be mentioned, namely, research carried out using the synchrotron workstations has limitations in terms of time and convenience. A Laboratory Synchrotron represents a breakthrough in the production of high flux density X-ray beams, and, on the contrary, offers freedom of creativity to scientists for use at their own laboratories.

References

1. M.A. Kumakhov, *Radiation of Channeling Particles in Crystals* (Energoatomizdat, Moscow: 1986).

2. M.A. Kumakhov, and F.F. Komarov, *Phys. Rep.* **191** (1990) 290.

3. P. Engström, S. Larsson, and A. Rindby, *Nucl. Instr. Meth.* A302 (1991) 547.

4. D.J. Thiel, D.H. Bilderback, A. Lewis, and E.A. Stern, *Nucl. Instr. Meth.* A317 (1992) 597.

5. S.B. Dabagov, *Physics-Uspekhi* **173** (No. 10) (2003) 1083.

6. T.J. Davis, D. Gao, T.E. Gureyev, A.W. Stevenson, and S.W. Wilkins, *Nature* **373** (1995) 595.

7. http://www.msc.com/protein/brochures/ruh-brochure.pdf

8. D.E. McRee, *Practical Protein Crystallography,* Sec. Edit. (San Diego, London, New York, etc., Academic Press: 1999).

9. http://www.unisantis.com

Frascati Physics Series Vol. XXXII (2003), pp. 315-326
19th INTERNATIONAL CONFERENCE ON X-RAY AND INNER-SHELL
PROCESSES – Roma, June 24 - 28, 2002

NUCLEATION OF Mo GRAINS IN $Mo/B_4C/Si$ MULTILAYERS DEPOSITED BY RF-MAGNETRON SPUTTERING

A. Patelli
Dipartimento di Ingegneria dell'Informazione – Università di Padova, via Gradenigo, 8/a - 35131 Padova Italy
J. Ravagnan, V. Rigato, G. Salmaso, D. Silvestrini
INFN-Laboratori Nazionali di Legnaro, viale dell'Università, 2 - 35020 Legnaro(PD) Italy
E. Bontempi, L. Depero
INSTM, Laboratorio di Strutturistica Chimica - Università di Brescia, via Branze, 38 - 25123 Brescia Italy
J.Th. De Hosson
Department of Applied Physics, University of Groningen, 9747 AG Groningen, The Netherlands

ABSTRACT

In last years, the comprehension of the relation between the different deposition parameters and the growth of Mo/Si multilayer mirrors has led to the possibility of increase the reflectance until the 70% at 13nm radiation. This improvement is principally due to an obtained increased smoothness and sharpness of the interfaces. Recently the introduction of diffusion barriers has further increased the mirror reflectance, but many physical aspects concerning their growth and interface formation need to be investigated. In particular Mo grain nucleation can influence the interface structure and morphology. The aim of the present work is to investigate this particular growth aspect as a function of the ion energy during the $Mo/B_4C/Si/B_4C$ multilayers deposition.

The multilayers presented in this paper have been produced by static deposition in a UHV chamber equipped with three magnetron sputtering sources driven by RF power supplies. Ion energy has been varied by DC biasing the sample-holder. Plasma diagnostic has been performed by Langmuir probe measurements in order to determine the Ar ion flux and energy impinging the

growing film. By X-ray diffraction and reflection it has been followed the evolution of the Mo layers at the different thickness and ion energy bombardment, showing the effects on Mo-crystal size, texture and interface smoothness.

1 INTRODUCTION

The development in the last decade of the Mo/Si multilayer mirrors has involved different application fields such as astrophysics [1, 2] and lithography [3, 4]. In the last years it has been shown that the use of a very thin boron carbide interlayer can increase the mirror reflectance to values higher than 70% [5, 6]. This reflectance increase is principally due to the reduced thickness of the Mo and Si interdiffused layers, in particular of the Mo-on-Si interface. As a matter of fact boron carbide acts as a diffusion barrier between the layers leading to a sharper change in refractive index. Since the presence of such diffusion barrier is highly relevant to the final normal incidence reflectance of the mirror, it is important to study the influence of such layer on the multilayer growth. In particular, the introduction of the B_4C layers can influence the crystals nucleation and structure of the Mo layers. On the other hand, layer' growth is influenced also by the deposition process. In sputtering deposition, the ion energy and flux assisting the growth and the adatoms energy play a central role on the definition of both crystal structure and interface roughness. Studies carried out on the Mo/Si multilayers have shown a roughness decrease with the decrease of the deposition working pressure [7]. Therefore the increase of the adatom energy of few eV leads to a sufficient increase in surface mobility to reduce the high frequency roughness. Recently the effects of the ion bombardment on Mo/Si [8] and on other multilayer structures have been reported [9]. The ions assistance during the growth leads to two competing mechanisms: increase of surface mobility, therefore interface flatness and preferential Mo grains (110) orientation on one side, increase of mixed layer thickness on the other side. Therefore, relative to those cases with only two elements in the periodic structure, the introduction of the diffusion barrier interlayer can induce changes not only in Mo crystal nucleation and structure but also their dependence on the deposition process parameters. In the present paper the effect of the ion bombardment during the growth of $Mo/B_4C/Si/B_4C$ multilayers will be considered focusing on Mo layer structure. In particular the effects on the

Mo crystals nucleation and on the amorphous to crystalline transition of the Mo layers will be studied and it will be pointed out the effect of the Ar^+ ion energy on Mo grain orientation and on the interface roughness.

2 EXPERIMENTAL

The experimental apparatus used at LNL for producing the X-Ray/EUV mirrors consists of three planar 2" UHV type II unbalanced magnetron sputter sources and a three-position biasable sample holder. The deposition process is static and in a sputtering up-ward configuration. Ar (99.9999%) is used as process gas at the operating pressure of $3.3{\cdot}10^{-3}$mbar. The base pressure of the chamber is about of $5.0{\cdot}10^{-7}$mbar. The distance between Mo and Si targets and substrate is set at 16.5cm, for B_4C the target to substrate distance is 10cm, and guarantees a film uniformity of better than 1% absolute over a region $2{\times}2cm^2$. Each source is driven by a RF power supply at 13.56MHz at the power of 60W for Mo, 150W for Si and 200W for B_4C. The effective deposition rates are similar for all the sources and are about $2.7{\cdot}10^{14}at/cm^2s$. Samples are biased with the aid of a power amplifier sourcing currents from –4A to +4A at bias voltages (V_B) from –100V to +100V.

Plasma diagnostic has been performed in order to know the Ar^+ energy and bombardment flux of the growing layers. This has been accomplished by means of a cylindrical Langmuir probe suited for RF plasma diagnostics and high-speed data acquisition (Scientific Systems SmartProbe^{TM}). The plasma density, plasma potential (V_p) and electron temperature measurements of the RF glow discharge have been performed for the different substrate bias applied at about 1cm from sample surface.

The X-ray microdiffraction spectra were collected using a D/max-RAPID Rigaku Microdiffractometer. This microdiffractometer is equipped with a cylindrical imaging plate (IP) detector and can measure two-dimensional (2D) X-ray diffraction patterns (XRD^2) from -45° to 160° (2θ). The integration of a 2D image can produce an intensity versus 2θ or versus β (along the Debye rings) spectrum, that can be analysed by standard powder diffraction analysis software. For these experiments, the irradiated area was 300 μm and the incident grazing angle of 5°.

The X-Ray Diffraction (XRD), and X-Ray Reflectivity (XRR) spectra in the co-planar specular and nonspecular configuration were collected with

a Bruker D8 Advance diffractometer, equipped with a Goëbel mirror. The angular resolution was 0.01 ° and the angular accuracy 0.001 ° .

The RBS and NRA measurements have been performed using the HVEC 2.5 MV and CN 7.0 MV Van de Graaff accelerators at the LNL – INFN. 2.2 MeV α-beams at the scattering angle of 170 ° has been used for the characterization of Mo, Ar and Si content. On the other side stoichiometry and absolute areal densities of B and C have been obtained by α-1.85 MeV RBS analysis at the scattering angle of 165 ° where both are essentially Rutherford [10, 11] and by nuclear reaction analysis, using ^{11}B(p,α)^{8}Be [12], ^{11}B(d,α_0)^{9}Be and ^{12}C(d,p)^{13}C reactions.

3 RESULTS

As a check for composition and thickness all the Mo/B_4C/Si/B_4C multilayers deposited were characterised by Ion Beam Analysis in order to obtain for all the multilayers studied the same design, independently from deposition parameters. The areal densities of each layer result on average for Mo, Si and B_4C respectively about 19, 22 and about $4.0 \cdot 10^{15}$at/cm^2, the latter with slight variations depending on the applied bias. The analyses on thick boron carbide films (∼1500Å) and on the multilayers reveal a boron/carbon ratio of 4.8±0.2, while the oxygen and nitrogen contents are lower than 1at%. The bias applied to the sample during the growth doesn't influence the stoichiometry of the carbide layers.

Plasma diagnostic, performed close to sample surface at the ground potential, indicate a plasma potential V_p = 24±1V, the electron temperature is 4.3±0.1eV and the ion flux on the sample surface is $4.0 \pm 0.2 \cdot 10^{14}$at/cm^{2}s. Since the deposition rates of B_4C, Si and Mo are of about $2.7 \cdot 10^{14}$at/cm^{2}s, the estimated ion-to-atom flux ratio on the growing surface is of about 1.5. Negative biases applied to the sample don't influence the plasma characteristics. On the other side at the bias of +20V, which is higher than the floating potential, the plasma shows an increase of +3V in its potential and a decrease in the ion flux to the surface of about 15%; the variation in electron temperature is negligible.

The study of the nucleation of the Mo nano-crystal has been performed by depositing multilayers with Mo thicknesses in the range from 20 to 45Å. In Mo/Si multilayers the transition amorphous-to-crystalline appears at a critical thickness of about 2nm. For this critical thickness an undesired increase of

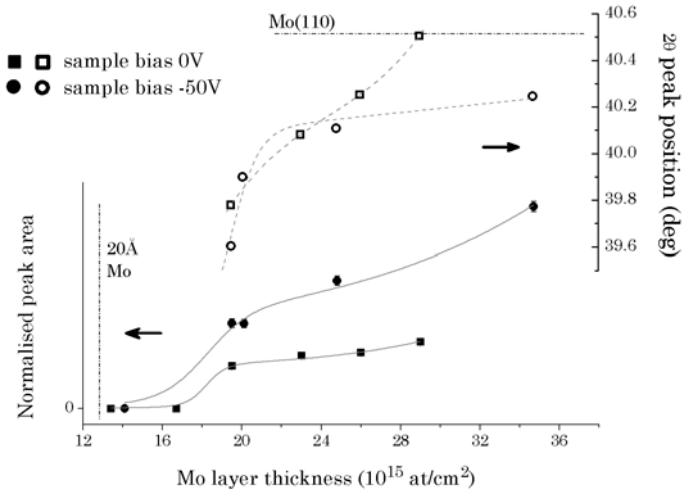

Figure 1: *Mo nano-crystals nucleation as a function of Mo layer thickness. The layer thickness normalised integral of the diffraction peak at about 2θ = 40 ° is shown on the left. On the right the peak position shift is reported.*

roughness is found. Above this thickness, interface flatness is recovered with a following thinning of the Si-on-Mo interface mixed layer [13]. The determination of the critical thickness is therefore essential for the optimisation of the structure. Since Si layers are amorphous and Mo nano-crystals, when present, grow with the (110) preferential orientation, as a marker of the crystallisation it can be considered the integral of the diffraction peak at 40.5 ° of the Mo(110) reflection normalised to the Mo layer atomic areal density. In the case of boron carbide on both interfaces the crystallisation trend obtained by $\theta - 2\theta$ XRD measurements is shown in Fig. 1. Two cases of sample bias are considered: 0 and –50V corresponding to bombarding energies of 24eV and 74eV respectively.

It can be observed that for the areal density corresponding to 20Å Mo thickness the layers are amorphous. The evident transition to nano-crystal nucleation appears between 16.7 and $19.5 \cdot 10^{15}$at/cm^2 (26-30Å) for the ground potential deposition and between 14.1 and $19.5 \cdot 10^{15}$at/cm^2 (22-30Å) for the –50V bias. The presence of the thin boron carbide layer seems therefore to increase the critical crystallisation thickness of Mo relative to Mo/Si multilay-

ers. In Mo/Si multilayers the transition thickness has been attributed to the presence of a critical content of Si in Mo layers [14]; the nucleation of Mo crystals begins for Si concentration lower than solubility limit of 7at%. The higher transition thickness in our case may be due to a deeper concentration profile of boron and carbon within the Mo layer. This is confirmed by the variation of the 2θ central position of the diffraction peak, which varies as a function of Mo layer thickness (Fig. 1 right). As a matter of fact the shift of the diffraction peak at about 40° should be attributed to the coexistence of Mo nano-crystals and of one or more Mo-B-C phases such as, for example, Mo_2C, that shows an intense reflection at about 39.4°, or Mo_2B_5 [15]. The presence of different phases is also confirmed by the presence of a diffraction peak at $2\theta = 35^\circ$ that should be attributed to a molybdenum boride and carbide phase (Fig. 2). No phases with boron and silicon should be expected since, by phase diagrams, B-Mo compounds are thermodynamically promoted. On the other hand it should be considered that the shift of the Mo(110) reflection can also be partly due to the stress introduced by the boron carbide deposition [16]. The stress in Mo layers may be also the cause of the different behaviour of the reflection shift at 0 and -50V sample bias. As a matter of fact at the higher energy of bombardment the shift is still present even in the thickest Mo layers.

To confirm the results obtained the crystal nucleation has been investigated also by TEM. A $Mo/B_4C/Si/B_4C$ multilayer with different Mo layers thickness has been produced at ground potential. To increase the statistic of the local TEM observation, for each thickness chosen (17, 20, 23, 25, 28, 30, 35Å) three periods have been deposited and the thickness sequence have been repeated twice from the thinnest to the thickest and vice versa. By the observation of the bright and dark field images, obtained isolating the Mo(110) contribution, it can be observed that the transition appears between the 25-28Å (Fig. 3a). For Mo layer thickness lower than 25Å the layers appear amorphous. At 25Å the crystals start to nucleate but more than a half of the Mo still remains amorphous. At 28Å ($\sim 19 \cdot 10^{15}$at/cm^2) the layer appears mostly crystallised. This transition is perfectly compatible with that observed by XRD measurements. Moreover the TEM can give further evidence of the presence of a Mo-B-C/Mo/Mo-B-C layered structure, consistent with the big shift of the peak to lower 2θ values as molybdenum layer thickness decreases. In fact is visible in the bright field image a dark amorphous region at both the

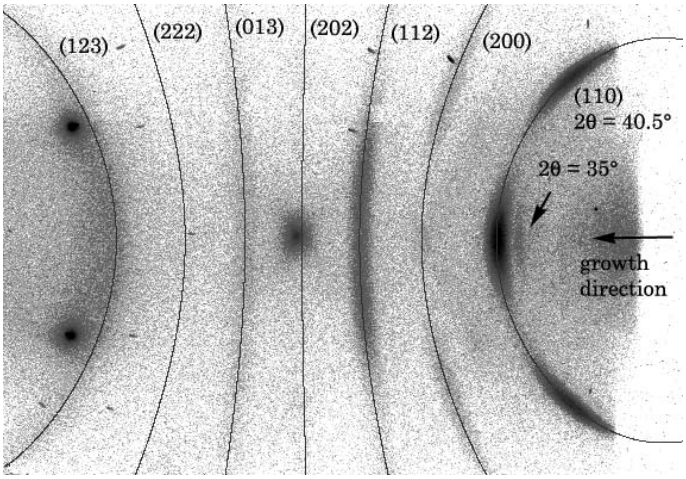

Figure 2: *μ-diffraction pattern of a $Mo/B_4C/Si$ multilayer produced at ground potential. Mo nano-crystals reflections are indexed (Mo layer thickness $\sim 19.7 \cdot 10^{15} at/cm^2$). A peak at about $2\theta = 35^\circ$ and a shift of the (110) reflection along the growth direction highlight the formation of different Mo-B-C phases.*

interfaces of the crystals (Fig. 3b).

These regions can be attributed to the presence of a mixed Mo-B-C compound, and their thickness is comparable with the Mo crystals thickness even for the 28Å Mo layers. In confirmation of this observation, also in the electron diffraction patterns obtained in cross section can be observed a ring at about 35° that in the Mo/Si multilayer structure have never been observed and that can be attributed to the formation of a Mo-B-C phase.

Ion bombardment has effects also on other aspects of crystal structure development and on the interface roughness of the multilayers. In Table 1 are shown the main results of the X-ray analysis. As previously observed the Mo diffraction peak shifts to lower 2θ values relative to Mo(110) reflection, highlighting the formation of B-C-Mo phases (Fig. 1). On the other hand the ion bombardment in both cases influences the angular spread of the Mo grains, revealing a clear dependence on the applied substrate bias. From the μ-XRD[2] patterns, in fact, we can determine the angular spread of the Mo peaks on the

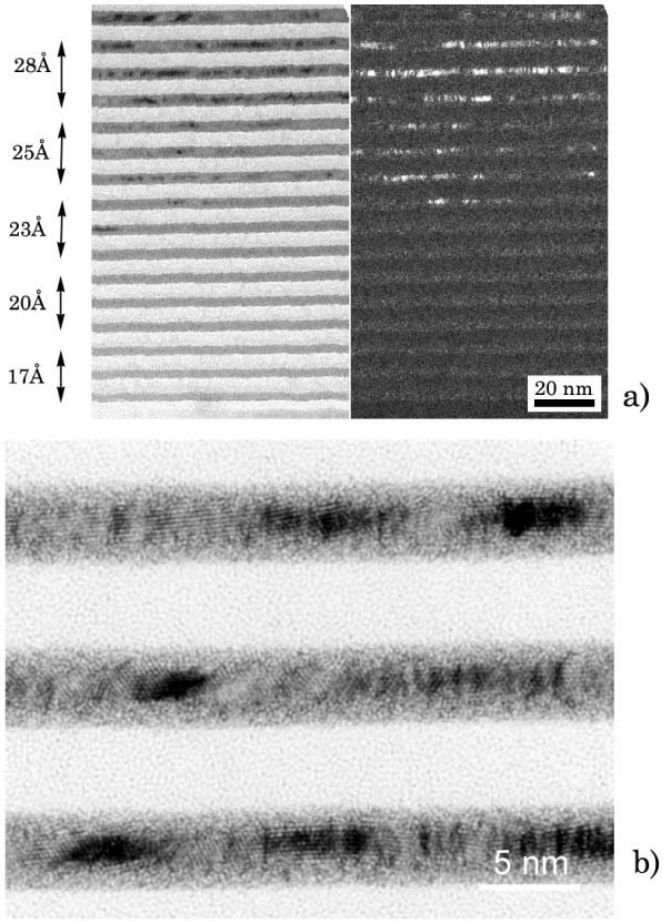

Figure 3: *TEM images of a Mo/B_4C/Si/B_4C multilayer with variable Mo layer thickness. a) Bright field and dark field images obtained by the selection of the Mo(110) reflection of different stacks with different Mo layer thickness (20, 23, 25, 28Å). b) HRTEM image of 28ÅMo layers. Mo crystals and interfaces can be observed.*

Debye rings (σ_β) as an indication of the degree of preferential orientation of Mo (110) crystals. The integral of the Bragg peak at about 40.5 ° obtained in the $\theta - 2\theta$ scans and the angular spread σ_β obtained by the μ-diffraction patterns (Tab. 1) show that at higher ion energy the angular spread is reduced, leading to a better oriented Mo (110) grain structure along the growth direction. This effect can also contribute, together with the possible different crystallisation degree, to explain the different normalised peak integral intensity shown in Fig. 1 for the different biases. Moreover the same effects can also explain the increase of the diffraction peak area as the Mo layer thickness increases (Fig. 1).

Table 1: *X-ray results (XRD, μ-XRD, XRR) of Mo/B_4C/Si multilayers produced at different substrate bias. $\theta - 2\theta$ XRD: 2θ position and layer thickness normalised integral of the diffraction peak at about 40.5 ° attributed to the Mo(110) reflection. μ-XRD pattern: angular spread σ_β of the Mo(110) reflection on the Debye ring. XRR rocking curve: ratio on 2^{nd} Bragg reflection between the intensities at Q_x 0 and 0.001Å^{-1}.*

Bias	XRD Norm. Integral (±5)	Peak pos 2θ (deg) (±0.1)	σ_β (deg) (±0.3)	$I_0/I_{0.001}$ (±20%)
+20V	74	40.1	16.0	0.0028
0V	110	40.3	13.2	0.0011
-50V	189	39.9	8.1	0.0002

This increase of crystal orientation degree as a function of ion energy is followed by an increase also of the smoothness. This effect is verified by the nonspecular XRR scans. Rocking curves on the second Bragg peak have been performed in order to investigate the diffused radiation. As a marker the ratio between the intensity of the second brag peak and the intensity at $Q_x = 0.001$Å^{-1} has been chosen. From the data reported in Table 1 can be observed that this ratio decreases of an order of magnitude as the ion energy increases. To characterise the roughness, detector scans were performed on the 2^{nd} Bragg peak (Fig. 4) [17]. The higher order peaks due to Bragg sheets are evident for the samples produced at lowest ion energy, at the substrate bias of +20V. The intensity of the higher order peaks decrease as the ion energy increases, showing a reduction of the correlated roughness. In the hypothesis

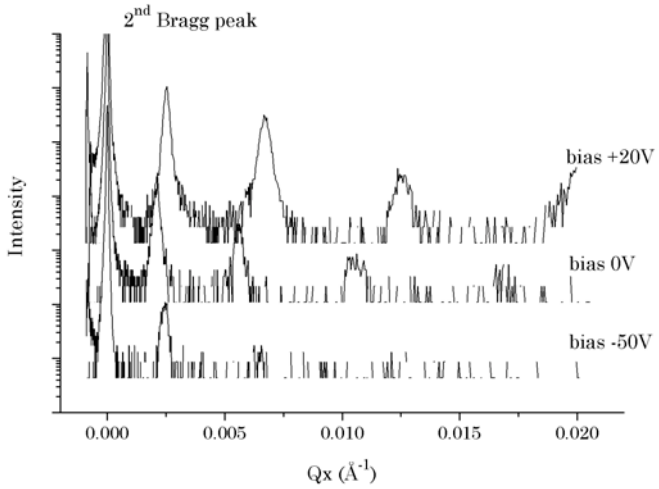

Figure 4: *Detector scans on the 2^{nd} Bragg reflection of Mo/B_4C/Si multilayers grown at different applied bias.*

that the high and mean frequency roughness in film growth is principally due to adatom mobility [18], the higher energy bombardment is able to increase surface mobility leading to increased flatness and to an abrupt reduction of interface morphology replication.

4 CONCLUSIONS

The results obtained show that the introduction of a very thin layer of B_4C at the interfaces besides determining sharper and more stable interfaces, affects both the molybdenum crystal nano-structure and interface morphology. The nucleation of the Mo grains has been shown to appear for thicker Mo thickness than in Mo/Si multilayer, between 26 and 30Å for multilayers prepared at ground potential (∼24eV ion bombardment). Increasing the ion energy the nucleation appears in the range 22 - 30Å. XRD and μ-XRD measurements reveal the presence of different phases confined at the interface of Mo layers. The results have been confirmed by the TEM analyses. The formation of a compound region of the Mo layers interfaces can be pointed out and attributed to the nucleation of the Mo-B-C phase. Confirmation of the presence of such

phase is obtained also by the electron diffraction pattern. On the other hand the most evident effect of the ion bombardment is visible on the crystal orientation degree and on the interface smoothness At higher bombarding energy ($\sim$74eV) the interfaces reveal a reduced correlated roughness achieving a reduction of more than one order of magnitude in diffused radiation.

References

1. Solar Orbiter, *A High Resolution Mission to the Sun and Inner Heliosphere*, Assessment Study Report, ESA-SCI (2000) 6, 2000.
2. Delaboudiniére et al., SPIE Proceedings 1742, 1992, 296.
3. A. M. Hawryluk and L. G. Sappala, *J. Vac. Sci. Technol.* B **6**, 2162 (1988).
4. E. Spiller, in *Soft X-Ray Optics*, SPIE Optical Engineering Press, Bellingham, Washington, DC, 1994, pp 183-184.
5. S. Bajt, J. Alameda, T. Barbee, et al., in Soft X-Ray and EUV Imaging Systems II, edited by D. A. Tichenor and J. A. Folta (SPIE, San Diego, California (USA), 2001), Vol. 4506, p. 65.
6. Wood J, Platonov Y. web-site: http://www-cxro.lbl.gov/ multilayer/survey.html
7. D. L. Windt, R. Hull, and W. K. Waskiewicz, Journal of Applied Physics 71, 2675 (1992).
8. V. Rigato, A. Patelli, G. Maggioni, et al., Surface and Coatings Technology 174-175, 40 (2003).
9. J. Birch, F. Ericksson, G. A. Johansson, et al., Vacuum 68, 275 (2003).
10. J. R. Liu, Z. S. Zheng, and W. K. Chu, Nuclear Instruments and Methods in Physics Research B 108, 1 (1996).
11. Y. Feng, Z. Zhou, Y. Zhou and G. Zhou, Nuclear Instruments and Methods in Physics Research B 86, 225 (1994).
12. J. Liu, X. Lu, X. Wang, et al., Nuclear Instruments and Methods in Physics Research B 190, 107 (2002).

13. S. Bajt, D. G. Stearns, and P. A. Kearney, Journal of Applied Physics 90, 1017 (2001).

14. I. A. Kopilets, V. V. Kondratenko, A.I. Fedorenko, et al., Journal of X-Ray Science and Technology 6, 141-149 (1996).

15. A. Costa e Silva and M.J. Kaufman, Intermetallics 5, 1-15 (1997).

16. T. W. Barbee and S. Bajt, in United States Patent No. US 6,396,900 (The Regents of the University of California (Oakland, CA), USA, 2002).

17. V. Holý, U. Pietsch, and T. Baumbach, High-Resolution X-Ray Scattering from Thin Films and Multilayers (Springer, Heidelberg, 1999).

18. D. G. Stearns and E. M. Guillikson, Physica B 283, 84 (2000).

Frascati Physics Series Vol. XXXII (2003), pp. 327-334
19th INTERNATIONAL CONFERENCE ON X-RAY AND INNER-SHELL
PROCESSES – Roma, June 24 - 28, 2002

ENRICO FERMI AND X-RAY IMAGING IN THE PERSPECTIVE OF X-RAY ASTRONOMY

Costantino Sigismondi
International Centre for Relativistic Astrophysics, Rome
Angelo Mastroianni
Department of Physics, University of Rome "La Sapienza"

ABSTRACT

Enrico Fermi studied the formation of images by X-rays and presented his first experimental work as a dissertation at the University of Pisa in the spring of 1922. Although his seminal ideas are not among the sources investigated by Riccardo Giacconi and Bruno Rossi when they proposed a telescope using X-rays, Fermi's thesis was the most complete study of X-ray physics during his time. Fermi used the technique of 'mandrels' to form optical surfaces. He anticipated the technique, used for the mirrors of *Exosat*, *Beppo-SAX*, *Jet-X*, and *XMM-Newton* telescopes, which is now a mainstay of X-ray optics.

1 Introduction

On the occasion of the centennial of the birth of Enrico Fermi in 1901, we made a study of the articles which he published on his degree thesis at the

University of Pisa in 1922. We examined his work from the perspective of X-ray astronomy.

Fermi entered the University of Pisa in 1918, at the age of 17, and prepared his thesis four years later. In that period Fermi became the leader of a little team of students (with Franco Rasetti and Nello Carrara), deciding and programming the measures. The experimental tools were used mainly for teaching, and Fermi's little group had to modify them with their own hands [1, 2].

Fermi extracted two papers from his thesis, describing his experimental methods [3, 4]. Firstly we look at these methods and the underlying physical principles (production of K_α lines, Bragg diffraction, casting curved mirrors with mandrels). Fermi used Bragg diffraction for generating his images in an astigmatic geometry, similar to the Rowland circle used in modern X-ray spectrometers.

X-ray Astronomy started in the early 1960s when Riccardo Giacconi and Bruno Rossi designed a rocket-borne X-ray telescope. They exploited reflection of X-rays under grazing incidence, discovered after Fermi's work by Arthur H. Compton [5] in 1923. The geometry of grazing-incidence optics was proposed by Hans Wolter [6, 7] in 1952 for applications in microscopy, following the studies of Paul Kirkpatrick [8] in 1950. These themes are outlined in the next section. (Incidentally, in 1947 Fermi studied a subject similar to X-ray grazing incidence: the reflection of neutrons on mirrors [9]).

Then we consider the *Exosat*, *Beppo-SAX*, *Jet-X*, and *XMM-Newton* X-ray observatories as examples of application of the mandrel technique to cast reflecting surfaces. In this respect Fermi can be considered a forerunner.

2 Fermi's thesis work

To image X-rays, Fermi applied the methods of M. de Broglie and M. G. Gouy [10, 3], who suggested using Bragg reflection from a cylinder of mica. De Broglie reflected X-rays from a convex surface of mica without obtaining a real focus; Gouy proposed theoretically the geometry of the cylinder to obtain it. Fermi explained the need to use Bragg reflection: "Röntgen rays are neither refracted nor reflected ... It follows that in X-ray optics the problem of obtaining images cannot be solved by means of lenses or spherical mirrors, as in ordinary optics." [4]

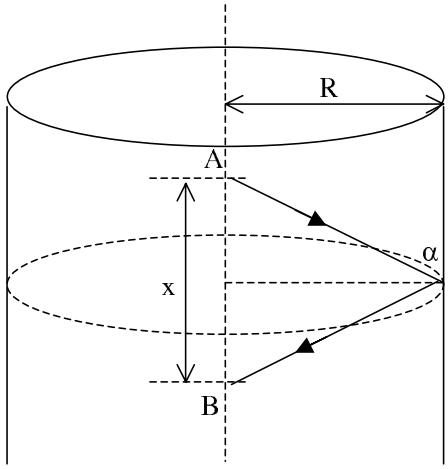

Figure 1: *Gouy's geometrical construction. This device produces astigmatic images, i.e., rays from a monochromatic point source do not pass through a single point in the focal plane, but instead have different foci in the dispersion and in the cross-dispersion directions.*

In Gouy's paper, cited by Fermi, the Bragg relation

$$n\lambda = 2dsin\alpha \tag{1}$$

where n is an integer, λ is the wavelength, d is the distance between the reticular planes, α is the complement of the incidence angle, reads as

$$\frac{1}{\lambda} = \frac{n}{4Rd}\sqrt{x^2 + 4R^2} \tag{2}$$

where R is the radius of the cylinder and x is the distance shown in Fig. 1.

The X-ray source is at A, the nth order image is formed at AB after reflection on that 'circular belt' (dashed in Fig. 1) of the cylinder where Bragg relation holds for the n^{th} order.

Fermi considered the more general case in which the source S and the image I are not placed exactly on the axis of the cylinder. He applied the formulae used for spherical mirrors to the projections of the rays on the plane of the 'belt', as shown in Fig. 2.

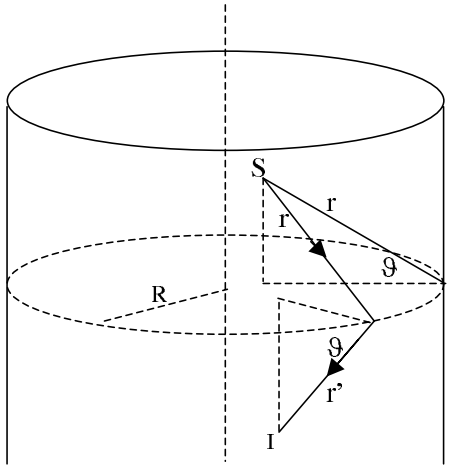

Figure 2: *Fermi's geometrical construction. The source and the image are both off axis. There are three rays: two of them covering a distance r from the source to the mica, and another focusing in I at a distance r′ from the mica, determined by equation (1). The Bragg reflection occurs on the whole dashed circle.*

The relation between r, r', and the radius of curvature R is given by the equation

$$\frac{1}{rcos\vartheta} + \frac{1}{r'cos\vartheta} = \frac{2}{R} \tag{3}$$

where $\vartheta = \frac{\pi}{2} - \alpha$ is the angle of incidence. This optical system is astigmatic.

Bragg diffraction is used nowadays for X-ray grating and crystal spectrometers, exploiting the Rowland-circle geometry [11, 12, 13], very similar to the one used by Fermi. This geometry introduces aberrations of order l^2/R^2, where l is the length of the grating and $L = 2R$ is its radius of curvature. This astigmatic optical system has been exploited in the design of such X-ray grating spectrometers as *XMM-Newton* [12]. In the case of Fermi, the Rowland circle has a radius $r = 1/2R$.

The apparatus used by Fermi in the thesis was made with a cathode sending electrons to a metal surface, the anticathode source of X-rays. The K-emission-line series was "made with the lines emitted after the jump of an

electron from any upper shell to the K shell" [3]. In Fermi's apparatus, the anticathode played the role of the slit in ordinary spectroscopy. The system was surrounded by the crystalline mirror and a photographic plate occupied the place where images formed. The whole system was enclosed in a vacuum tube.

Fermi shaped the mica crystal using a *mandrel*: he fixed the mica to a metal cylinder by means of sealing wax. When the wax cooled, the mirror was ready for use. Fermi made mirrors of about 4×6 cm^2 (excluding the irregular parts), which he checked with ordinary light. With this experimental apparatus, Fermi was able to produce images with K lines of iron. In his paper [4] he showed also a two-dimensional image of an "X" formed by the X-ray emission of two copper wires arranged on the anticathode to form a cross.

3 Grazing incidence of X-rays on metal

The problem of obtaining images with grazing incident rays was first considered by Hans Wolter [6, 7]. It is possible to obtain images using two coaxial mirrors, a parabolic and a hyperbolic one, with the same axis and coincident foci (see Fig. 3). This configuration obeys the Abbé sine conditions for aplanaticity [14].

Besides Bragg diffraction, reflection of X-rays from a high-Z metal surface can be obtained at grazing incidence, for incidence angles $\vartheta leq \vartheta_c$ measured with respect to the surface metal. The discovery of this effect was due to Arthur H. Compton, who published his work in 1923 [5].

The critical angle is given by the approximate expression

$$\vartheta_c = \frac{1.65^o}{E(keV)} \sqrt{\frac{Z\rho}{M}}, \tag{4}$$

where M is atomic weight, Z the atomic number and ρ the density of the metal in $g \cdot cm^{-3}$).

Papers by Paul Kirkpatrick [8] and Hans Wolter [6, 7] carried the principles used by Giacconi and Rossi [15] in preparing the first successful mission with a rocket-borne X-ray telescope in 1962 [16, 17, 18, 19].

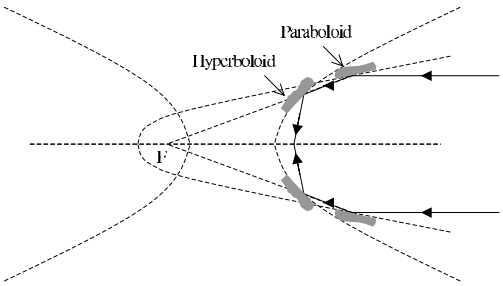

Figure 3: *Wolter mirror-configuration type 1: Paraboloid and Hyperboloid.*

4 Mandrel techniques in X-ray astronomy

Nowadays the Fermi's technique to cast mirrors with mandrels is a mainstay of optical manufacturing. As examples in X-ray astronomy [12, 20] we can mention the *Exosat* LE mirrors, *Beppo-SAX* [21], *Jet-X*, and *XMM-Newton*. In particular, the telescope of the Italian-Dutch satellite *Beppo-SAX* is made up of 30 confocal and coaxial mirrors [22]. The geometry of the mirrors is the tronco-conical approximation of the exact Wolter-1 geometry; therefore the telescope does not focus exactly at one point a point-like source at infinity on axis, but rather concentrates the photons in a small spot. From this property it is called a 'Concentrator' (see the paper by one of us [21] for a more complete description of the imaging properties of the *Beppo-SAX* Concentrator with extended sources). The gold mirrors are electroformed around aluminum mandrels coated with nickel. Different expansion coefficients with temperature allow the separation of the mirrors from the mandrels [23]. In this way a gold surface with an accuracy of ~ 1 Å has been realized.

5 Conclusions

After the thesis, Fermi used X-ray physics again only in his research on molecules and crystals [24] (in the 1930s) and in his work on the reflection of neutrons [9]. At the time of his thesis, he was extremely active in theoretical physics. In 1922 Fermi was preparing a theoretical thesis for the prestigious Scuola Normale Superiore in Pisa, which he was attending at the same time as the University. The thesis demonstrated some theorems of probability theory for application

to the motion of comets [25)]. Also at the same time Fermi was becoming an authority on quantum and relativistic theories. From his letters to his friend Enrico Persico [2)] it appears evidently not so much enthusiasm for X-rays. It is also to be considered that at that time, a theoretician had no hope to make a theoretical thesis, because only experimental works could be considered real physics. This was the reason why Fermi choosed the field of X-rays for his thesis [25, 26, 2)]. It was Fermi the one who changed this custom in italian physics, teaching theoretical physics and supervisioning theoretical thesis, the one of Ettore Majorana being a brilliant example. Looking at Fermi's biography, it appears again his very little interest in X-rays, we don't need here to recall the fundamental results in theoretial and experimental physics obtained by Fermi in Rome and in the United States. Our conclusion is that although Fermi's work on X-rays contained many seminal ideas, it did not contribute directly to the first steps in X-ray astronomy. Still it is worth repeating that the thesis of Fermi was the most complete work on X-ray physics in its time.

References

1. E. Fermi, Note e Memorie (Accademia Nazionale dei Lincei), **1** (1962)
2. E. Segrè, Enrico Fermi, fisico, Zanichelli (1987).
3. E. Fermi, Nuovo Cimento, **24**, 133 (1922).
4. E. Fermi, Nuovo Cimento, **25**, 63 (1923).
5. A. H. Compton, Philosophical Magazine **45**, 1121 (1923).
6. H. Wolter, Annalen der Physik, **10**, 94 (1952).
7. H. Wolter, Annalen der Physik, **10**, 286 (1952).
8. P. Kirkpatrick, Nature, **166**, 251 (1950)
9. E. Fermi *et al.* Phys. Soc. Cambridge Conference Report, **92** (1947).
10. M. G. Gouy, Com. Ren. de l'Ac. des Sc., **161**, 765 (1915)
11. F. Paerels, in J. van Paradijs & J. A. M. Bleeker (eds.), *X-ray Spectroscopy in Astrophysics*, Springer (1999).

12. R. Willingale, in J. van Paradijs & J. A. M. Bleeker (eds.), *X-ray Spectroscopy in Astrophysics*, Springer (1999).

13. H. A. Rowland, The Observatory, **5**, 224 (1882).

14. R. N. Wilson, Reflecting Telescope Optics I, Springer (1996).

15. R. Giacconi *et al.*, JGR, **65**, 773 (1960).

16. R. Giacconi *et al.*, Phys. Rev. Lett., **9**, 439 (1962).

17. H. Gursky, in H. Gursky, R. Ruffini & L. Stella (eds.) *Exploring the Universe*, World Scientific Pub., (2000).

18. B. Rossi, Adunanze Straordinarie per il Conferimento dei Premi Antonio Feltrinelli - Accademia Nazionale dei Lincei, **1**, 199 (1972).

19. L. P. van Speybroeck, in H. Gursky, R. Ruffini& L. Stella (eds.) *Exploring the Universe* (World Scientific Pub. (2000).

20. R. Willingale, in Encyclopedia of Astronomy and Astrophysics, IOP Publishing, **2**, 1049 (2000)

21. C. Sigismondi, Nuovo Cimento, **112**, 501 (1997).

22. G. Conti *et al.*, Proc. SPIE, **2011**, 118 (1993).

23. G. Conti *et al.*, Proc. SPIE, **1140**, 376 (1989).

24. E. Fermi, Molecole e Cristalli, Zanichelli (1938)

25. E. Fermi, publ. in Note e Memorie (Accademia Nazionale dei Lincei), **1**, 227 (1922)

26. M. de Maria, I grandi della Scienza (publ. by *Le Scienze*), **8**, (1999).

27. E. Fermi, Note e Memorie (Accademia Nazionale dei Lincei), **2** (1965)

28. J. D. Jackson, Classical Electrodynamics, John Wiley & Sons (1950)

29. B. Pontecorvo, Enrico Fermi, Studio Tesi (1993)

30. L. Puccianti, Nuovo Cimento, **25**, 307 (1923).

31. R. Vergara Caffarelli, Il Nuovo Saggiatore, **17**, 8 (2001).

Frascati Physics Series Vol. XXXII (2003), pp. 335-340
19th INTERNATIONAL CONFERENCE ON X-RAY AND INNER-SHELL
PROCESSES – Roma, June 24 - 28, 2002

QUANTITATIVE DETERMINATION OF THE EFFECT OF THE HARMONIC COMPONENT IN MONOCHROMATISED SYNCHROTRON X-RAY BEAM EXPERIMENTS

C.Q. Tran, M. de Jonge, Z. Barnea, B. B. Dhal, C. T. Chantler
School of Physics, University of Melbourne, Vic 3010, Australia

ABSTRACT

Harmonic contamination has limited many synchrotron experiments, often without the users realising the magnitude of the problem. We demonstrate a multiple-foil method for the quantitative determination of the fraction of the (333) third-order harmonic in a synchrotron x-ray beam monochromatised by a monolithic silicon (111) channel-cut monochromator. The method is able to produce quantification of the effect of the harmonic component below the 0.01% level for the first time.

1 Introduction

Monochromators select from a given spectrum a series of harmonics whose wavelengths satisfy the Bragg equation for the monochromator diffracting planes.

Some harmonics can be minimized using diffracting planes with 'forbidden' second-order reflections as in the case of the (111) planes of silicon and germanium monochromators. However, third-order and higher harmonics may be present, especially when their intensity in the source spectrum is significant. Accurate studies in which the monochromatic nature of the x-rays is important require, therefore, a method for the quantitative determination of the harmonic component in the x-ray beam. The International Union of Crystallography (IUCr) project to resolve discrepancies between experimentally determined attenuation coefficients reported that in earlier experiments 'one quarter had an incident beam which may have had second-harmonic contamination', and so were rejected. [1] Such harmonic components occur in synchrotron and laboratory x-ray beams and are often assumed to be insignificant without quantification of their effect on experimental results.

Most experimental configurations minimise the harmonic component in the beam (e.g. by detuning), but the reduction of the harmonic fraction by two orders of magnitude may still be unacceptable for many studies. The primary problem with many studies relating to attenuation or scattering is alluded to by Creagh and Hubbell [1] when they observe that 'if a plot of $\ln(I/I_0)$ against thickness... does not yield a straight line then no unique x-ray attenuation coefficient exists and an investigation must take place to establish what is the cause of this nonlinearity.' Determination of the harmonic components by absorption of the monochromatised beam by multiple foils is well known in the literature. [2] We have developed this technique for use with synchrotron beams and ion-chamber detectors, and extended it to provide accurate knowledge of the beam spectral composition.

This approach is an essential ingredient in recent form factor measurements. [4] The technique relies on the log-linearity of x-ray absorption by atomic materials. Scattering cross-sections are often non-linear on such a log plot, but this non-linearity makes only a small correction in the X-ray range of energies.

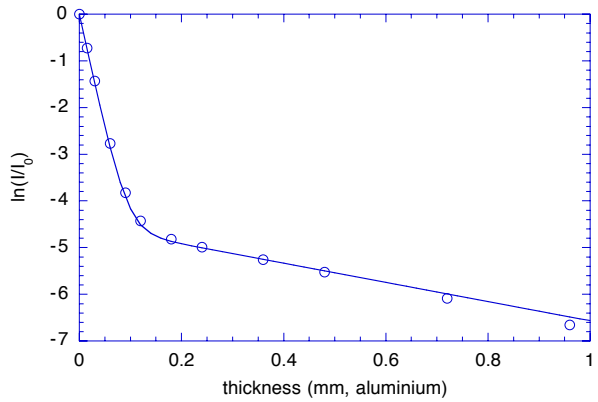

Figure 1: *The attenuation,* $\ln(I/I_0)$*, as a function of the thickness of aluminium absorber in the x-ray beam with a silicon monochromator set to 5 keV.* ∘ *- experimental results; solid line - curve of best fit corresponding to an admixture of* $(1.09 \pm 0.02)\%$ *third-order harmonic (15 keV).*

2 The effect of harmonics in attenuation measurement

Figure 1 shows the measured attenuation of eleven sets of aluminium foils with thicknesses between 15 μm and 1 mm, in the path of an x-ray beam monochromated by a detuned, double reflection silicon (111) channel-cut monochromator set to select 5 keV X-rays. The slope at low thicknesses gives the attenuation coefficient for dominant first order harmonic radiation (i.e. 5 keV X-rays) while the slope for large thicknesses gives the attenuation coefficient for third order harmonic radiation (i.e. the more penetrating 15 keV X-rays) The second order reflection is 'forbidden'.

The linearity of the slope is compromised even for $-2 < \ln[I/I_0] < 0$, where I_0 is the incident flux and I the attenuated flux. To account for the slope, it is necessary to fit the proper equation for the harmonic fraction x, and the fundamental and higher harmonic attenuation coefficients μ_f and μ_h using $I = I_O[(1-x)e^{-\mu_f t} + xe^{-\mu_h t}]$ for the given series of thicknesses t. The third order harmonic is seen by the deviation from linearity at low attenuation and by the inflection in the plot as the lower energy flux becomes heavily attenuated.

However, the harmonic fraction is only obvious as the slope of the second linear part of the graph above log ratios of 5 or more. In this example, this corresponds to thicknesses of 0.6 mm and to a first order attenuation log ratio of $\ln[I/I_0] \simeq -25$. We have probed the attenuation over a range far exceeding the 'recommended' [1] Nordfors [3] range of $(-4 < \ln[I/I_0] < -2)$; corresponding to $(-30 < \ln[I/I_0] < 0)$ for the fundamental energy. Sampling the linearity of the attenuation over a much wider range than in previous investigations enables a more extensive diagnosis of systematic effects including detector linearity, harmonic content, dark current offsets and saturation.

Experimental results based on a small part of this curve will be in significant potential error, especially where the absorption coefficients are not known (and they are rarely known to better than 1%). In this example, the thicknesses of the aluminium foils were not well known. The requirement of precise knowledge of foil thickness was avoided by using multiples of a single foil for each of these thicknesses. In this way the ratio of thicknesses of each of the absorbers was well defined. The determined harmonic percentage is 1.09% with an uncertainty of 0.02% as the one standard deviation uncertainty to a function fitting for both orders of radiation (without any assumption as to the attenuation coefficients for either).

The measurements were carried out by using a metal 'daisy wheel' on whose perimeter were mounted eleven different thicknesses of foils. These foils were placed in the beam by suitable rotation of the daisy wheel. This technique is accurate, reproducible and rapid. The monitor and detector used throughout this work were matched nitrogen gas-flow ion-chambers. The work was performed at the bending magnet beamline 20B of the Photon Factory synchrotron at Tsukuba.

Use of relatively calibrated sample thicknesses prevents us from determining the attenuations μ_f and μ_h from this measurement, but the harmonic component remains very well defined. Any good attenuation measurement

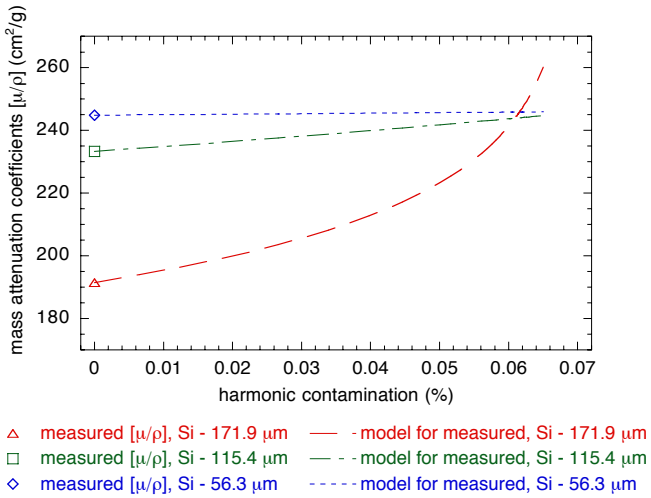

Figure 2: *Effect of third-order harmonic contamination in attenuation measurements using Si(111) monochromator and three silicon sample thicknesses at 5 keV. All three measurements are consistent with a unique percentage of third-order harmonic contamination of about 0.06%.*

should probe the harmonic component of the beam if it aims to be accurate at the sub-percent level. Surprisingly, the harmonic contamination in numerous experiments may exceed 10% without the major problem being obvious to the experimenters.

3 A three-foil experiment showing the effect of the harmonic fraction and its energy dependence

To perform an actual attenuation measurement, it is efficient to use a smaller number of carefully calibrated thicknesses. A minimum of three samples of accurately known thickness is required to simultaneously determine the harmonic percentage, and the fundamental and higher harmonic attenuation coefficients.

If μ_h is provided by a separate experiment (or theory) then use of three samples overdetermines the problem and allows for error analysis or the possible observation of an additional harmonic or other non-linearity. Figure 2 shows the variation of the attenuation of these three thicknesses at 5 keV when an admixture of 15 keV x-rays (due to diffraction by the (333) plane of the silicon monochromator) is present in the incident x-ray beam. The three points are

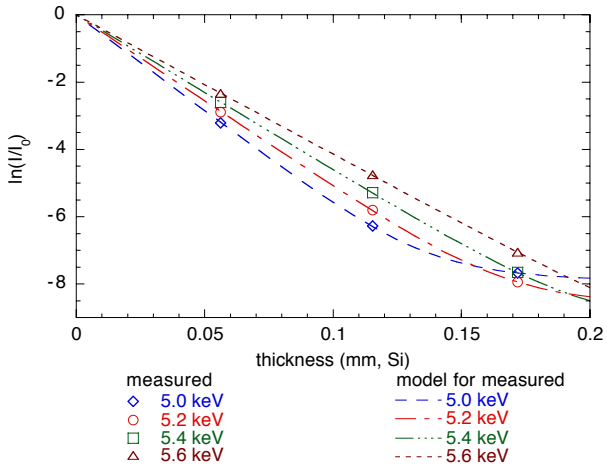

Figure 3: *A harmonic component measurement with three well calibrated thicknesses provides a constant and reliable indicator of accuracy in attenuation measurements. Error bars are given by the thickness of the line.*

experimental curves, where the measurements only become consistent for the correct admixture of 15 keV X-rays. This (least-squares) fit can be performed using theoretical values for the absorption of silicon for 15-keV x-rays. [5, 6] The uncertainty of 1% in the tabulated value has negligible effect on the uncertainty. The three lines converge for a fraction 0.06% of 15-keV x-rays. The fitted one standard deviation uncertainty is 0.007%. For this analysis, a quite thick sample is crucial.

Figure 3 shows the fitted $\ln(I/I_0)$ curves of the three-foil measurements as functions of thickness, with decreasing harmonic contamination as the energy is raised. [4] The final uncertainty depends on the accuracy of the sample thicknesses and the counting statistics. Larger attenuation ranges also yield higher accuracy.

Figure 4 shows the percentage of third-order harmonic as a function of the energy of the fundamental x-rays. The energy dependence of the percentage of harmonic contamination detected in our experiment is due to the fundamental output spectrum of the synchrotron, the intensity of the monochromator diffraction of x-rays of the various energies (with the given detuning current

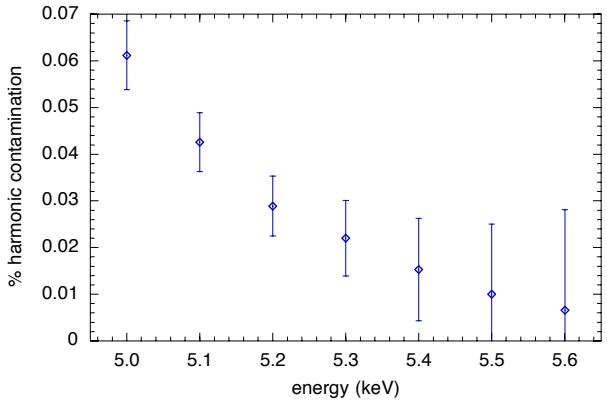

Figure 4: *Energy variation of the fraction of harmonic contamination in the example chosen (at maximum detuning).*

and its effect on the suppression of the harmonic), and the relative detection efficiency of the detector for the fundamental and harmonic x-rays. Using this technique it is possible to correct for very small fraction of harmonic contamination eg. 0.01% at 5.6 keV.

In other work, [7] we show that the likelihood of residual harmonic contamination significantly affecting synchrotron experiments is much higher than often assumed, especially on an ID line where the third harmonic can often have high intrinsic flux and be transmitted with minimal loss of intensity by any monochromator crystals and through any windows or other attenuation path.

The multiple-foil method can be used as a sensitive diagnostic method for the quantitative determination of the fraction of harmonic radiation in a monochromatised x-ray beam. The method can simultaneously also provide quantitative information about nonlinear detector response such as may occur at high counting rates. The determination of the harmonic fraction is the result of a number of measurements and thus is insensitive to errors in the thickness determination of the individual foils. The simplicity of the method and the ease with which it can be automated renders it suitable as a diagnostic test in

a large variety of experiments.

4 Acknowledgements

We acknowledge encouragement from D. C. Creagh. The work was performed at the Australian National Beamline Facility with support from the Australian Synchrotron Research Program, which is funded by the Commonwealth of Australia under the Major National Research Facilities program.

References

1. D.C. Creagh, J.H. Hubbell, Acta Cryst.**7** 102-112 (1987).
2. Z. Barnea, J. Mohyla, J. Appl. Cryst. **7** 298-299 (1974).
3. B. Nordfors B., Arkiv für Fysik **18** 37-47 (1960).
4. C.T. Chantler, C.Q. Tran, D. Paterson, D.J. Cookson & Z. Barnea Phys. Lett. A **286** 338-346 (2001).
5. C.T. Chantler, J. Phys. Chem. Ref. Data **24** 71-643 (1995).
6. C.T. Chantler, J. Phys. Chem. Ref. Data **29** 597-1048 (2000).
7. C.Q. Tran, Z. Barnea, M. de Jonge, B.B. Dhal, D. Paterson, D.J. Cookson, C.T. Chantler, submitted to X-ray Spectroscopy (2002).

Authors Index

Author Index

Participants

Silvio a Beccara	Università di Trento	Italy	abeccara@science.unitn.it
Stefano Agrestini	Università di Roma "La Sapienza"	Italy	stefano.agrestini@roma1.infn.it
Helena Aksela	University of Oulu	Finland	helena.aksela@oulu.fi
Seppo Aksela	University of Oulu	Finland	seppo.aksela@oulu.fi
Miron Ya Amusia	The Hebrew University Ioffe Physical	Israel Russia	amusia@vms.huji.ac.il
Iztok Arcon	Nova Gorica Polytechnic	Slovenia	iztok.arcon@ses-ng.si
George Brad Armen	University of Tennessee	USA	garmen@utk.edu
Lorenzo Avaldi	CNR	Italy	lorenzo.avaldi@mlib.cnr.it
Yohko Awaya	Musashino Art University - Tokyo	Japan	awaya@musabi.ac.jp
Arkadiy Baltenkov	Arifov Institute of Electronics	Uzbekistan	arkadiy@ariel.tashkent.su
Uwe Becker	Abteilung Oberflächenphysik - Berlin	Germany	becker_u@fhi-berlin.mpg.de
Peter Beiersdorfer	Lawrence Livermore National Laboratory	USA	beiersdorfer@llnl.gov
Ronaldo Bellazini	University of Pisa	Italy	ronaldo.bellazzini@pi.infn.it
Stefano Bellucci	INFN-LNF	Italy	bellucci@lnf.infn.it
Maurizio Benfatto	INFN-LNF	Italy	benfatto@lnf.infn.it
Uwe Bergmann	Lawrence Berkeley National Laboratory	USA	ubergmann@lbl.gov
Nora Berrah	Western Michigan University	USA	berrah@wmich.edu
Antonio Bianconi	Università di Roma "La Sapienza"	Italy	antonio.bianconi@roma1.infn.it
Sergey Bobashev	Ioffe Physico-Technical Institute RAS	Russia	s.bobashev@pop.ioffe.rssi.ru
Gunther Borchert	FRM II of the TUM	Germany	gunther.borchert@frm2.tum.de
Francesco Bossa	Università di Roma "La Sapienza"	Italy	bossam@caspur.it
Maxim Boyanov	University of Notre Dame	USA	mboyanov@nd.edu
Emilio Burattini	INFN-LNF	Italy	burattini@lnf.infn.it
Antonio Calò	University of Oulu	Finland	acalo@sun3.oulu.fi

Gaetano Campi	Università di Roma "La Sapienza"	Italy	gaetano.campi@roma1.infn.it
Maria Luisa Carvalho	University of Lisbon	Portugal	luisa@cii.fc.ul.pt
Júlio Cezar	Laboratório Nacional de Luz Síncrotron	Brazil	julio@lnls.br
Jean-Philippe Champeaux	LIXAM	France	jean-philippe.champeaux@lixam.u-psud.fr
Dominique Chandesris	Soleil-LURE CNRS	France	dominique.chandesris@lure.u-psud.fr
Christopher Thommas Chantler	University of Melbourne	Australia	chantler@physics.unimelb.edu.au
Jean-Francois Chemin	CNRS-IN2P3	France	chemin@cenbg.in2p3.fr
Mau Hsiung Chen	Lawrence Livermore National Laboratory	USA	chen7@llnl.gov
Jin- Ming Chen	Synchrotron Radiation Research Center	Taiwan	jmchen@srrc.gov.tw
Giannantonio Cibin	INFN-LNF	Italy	giannantonio.cibin@lnf.infn.it
Gianfelice Cinque	INFN-LNF	Italy	cinque@lnf.infn.it
Marcello Colapietro	Università di Roma "La Sapienza"	Italy	colapietro@axcasp.caspur.it
Laurent Cormier	University of Paris 6&7	France	cormier@lmcp.jussieu.fr
Enrico Costa	IAS CNR	Italy	costa@ias.rm.cnr.it
Matteo D'Astuto	ESRF	France	astuto@esrf.fr
Sultan Dabagov	INFN-LNF	Italy	dabagov@lnf.infn.it
Giuseppe Dattoli	ENEA	Italy	dattoli@frascati.enea.it
Denis Dauvergne	IPNL	France	d.dauvergne@ipnl.in2p3.fr
Ivan Davoli	Universita` di Roma Tor Vergata	Italy	ivan.davoli@roma2.infn.it
Alberto De Fanis	Tohoku University	Japan	fanis@rism.tohoku.ac.jp
Monica De Simone	Università di Roma Tre	Italy	monica.desimone@elettra.trieste.it
Piero Decleva	Universita' di Trieste	Italy	decleva@univ.trieste.it
Claudia Dell'omo	Università di Roma "La Sapienza"	Italy	claudia.dell'omo@roma1.infn.it
Christine Dezarnaud-Dandine	Laboratoire de Chimie-Phisique, Matiere et Rayonement	France	christine.desarnaud-dandine@lct.jussieu.fr
Sergio Di Matteo	INFN-LNF	Italy	dimatteo@lnf.infn.it
Vladimir E. Dmitrienko	Institute of Crystallography Moscow	Russia	dmitrien@ns.crys.ras.ru
Jean-Claude Dousse	University of Fribourg	Switzerland	jean-claude.dousse@unifr.ch

Guenter Draeger	Martin-Luther-Universitaet	Germany	draeger@physik.uni-halle.de
Hubert Ebert	University of Munich	Germany	hubert.ebert@cup.uni-muenchen.de
Simon Erenburg	Institute of Inorganic Chemistry SR RAS	Russia	simon@che.nsk.su
Charles Fadley	LBNL	USA	fadley@lbl.gov
Anatoly Faenov	MISDC of VNIIFTRI	Russia	faenov@orc.ru
Roberto Felici	ESRF	France	felici@esrf.fr
Matteo Filippi	Università di Roma “La Sapienza"	Italy	matteo.filippi@roma1.infn.it
Alain Fontaine	CNRS&ESRF	France	fontaine@labs.polycnrs-gre.fr
Paolo Fornasini	Università degli Studi di Trento	Italy	fornasin@science.unitn.it
Donald S. Gemmell	Argonne National Laboratory	USA	gemmell@anl.gov
Ettore Giovanni Gigante	Università di Roma “La Sapienza"	Italy	g.gigante@caspur.it
Pieter Glatzel	University of California	USA	pglatzel@lbl.gov
Efim Gluskin	Argonne National Laboratory	USA	gluskin@aps.anl.gov
Rolly Grisenti	Universita' degli Studi di Trento	Italy	grisenti@science.unitn.it
Renaud Guillemin	University of Nevada	USA	rguillemin@lbl.gov
Karl Heinz Hallmeier	Universitaet Leipzig	Germany	khall@rz.uni-leipzig.de
Jorgen E. Hansen	University of Amsterdam	Netherlands	jorgenh@nikhef.nl
Sami Heinäsmäki	University of Oulu	Finland	sami.heinasmaki@oulu.fi
Hans Hertz	SCFAB	Sweden	hertz@biox.kth.se
Atsunari Hiraya	Hiroshima University	Japan	hiraya@sci.hiroshima-u.ac.jp
Hirofumi Oohashi	Kyoto University	Japan	hirof@elec.kuicr.kyoto-u.ac.jp
Sabbir Hossain	Western Michigan University	USA	sabbir.hossain@wmich.edu
Joanna Hoszowska	ESRF	France	hoszowska@esrf.fr
Marie-Jeanne Hubin-Franskin	Université de Liège	Belgium	mjfranskin@ulg.ac.be
Ksenofont Ilakovac	University of Zagreb	Croatia	ilakovac@phy.hr
Yuki Iwata	Osaka Electro-Communication University	Japan	m01106@isc.osakac.ac.jp
Toshiaki Iwazumi	Institute of Materials Structure Science	Japan	toshiaki.iwazumi@kek.jp

Philippe Jonnard	Université Pierre et Marie Curie	France	jonnard@ccr.jussieu.fr
Loic Journel	Université Pierre et Marie Curie	France	journel@ccr.jussieu.fr
Nikolay Kabachnik	University of Bielefeld	Germany	nkabach@physik.uni-bielefeld.de
Akihiro Kagamihata	Osaka Electro-Communication University	Japan	m01111@isc.osakac.ac.jp
Peter Kappen	DESY	Germany	peter.kappen@desy.de
Romualdas Karazija	Institute of Theoretical Physics and Astronomy	Lithuania	email:karazija@itpa.lt
Matjaz Kavcic	J. Stefan Institute	Slovenia	matjaz.kavcic@ijs.si
Jun Kawai	Kyoto University	Japan	jkawai@process.mtl.kyoto-u.ac.jp
Richard Kelley	NASA Goddard Space Flight Center	USA	kelley@milkyway.gsfc.nasa.gov
Sabine Kessler	American Institute of Physics	USA	skessler@aip.org
Matjaz Kobal	Jozef Stefan Institute	Slovenia	matjaz.kobal@ijs.si
Andrei Kochur	Rostov State University	Russia	agk@jeo.ru
Alojz Kodre	J. Stefan Institute	Slovenia	alojz.kodre@fmf.uni-lj.si
Pawel Korecki	University of Mining	Poland	korek@castor.if.uj.edu.pl
Akio Kotani	University of Tokyo	Japan	kotani@issp.u-tokyo.ac.jp
Bertold Krässig	Argonne National Laboratory	USA	kraessig@anl.gov
Michael Krisch	ESRF	France	krisch@esrf.fr
Michele Lamoureux	CNRS	France	mla@ccr.jussieu.fr
Marei Odile Lampert	Canberra Eurisys S.A	France	molampert@canberraeurisys.com
Allen Landers	Western Michigan University	USA	allen.landers@wmich.edu
Alessandra Lanzara	University of California	USA	alessa@stanford.edu
Patrick Le Fevre	CNRS	France	patrick.le.fevre@lure.u-psud.fr
Jon Levin	University of Tennessee	USA	jlevin@utk.edu
Ingolf Lindau	Lund University	Sweden	ingolf.lindau@sljus.lu.se
Dennis Lindle	University of Nevada	USA	lindle@nevada.edu
Xinwen Ma	Chinese Academy of Science	China	x.ma@gsi.de
Pavel Machek	Martin-Luther-Universitaet	Germany	machek@physik.uni-halle.de

Artem P. Malakho	Moscow State University	Russia	cryo161a@nabla.phys.msu.ru
Pier Andrea Mandò	Università di Firenze	Italy	mando@fi.infn.it
Steven T. Manson	Georgia State University	USA	smanson@gsu.edu
Alena N. Maratkanova	Ural Branch of Russian	Russia	alyona_m@newmail.ru
Augusto Marcelli	INFN-LNF	Italy	augusto.marcelli@lnf.ifn.it
Nils O.T. Martensson	MAX-Laboratory	Italy	nils.martensson@maxlab.lu.se
Guido Martinelli	Università di Roma "La Sapienza"	Italy	marti@roma1.infn.it
Michael Martins	Universitaet Hamburg	Germany	michael.martins@desy.de
Mastroianni	Università di Roma "La Sapienza"	Italy	mastroianni@icra.it
Masahiko Matsubara	University of Tokyo	Japan	matubara@issp.u-tokyo.ac.jp
Aleksi Mattila	University of Helsinki	Finland	aleksi.mattila@helsinki.fi
Mikhail Mazuritsky	Rostov University	Russia	mazurmik@icomm.ru
Michael Meyer	LURE	France	meyer@lure.u-psud.fr
Andrej Mihelic	Jozef Stefan Institute	Slovenia	andrej.mihelic@ijs.si
Catalin Miron	LURE	France	catalin.miron@lure.u-psud.fr
Robert Moberg	Gammadata Scienta AB	Sweden	robert.moberg@gammadata.se
Alexander Moewes	University of Saskatchewan	Canada	moewes@usask.ca
Paul Mokler	GSI-Darmstadt	Germany	p.mokler@gsi.de
Giulio Monaco	ESRF	France	gmonaco@esrf.fr
Paul Morin	Centre Universitaire Paris-Sud	France	morin@soleil.u-psud.fr
Annibale Mottana	Universita` di "Roma Tre"	Italy	mottana@uniroma3.it
Takeshi Mukoyama	Kansai Gaidai University	Japan	mukoyama@kansaigaidai.ac.jp
Yasuji Muramatsu	Atomic Energy Research Institute	Japan	murama@spring8.or.jp
Jose Mustre de Leon	Los Alamos Laboratory	Mexico	mustre@kin.mda.cinvestav.mx
Velaug Myrseth	University of Bergen	Norway	velaug.myrseth@kj.uib.no
Shun-ichi Nakai	Utsunomiya University	Japan	nakai@cc.utsunomiya-u.ac.jp
Nobuyuki Nakamura	RIKEN	Japan	nobuyuki@postman.riken.go.jp
Yoshihito Namito	KEK	Japan	yoshihito.namito@kek.jp
Calogero R. Natoli	INFN-LNF	Italy	natoli@lnf.infn.it
Juha Nikkinen	University of Oulu	Finland	juha.nikkinen@oulu.fi

Shigeoka Nobuyuki	Kyoto University	Japan	shigeoka@elec.kuicr.kyoto-u.ac.jp
Patrick O'Keeffe	LURE	France	patrick.okeeffe@lure.u-psud.fr
Hiroyuki Oyanagi	University of Tsukuba	Japan	h.oyanagi@aist.go.jp
Jana Padeznik Gomilsek	University of Maribor	Slovenia	jana.padeznik@uni-mb.si
Marek Pajek	Swietokrzyska Academy	Poland	pajek@pu.kielce.pl
Patrick Palmeri	NASA Goddard Space Flight Center	USA	palmeri@sobolev.gsfc.nasa.gov
Luigi Palumbo	Università di Roma "La Sapienza"	Italy	luigi.palumbo@uniroma1.it
Selim Pasic	University of Zagreb	Croatia	spasic@phy.hr
Alessandro Patelli	INFN-LNL	Italy	patelli@lnl.infn.it
Michael Paulus	University of Dortmund	Germany	paulus@physik.uni-dortmund.de
Rupert Perera	Lawrence Berkley Laboratory	USA	rcperera@lbl.gov
Cínthia Piamonteze	LNLS	Brazil	cinthia@lnls.br
Maria Novella Piancastelli	Università di Roma "Tor Vergata"	Italy	piancastelli@roma2.infn.it
Piero Pianetta	Stanford University	USA	pianetta@slac.stanford.edu
Richard H. Pratt	University of Pittsburgh	USA	rpratt@pitt.edu
Aline Ramos	LNLS	Brazil	aramos@lnls.br
Denis Raoux	Centre Universitaire Paris-Sud	France	raoux@soleil.u-psud.fr
Valentino Rigato	INFN-Laboratori Nazionali di Legnaro	Italy	valentino.rigato@lnl.infn.it
Benjamin V. Robouch	INFN-LNF	Italy	benjamin.robouch@lnf.infn.it
Giancarlo Ruocco	Università di Roma "La Sapienza"	Italy	giancarlo.ruocco@roma1.infn.it
Leif J. Sæthre	University of Bergen	Norway	leif.sathre@kj.uib.no
Naurang Saini	Università di Roma "La Sapienza"	Italy	saini@roma1.infn.it
Norio Saito	AIST	Japan	norio.saito@aist.go.jp
Maria Sansone	Università di Roma "La Sapienza"	Italy	maria.sansone@roma1.infn.it
Karl-Heinz Schartner	Justus-Liebig-Universitaet Giessen	Germany	schartner@exp1.physik.uni-giessen.de
Martin Schenkel	University of Dortmund	Germany	schenkel@physik.uni-dortmund.de
Sebastiano Sciuti	Università di Roma "La Sapienza"	Italy	sciuti@uniroma1.it
Sarvjit Shastri	Argonne National Laboratory	USA	shastri@aps.anl.gov

Sergei Sheinerman	St. Petersburg State Maritime Technical University	Russia	sheinerman@unitel.spb.ru
Tomohiro Shibata	University of Notre Dame	USA	tshibata@nd.edu
Costantino Sigismondi	Università di Roma “La Sapienza”	Italy	sigismondi@icra.it
Marc Simon	LURE	France	simon@lure.u-psud.fr
Alexander Soldatov	Rostov University	Russia	soldatov@phys.rsu.ru
Andrey Solov'yov	A.F. Ioffe Physical-Technical Institute	Russia	solovyov@rpro.ioffe.rssi.ru
Stephen Southworth	Argonne National Laboratory	USA	southworth@anl.gov
Itzhak T. Steinberger	The Hebrew University	Israel	steinber@vms.huji.ac.il
Christian Sternemann	University of Dortmund	Germany	sternemann@physik.uni-dortmund.de
Wayne Stolte	University of Nevada	USA	wcstolte@lbl.gov
Stefano Stranges	Università di Roma “La Sapienza”	Italy	stefano.stranges@uniroma1.it
Béla Sulik	HMI	Germany	sulik@hmi.de
Svante Svensson	Uppsala University	Sweden	svante.svensson@fysik.uu.se
Kazuo Taniguti	Osaka Electro-Communication University	Japan	taniguti@isc.osakac.ac.jp
John Tanis	Western Michigan University	USA	tanis@wmich.edu
Ken T. Taylor	The Queen's University of Belfast	UK	k.taylor@qub.ac.uk
Helio C.N. Tolentino	Laboratório Nacional de Luz Síncrotron LNLS	Brasil	helio@lnls.br
Francesca Tombolini	INFN-LNF	Italy	francesca.tombolini@lnf.infn.it
Chanh Quoc Tran	University of Melbourne	Australia	tran@physics.unimelb.edu.au
Masayuki Uda	Waseda University	Japan	muda@mn.waseda.ac.jp
Kiyoshi Ueda	Tohoku University	Japan	ueda@tagen.tohoku.ac.jp
Punita Verma	Vaish College	India	punita_v2001@hotmail.com
Jens Viefhaus	Institut der Max	Germany	viefhaus@fhi-berlin.mpg.de
Aurel Mihai Vlaicu	National Institute for Materials Science	Japan	amvlaicu@sp8sun.spring8.or.jp

Maarten Vos	Australian National University	Australia	vos107@rsphysse.anu.edu.au
Philippe Wernet	Stanford University	USA	wernet@stanford.edu
Ziyu Wu	Chinese Academy of Sciences	China	wuzy@ihep.ac.cn
Francois Wuilleumier	Laboratoire de Spectroscopie Atomique et Ionique	France	francois.wuilleumier@lsai.u-psud.fr
Victor G. Yarzhemsky	Institute of General and Inorganic Chemistry of RAS	Russia	vgyar@igic.ras.ru
Hiroaki Yoshida	Hiroshima University	Japan	hyoshida@sci.hiroshima-u.ac.jp
Gianluigi Zangari	Università di Roma “La Sapienza”	Italy	gianluigi.zangari@roma1.infn.it
Michael Zharnikov	Universität Heidelberg	Germany	michael.zharnikov@urz.uni-heidelberg.de

Frascati Physics Series Volumes

Volume I – *Heavy Quarks at Fixed Target*
Eds. S. Bianco and F.L. Fabbri
Frascati, May 31-June 2, 1993
ISBN 88-86409-00-1

Volume II – Special Issue, *Les Rencontres de Physique de la Vallée d'Aoste - Results and Perspectives in Particle Physics*
Ed. M. Greco
La Thuile, Aosta Valley, March 5 -11, 1995
ISBN 88-86409-03-6

Volume III – *Heavy Quarks at Fixed Target*
Ed. B. Cox
University of Virginia, Charlottesville
October 7-10, 1994,
ISBN 88-86409-04-4

Volume IV – *Workshop on Physics and Detectors for DA□NE*
Eds. R. Baldini, F. Bossi, G. Capon, G. Pancheri
Frascati, April 4-7, 1995
ISBN 88-86409-05-2

Volume V – Special Issue, *Les Rencontres de Physique de la Vallée d'Aoste - Results and Perspectives in Particle Physics*
Ed. M. Greco
La Thuile, Aosta Valley, March 3-9, 1996
ISBN 88-86409-07-9

Volume VI – *Calorimetry in High Energy Physics*
Eds. A. Antonelli, S. Bianco, A. Calcaterra, F.L. Fabbri
Frascati, June 8-14, 1996
ISBN 88-86409-10-9

Volume VII – *Heavy Quarks at Fixed Target*
Ed. L. Köpke
Rhinefels Castle, St. Goar, October 3-6, 1996
ISBN 88-86409-11-7

Volume VIII – *ADONE a milestone on the particle way*
Ed. V. Valente –1997
ISBN 88-86409-12-5

Volume IX – Special Issue, *Les Rencontres de Physique de la Vallée d'Aoste – Results and Perspectives in Particle Physics*
Ed. M. Greco
La Thuile, Aosta Valley, March 2-8, 1997
ISBN-88-86409-13-3

Volume X – *Advanced ICFA Beam Dynamics*
Workshop on Beam Dynamics Issue for e^+e^- Factories
Eds. L. Palumbo, G. Vignola
Frascati, October 20-25, 1997
ISBN 88-86409-14-1

Volume XI – *Proceedings of the XVIII International Conference on Physics in Collision*
Eds. S. Bianco, A. Calcaterra, P. De Simone, F. L. Fabbri
Frascati, June 17-19, 1998
ISBN 88-86409-15-X

Volume XII – *Special Issue, Les Rencontres de Physique de la Vallée d'Aoste - Results and Perspectives in Particle Physics*
Ed. M. Greco
La Thuile, Aosta Valley, March 1-7, 1998
ISBN 88-86409-16-8

Volume XIII – *Bruno Touschek and the Birth of the e^+e^-*
Ed. G. Isidori
Frascati, 16 November, 1998
ISBN 88-86409-17-6

Volume XIV – Special Issue, *Les Rencontres de Physique de la Vallée d'Aoste - Results and Perspectives in Particle Physics*
Ed. M. Greco
La Thuile, Aosta Valley, February 28-March 6, 1999
ISBN 88-86409-18-4

Volume XV –*Workshop on Hadron Spectroscopy*
Eds. T. Bressani, A. Feliciello, A. Filippi
Frascati, March 8 –2 1999
ISBN 88-86409-19-2

Volume XVI –*Physics and Detectors for DA□NE*
Eds. S. Bianco, F. Bossi, G. Capon, F.L. Fabbri, P. Gianotti, G. Isidori, F. Murtas
Frascati, November 16 -19, 1999
ISBN 88-86409-21-4

Volume XVII – *Special Issue, Les Rencontres de Physique de la Vallée d'Aoste - Results and Perspectives in Particle Physics*
Ed. M. Greco
La Thuile, Aosta Valley, February 27 –March 4, 2000
ISBN 88-86409-23-0

Volume XVIII – *LNF Spring School*
Ed. G. Pancheri
Frascati 15-20 May, 2000
ISBN 88-86409-24-9

Volume XIX – *XX Physics in Collision*
Ed. G. Barreira
Lisbon June 29-July1st. 2000
ISBN 88-86409-25-7

Volume XX – *Heavy Quarks at Fixed Target*
Eds. I. Bediaga, J. Miranda, A. Reis
Rio de Janeiro, Brasil, October 9-12, 2000
ISBN 88-86409-26-5

Volume XXI –*IX International Conference on Calorimetry in High Energy Physics*
Eds. B. Aubert, J. Colas, P. Nédélec, L. Poggioli
Annecy Le Vieux Cedex, France, October 9-14, 2000
ISBN 88-86409-27-3

Volume XXII – *Special Issue, Les Rencontres de Physique de la Vallée d'Aoste - Results and Perspectives in Particle Physics*
Ed. M. Greco
La Thuile, Aosta Valley, March 4-10 , 2001
ISBN 88-86409-28-1

Volume XXIII – *XXI Physics in Collision*
Ed. Soo-Bong Kim
Seoul, Korea, June 28 –30, 2001
ISBN 88-86409-30-3

Volume XXIV – *International School of Space Science –2001 Course on: Astroparticle and Gamma-ray Physics in Space*
Eds. A. Morselli, P. Picozza
L'Aquila, Italy, August 30 –September 7, 2000
ISBN 88-86409-31-1

Volume XXV – *TRDs for the 3rd Millennium Workshop on Advanced Transition Radiation Detectors for Accelerator and Space Applications*
Eds. N. Giglietto, P. Spinelli
Bari, Italy, September 20-23, 2001
ISBN 88-86409-32-X

Volume XXVI – *KAON 2001*
International Conference on CP Violation
Eds. F. Costantini, G. Isidori, M. Sozzi
Pisa Italy, June 12th –17th, 2001
ISBN 88-86409-33-8

Volume XXVII – *Special Issue, Les Rencontres de Physique de la Vallée d'Aoste - Results and Perspectives in Particle Physics*
Ed. M. Greco
La Thuile, Aosta Valley, March 3-9, 2002
ISBN 88-86409-34-6

Volume XXVIII – *Heavy Quarks at Leptons 2002*
Eds. G. Cataldi, F. Grancagnolo, R. Perrino, S. Spagnolo
Vietri sul mare (Italy), May 27th – June 1st, 2002
ISBN 88-86409-35-4

Volume XXIX
Workshop on Radiation Dosimetry: Basic Technologies, Medical Applications, Environmental Applications
Ed. A. Zanini
Rome (Italy), February 5–6, 2002
ISBN 88-86409-36-2

Volume XXIX – Suppl.
Workshop on Radiation Dosimetry: Basic Technologies, Medical Applications, Environmental Applications
Ed. A. Zanini
Rome (Italy), February 5–6, 2002
ISBN 88-86409-36-2

Volume XXX – *Special Issue, Les Rencontres de Physique de la Vallée d'Aoste - Results and Perspectives in Particle Physics*
M. Greco
La Thuile, Aosta Valley, March 9-15, 2003
ISBN 88-86409-39-9

Volume XXXI
Frontier Science 2002 – Charm, Beauty and CP, First International Workshop on Frontier Science
L. Benussi, R. de Sangro, F.L. Fabbri, P. Valente
Frascati, October 6-11 2002
ISBN 88-86409-37-0

Volume XXXII
19th International Conference on x-ray and Inner-Shell Processes
A. Bianconi, A. Marcelli, N.L. Saini
Università di Roma "La Sapienza" June 24-28, 2002
ISBN 88-86409-39-07